Methodologies to Solve the Vibrational Schrödinger Equation

Mark A. Boyer

A dissertation
submitted in partial fulfillment of the
requirements for the degree of

Doctor of Philosophy

University of Washington

2022

Reading Committee:
Anne B. McCoy, Chair
Sotiris S. Xantheas
Charles C. Campbell

Program Authorized to Offer Degree:
Chemistry

University of Washington

Abstract

Methodologies to Solve the Vibrational Schrödinger Equation

Mark A. Boyer

Chair of the Supervisory Committee:
Professor Anne B. McCoy
Chemistry

The solution of the vibrational Schrödinger equation is of fundamental importance in the interpretation of infrared spectra and the information about the fundamental physics encoded therein. Unfortunately, due to the high dimensionality of vibrational problems, a direct solution rarely presents itself. Therefore, the development of models and methods to provide approximate solutions is crucial to the effective use of vibrational spectroscopies. In this work, various methods to solve the Schrödinger equation and models built off of such methods are presented, applied, and analyzed. First, a broad overview of the key methods in constructing representations of the molecular Hamiltonian is provided. Next, highly-accurate, low-dimensional approaches are applied to understand an interesting correlation between the frequencies of hydrogen bonds and OH bond lengths as well as to the interpretation of the vibrational spectrum of the H_5^+ molecular ion. After that, vibrational perturbation theory, an approximate, high-dimensional method is introduced and our recent developments in extending the method are discussed. Finally, recent work on using vibrational perturbation theory to identify resonances is introduced and a brief discussion of possible ways to combine vibrational perturbation theory with low-dimensional approaches is provided.

TABLE OF CONTENTS

LIST OF FIGURES

LIST OF TABLES

ACKNOWLEDGMENTS

I want to express my sincere appreciation to my friends and family, for telling me to work when I was lagging and to rest when I was burning out. I would also like to thank my advisor, Anne, for continuing to support and provide guidance despite my flakiness and I would like to apologize for the numerous gray hairs I have caused. I also want to thank the entire McCoy group for being a great crew and in particular Victor for always being there for me, Ryan for being my primary sounding board and knowing what's up, Rachel for being the first line of defense between me and unleashing buggy code and bad explanations on the world and for allowing me to help her set up McCode Academy, and Jacob for making me laugh even when I was down. It has been a journey, often fun, sometimes a slog, and I will always appreciate my time in Seattle. Finally, I'd like to thank the Link. I may have missed my train every day, but I'm glad there was always one 10 minutes away (excluding fires, construction, people having a breakdown on the tracks, etc.)

DEDICATION

to my sisters and parents, for always supporting a big nerd like me

Chapter 1

INTRODUCTION

Molecular vibrations play an integral role in many facets of chemistry, from informing the mechanisms by which reactions proceed to facilitating the flow of electrons both between molecules and on a single molecule. While it is convenient to imagine molecules as rigid collections of balls and sticks, as one would see in a textbook–or more likely when Googling a given molecule–this picture does not reflect the reality that molecules and complexes are in constant motion, moving through space, tumbling on axis, and vibrating. Even at low temperature, even at absolute zero, a molecule has some amount vibrational energy–is to some degree in flux. This zero-point vibrational energy means that the rigid ball-and-stick model misses out on important physical effects. When vibrations are accounted for, bond lengths may be longer, on average, than one would predict from the minimum-energy geometry; symmetries may be broken or apparent asymmetries may disappear; dipole moments may change orientation. These effects will all affect the reactivity of a given molecule or the stability of a molecular complex. Unfortunately, if one wants to construct a fully accurate chemical model, vibrations matter.

For over a century, infrared spectroscopy has been the primary tool for probing the vibrations of molecules and complexes. In isolation, however, an infrared spectrum has little utility. It becomes useful only when combined with a physical model with which to interpret the peaks in the spectrum. As the Schrödinger equation informs us that molecular systems can only exist in discrete energetic states, such a model is able to tell us which transition between the molecular energy levels any given peak in the spectrum corresponds to. An infrared photon, having an energy between $\sim$150 and 15000 cm^{-1}, when absorbed will correspond to an excitation of one of the allowed vibrational states in the systems,

potentially with some rotational contribution as well. The most general possible model is the full Hamiltonian of the molecular system. It is however rare that we are able to use the full Hamiltonian in directly solving the Schrödinger equation. This is due to what is often called the curse of dimensionality, in which problems that are straightforward to solve in one or two dimensions quickly become intractable as the dimension increases. A system with N atoms requires $3N$ Cartesian coordinates to fully describe the positions of its atoms, and therefore has $3N$ degrees of freedom that must be accounted for. It is therefore necessary to develop both reduced-dimensional modeling techniques as well approximation methods that can be applied in full-dimensionality.

The space of methods in vibrational spectroscopy is large, taking ideas from every branch of mathematics, and there is often a trade off between the accuracy of a method and its computational expense, or even tractability. At the lower accuracy, lower cost side of this spectrum is the harmonic approximation, introduced by Wilson and coworkers in the early days of the studies of vibrations, which uses a quadratic expansion of the molecular Hamiltonian.[1] Higher-accuracy results can be obtained with a moderate increase in computational cost by starting with the harmonic approximation and applying vibrational perturbation theory.[2,3] At the other end of the spectrum lie methods derived from representation theory. These methods, like finite basis and discrete variable representations[4] provide exact solutions to the vibrational Schrödinger equation. However, these methods are rarely applicable in full dimensionality, often requiring more memory than is available even at high-performance computing facilities–although stochastic methods such as diffusion Monte Carlo provide a notable exception.[5,6] More specific detail on these methods and others will be provided later on in this work. The core of practical quantum chemistry, then, is found somewhere between these two extremes, making use of reduced dimensional models which the use of high-accuracy methods is required and the using more approximate methods when possible.

In this work, we will first describe in more detail the core concepts and methods used. Then we will describe applications of two reduced dimensional approaches. First beginning in 2D, we will introduce a study of an interesting structure-spectral correlation in water and

ion-water clusters, which was analyzed primarily with 1D models. Next, we will look at the vibrations of the H_5^+ molecular ion under a 4D model, using an adiabatic separation. The second portion of this work will detail some of our recent developments in extending vibrational perturbation theory (VPT). We will first introduce a modern take on an old approach to VPT and discuss its benefits in the light of advances in computing. Then we will show how this approach can be extended to include the effects of vibrational resonances and why resonances matter.

This is of course only a partial accounting of the work done in the past five years while I have been at the University of Washington, and some works have been omitted in the interest of space. Among those are applications of vibrational perturbation theory to a radical analog of *tert*-butyl hydrogen peroxide[7] as well as to complexes of halides with HOCl.[8,9] Similarly, a large number of software tools and algorithmic developments have been made but have not been able to be described elsewhere. These may be found on the group's GitHub page (github.com/McCoyGroup) and include, among others, a black-box package for diffusion Monte Carlo simulations adapted for high-performance computing environments with a built-in foreign function interface for python with automatic threading, an efficient package for discrete variable representations in arbitrary dimensions, a package for the automatic construction and solution of analytic model Hamiltonians, as well as a large (>50000 lines of code) suite of optimized tools for scientific software developers.

Chapter 2

THE MOLECULAR HAMILTONIAN AND ITS REPRESENTATIONS

2.1 Introduction

For a system with N atoms, and therefore $3N$ Cartesian coordinates/degrees of freedom, the total molecular Hamiltonian is given by

$$H = \sum_{i=1}^{3N} \frac{p_i^2}{2m} + V(\chi_1, \chi_2, ..., \chi_{3N}) \tag{2.1}$$

in which p_i is the momentum operator for coordinate χ_i, the x, y, or z component of the position of one of the atoms in the system, and V is the potential energy function for the system, which in the works described below is uniformly chosen to be the energy of the electronic ground state of the system under the Born-Oppenheimer approximation, although with appropriate care electronic excited states may be treated. It is, in some sense, more natural to replace the coordinates, χ_i, with mass-weighted versions

$$\xi_i = \sqrt{m_i}\chi_i \tag{2.2}$$

This form of the Hamiltonian, while totally general, admits neither an easy route to reducing dimension nor easy solution via approximate methods, with the noted exception of diffusion Monte Carlo. It is advantageous to reexpress the Hamiltonian in internal coordinates. This is done by defining a transformation, $\mathcal{T}$, from our 3N mass-weighted Cartesian coordinates, $\{\xi_i\}$, to a corresponding set of 3N-6 internal coordinates, $\{r_i\}$. The reduction in dimension occurs because we require six coordinates to describe the embedding of our system

in Cartesian space (3 for the center of mass, 3 for the system orientation). As our internal coordinates are no longer along rectilinear Cartesian coordinates, we will need to borrow from the general relativity community and introduce a *metric tensor*, G, to account for the fact that Euclidean distances have become curvilinear arclengths. In the chemical theory literature, this tensor is more commonly known as the Wilson G-matrix, being popularized in chemical theory by Wilson.[10] Despite the intimidating name, this matrix has a simple form. We first introduce the Jacobian matrix for the coordinate transformation

$$J_{ij} = \frac{\partial r_j}{\partial \xi_i} \tag{2.3}$$

and then

$$G = J^{\intercal} J \tag{2.4}$$

With this transformation in place, the Hamiltonian may be expressed as

$$H = \sum_{i,j=1}^{3N-6} p_i G_{ij} p_j + V(r_1, r_2, ..., r_{3N-6}) + V'(r_1, r_2, ..., r_{3N-6}) \tag{2.5}$$

where V' is an artefact of choosing to write the kinetic energy in the convenient form $p_i G_{ij} p_j$.

2.2 Discrete Variable Representation

This internal coordinate form of the Hamiltonian allows for the development of reduced dimensional models. One effective approach for the construction of these models is through discrete variable representation (DVR). A good primer on discrete variable representations and their applications may be found in a review by Light and Carrington,[4] and we provide here only a few key ideas and results. We will focus, initially, on one-dimensional representations and then construct higher-dimensional representations from these lower-dimensional ones.

To construct a DVR for a given internal coordinate of interest, r, it is first obtain a

representation of the coordinate operator in a given basis, $\{\phi_i\}$

$$R_{ij} = \langle \phi_i | \, r \, | \phi_j \rangle \tag{2.6}$$

Traditional choices for ϕ_i are the classical orthogonal polynomials and the DVR developed by Colbert and Miller based on Fourier functions[11] is particularly convenient. By diagonalizing R, one obtains a transformation to a new basis, $\phi_i^{(DVR)}$, where each basis function is localized around a grid point, ρ_n, which correspond to the eigenvalues of R. In this localized basis, not only is the representation of r diagonal, but so is the representation of any operator that depends only on r and not on its derivatives. Importantly, this class of operators includes the potential energy function, V, leading to a representation where the values along the diagonal are simply the potential energy evaluated at the grid points, or $\mathbf{V}_{nm} = V(\rho_n)\delta_{nm}$. For other operators not of this form, in particular the kinetic energy operator, $p_r G_{rr} p_r$, a representation may be obtained in the original basis, $\{\phi_i\}$, and transformed to the DVR basis. Alternately analytic forms may be derived in the limit of the infinite basis, as done by Colbert and Miller for p_r^2 in their work with the Fourier basis[11] or as done by McCoy *et al.* for the representations of the momentum, p_r.[12,13]

To go beyond one-dimension, one constructs a basis as a direct product of DVR basis functions in each dimension. This idea is discussed in detail in the work of Light and Carrington. In doing so, unless the coordinates are chosen well, this will also necessitate the development of a representation of $p_i G_{ij} p_j$. Such a representation is a straightforward application of representations developed in one dimension for p_r with a direct product basis.

Discrete variable representations have many extensions, in particular they may be used in a *potential optimized* DVR approach[4] or they can be used in adiabatic separations as will be seen in Chapter 4.

2.3 Normal Modes

Alongside DVRs, another coordinate choice is the *normal mode* representation. The goal in this representation is to find a set of coordinates, q_i, in which it is possible to write the Hamiltonian as a sum of one-dimensional Hamiltonians

$$H = \frac{\hbar}{2} \sum_{i}^{3N-6} \omega_i (p_i^2 + q_i^2) \tag{2.7}$$

To obtain these modes, the Hessian matrix of the potential function, F, is evaluated at the minimum energy geometry and the generalized eigenvalue problem $Fq_i = (\omega_i)^2 G q_i$ is solved. This provides both the desired coordinates, q_i, as well as the associated frequencies ω_i. These modes provide a good initial solution to the full vibrational Schrödinger equation and as will be seen in Chapter 5 provide a good zero-order picture for more accurate solution methods.

It is worth noting that there is broad flexibility as to the choice of coordinates with respect to which the Hessian is obtained. If the set of coordinates is chosen to be $3N-6$ internal coordinates, the normal modes obtained will be expansions in these internal coordinates. It is however also possible to chooses these coordinates to be the $3N$ mass-weighted Cartestian coordinates of the system. In this case, the normal modes obtained will be expansions in the displacements of the mass-weighted Cartesian coordinates of the system. As the G-matrix is the identity matrix wen using mass-weighted Cartesian coordinates, the generalized eigenvalue problem from before reduces to finding the eigenvalues and eigenvectors of the Hessian matrix with respect to the mass-weighted Cartesian coordinates. As is necessary, given that there are $3N$ Cartesian coordinates, $3N$ eigenvalues and eigenvectors will be obtained from this analysis. Six of these, however, will have a frequency of zero, or more commonly very close to zero, as in the absence of an external electric field, the potential energy must be invariant to the rotations and translations of the system. Therefore, the normal modes with a frequency of zero will be linear combinations of the rotations and translations of the system and may be safely discarded.

Alternately, one may handle these modes *a priori*. To do so, one may first note that it is possible to write down explict forms for the generators of the translational and rotational motions. The derivation is detailed by Miller, Handy, and Adams,[14] but the key idea is to introduce the Eckart conditions, which any vibrational motion must satisfy and which provide a mathematical formalism for the notion that a vibration is decoupled from the overall translation and rotation of the system.

$$\sum_{n=1}^{N} \Delta\vec{\xi_n} = \vec{0} \tag{2.8}$$

$$\sum_{n=1}^{N} \Delta\vec{\xi_n} \times \Delta\vec{\xi_n} = \vec{0} \tag{2.9}$$

where $\Delta\vec{\xi_n}$ is the vector of such displacements for the nth atom in the system. Any vibration, expressed in terms of the displacements of the mass-weighted Cartesian coordinates of the system, must satisfy these conditions. By contrast, the translations and rotations cannot satisfy these conditions, and in particular the three translational coordinates ill not satisfy Eq. (2.8) and the rotational coordinates will not satisfy Eq. (2.9). From this, it is possible to determine three translational eigenvectors, the elements of which are given by

$$(T_\alpha)_{n,\beta} = \sqrt{\frac{m_n}{M}}\delta_{\alpha,\beta} \tag{2.10}$$

where M is the total mass of the system, $\alpha \in \{x, y, z\}$, m_n is the mass of the nth atom, and β indicates we are considering either the x, y, or z component of the nth atom. T_α is then the translation eigenvector in the α direction. The rotations are slightly more complicated, as the evalutation of cross product in matrix form requires the use of the Levi-Cevita tensor, $\epsilon_{\alpha,\beta,\gamma}$, which is also known the totally antisymmetric tensor or the direction cosine tensor. The expression for the rotation eigenvector about the α axis is then given by

$$(R_\alpha)_{n,\beta} = \sum_{\gamma\in\{x,y,z\}} -(I_0)_\alpha^{-1/2} \cdot \epsilon_{\alpha,\beta,\gamma}\xi_{n,\gamma} \tag{2.11}$$

where $\xi_{n,\gamma}$ is the γ component of the mass-weighted Cartesian coordinates for the nth atom and $(I_0)_\alpha^{-1/2}$ is the row of the square root of the inverse moment of inertia tensor for the α axis.

From these, the projector $(I - T - R)$ may be defined, which when applied to the Hessian matrix of the system removes any contribution from the translational and rotational motions. Upon diagonalizing, six modes with frequencies identical to zero will be obtained, corresponding to combinations of rotations and translations.

2.3.1 Reaction Path Normal Modes

The method for obtaining normal modes detailed above only applies to normal modes evaluated at a stationary point on the potential. This is because the desired form of the Hamiltonian contains q_i^2, and so the contribution to the expansion of the potential from the gradient is assumed to be zero. As detailed by Miller, Handy, and Adams, by making use of a reaction path normal mode analysis, it is possible to obtain normal modes at positions away from a stationary point by noting that the expansion of the potential at such non-stationary point is given by

$$V(\vec{\xi}) = \sum_{i=1}^{3N} \frac{\partial V}{\partial \xi_i} \Delta\xi_i + \sum_{i,j=1}^{3N} \frac{1}{2} \frac{\partial V}{\partial \xi_i \partial \xi_j} \Delta\xi_i \Delta\xi_j \tag{2.12}$$

By defining $\vec{a}$ to be the unit vector in the direction of the gradient of the potential, we will note that we can project out the entirety of the gradient contribution. Combining this with the projectors for the translations and rotations from before, we can construct a $3N - 7$ dimensional subspace in which the contribution to the expansion of the potential energy from the gradient vanishes. From this, we can write

$$V_{\mathrm{RP}}(\vec{\xi}) = \sum_{i,j=1}^{3N-7} \frac{1}{2} \frac{\partial V}{\partial q_i \partial q_j} \Delta q_i \Delta q_j \tag{2.13}$$

where the q_i will now be the *reaction path* normal modes, or the normal modes orthogonal to the motion along the coordinate that minimizes the potential energy and V_{RP} is the expansion

of the potential in the space of these modes. As before, these modes and their associated frequencies are then obtained by diagonalizing PFP but now for $P = I - T - R - \vec{a}$.

This analysis was performed in the mass-weighted Cartesian coordinates, but in certain cases the analysis can be even easier in internal coordinates. The main insight here is that often one is interested in obtaining the potential along some internal coordinate a while allowing all other coordinates to relax to their optimized value. In this case, the direction of the gradient is clearly along the vector corresponding to displacements of the a coordinate. Therefore, we may simply use the Hessian matrix with respect to the $3N - 7$ *internal* coordinates excluding the a coordinate. By evaluating the G-matrix in this subspace as well, we may simply use the generalized eigenvalue problem approach from before and obviate the need for any projection operators. On the other hand, if one is not optimizing the energy with respect to all coordinates but one, the identification of the a mode may not be possible *a priori* and the use of the potential gradient unit vector once again becomes necessary.

2.4 Mixed Representations

It is often the case that the use of only a single representation proves insufficient to accurately model the vibration spectrum of a molecule, ion, or complex. The highly-accurate discrete variable representations become prohibitively expensive while the normal mode representations are insufficiently accurate unless large basis sets are used. To alleviate both of these issues, a mixed model is often used. In this model, an important coordinate or subspace of coordinates is first identified. In a study of a radical analog of *tert*-butyl hydrogen peroxide, these motions were the OH stretching motion of the peroxide group and its torsional motion.[7] A mixed representation is then developed, where these coordinates will be treated through DVRs and the remaining coordinates will contribute via a cheaper approach, often something like the reaction path normal modes discussed previously. These less important modes can then contribute zero-point energy effects or other quantities as a function of the important coordinates. The DVRs in the important modes may then be

solved directly or through something like an adiabatic approximation.In this way, a solution is obtained in which effects of all of the degrees of freedom of the system are included, but the computational cost is lowered as the less-important degrees of freedom are treated with cheaper approaches.

2.5 Conclusion

Constructing a molecular Hamiltonian for a given chemical system is fundamental for making connections between experimental observables and underlying physical reality. One has broad flexibility in terms of the specific method used in the representation of the Hamiltonian. Two very commonly used representations are the discrete variable representation, in which a basis is chosen to allow the representation of the system's potential energy to be as simple as possible, and the normal mode representation, which provides the best representation under the approximation that the potential energy is diagonal. Formally, all representations of the Hamiltonian are equivalent. That is, once diagonalized, the values of the energies and any other properties for the system will be the same. The only difference between representations, then, is in the model used to interpret the results obtained. Formally, there is also a true, exact Hamiltonian which if constructed would allow one to solve the molecular Schrödinger equation exactly. In reality, the need to construct the representation of such a Hamiltonian on a real-world computer makes creating an representation of the total molecular Hamiltonian impossible, or at least intractable, in most cases. Moreover, this unfortunate restriction to real-world hardware means the choice of representation matters, as different representations will be better suited to solving different problems. In the rest of this work, various representations will be used, ranging from one-dimensional discrete variable representations to full-dimensional representations constructed from normal modes.

Chapter 3

BEYOND BADGER'S RULE: THE ORIGINS AND GENERALITY OF THE STRUCTURE–SPECTRA RELATIONSHIP OF AQUEOUS HYDROGEN BONDS

Reproduced with permission from [Mark A. Boyer, Ondrej Marsalek, Joseph P. Heindel, Thomas E. Markland, Anne B. McCoy, and Sotiris S. Xantheas. Beyond Badger's Rule: The Origins and Generality of the Structure-Spectra Relationship of Aqueous Hydrogen Bonds. *J. Phys. Chem. Lett.*, 10(5):918–924, mar 2019]

3.1 Introduction

Hydrogen bonding plays a critical role in phenomena ranging from aqueous solvation and reactivity, biological structure and function to homogeneous catalysis and atmospheric processes. A hallmark of hydrogen bond formation is the decrease (red shift) of the vibrational frequency of the covalent bond, which participates in the hydrogen bond, relative to the isolated species. Due to the wide variety of hydrogen bond strengths observed in gas and condensed phase systems, these red shifts range from a few tens to more than 2000 cm^{-1}.[16] Vibrational spectroscopies, such as infrared (IR) and Raman, can be used to probe these shifts in environments ranging from simple clusters[17–22] to more complicated aqueous solutions.[23–27]

Due to the broad availability and applicability of vibrational spectroscopy techniques, there have been extensive experimental and theoretical studies of the vibrational shifts in hydrogen-bonded systems. These studies demonstrated a number of intriguing correlations between shifts in the covalent bond vibrational frequency and the structural and energetic properties of the hydrogen bond.[28–36] Perhaps the most remarkable of these correlations

is the one between the increase in the equilibrium OH covalent bond length of the hydrogen bond donor (R_e) and the corresponding decrease in the harmonic frequency associated with that OH bond (ω).[31,32,37] This correlation, which has been well established for over 50 years,[16] has been observed experimentally[30,36,38–40] for intra- and inter-molecular hydrogen bonds and theoretically using various levels of electronic structure methods[31,41,42] as well as simple, but physically insightful, models of hydrogen bonds.[32,37,43,44] What is particularly noteworthy about this correlation is that the relationship is surprisingly robust over a wide range of hydrogen bond strengths, both with respect to its linearity as well as the value of the slope obtained. For example in a series of studies, one of us investigated the linear relationship between the shift in the harmonic OH stretch frequency from that of an isolated water molecule ($\Delta\omega$) and the shift in the equilibrium OH bond length from its value in an isolated water molecule (ΔR_e)[42] for a broad range of hydrogen-bonded systems. These included clusters of water molecules (where $\Delta\omega/\Delta R_e = -20.2$ cm^{-1}/0.001 Å),[31,42] hydrogen-bonded complexes of alcohols ($\Delta\omega/\Delta R_e = -20.4$ cm^{-1}/0.001 Å),[45] and hydrogen-bonded complexes involving HCl ($\Delta\omega/\Delta R_e = -15.7$ cm^{-1}/0.001 Å).[46] Interestingly, when calculations on water clusters were performed at the Hartree-Fock, MP2 and CCSD(T) levels of theory, this shift was observed to be independent of the level of electronic structure theory used.[42] However, while the previous theoretical predictions offer useful insights into the interplay between the underlying molecular structure and the corresponding stretching vibration of the hydrogen-bonded OH bond, they have mainly focused on the relationship between the changes in the equilibrium bond lengths and the corresponding harmonic frequencies. As such, they are limited in their connection with the experimentally observed structures, which are associated with larger vibrationally averaged bond lengths (R_0) and corresponding anharmonic transition frequencies (ν), which include substantial anharmonicities.

Here we show that the universal linear correlation between the elongation of the covalent bond and the corresponding red shift of the vibrational frequency persists for both equilibrium/harmonic and vibrationally averaged/anharmonic pairs. We demonstrate this by extending both the range of water clusters considered to incorporate halide and hydronium

ions as well as the system size, extending from clusters to liquid water. By doing this we show that, owing to the robustness of this correlation, one can accurately reconstruct the condensed phase OH stretching region of the spectra from knowledge of the vibrationally averaged bond length distribution. Finally, we explore the underlying origin of this correlation using a simple model of the hydrogen bond. We also investigate how this correlation can be used to elucidate the success of the frequently employed electric field mapping approaches to obtain vibrational spectra.[47–53]

3.2 Theoretical Methods

Second order vibrational perturbation theory (VPT2) is used to evaluate the zero-point averaged bond lengths (R_0), which are used to evaluate the correlations between these quantities and the anharmonic frequencies, the later are also obtained using VPT2. Following standard approaches for vibrational perturbation theory, the Hamiltonian is partitioned as

$$H = H^{(0)} + H^{(1)} + H^{(2)} + \cdots \tag{3.1}$$

where $H^{(0)}$ contains the harmonic terms in the Hamiltonian, expressed in dimensionless normal mode coordinates and their conjugate momenta

$$H^{(0)} = \frac{1}{2}\sum_m \omega_m (p_m^2 + q_m^2) \tag{3.2}$$

and $\hbar = 1$ throughout this discussion. The first order correction, $H^{(1)}$, contains cubic terms in the normal coordinates and their conjugate momenta, the second order correction contains quartic terms, and so forth. In the same manner, R is expanded as

$$R = R_e + R^{(1)} + R^{(2)} + \cdots \tag{3.3}$$

where R_e provides the equilibrium OH bond length, $R^{(1)}$ contains linear terms in the expansion of R in normal coordinates, while $R^{(2)}$ contains quadratic terms. If the normal

coordinates are constructed as linear combinations of displacements of internal coordinates, the expansion of R contains only linear terms. In this case,

$$R_0 \approx -\frac{1}{4}\sum_m \frac{1}{\omega_m}\frac{\partial R}{\partial q_m}\sum_l \left(\frac{\partial^3 V}{\partial q_l^2 \partial q_m} + \frac{\partial G_{ll}}{\partial q_m}\right) \tag{3.4}$$

where G_{ll} represents a diagonal element of the Wilson G-matrix.[1]

The expansion will contain higher order terms when the normal coordinates are expressed as linear combinations of the displacements of Cartesian coordinates, as is typically used in the normal mode analyses implemented in electronic structure program packages like Gaussian.[54] In this case,[55,56]

$$R_0 \approx -\frac{1}{4}\sum_m \left[\frac{1}{\omega_m}\frac{\partial R}{\partial q_m}\sum_l \frac{\partial^3 V}{\partial q_l^2 \partial q_m} - \frac{\partial^2 R}{\partial q_m^2}\right] \tag{3.5}$$

For the evaluation of the vibrationally averaged bond lengths using Eq. 3.5, the cubic force constants were obtained from a VPT2 calculation performed using Gaussian 09,[54] while the second derivatives of the bond lengths with respect to the normal coordinates were evaluated numerically using a second order finite difference scheme.

3.2.1 Analysis of a Morse Oscillator in a Uniform Electric Field

A common way to explore the dependence of OH bond lengths, stretch frequencies and intensities on the local environment is to represent the local environment by the electric field, which arises from the electrostatic properties of other molecules in the system. We focus on an analytic exploration of these effects, asking how the frequency and intensity of this oscillator is affected by the field strength. In this analysis, we consider a quadratic expansion of the component of the dipole moment along the OH bond in terms of the OH bond length, R. Specifically,

$$H = H_M - \vec{\mathcal{E}}\cdot\vec{\mu} = \frac{p^2}{2\mu} + D_e\left(1 - e^{-\alpha\Delta R}\right)^2 - \mathcal{E}_{\mathrm{OH}}\left(\mu^{(1)}\Delta R + \frac{\mu^{(2)}}{2}\Delta R^2\right) \tag{3.6}$$

where $\vec{\mathcal{E}}$ is the field strength which has a projection along the hydrogen-bonded OH bond of $\mathcal{E}_{\mathrm{OH}}$, while $\mu^{(1)}$ and $\mu^{(2)}$ provide the first and second derivatives of the dipole moment parallel to the OH bond when the dipole moment is expanded about the equilibrium configuration for the water molecule. The Morse oscillator is described by the dissociation energy, $D_e = 0.9997$ aJ, and a range parameter, $\alpha = 2.0531$ Å^{-1}, where the values of D_e and α are taken from the water potential developed by Halonen and Carrington (Fit 1).[57] Finally μ represents the reduced mass of OH. Expanding the potential to second order, we find that the minimum in the potential,

$$R_e(\mathcal{E}_{\mathrm{OH}}) \approx R_e(0) + \frac{\mathcal{E}_{\mathrm{OH}}\mu^{(1)}}{2D_e\alpha^2 - \mathcal{E}_{\mathrm{OH}}\mu^{(2)}} \tag{3.7}$$

Likewise, if we evaluate the second derivative of the potential at this geometry, we obtain

$$\left.\frac{d^2V}{dR^2}\right|_{r_e(\mathcal{E}_{\mathrm{OH}})} = 2D\alpha^2 - 6D\alpha^3(R_e(\mathcal{E}_{\mathrm{OH}}) - R_e(0)) - \mathcal{E}_{\mathrm{OH}}\mu^{(2)} \tag{3.8}$$

and a field-dependent frequency of

$$\omega(\mathcal{E}_{\mathrm{OH}}) = \omega(0) - \frac{3\alpha\omega(0)}{2}\left(R_e(\mathcal{E}_{\mathrm{OH}}) - R_e(0)\right) - \frac{\mu^{(2)}\omega(0)}{4D_e\alpha^2}\mathcal{E}_{\mathrm{OH}} \tag{3.9}$$

Combining, the above relationships and retaining the field-independent terms,

$$\frac{\omega(\mathcal{E}_{\mathrm{OH}}) - \omega(0)}{R_e(\mathcal{E}_{\mathrm{OH}}) - R_e(0)} = -\frac{3\alpha\omega(0)}{2} - \frac{\omega(0)\mu^{(2)}}{2\mu^{(1)}} \tag{3.10}$$

The first term in Eq. 3.10 depends only on the parameters of the Morse potential, while the second is sensitive to the environment as the non-zero second derivative of the dipole surface reflects the fact that the partial charge of the transferring proton increases as the OH bond is extended.

When we introduce anharmonicity, the frequency is shifted by

$$\nu(\mathcal{E}_{\mathrm{OH}}) - \omega(\mathcal{E}_{\mathrm{OH}}) = -2\omega x(\mathcal{E}_{\mathrm{OH}}) \tag{3.11}$$

where ωx is the standard anharmonicity constant. Analysis of the Morse oscillator, yields

$$-2\omega x(\mathcal{E}_{\rm OH}) = -\frac{\omega^2(\mathcal{E}_{\rm OH})}{4D(\mathcal{E}_{\rm OH})} = -\frac{\alpha^2(\mathcal{E}_{\rm OH})}{\mu} \tag{3.12}$$

Using the above relationship for $R_0(\mathcal{E})$,

$$R_0(\mathcal{E}_{\rm OH}) - R_e(\mathcal{E}) = -\frac{1}{4\omega(\mathcal{E}_{\rm OH})}\frac{\partial^3 V}{\partial R^3}\sqrt{\frac{1}{\mu\omega(\mathcal{E}_{\rm OH})}} \tag{3.13}$$

since in this one-dimensional case, $q = R/\sqrt{\mu\omega(\mathcal{E}_{\rm OH})}$. Rearranging, results in the relationship

$$\frac{\nu(\mathcal{E}_{\rm OH}) - \omega(\mathcal{E}_{\rm OH})}{R_0(\mathcal{E}_{\rm OH}) - R_e(\mathcal{E}_{\rm OH})} = -\frac{4\alpha(\mathcal{E}_{\rm OH})\omega(\mathcal{E}_{\rm OH}))}{3} \tag{3.14}$$

This result shows that as the ratio of the decrease in frequency to the increase in OH bond length with the inclusion of anharmonicity is similar in magnitude to the proportionality constant found for the ratio between the shift in the harmonic frequency to the shift in the equilibrium bond length resulting from interaction with an external field. In this way, the effect of anharmonicity is to shift the position of the point along the $\Delta\omega$ vs. ΔR correlation, developed above, rather than shifting it away from this line. Rewriting this expression,

$$\begin{aligned}
\nu(\mathcal{E}_{\rm OH}) - \nu(0) &= \omega(\mathcal{E}_{\rm OH}) - \omega(0) - \frac{4}{3}\alpha(\mathcal{E}_{\rm OH})\omega(\mathcal{E}_{\rm OH})\left(R_0(\mathcal{E}_{\rm OH}) - R_e(\mathcal{E}_{\rm OH})\right) \\
&\quad + \frac{4}{3}\alpha(0)\omega(0)\left(R_0(0) - R_e(0)\right) \\
&\approx \omega(\mathcal{E}_{\rm OH}) - \omega(0) \\
&\quad - \frac{4}{3}\alpha(0)\omega(0)\left[\left(R_0(\mathcal{E}_{\rm OH}) - R_0(0)\right) - \left(R_e(\mathcal{E}_{\rm OH}) - R_e(0)\right)\right]
\end{aligned} \tag{3.15}$$

3.3 Results and Discussion

To start, we have investigated the correlations between the OH bond lengths (R_e or R_0) and the OH stretch frequency (ω or ν, respectively) for a series of water clusters and water clusters containing hydronium or halide ions. The list of the clusters considered in this work along with their structures is provided in Tables 3.1 to 3.4 and illustrated in Figures 3.1 to 3.3. Here the anharmonic frequencies are calcualted using second-order vibrational perturbation theory (VPT2) calculations, based on MP2/aug-cc-pVDZ calculations of the electronic structure as implemented in Gaussian 09,[54] while the vibrationally averaged bond lengths are evaluated using[55,56,58]

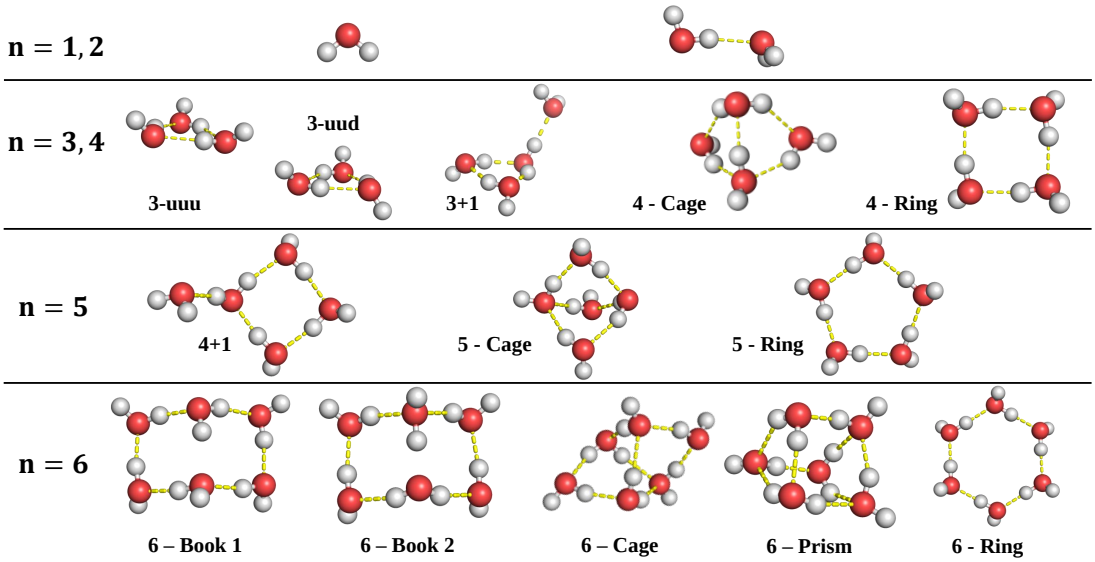

Figure 3.1: Neutral water clusters considered in this study, $(H_2O)_n$, where n is the number of water molecules in each cluster.

$$R_0 = R_e - \sum_{m=1}^{3N-6} \left[\frac{1}{4\omega_n} \frac{\partial R}{\partial q_m} \sum_{l=1}^{3N-6} \frac{\partial^3 V}{\partial q_l^2 \partial q_m} - \frac{\partial^2 R}{\partial q_m^2} \right] \tag{3.16}$$

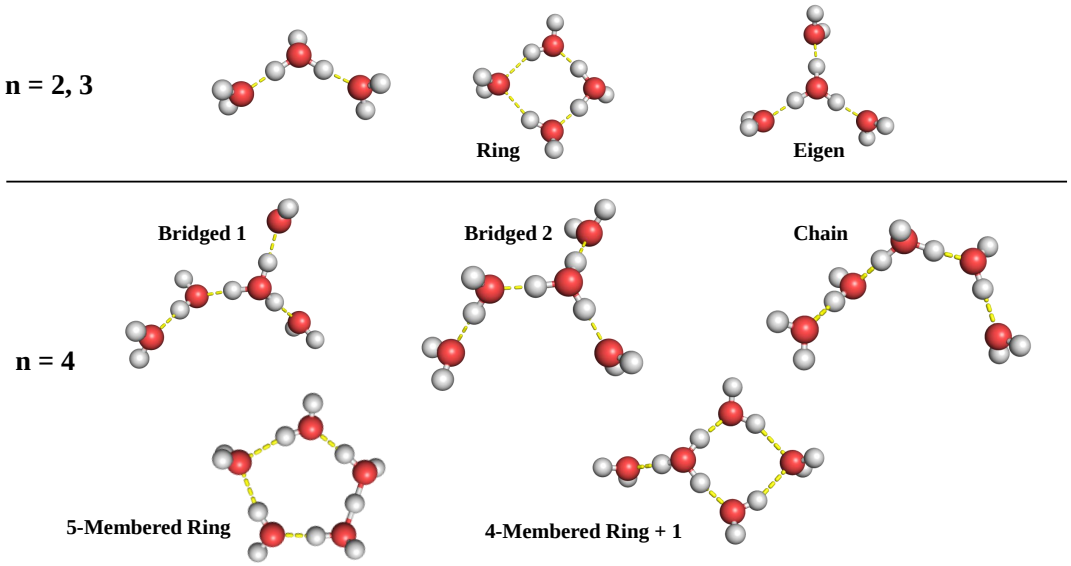

Figure 3.2: Hydronium-water clusters considered in this study, $H_3O^+(H_2O)_n$, where n is the number of water molecules in each cluster.

where the summations are over the normal modes, q_m, with harmonic frequencies ω_m. Here and in the following equations, $\hbar = 1$. We should note that these quantities differ from the S_z values reported in the outputs of some electronic structure calculations through the inclusion of the $\partial^2 R/\partial q_m^2$ term. In the absence of this term, the S_z value corresponds to changes in the projection of the OH bond length onto OH bond vector in the equilibrium structure, which is often shorter than the vibrationally averaged OH bond length.

The correlation between changes in the anharmonic frequencies with respect to changes in the vibrationally averaged length of the associated OH bond, computed relative to the values for an isolated water molecule calculated at the same level of theory, is shown in Figure 3.4. This plot also contains the results obtained based on the equilibrium structures and the corresponding harmonic frequencies. Interestingly all of the data lie along a single line, with a slope of -19.1 cm^{-1}/0.001 Å, and R^2=0.9938. The results are also divided

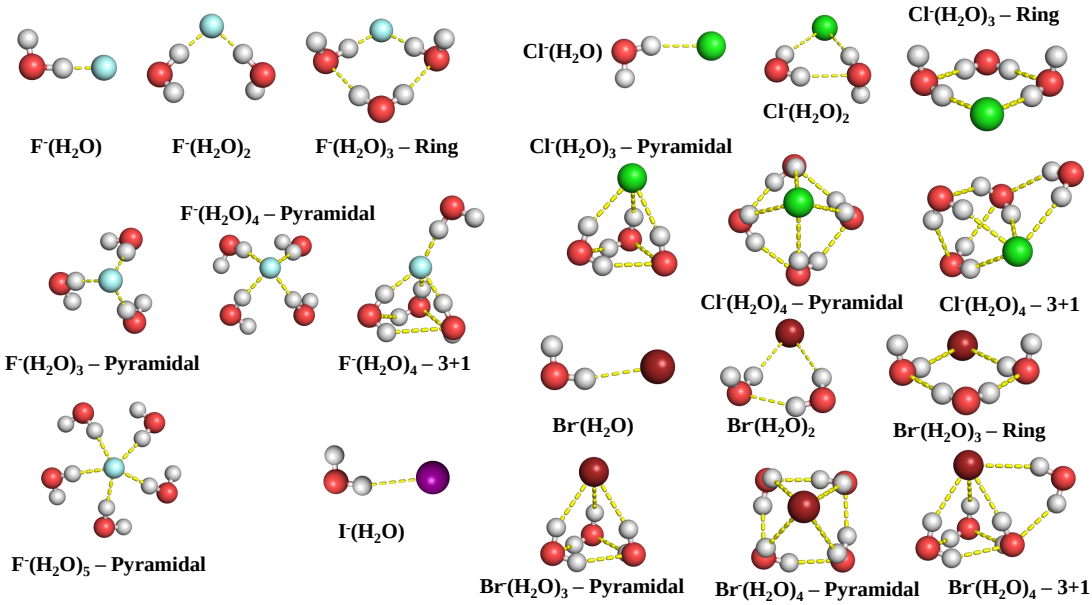

Figure 3.3: Halide-water complexes considered in this study, $X^{-}(H_2O)_n$, where n is the number of water molecules in each cluster.

according to the type of system (e.g. water clusters, hydronium water clusters, and various halide water clusters, the latter containing both the ion-water and water-water hydrogen bonds). The correlations for each of these systems are individually provided in Figures 3.5 to 3.9. While the slopes vary slightly among these systems, they are all between -17.6 and -20.1 cm^{-1}/0.001 Å.

Based on the apparent universality of this correlation for a wide range of water clusters, we repeated the analysis using the results of *ab initio* molecular dynamics (AIMD) simulations of liquid water using the revPBE-D3 density functional. This level of electronic structure theory has been shown to reproduce the experimental infrared spectrum of liquid water.[59] This analysis of the AIMD trajectory allows us to explore the correlation between OH frequencies, bond lengths and their environment in liquid wate. The results are provided in Figure 3.10. Again, the data lies close to a single line, with a slope of -18.8 cm^{-1}/0.001 Å, which is

0.3 cm^{-1}/0.001 Å smaller than the value obtained for the hydrogen bonded clusters. The present study demonstrates that the same slope can be used to describe the correlation between frequency shifts and elongations of the corresponding OH bond length obtained from harmonic and anharmonic data in both water clusters and in liquid water.

The question naturally arises as to the origin of this correlation. To answer this question, we modeled the OH bond as a Morse oscillator in the presence of an external electric field. Here the electric field is used to approximate the perturbation to an OH oscillator upon hydrogen bond formation. For this system,

$$H = H_{\mathrm{M}} - \vec{\mathcal{E}} \cdot \vec{\mu} = \frac{p^2}{2\mu} + D_e \left(1 - \exp\left[-\alpha \Delta R\right]\right)^2 - \mathcal{E}_{\mathrm{OH}} \left(\mu^{(1)} \Delta R + \frac{\mu^{(2)} \Delta R^2}{2}\right) \tag{3.17}$$

where D_e represents the dissociation energy of the Morse oscillator and α determines the width of the potential, while $\mu^{(n)}$ represents the nth derivative of the dipole moment vector along the OH bond evaluated at $\Delta R = 0$, and $\mathcal{E}_{\mathrm{OH}}$ provides the magnitude of the electric field along the OH bond axis. The truncation of the expansion of the dipole at second order is supported by fits to scans of the dipole moment along the hydrogen-bonded OH bond in the water dimer, shown in Figures 3.11 and 3.12.

As discussed above, expanding the potential to second order in the bond displacement, and evaluating the electric field-dependent equilibrium bond length, $R_e(\mathcal{E}_{\mathrm{OH}})$, and harmonic frequency, $\omega(\mathcal{E}_{\mathrm{OH}})$, allows us to develop an expression for

$$\frac{\Delta\omega}{\Delta R_e} = -\frac{\omega(\mathcal{E}_{\mathrm{OH}}) - \omega(\mathcal{E}_{\mathrm{OH}} = 0)}{R_e(\mathcal{E}_{\mathrm{OH}}) - R_e(\mathcal{E}_{\mathrm{OH}} = 0)} = -1.5\alpha\omega(\mathcal{E}_{\mathrm{OH}} = 0) - \frac{\mu^{(2)}}{2\mu^{(1)}}\omega(\mathcal{E}_{\mathrm{OH}} = 0) \tag{3.18}$$

In addition, we show that

$$\Delta\nu(\mathcal{E}_{\mathrm{OH}}) - \Delta\omega(\mathcal{E}_{\mathrm{OH}}) \approx -\frac{4\alpha\omega(\mathcal{E}_{\mathrm{OH}} = 0)}{3} \left(\Delta R_0(\mathcal{E}_{\mathrm{OH}}) - \Delta R_e(\mathcal{E}_{\mathrm{OH}})\right) \tag{3.19}$$

Using values for ω and α for a Morse oscillator model of the OH stretch of water developed by Halonen and Carrington,[57] the first term in Eq 3.18 gives $-1.5\alpha\omega = -12$ cm^{-1}/0.001 Å, and is independent of the environment of the OH bond. The second term depends on the ratio of the dipole derivatives, $\mu^{(2)}/\mu^{(1)}$, and thus depends on the environment the OH bond experiences. However, calculations based on the equilibrium structure of the water dimer (described below) yield a value of -9 cm^{-1}/0.001 Å for the second term in Eq. 3.18. This results in a ratio of the change in frequency with OH covalent bond length of -21 cm^{-1}/0.001 Å, which is in good agreement with the results reported in Figure 3.4. The anharmonicity correction in Eq. 3.19 indicates that a shift in ΔR_0 relative to the corresponding ΔR_e by 0.001 Å should lead to a roughly -10.7 cm^{-1} shift in the $\Delta\nu$ relative to $\Delta\omega$. This would lead to the expectation that the slope obtained, when only the anharmonic data that is included in Figure 3.4 is considered, will be less steep than the slope that is obtained when only the harmonic values are considered. This is consistent with our results for the water clusters, where the slope for the equilibrium values is -20.6 cm^{-1}/0.001 Å, while the slope when only the zero-point information is included was decreased in magnitude to a value of -19.7 cm^{-1}/0.001 Å (see Figures 3.6 and 3.7).

This model, which is based on the hydrogen-bonding environment of an isolated OH bond in a water molecule reproduces the observed trends. As can be seen from the results provided in the left panel of Figure 3.13, changing the OO distance (R_{OO}) in the dimer at which the dipole derivatives are evaluated from 2.75 to 3.75 Å leads to calculated $\Delta\omega(\mathcal{E})/\Delta R_e(\mathcal{E})$ ratios that range from -16 to -22 cm^{-1}/0.001 Å. This range is consistent with the range of $\Delta\omega/\Delta R_e$ and $\Delta\nu/\Delta R_0$ ratios found in our data set, and plotted in the right panel of Figure 3.13. This range is also in line with the range of OO distances found for the first coordination shell of hydrogen bonded liquids.

It is interesting to consider the origin of the range of the ratios of the frequency shifts to the change in the OH distances seen in the right panel of Figure 3.13. To aid in understanding, the data has been divided into the contributions from different system types, water and hydronium water clusters (plotted with the blue dot-dashed curve) and halide water clusters

(plotted with the green dashed curve). While both distributions have similar breadth, and sample the same range of $\Delta\omega/\Delta R_e$ values as the data reported in the left panel of this figure, the halide water distribution shows two distinct peaks. The range of values of $\Delta\omega/\Delta R_e$ and the bimodality of the halide water distribution both reflect the fact that the response of the OH frequency and OH bond length to the environment depends on the dipole response to the environment. For example, the two peaks in the $X^-(H_2O)_n$ distribution (green dashed line) reflect the two types of hydrogen bonds in these clusters. The peak above 18 $cm^{-1}/0.001$ Å reflects hydrogen bonds between a water molecule and the halide ion, while the peak below 18 $cm^{-1}/0.001$ Å reflects hydrogen bonds between two water molecules.

Since the term in Eq. 3.17 that depends on the dipole derivatives contributes roughly a third of the magnitude of the ratio of the shifts in frequencies to the shifts in OH bond lengths, a 50% a change in the size of $\mu^{(2)}/\mu^{(1)}$ changes the resulting slope only by ∼10%. This explains why the data reported in Figure 3.4 can be modeled by a linear correlation. Finally, as we consider the linear fit of the $\Delta\omega/\Delta R_e$ values as a function of $\mu^{(2)}/\mu^{(1)}$ in Figure 3.13, we find that the slope is close to the 3870 cm^{-1} harmonic frequency of an OH bond based on the Morse oscillator model used in this study. Likewise, the intercept is close to the $-1.5\omega\alpha = -12$ $cm^{-1}/0.001$ Å value anticipated by Eq. 3.18.

Based on the values for $R_0(\mathcal{E}_{OH}) - R_0(0)$ and for $R_e(\mathcal{E}_{OH}) - R_e(0)$ reported in Tables 3.1 to 3.4, we find that the difference between these two quantities is small (roughly 5% of the value of $R_e(\mathcal{E}_{OH}) - R_e(0)$). The above relationship anticipates the fact that the same holds in the size of the shift in the anharmonic frequency with electric field compared to the harmonic frequency (from Tables 3.1 - 3.4, this is roughly 6% of the value of the shift in frequency with electric field). Based on these results, it is not surprising that the harmonic and anharmonic results lie on the same curve as seen in Figure 3.4.

To further explore and to test the validity of the analytic results described above, we have investigated a series of models, using numerical approaches to evaluate the frequency and bond length displacements. For this part of the study, the electronic structure calculations were performed at the MP2/aug-cc-pVDZ level of theory and basis as implemented in

Gaussian 09[54] to be consistent with the work on the water clusters.

In the first set of calculations, we focus on the shifts in frequencies and bond lengths when $\mu^{(2)}$ in Eq. 3.6 is zero, and the potential is described using a Morse oscillator. For a harmonic treatment the equilibrium bond length and harmonic frequency are evaluated analytically over a range of values of $\mathcal{E}_{\mathrm{OH}}$. The results are plotted in Figure 3.14, and are fit to a line with an intercept at the origin. As is seen, the slope of the fit line, -11.3 cm^{-1}/0.001 Å, is close to the expected value of -12 cm^{-1}/0.001 Å. When anharmonicity in the potential is accounted for in the evaluation of ν and R_0, the slope is increased to -11.1 cm^{-1}/0.001 Å. These results are plotted and fit to a line in Figure 3.15. This reduction in the magnitude of the slope is consistent with the results provided in Eqs. 3.19 and 3.15, as discussed in the main text.

If the Morse oscillator is replaced by the potential obtained by scanning the OH bond length in water obtained at the MP2/aug-cc-pVDZ level of theory and basis, with the other OH bond length and HOH angle constrained to their equilibrium values, the slopes decrease to -12.4 and -11.8 for the harmonic and anharmonic results, respectively. These results are provided in Figures 3.16 and 3.17 and demonstrate that the Morse oscillator provides a reasonable approximation to the potential along an intramolecular OH stretch in water.

For both of these models and those described below, the anharmonic energies and wave functions are evaluated using a discrete variable representation[11] based on an evenly space grid of 251 points ranging from $\Delta R = -0.4$ Å to 1.0 Å, and μ is the reduced mass of the OH stretch.

Clearly, a linear approximation to the dipole moment is insufficient to describe the response of the OH stretch frequency and the bond length to the external field. In the third system, we evaluated the OH stretch potential for an OH bond in water in the presence of various electric field strengths, where the external field is included in the electronic structure calculation. The results are provided in Figures 3.18 and 3.19. This explicit consideration of the electric field decreases the slopes of these plots to -14.5 cm^{-1}/0.001 Å (harmonic) and -14.1 cm^{-1}/0.001 Å (anharmonic), which are close to the value of -16 cm^{-1}/0.001 Å

reported by Hermansson[47] based on a different level of electronic structure theory.

Finally, we look at the dependence of the OH stretch frequency in the context of a hydrogen-bonding environment. This is accomplished by using the Hamiltonian provided in Eq. 3.6 where the dipole derivatives are based on scans of the length of the hydrogen-bonded OH bond for a specified OO distance in water dimer. Specifically, we constrain the O-H$\cdots$O angle in the dimer to 180°, and perform a scan of the potential and dipole surfaces of water dimer, in which the OO distance ranges from 2.5721 Å to 3.8221 Å in increments of 0.05 Å, optimizing the four OH bond lengths, while keeping all other coordinates constrained to their values in the equilibrium configuration of the dimer. At each point in this scan, the hydrogen-bonded OH bond length is varied from 0.57274 Å to 1.82274 Å in increments of 0.01 Å, keeping all other internal degrees of freedom constrained to the values obtained from the scan of the OO distance, R_{OO}. We fit the projection of the dipole moments along the hydrogen-bonded OH bond, obtained from the scan, to a quadratic polynomial in ΔR. A sample of the data obtained with $R_{\mathrm{OO}} = 2.97$ Å and a quadratic fit to that data are provided in Figure 3.11, noting the accuracy of the quadratic fit. This dipole surface was then used in conjunction with the Morse oscillator described above to generate a set of potential curves based on Eq. 3.6, using a range of field strengths, $\mathcal{E}$.

The resulting correlations between the frequencies and OH bond lengths for $R_{\mathrm{OO}} = 2.97$ Å and various values of $\mathcal{E}_{\mathrm{OH}}$ are provided in Figure 3.20 for the harmonic frequencies and equilibrium bond lengths and Figure 3.21 for the anharmonic frequencies and vibrationally averaged OH distances. These data sets are fit to lines with slopes of -21.3 and -20.5 $\mathrm{cm}^{-1}/0.001$Å, respectively. Analogous calculations were performed using expansion of the dipole moment along the hydrogen bonded OH bond for other values of the OO distance, and the resulting slopes are summarized in Figures 3.13, 3.22 and 3.23, and associated data are provided in Table 3.5. Analysis of the parameters in linear fits to these data show slopes of 3800 cm^{-1} and 3400 cm^{-1} for the harmonic and anharmonic analyses, while the intercepts are found to be 11.6 and 11.8 $\mathrm{cm}^{-1}/0.001$ Å, respectively. The values for the harmonic data are consistent with the slope and intercept anticipated by Eq. 3.10, where the slope is equated

to the OH stretch frequency, 3884 cm^{-1}, and the intercept is -1.5$\omega\alpha \approx -12$ cm^{-1}/0.001 Å.

Based on the observed correlation between the OH bond lengths and the associated frequency, one can ask if such a correlation can be used to reconstruct the IR spectrum of water from the vibrationally averaged OH bond lengths of all of the water molecules in the AIMD simulation. This bond-length distribution is provided in Figure 3.24. Because we are interested in the vibrationally averaged OH bond lengths and not the instantaneous values of the OH distance, we have used Fourier filtering with a frequency cutoff of 800 cm^{-1} to remove the high frequency components to the OH stretch oscillations. Based on this data, we generated an IR spectrum by scaling the calculated vibrational density of states (VDOS) (plotted in Figure 3.24) using the slope of -18.8 cm^{-1}/0.001 Å obtained from analysis of the results reported in Figure 3.10 along with the ratio of the dipole derivatives obtained from an analysis of the water dimer using the revPBE functional with the D3BJ dispersion correction[60] and the def2-TZVPP[61] basis set, as implemented in NWChem 6.8 (see Figure 3.12).[62]

Specifically, to perform this reconstruction, a given bond-length R is converted into a frequency by

$$\omega(R) = \omega_{\text{ref}} - 18.8 \text{ cm}^{-1}/0.001 \text{ Å } (R - R_{\text{ref}}) \tag{3.20}$$

where $\omega_{\text{ref}} = 3793$ cm^{-1} is obtained by finding the maximum frequency sampled by the AIMD simulation of water clusters using the revPBE-D3 functional. This maximum is chosen as the onset of the distribution, where we identify the maximum frequency in the frequency distribution with a height that is at least 0.01% of the maximum value of the distribution shown in Figure 3.10. Likewise, $R_{\text{ref}} = 0.9649$ Å is the minimum OH bond length in a Fourier filtered distribution of OH bond lengths with a cutoff frequency of 800 cm^{-1} where the value of the VDOS is at least 0.01% of the maximum value of this distribution.

To obtain the spectrum shown in Figure 3.25, the intensity is then given by

$$I(R) \propto p(R) \left(\frac{\partial \mu}{\partial R} \right)^2 \tag{3.21}$$

where μ is the dipole response along the hydrogen-bonded OH bond, which has been obtained from a scan of this OH bond in a water dimer at the revPBE-D3 level of theory using NWChem 6.8.[62] To obtain the data shown in Figure 3.12, the dipole moment is calculated for for each geometry along the scan and the projection of the dipole moment along the hydrogen-bonded OH bond is fit to a quadratic polynomial in the OH bond length displacement, ΔR_{OH}. The square of the dipole derivative is scaled by p, which is is the probability density function for the Fourier filtered OH bond lengths obtained from the same AIMD simulation, as described above.

In Figure 3.25, to facilitate a comparison with the spectrum calculated from the dipole-dipole correlation function obtained using *ab initio* molecular dynamics (AIMD) simulations based on the same level of electronic structure theory,[59] the reconstructed spectrum is also shifted so the peak in the reconstructed spectrum lies at the same frequency as the peak in the AIMD spectrum. Based on our use of the -18.8 cm^{-1}/0.001 Å proportionality constant to obtain the frequencies, the shift of 50 cm^{-1} corresponds to a displacement in R_e of 0.0027 Å. Such a shift is well within the accuracy with which we can obtain the reference OH bond length from Figure 3.24. As is seen, this protocol yields a spectrum that is in good agreement with the one obtained from AIMD simulation including the shape of the red side of the OH stretching band.

The above analysis illustrates a powerful result of this work. A molecular dynamics or quantum calculation that provides the equilibrium or zero-point averaged OH bond lengths can be converted into a spectrum using the average value of $\Delta\omega/\Delta R_e$, obtained from the simulation, along with the corresponding ratio of the first and second derivative of the dipole moment function, evaluated based on the water dimer.

The theoretical approach used to derive the correlation between shifts in harmonic fre-

quencies and OH bond lengths is based on the response of the OH oscillator to its local environment, specifically the electric field due to nearby water molecules or ions. Such a model has been used in studies of the vibrational spectra of liquid water, where the OH stretch frequency is found to vary linearly with the electric field strength, $\mathcal{E}$, which arises from the local environment of the OH bond.[48–52] The resulting correlations have motivated the construction of models that are used to understand or reconstruct experimental spectra of liquid water. For example, Smith *et al.* mapped electric field distributions obtained from classical simulations of potassium halides dissolved in aqueous solutions onto Raman spectra using[52]

$$\omega = \left(160.514 \text{ cm}^{-1} \text{ V}^{-1} \text{ Å}\right) \mathcal{E} + 3745 \text{ cm}^{-1} \tag{3.22}$$

where the coefficients in Eq. 3.22 were obtained from a fit of the calculated local electric field distribution based on empirical model of pure water to the Raman spectrum of HOD in D_2O. In the present study, we derive the linear correlation between OH vibrational frequencies and the external field strength, where the value of $d\omega/d\mathcal{E}$ depends on the OH stretch frequency, its anharmonicity, and the projection of the second derivative of the dipole moment of the water molecule onto the hydrogen-bonded OH bond. Substituting the parameters for the Morse oscillator, and the dipole derivatives for water dimer with $R_{\text{OO}} = 2.97$ Å, obtained in the present study, into Eq. 3.9, we find $d\omega/d\mathcal{E} = 140$ cm^{-1} V^{-1} Å, a value that is in very good agreement with the empirical value provided in Eq. 3.22. Changing the OO distance in water dimer at which the dipole derivatives are evaluated will alter their values, and modulate the ratio slightly. In addition to noting that the model that was derived in this work reproduces previously determined linear correlations between OH stretch frequencies and electric field strength, we also find that the equilibrium OH bond length depends linearly on the size of $\mathcal{E}$. Combining these results leads to the linear correlation between the shift in the OH stretch frequency and the shift in the OH bond length seen in Figures 3.4 and 3.10.

In summary, in this work we have extended the previously described correlation between

the equilibrium OH bond lengths and the harmonic frequency for OH bonds in hydrogen bonding environments to include the effects of anharmonicities. Based on cluster studies, we found that the anharmonic results displaye roughly the same ratio of frequency shifts to changes in vibrationally averaged bond lengths as is found at the harmonic level. We extended this work from clusters to explore the correlation based on an AIMD simulation of liquid water, and obtained roughly the same ratio of the frequency to OH bond length changes as was obtained for the clusters, despite the use of a different level of electronic structure theory for the two types of calculations. This apparent insensitivity of the value of $\Delta\omega/\Delta R_e$ to the level of electronic structure theory and method used to evaluate the harmonic frequencies and equilibrium bond lengths being fit is consistent with the results of an earlier study in which different levels of electronic structure theory were shown to lead to the same value of $\Delta\omega/\Delta R_e$ despite providing different frequency shifts originating from the different elongations of the hydrogen bonded OH.[42] The fact that different levels of electronic structure theory produce different harmonic/anharmonic frequencies can be attributed to the fact that these calculations primarily yield different equilibrium bond lengths and secondary different shapes of the OH potential that affects the vibrationally averaged structures and resulting anharmonic frequencies.

The reported correlations were explained using a model based on the perturbation of a one-dimensional OH oscillator by an external electric field. Based on this model, we developed a simple expression that captures the reported results. It also provided results that are consistent with a series of one-dimensional studies of water in several environments. Finally, we explored the relationship between these models and those used in earlier studies of liquid water and find that they provide theoretical support for previously developed empirical relationships between OH stretch frequencies and the environment as described by the local electric field. We expect that our results will provide additional insights into the various correlations between OH bond lengths, frequencies and the local environment of the OH bond in complex environments.

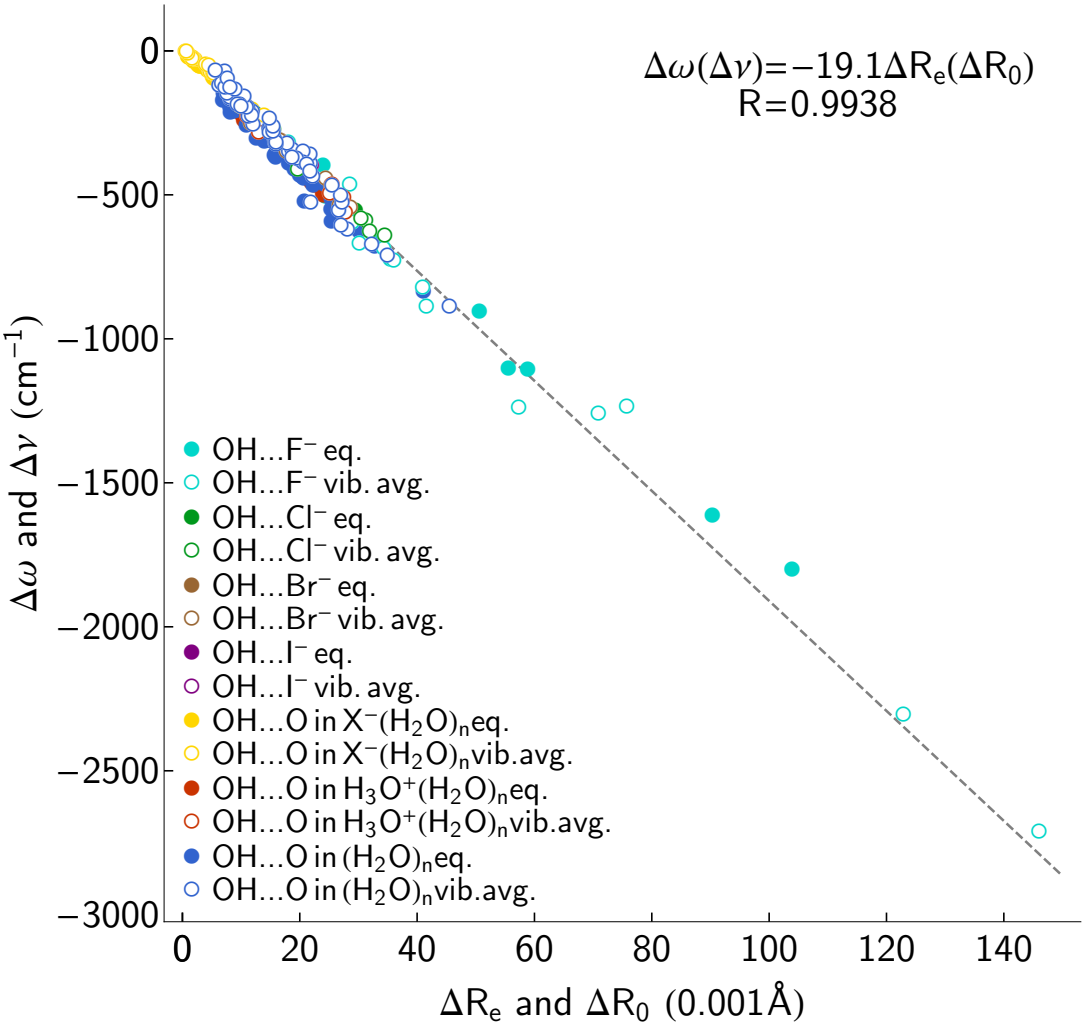

Figure 3.4: Correlations of $\Delta\omega$ to ΔR_e and $\Delta\nu$ to ΔR_0 for the OH$\ldots$X$^-$ and OH$\ldots$O vibrations in the $(H_2O)_n$, n=2-6, $X^-(H_2O)_n$, n=1-5, X=F, Cl, Br, I, and $H_3O^+(H_2O)_n$, n=3,4 clusters. The shifts are computed with respect to the equilibrium (vibrationally averaged) bond length and the average of the symmetric and antisymmetric harmonic (anharmonic) OH vibrations of the gas phase water monomer.

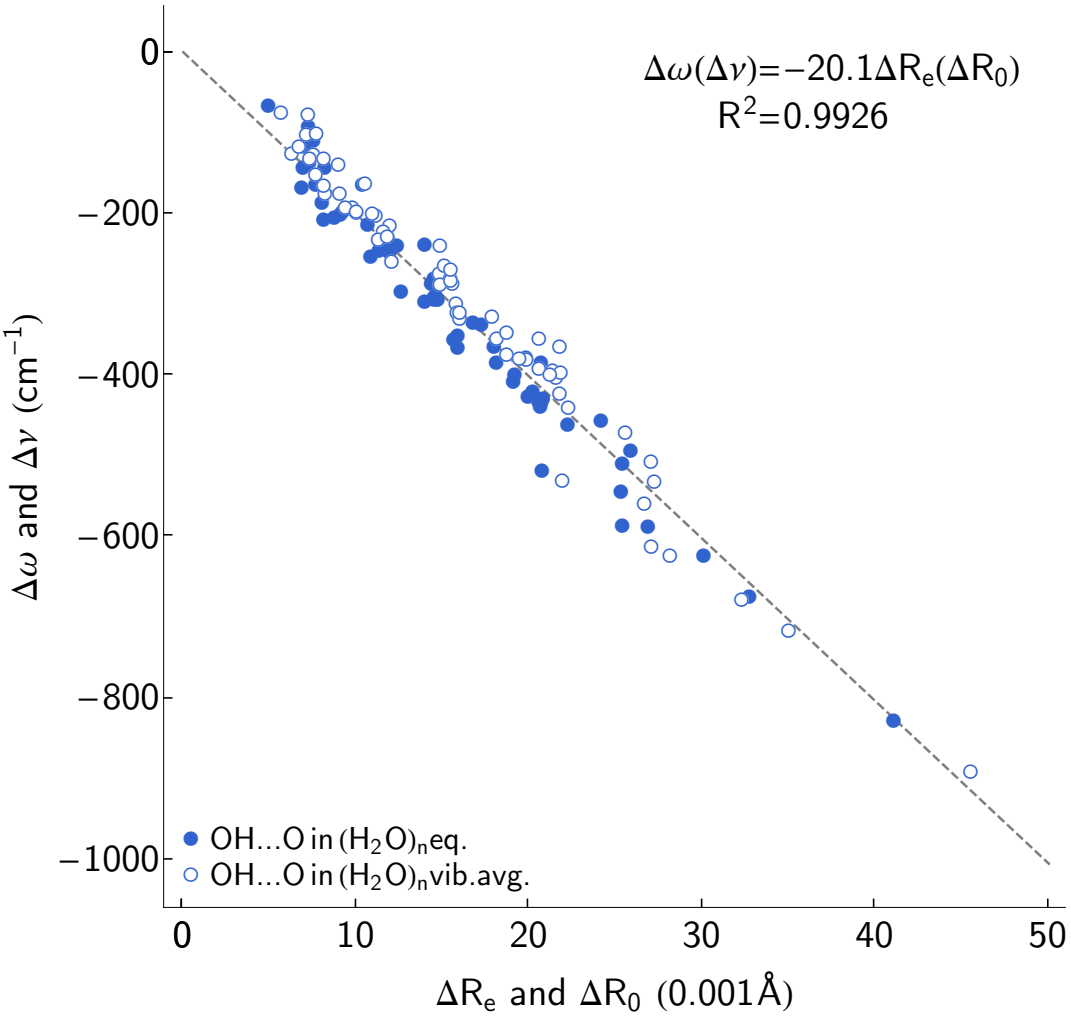

Figure 3.5: The same as Figure 3.4, but considering only the hydrogen-bonded OH bonds in water clusters.

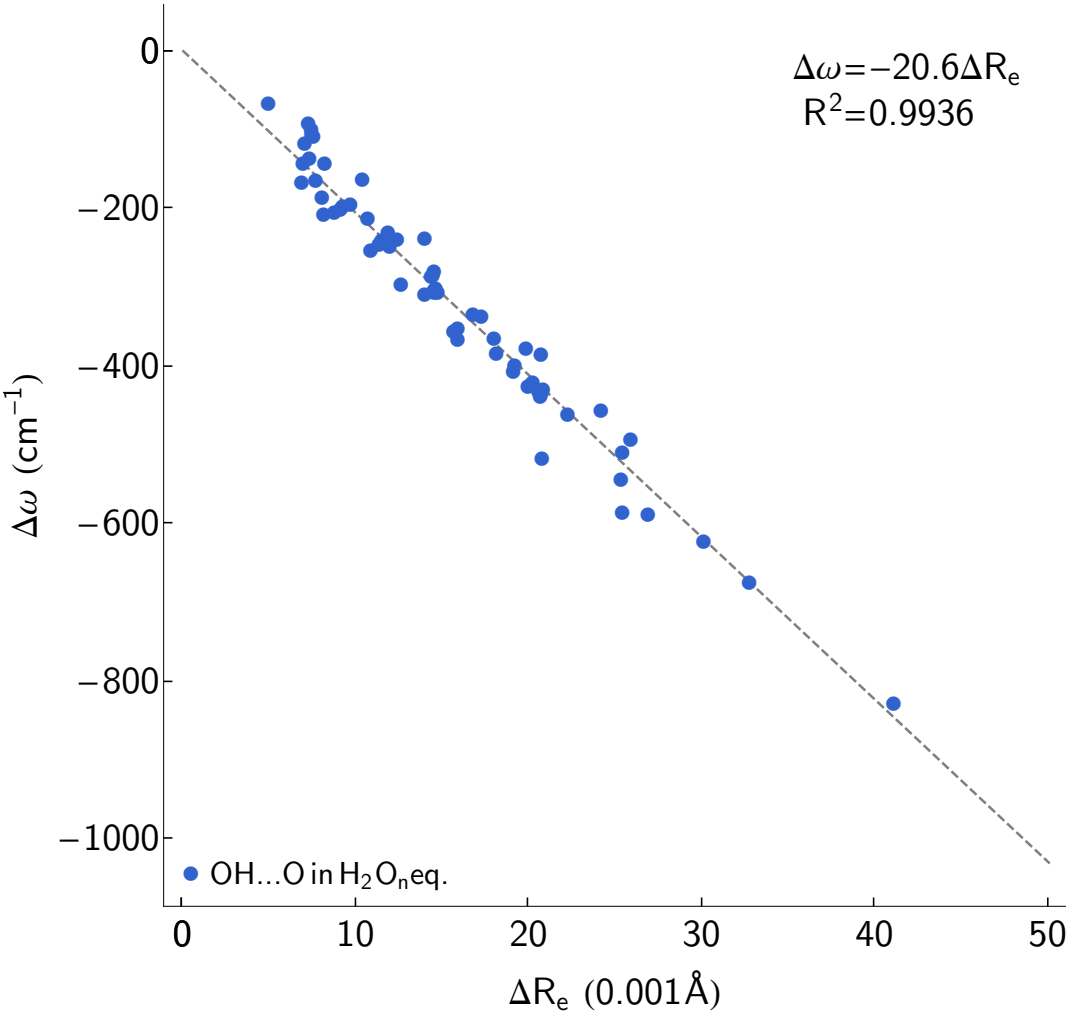

Figure 3.6: The same as Figure 3.5, but only considering the harmonic frequencies and equilibrium OH bond lengths.

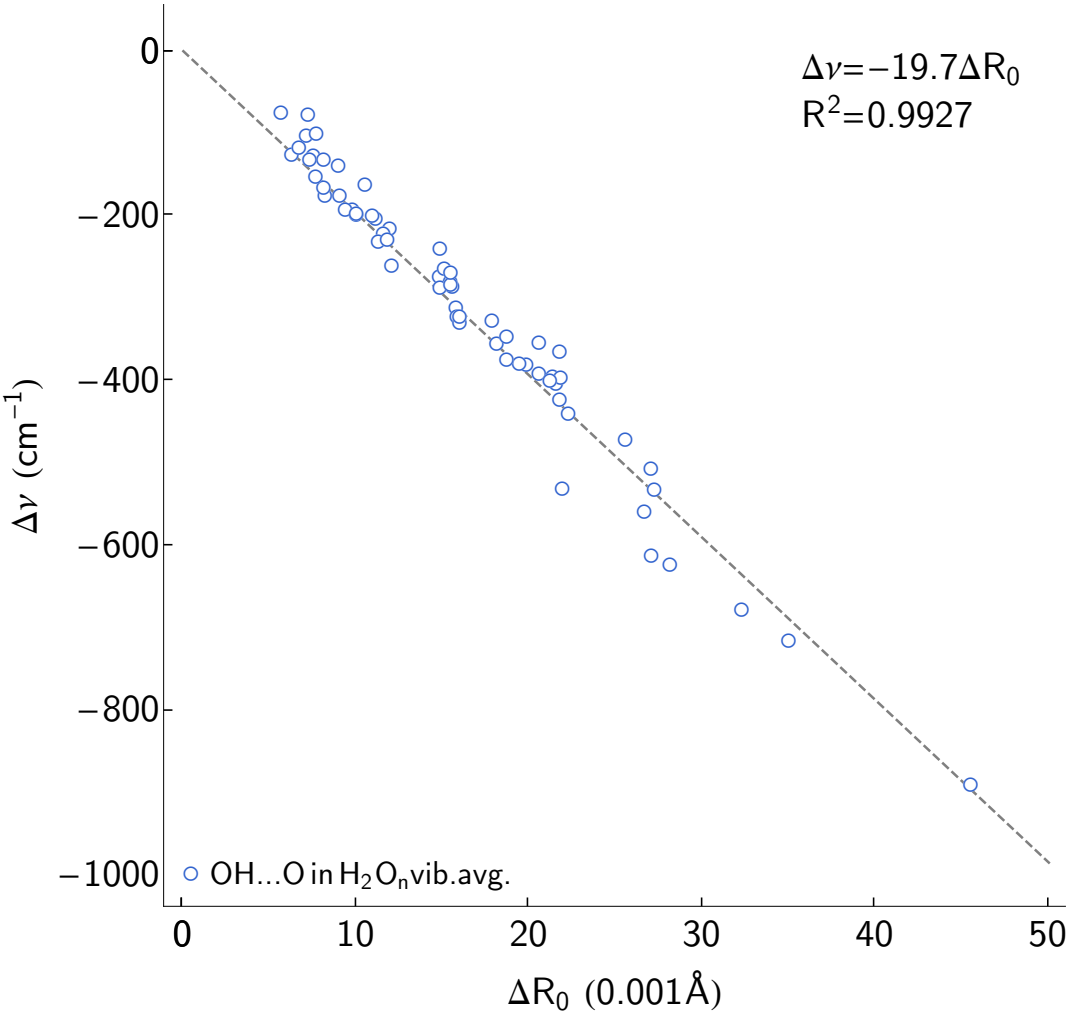

Figure 3.7: The same as Figure 3.5, but only considering the anharmonic frequencies and zero-point averaged OH bond lengths.

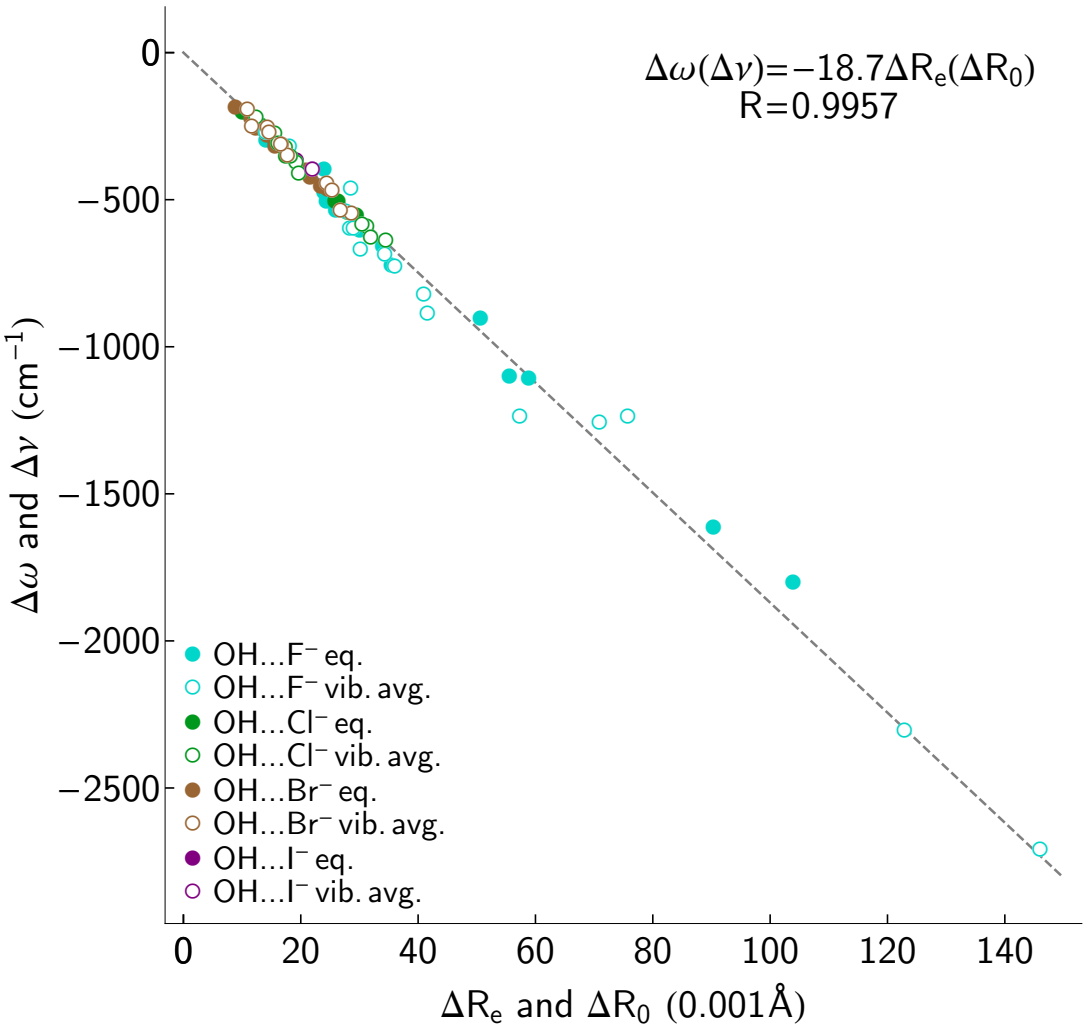

Figure 3.8: The same as Figure 3.4, but considering only the halide-bound OH bonds in halide-water complexes.

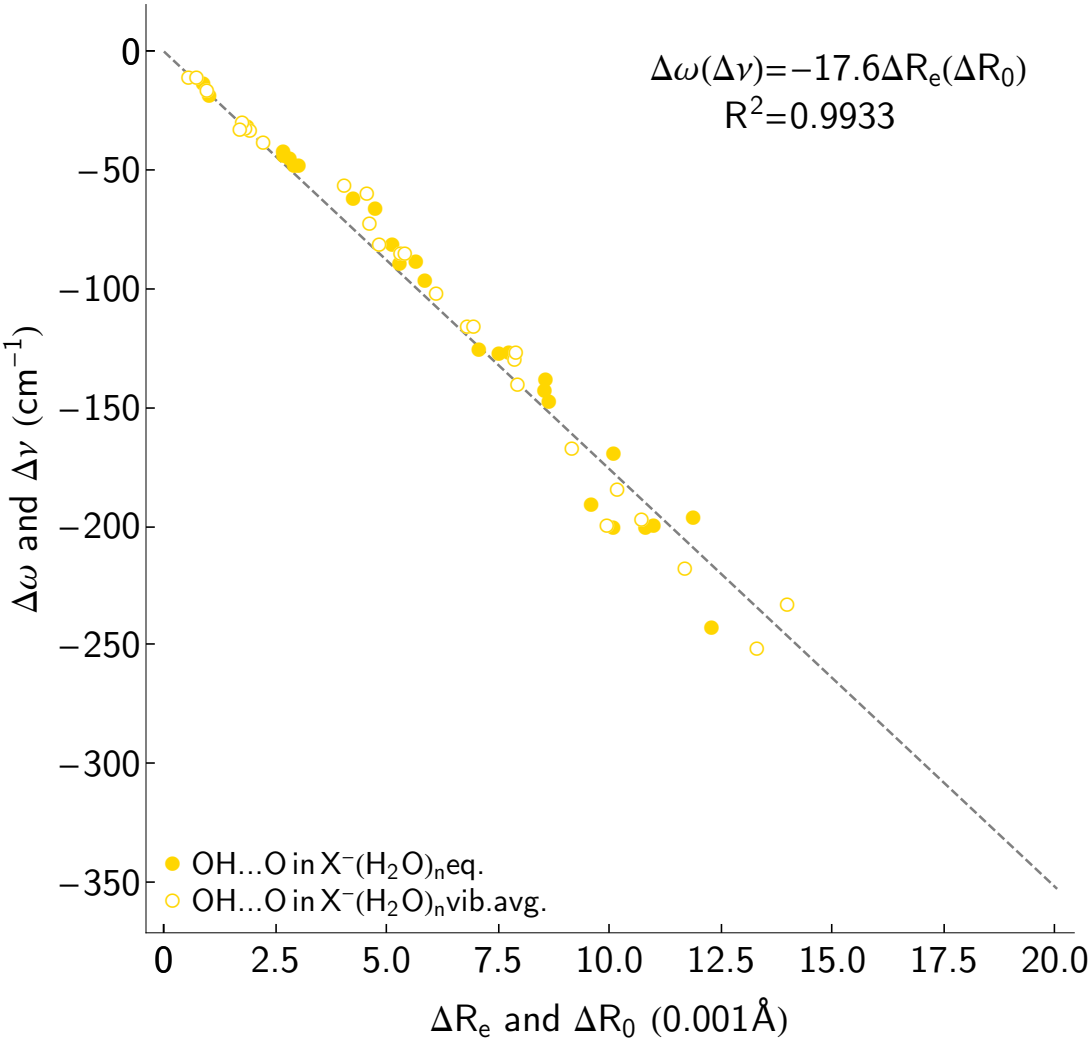

Figure 3.9: The same as Figure 3.4, but considering only the water-bound OH bonds between water molecules in halide-water complexes.

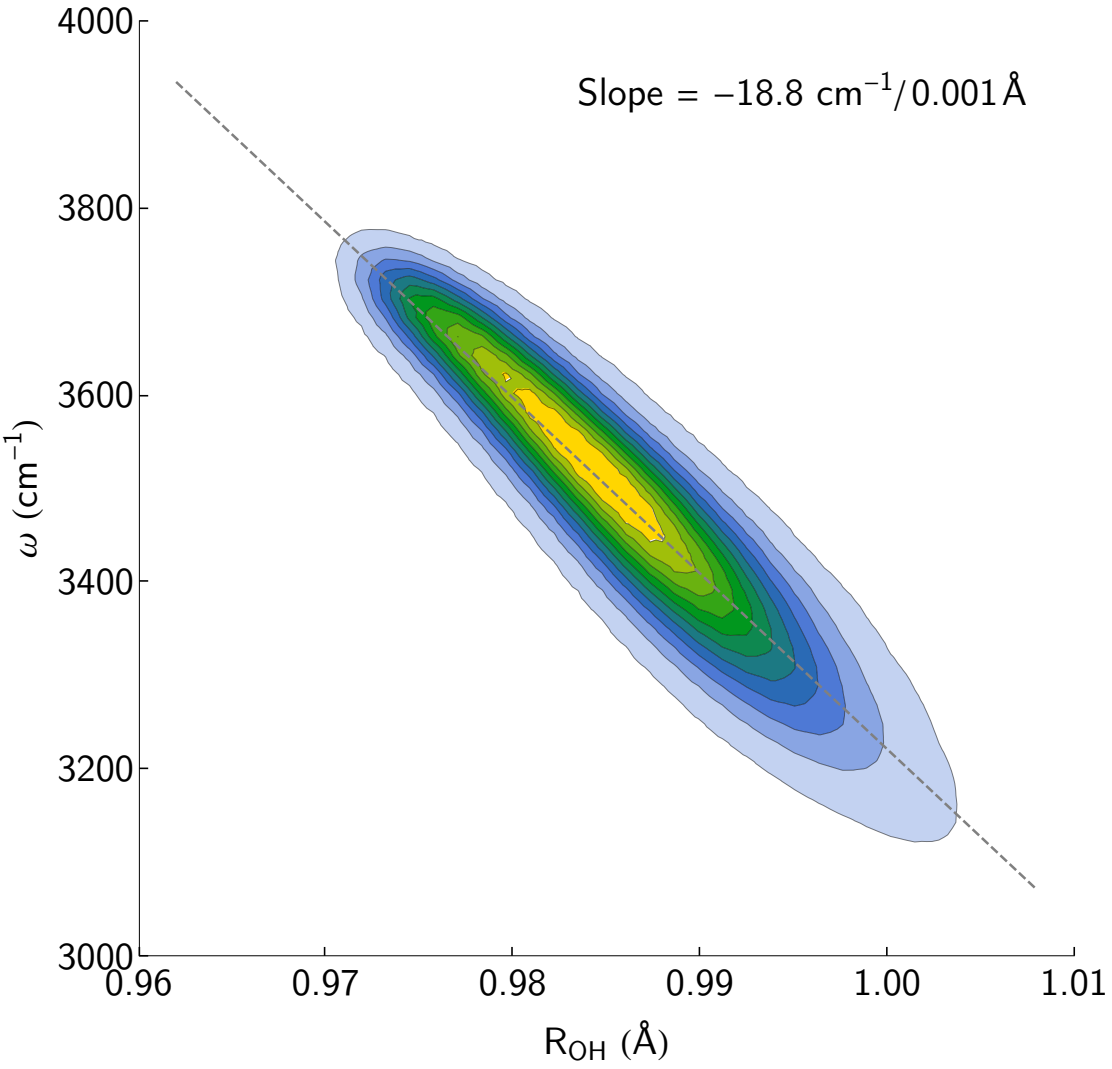

Figure 3.10: The correlation of R_{OH} and ω as obtained from an AIMD trajectory of liquid water at 300 K at the revPBE-D3 level of theory.

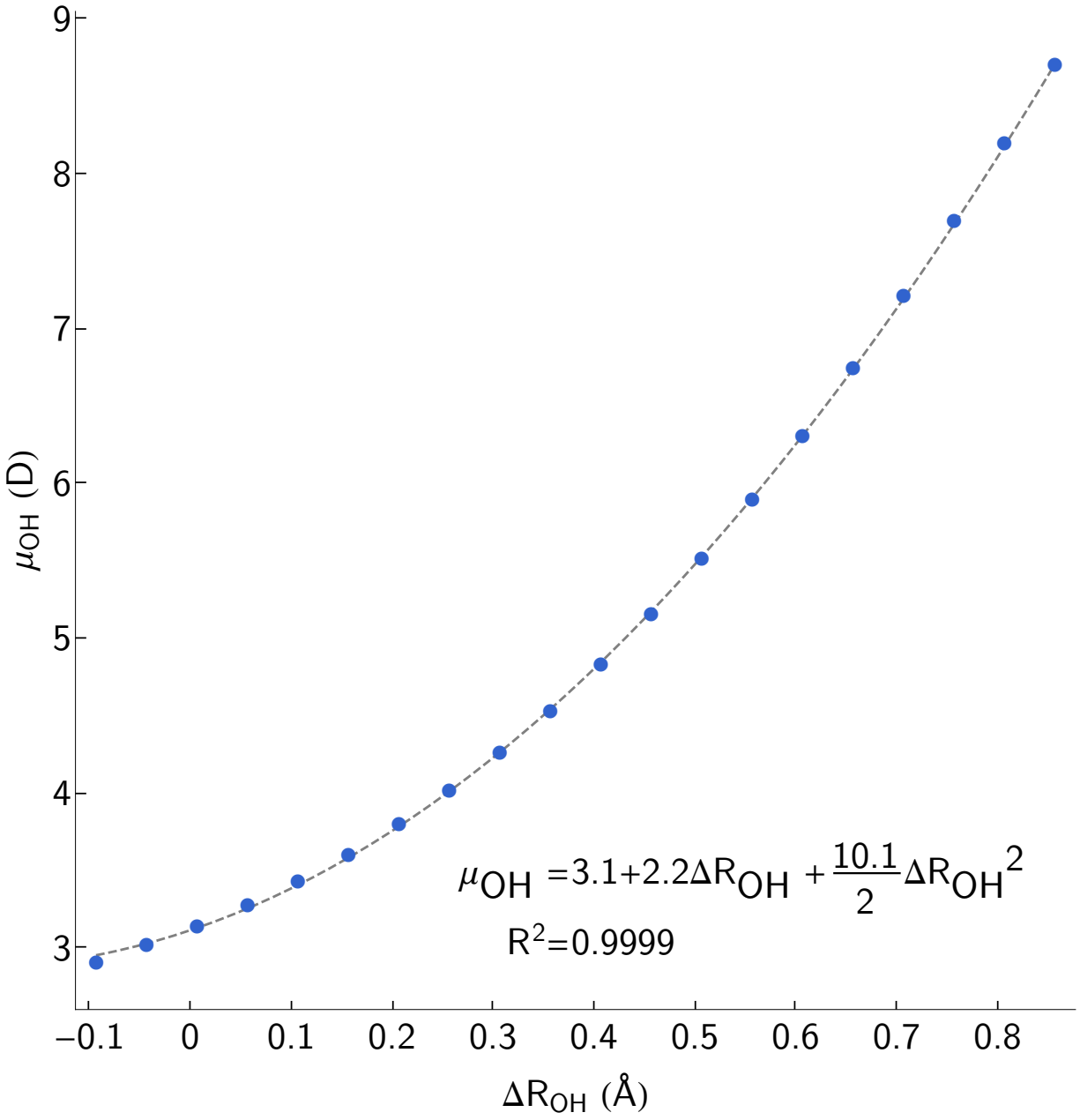

Figure 3.11: Dipole moment along the hydrogen-bonded OH bond in water dimer evaluated at the MP2/aug-cc-pVDZ level of theory, with R_{OO} = 2.97 Å, plotted as a function of the displacement of the OH bond length and fit to a quadratic polynomial.

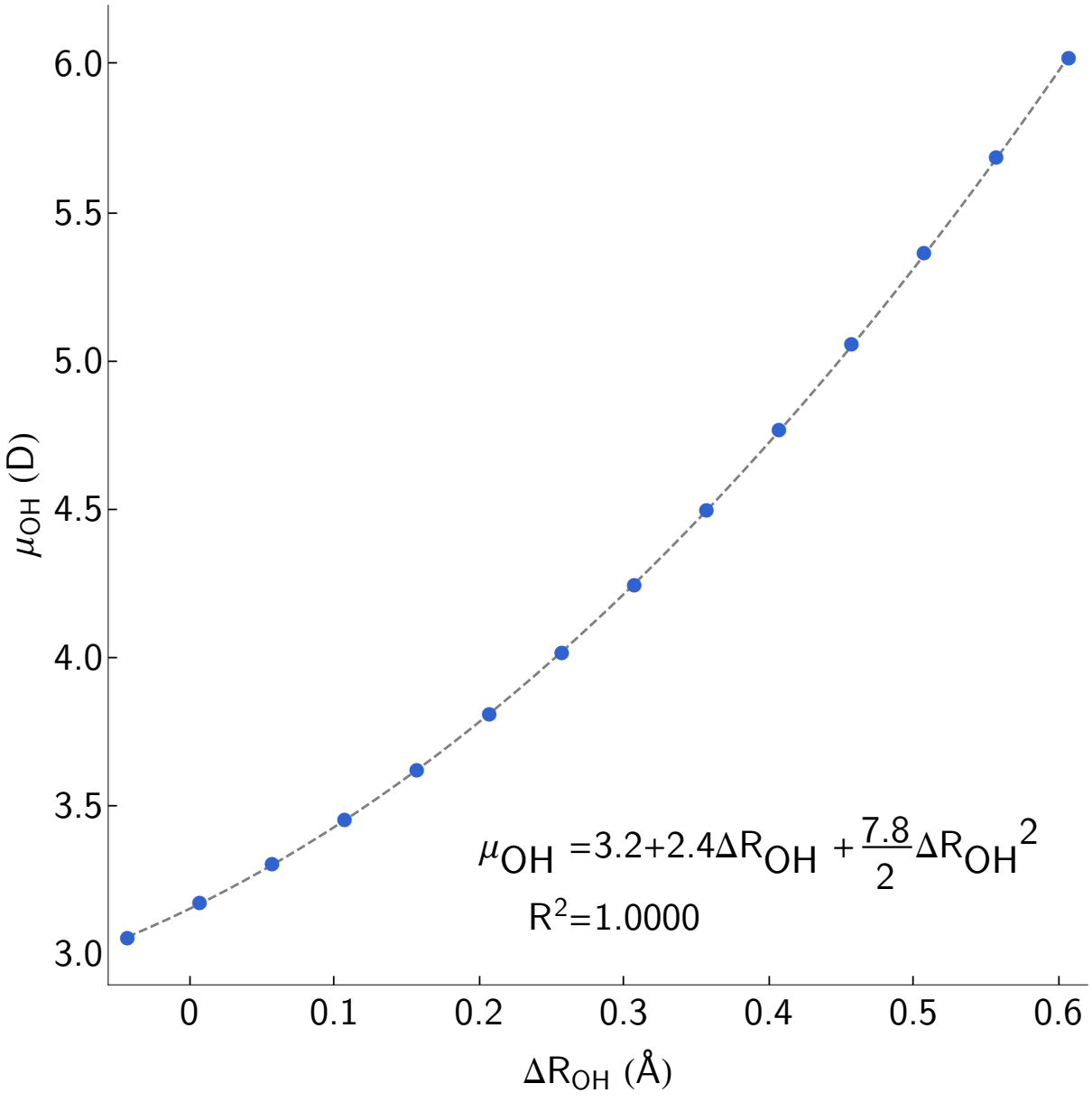

Figure 3.12: The same as Figure 3.11 where the calculation is performed at the revPBE-D3 level of theory using NWChem with an OO distance of 2.97 Å.

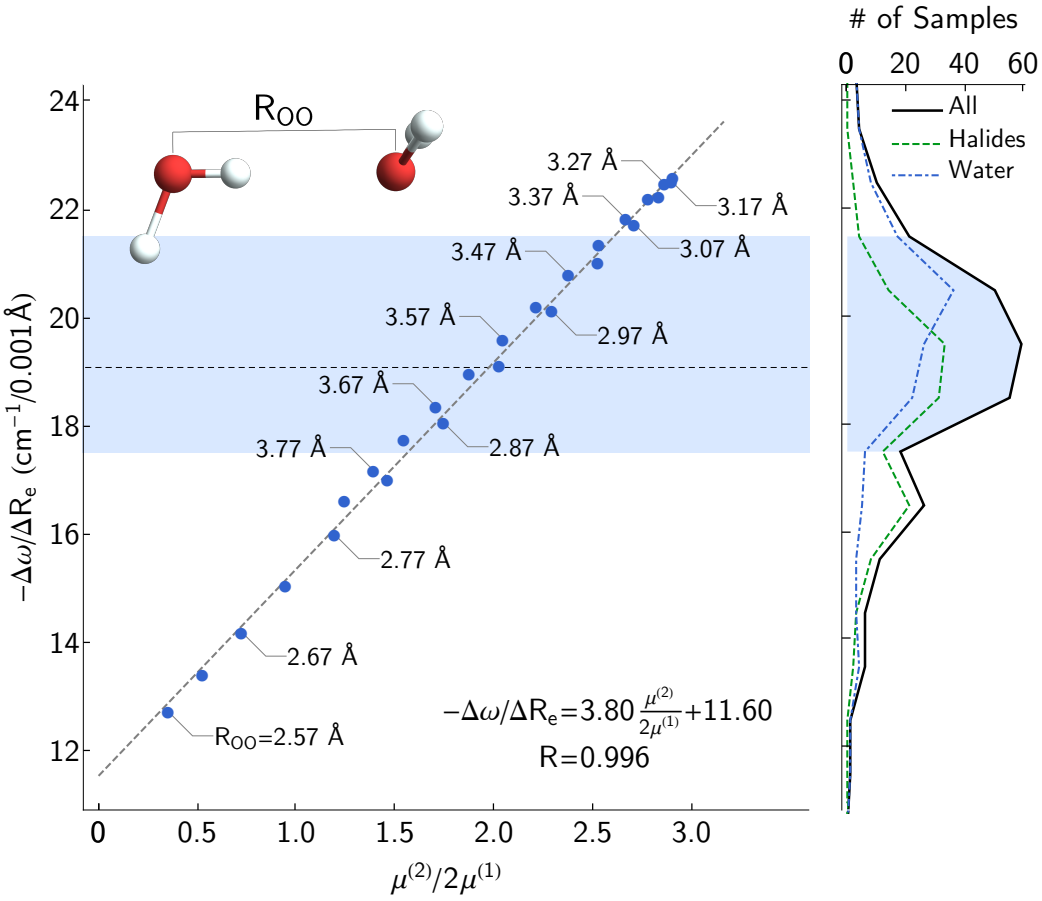

Figure 3.13: The calculated value of $\Delta\omega/\Delta R_e$ is plotted as a function of the OO distance in water dimer used to evaluate the ratio of the dipole derivatives (left panel) is compared to the range of this ratio obtained for the data plotted in Figure 3.4. The blue shading is provided to highlight results for which 17.5 cm^{-1}/0.001 Å $< d\omega/dR_e <$ 21.5 cm^{-1}/0.001 Å, while the dashed line in the left panel indicates the value of $\Delta\omega/\Delta R_e$ = 19.1 cm^{-1}/0.001 Å obtained from an analysis of the data plotted in Figure 3.4.

				Equilibrium geometry							Vibrationally averaged geometry					
				R_e	ω_1	ω_2	$(\omega_1+\omega_2)/2$	ΔR_e (Å)	$\Delta\omega$ (cm^{-1})	s	ν_1	ν_2	$(\nu_1+\nu_2)/2$	ΔR_0 (Å)	$\Delta\nu$ (cm^{-1})	s
I. Hydrogen bonded OH stretches in $X^-(H_2O)_n$, X=F, Cl, Br, I and n=1-5																
H_2O			avdz	0.965929	3803.30	3937.53	3870.42	0	0	n/a	3621.10	3744.74	3682.92	0	0	n/a
			avtz	0.961369	3821.89	3947.72	3884.81	0	0	n/a	3654.21	3767.73	3710.97	0	0	n/a
$F^-(H_2O)$		ion-water	avdz	1.056266	2264.35			0.090337	-1606.07	**17.8**	1369.47			0.122951	-2313.45	**18.8**
		ion-water	avtz	1.065300	2089.72			0.103931	-1795.09	**17.3**	992.04			0.146056	-2718.93	**18.6**
$F^-(H_2O)_2$		ion-water	avdz	1.021477	2775.15			0.055548	-1095.27	**19.7**	2437.65			0.057403	-1245.27	**21.7**
		ion-water	avdz	1.016549	2973.19			0.050620	-897.23	**17.7**	2438.89			0.075814	-1244.03	**16.4**
		water-water	avdz	n/a	n/a			n/a	n/a	n/a	n/a			n/a	n/a	n/a
$F^-(H_2O)_3$	Pyramidal	ion-water	avdz	0.999909	3217.16			0.033980	-653.26	**19.2**	2853.09			0.041042	-829.83	**20.2**
		water-water	avdz	0.967802	3839.38			0.001873	-31.04	**16.6**	3671.16			0.000560	-11.76	**21.0**
	Ring	ion-water	avdz	1.024804	2770.23			0.058875	-1100.19	**18.7**	2416.52			0.070970	-1266.40	**17.8**
		water-water	avdz	0.978218	3628.43			0.012289	-241.99	**19.7**	3430.63			0.013308	-252.29	**19.0**
$F^-(H_2O)_4$	Pyramidal	ion-water	avdz	0.989886	3401.69			0.023957	-468.72	**19.6**	3076.33			0.028391	-606.59	**21.4**
		water-water	avdz	0.968954	3823.30			0.003025	-47.11	**15.6**	3643.55			0.002234	-39.37	**17.6**
	3+1	ion-water	avdz	0.995963	3273.02			0.030034	-597.40	**19.9**	2989.22			0.034403	-693.71	**20.2**
		ion-water	avdz	0.991895	3340.57			0.025966	-529.85	**20.4**	3005.80			0.030228	-677.12	**22.4**
		ion-water	avdz	0.990325	3371.33			0.024396	-499.08	**20.5**	3078.43			0.029016	-604.49	**20.8**
		ion-water	avdz	0.989921	3478.39			0.023992	-392.02	**16.3**	3211.42			0.028575	-471.50	**16.5**
		water-water	avdz	0.968853	3822.90			0.002924	-47.51	**16.2**	3648.58			0.001932	-34.34	**17.8**
		water-water	avdz	0.968621	3827.43			0.002692	-42.98	**16.0**	3649.43			0.001833	-33.49	**18.3**
		water-water	avdz	0.968609	3828.98			0.002680	-41.43	**15.5**	3652.11			0.001764	-30.81	**17.5**
$F^-(H_2O)_5$	Pyramidal	ion-water	avdz	1.001384	3151.97			0.035455	-718.44	**20.3**	2788.39			0.041648	-894.54	**21.5**
		ion-water	avdz	0.995400	3284.82			0.029471	-585.60	**19.9**	2947.74			0.036060	-735.19	**20.4**
		ion-water	avdz	0.990338	3406.89			0.024409	-463.52	**19.0**	3135.36			0.027753	-547.57	**19.7**
		ion-water	avdz	0.981569	3569.82			0.015640	-300.60	**19.2**	3355.24			0.018103	-327.68	**18.1**
		ion-water	avdz	0.980001	3578.18			0.014072	-292.24	**20.8**	3402.80			0.014071	-280.12	**19.9**
		water-water	avdz	0.976919	3671.62			0.010990	-198.80	**18.1**	3464.33			0.011695	-218.59	**18.7**
		water-water	avdz	0.972999	3745.54			0.007070	-124.88	**17.7**	3579.80			0.006116	-103.12	**16.9**
		water-water	avdz	0.968754	3825.94			0.002825	-44.47	**15.7**	3649.11			0.001711	-33.81	**19.8**
		water-water	avdz	0.966948	3852.74			0.001019	-17.67	**17.3**	3665.45			0.000969	-17.47	**18.0**
		water-water	avdz	0.966812	3857.79			0.000883	-12.63	**14.3**	3670.98			0.000736	-11.94	**16.2**

Table 3.1: Frequency and bond shift data in $X^-(H_2O)_n$. All harmonic frequencies, ω, and anharmonic frequencies, ν, are reported in cm^{-1}. Equilibrium bond lengths, R_e, and vibrationally averaged bond length shifts, ΔR_0, are reported in angstroms.

				Equilibrium geometry							Vibrationally averaged geometry					
				R_e	ω_1	ω_2	$(\omega_1+\omega_2)/2$	ΔR_e (Å)	$\Delta\omega$ (cm^{-1})	s	ν_1	ν_2	$(\nu_1+\nu_2)/2$	ΔR_0 (Å)	$\Delta\nu$ (cm^{-1})	s
$Cl^-(H_2O)$		ion-water	avdz	0.992267	3371.01			0.026338	-499.41	19.0	3084.23			0.031285	-598.69	19.1
		ion-water	avtz	0.990828	3338.16			0.029459	-546.65	18.6	3062.70			0.034576	-648.27	18.7
$Cl^-(H_2O)_2$		ion-water	avdz	0.993813	3332.94			0.027884	-537.48	19.3	3047.86			0.032012	-635.06	19.8
		ion-water	avdz	0.979850	3613.01			0.013921	-257.41	18.5	3353.76			0.017470	-329.16	18.8
		water-water	avdz	0.971222	3781.74			0.005293	-88.68	16.8	3609.44			0.004616	-73.48	15.9
$Cl^-(H_2O)_3$	Pyramidal	ion-water	avdz	0.982339	3561.92			0.016410	-308.50	18.8	3302.85			0.019286	-380.08	19.7
		water-water	avdz	0.973448	3743.78			0.007519	-126.64	16.8	3566.12			0.006814	-116.80	17.1
	Ring	ion-water	avdz	0.991790	3370.18			0.025861	-500.23	19.3	3091.37			0.030520	-591.55	19.4
		water-water	avdz	0.976015	3670.80			0.010086	-199.62	19.8	3484.61			0.010725	-198.31	18.5
$Cl^-(H_2O)_4$	Pyramidal	ion-water	avdz	0.979165	3630.18			0.013236	-240.24	18.2	3401.25			0.015622	-281.67	18.0
		water-water	avdz	0.976740	3670.59			0.010811	-199.82	18.5	3482.13			0.009947	-200.79	20.2
	3+1	ion-water	avdz	0.983383	3523.81			0.017454	-346.61	19.9	3263.71			0.019707	-419.21	21.3
		ion-water	avdz	0.981613	3571.86			0.015684	-298.56	19.0	3320.60			0.018289	-362.32	19.8
		ion-water	avdz	0.979672	3611.37			0.013743	-259.04	18.8	3365.87			0.016199	-317.05	19.6
		ion-water	avdz	0.975995	3673.41			0.010066	-197.00	19.6	3455.39			0.012436	-227.53	18.3
		water-water	avdz	0.974569	3723.85			0.008640	-146.57	17.0	3541.87			0.007941	-141.05	17.8
		water-water	avdz	0.973670	3744.18			0.007741	-126.23	16.3	3566.00			0.006950	-116.92	16.8
		water-water	avdz	0.971052	3790.02			0.005123	-80.40	15.7	3600.71			0.004835	-82.21	17.0
		water-water	avdz	0.970183	3809.37			0.004254	-61.04	14.3	3625.48			0.004049	-57.45	14.2
				Equilibrium geometry							Vibrationally averaged geometry					
				R_e	ω_1	ω_2	$(\omega_1+\omega_2)/2$	ΔR_e (Å)	$\Delta\omega$ (cm^{-1})	s	ν_1	ν_2	$(\nu_1+\nu_2)/2$	ΔR_0 (Å)	$\Delta\nu$ (cm^{-1})	s
$Br^-(H_2O)$		ion-water	avdz	0.986811	3476.87			0.020882	-393.55	18.8	3229.96			0.024486	-452.96	18.5
		ion-water	avtz	0.985954	3425.90			0.024585	-458.91	18.7	3156.92			0.028725	-554.05	19.3
$Br^-(H_2O)_2$		ion-water	avdz	0.989323	3421.01			0.023394	-449.41	19.2	3138.25			0.026824	-544.67	20.3
		ion-water	avdz	0.977454	3652.80			0.011525	-217.62	18.9	3419.27			0.014356	-263.65	18.4
		water-water	avdz	0.971789	3774.55			0.005860	-95.86	16.4	3596.81			0.005312	-86.11	16.2
$Br^-(H_2O)_3$	Pyramidal	ion-water	avdz	0.980243	3597.58			0.014314	-272.83	19.1	3363.17			0.016792	-319.76	19.0
		water-water	avdz	0.974476	3728.45			0.008547	-141.96	16.6	3552.29			0.007870	-130.63	16.6
	Ring	ion-water	avdz	0.987515	3453.25			0.021586	-417.17	19.3	3206.44			0.025415	-476.48	18.7
		water-water	avdz	0.975518	3680.11			0.009589	-190.30	19.8	3497.33			0.010180	-185.59	18.2
$Br^-(H_2O)_4$	Pyramidal	ion-water	avdz	0.978233	3620.76			0.012304	-249.66	20.3	3423.16			0.011695	-259.76	22.2
		water-water	avdz	0.977811	3674.95			0.011882	-195.47	16.5	3448.97			0.013994	-233.95	16.7
	3+1	ion-water	avdz	0.981539	3559.80			0.015610	-310.61	19.9	3323.33			0.017787	-359.59	20.2
		ion-water	avdz	0.980203	3597.06			0.014274	-273.36	19.2	3362.06			0.016653	-320.86	19.3
		ion-water	avdz	0.978455	3624.79			0.012526	-245.62	19.6	3403.83			0.014636	-279.09	19.1
		ion-water	avdz	0.974780	3689.21			0.008851	-181.21	20.5	3481.99			0.010970	-200.93	18.3
		water-water	avdz	0.976020	3701.70			0.010091	-168.71	16.7	3514.52			0.009156	-168.40	18.4
		water-water	avdz	0.974493	3733.10			0.008564	-137.31	16.0	3555.22			0.007900	-127.70	16.2
		water-water	avdz	0.971583	3782.51			0.005654	-87.90	15.5	3597.05			0.005412	-85.88	15.9
		water-water	avdz	0.970672	3805.17			0.004743	-65.25	13.8	3622.15			0.004559	-60.77	13.3
$I^-(H_2O)$		ion-water	avtz	0.980587	3524.61			0.019218	-360.20	18.7	3305.10			0.022027	-405.87	18.4

Key: Ion-water hydrogen bonded O-H...X; Water-water hydrogen bonded O-H...O; Free OH stretch

Table 3.2: Same as Table 3.1 for $X^-(H_2O)_n$ (X = Cl, Br and I).

II. Hydrogen bonded OH stretches in $(H_2O)_n$, n=2-6 (various isomers)

				Equilibrium geometry							Vibrationally averaged geometry					
				R_e	ω_1	ω_2	$(\omega_1+\omega_2)/2$	ΔR_e (Å)	$\Delta\omega$ (cm^{-1})	s	ν_1	ν_2	$(\nu_1+\nu_2)/2$	ΔR_0 (Å)	$\Delta\nu$ (cm^{-1})	s
H_2O			avdz	0.965929	3803.30	3937.53	3870.42	0	0	n/a	3621.10	3744.74	3682.92	0	0	n/a
			avtz	0.961369	3821.89	3947.72	3884.81	0	0	n/a	3654.21	3767.73	3710.97	0	0	n/a
$(H_2O)_2$		H-bonded	avdz	0.972826	3704.47			0.006897	-165.94	**24.1**	3553.95			0.006322	-129	**20.4**
$(H_2O)_3$	**uud**	H-bonded	avdz	0.978556	3574.76			0.012627	-295.66	**23.4**	3419.45			0.012097	-263	**21.8**
		H-bonded	avdz	0.978323	3632.51			0.012394	-237.91	**19.2**	3464.40			0.011987	-219	**18.2**
		H-bonded	avdz	0.977813	3641.31			0.011884	-229.11	**19.3**	3476.29			0.011178	-207	**18.5**
	uuu	H-bonded	avdz	0.977442	3631.71			0.011513	-238.71	**20.7**	3480.53			0.010057	-202	**20.1**
$(H_2O)_4$	**3+1**	H-bonded	avdz	0.984071	3487.75			0.018142	-382.67	**21.1**	3324.09			0.018165	-359	**19.8**
		H-bonded	avdz	0.977909	3622.99			0.011980	-247.42	**20.7**	3457.44			0.011623	-225	**19.4**
		H-bonded	avdz	0.974089	3663.92			0.008160	-206.50	**25.3**	3503.92			0.008238	-179	**21.7**
		H-bonded	avdz	0.973488	3762.64			0.007559	-107.78	**14.3**	3602.48			0.007260	-80	**11.1**
	Cage	H-bonded	avdz	0.988185	3410.39			0.022256	-460.03	**20.7**	3239.07			0.022296	-444	**19.9**
		H-bonded	avdz	0.975193	3674.85			0.009264	-195.56	**21.1**	3503.78			0.009099	-179	**19.7**
		H-bonded	avdz	0.974001	3685.71			0.008072	-184.71	**22.9**	3514.11			0.008168	-169	**20.7**
		H-bonded	avdz	0.973636	3707.67			0.007707	-162.74	**21.1**	3527.41			0.007699	-156	**20.2**
		H-bonded	avdz	0.973207	3779.12			0.007278	-91.29	**12.5**	3576.75			0.007173	-106	**14.8**
	Ring	H-bonded	avdz	0.985135	3472.95			0.019206	-397.47	**20.7**	3298.77			0.019882	-384	**19.3**
$(H_2O)_5$	**4+1**	H-bonded	avdz	0.991268	3327.43			0.025339	-542.99	**21.4**	3119.72			0.026698	-563	**21.1**
		H-bonded	avdz	0.986168	3450.89			0.020239	-419.53	**20.7**	3284.61			0.021404	-398	**18.6**
		H-bonded	avdz	0.983938	3506.55			0.018009	-363.86	**20.2**	3332.41			0.018747	-351	**18.7**
		H-bonded	avdz	0.980688	3565.21			0.014759	-305.21	**20.7**	3392.99			0.015599	-290	**18.6**
		H-bonded	avdz	0.972905	3729.31			0.006976	-141.11	**20.2**	3562.61			0.006743	-120	**17.8**
	Cage	H-bonded	avdz	0.992831	3283.56			0.026902	-586.86	**21.8**	3055.81			0.028179	-627	**22.3**
		H-bonded	avdz	0.991826	3378.23			0.025897	-492.19	**19.0**	3147.48			0.027272	-535	**19.6**
		H-bonded	avdz	0.976815	3618.55			0.010886	-251.86	**23.1**	3447.52			0.011332	-235	**20.8**
		H-bonded	avdz	0.977296	3626.08			0.011367	-244.34	**21.5**	3450.73			0.011855	-232	**19.6**
		H-bonded	avdz	0.976640	3658.53			0.010711	-211.89	**19.8**	3479.16			0.010977	-204	**18.6**
		H-bonded	avdz	0.976327	3708.09			0.010398	-162.33	**15.6**	3516.83			0.010551	-166	**15.7**
	Ring	H-bonded	avdz	0.986709	3353.78			0.020780	-516.63	**24.9**	3148.51			0.021959	-534	**24.3**
		H-bonded	avdz	0.986614	3433.32			0.020685	-437.09	**21.1**	3276.18			0.021585	-407	**18.8**
		H-bonded	avdz	0.986774	3442.18			0.020845	-428.24	**20.5**	3282.79			0.021858	-400	**18.3**
		H-bonded	avdz	0.986652	3486.95			0.020723	-383.47	**18.5**	3314.61			0.021809	-368	**16.9**
		H-bonded	avdz	0.985777	3494.00			0.019848	-376.41	**19.0**	3325.06			0.020614	-358	**17.4**

Table 3.3: Same as Table 3.1 for $(H_2O)_n$ (n=1-5).

				Equilibrium geometry							Vibrationally averaged geometry					
				R_e	ω_1	ω_2	$(\omega_1+\omega_2)/2$	ΔR_e (Å)	$\Delta\omega$ (cm^{-1})	s	ν_1	ν_2	$(\nu_1+\nu_2)/2$	ΔR_0 (Å)	$\Delta\nu$ (cm^{-1})	s
$(H_2O)_6$	Cage	H-bonded	avdz	0.996056	3248.51			0.030127	-621.91	20.6	3001.09			0.032315	-682	21.1
		H-bonded	avdz	0.985907	3445.55			0.019978	-424.86	21.3	3287.87			0.020605	-395	19.2
		H-bonded	avdz	0.985043	3464.25			0.019114	-406.16	21.2	3299.68			0.019480	-383	19.7
		H-bonded	avdz	0.982717	3537.21			0.016788	-333.20	19.8	3351.60			0.017898	-331	18.5
		H-bonded	avdz	0.980306	3585.09			0.014377	-285.33	19.8	3405.27			0.014845	-278	18.7
		H-bonded	avdz	0.975049	3670.74			0.009120	-199.67	21.9	3486.80			0.009822	-196	20.0
		H-bonded	avdz	0.974156	3728.57			0.008227	-141.85	17.2	3539.78			0.009019	-143	15.9
		H-bonded	avdz	0.973392	3765.61			0.007463	-104.81	14.0	3551.96			0.007563	-131	17.3
	Prism	H-bonded	avdz	0.998695	3196.98			0.032766	-673.43	20.6	2963.27			0.035029	-720	20.5
		H-bonded	avdz	0.986671	3437.54			0.020742	-432.88	20.9	3279.44			0.021247	-403	19.0
		H-bonded	avdz	0.983208	3534.67			0.017279	-335.74	19.4	3304.94			0.018743	-378	20.2
		H-bonded	avdz	0.980496	3565.25			0.014567	-305.17	20.9	3367.99			0.015812	-315	19.9
		H-bonded	avdz	0.974713	3667.05			0.008784	-203.37	23.2	3487.02			0.009424	-196	20.8
		H-bonded	avdz	0.975625	3677.39			0.009696	-193.03	19.9	3481.74			0.010051	-201	20.0
		H-bonded	avdz	0.972995	3754.61			0.007066	-115.80	16.4	3547.23			0.007349	-136	18.5
		H-bonded	avdz	0.973385	3771.55			0.007456	-98.87	13.3	3578.80			0.007752	-104	13.4
		H-bonded	avdz	0.970902	3805.12			0.004973	-65.29	13.1	3604.70			0.005697	-78	13.7
	Book_1	H-bonded	avdz	0.991350	3285.43			0.025421	-584.99	23.0	3066.57			0.027096	-616	22.7
		H-bonded	avdz	0.991344	3362.29			0.025415	-508.13	20.0	3172.77			0.027072	-510	18.8
		H-bonded	avdz	0.990123	3414.88			0.024194	-455.54	18.8	3208.27			0.025599	-475	18.5
		H-bonded	avdz	0.981600	3515.72			0.015671	-354.70	22.6	3356.96			0.015871	-326	20.5
		H-bonded	avdz	0.980565	3570.07			0.014636	-300.34	20.5	3399.06			0.015479	-284	18.3
		H-bonded	avdz	0.980399	3586.18			0.014470	-284.24	19.6	3415.53			0.015136	-267	17.7
		H-bonded	avdz	0.973260	3734.82			0.007331	-135.60	18.5	3547.23			0.008161	-136	16.6
	Book_2	H-bonded	avdz	1.007023	3043.23			0.041094	-827.19	20.1	2788.35			0.045548	-895	19.6
		H-bonded	avdz	0.981842	3505.79			0.015913	-364.62	22.9	3349.32			0.016021	-334	20.8
		H-bonded	avdz	0.981842	3520.07			0.015913	-350.34	22.0	3356.99			0.016022	-326	20.3
		H-bonded	avdz	0.979926	3563.08			0.013997	-307.34	22.0	3391.79			0.014892	-291	19.5
		H-bonded	avdz	0.980471	3567.79			0.014542	-302.62	20.8	3395.83			0.015504	-287	18.5
		H-bonded	avdz	0.980470	3591.19			0.014541	-279.23	19.2	3410.24			0.015504	-273	17.6
		H-bonded	avdz	0.979926	3633.35			0.013997	-237.07	16.9	3439.54			0.014893	-243	16.3
	Ring	H-bonded	avdz	0.986519	3439.30			0.020590	-431.11	20.9	3256.28			0.021800	-427	19.6

III. Hydrogen bonded OH stretches in $H3O+(H_2O)_n$, n=3-4 (various isomers)

				Equilibrium geometry							Vibrationally averaged geometry					
				R_e	ω_1	ω_2	$(\omega_1+\omega_2)/2$	ΔR_e (Å)	$\Delta\omega$ (cm^{-1})	s	ν_1	ν_2	$(\nu_1+\nu_2)/2$	ΔR_0 (Å)	$\Delta\nu$ (cm^{-1})	s
H_2O			mp2/a	0.965929	3803.30	3937.53	3870.42	0	0	n/a	3621.10	3744.74	3682.92	0	0	n/a
			mp2/a	0.961369	3821.89	3947.72	3884.81	0	0	n/a	3654.21	3767.73	3710.97	0	0	n/a
$H3O+(H_2O)$	Ring	H-bonded	avdz	0.977693	3632.00			0.011764	-238.42	20.3	3389.812			0.013095	-293	22.4
$H3O+(H_2O)$	B	H-bonded	avdz	0.988458	3410.00			0.022529	-460.42	20.4	3210.704			0.025580	-472	18.5
	B2	H-bonded	avdz	0.987874	3419.00			0.021945	-451.42	20.6	3180.475			0.025158	-502	20.0
	C	H-bonded	avdz	0.990033	3375.00			0.024104	-495.42	20.6	3114.421			0.027846	-568	20.4
		H-bonded	avdz	0.989838	3383.00			0.023909	-487.42	20.4	3164.138			0.027544	-519	18.8
	R	H-bonded	avdz	0.976377	3634.00			0.010448	-236.42	22.6	3446.591			0.011073	-236	21.3
		H-bonded	avdz	0.975980	3656.00			0.010051	-214.42	21.3	3455.216			0.011196	-228	20.3

H-Bonded O-H...O

Table 3.4: Same as Table 3.1 for $(H_2O)_6$ and $H_3O^+(H_2O)_n$.

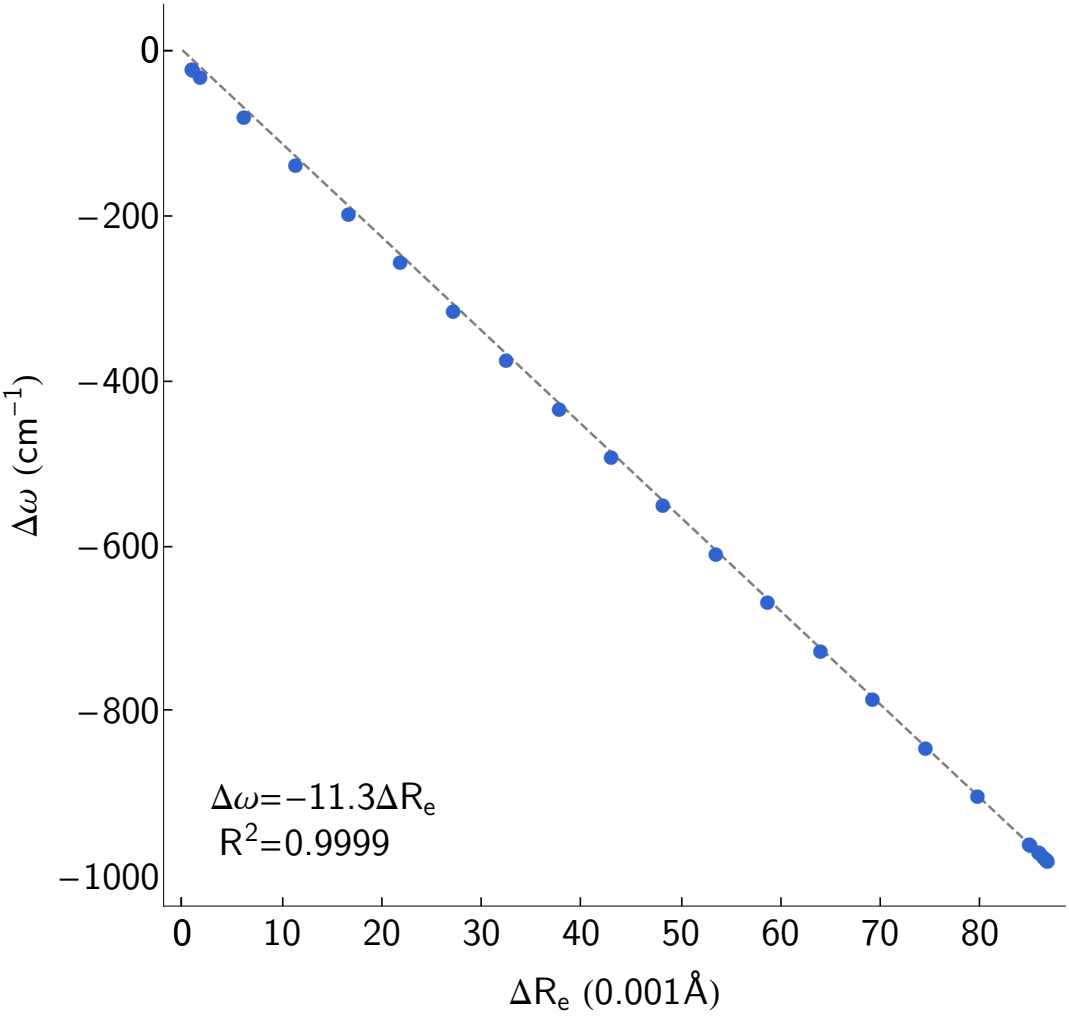

Figure 3.14: The change in the harmonic frequency, $\Delta\omega$ from the value in the absence of an external electric field is plotted as a function of the shift in the equilibrium bond length, ΔR_e. Here the OH bond is represented by a Morse oscillator using parameters used to model the OH stretch in water,[57] and the dipole moment is assumed to be a linear function of the OH bond length, and independent of the field strength. The results are fit to a line that is constrained to go through the origin. The slope matches the expected value of $-1.5\alpha\omega = -12$ cm^{-1}/0.001 Å, discussed in the text.

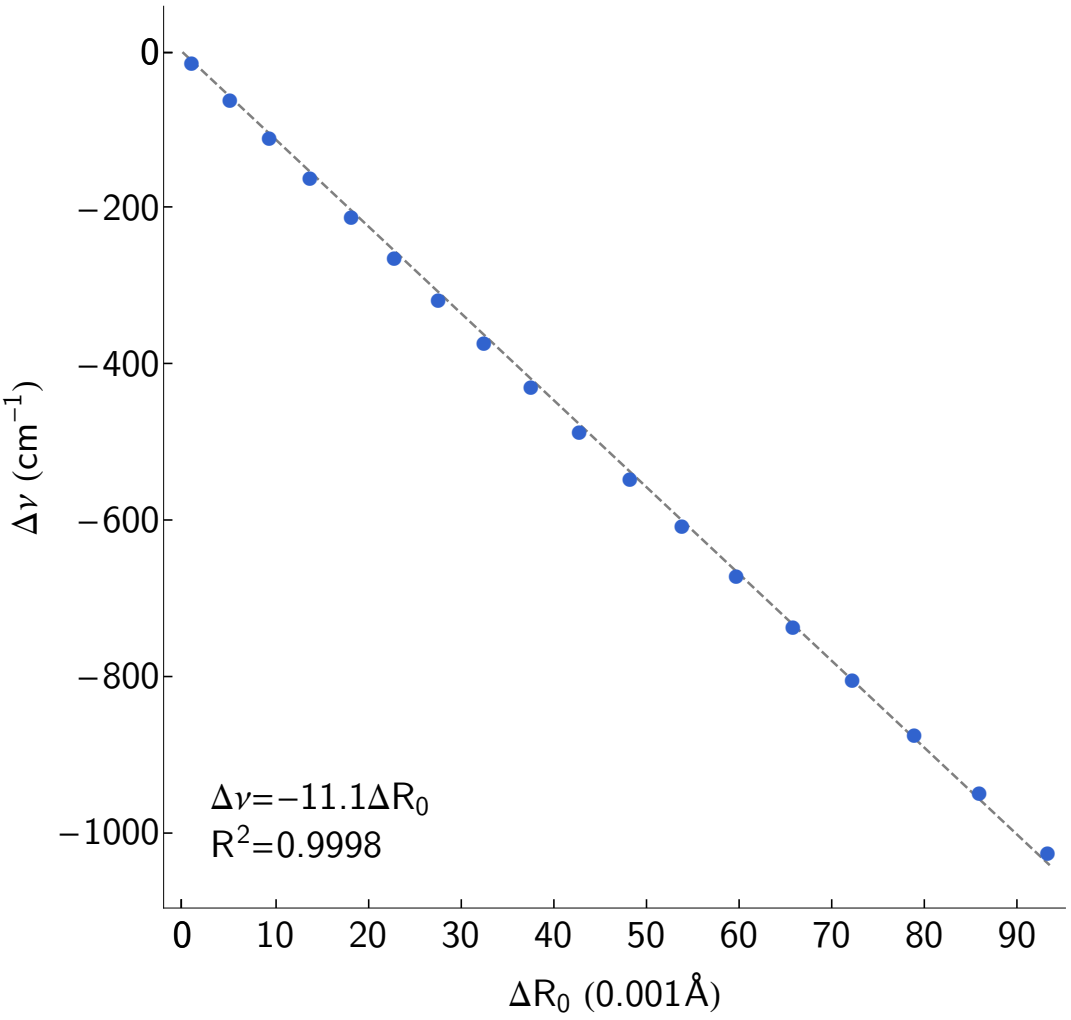

Figure 3.15: The same as Figure 3.14, showing the correlation between the shift in the anharmonic frequency, $\Delta\nu$ as a function of the shift in the zero-point averaged OH bond length, ΔR_0.

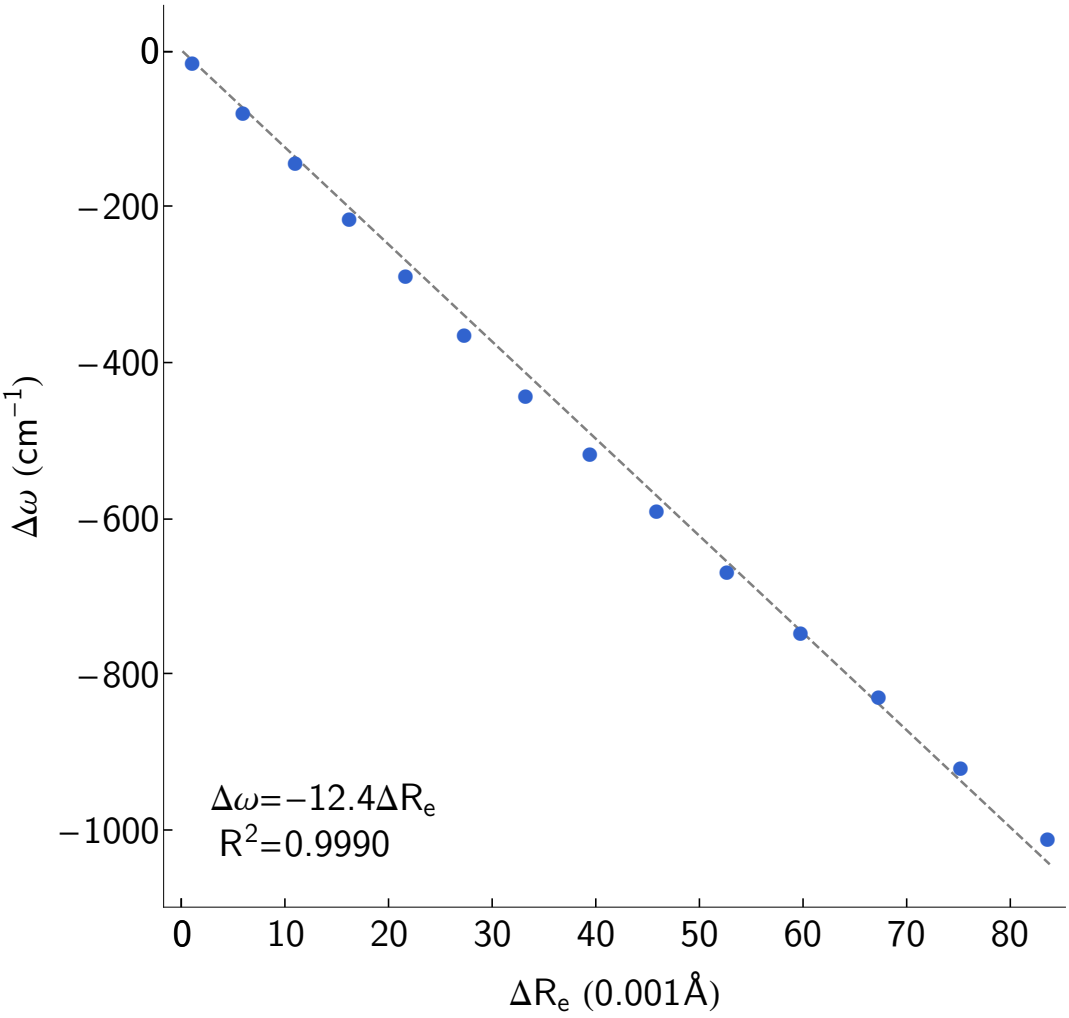

Figure 3.16: The same as Figure 3.14, using a one-dimensional scan of the potential as a function of the OH bond length in water evaluated at the MP2/aug-cc-pVDZ level of theory/basis, evaluated using Gaussian 09.

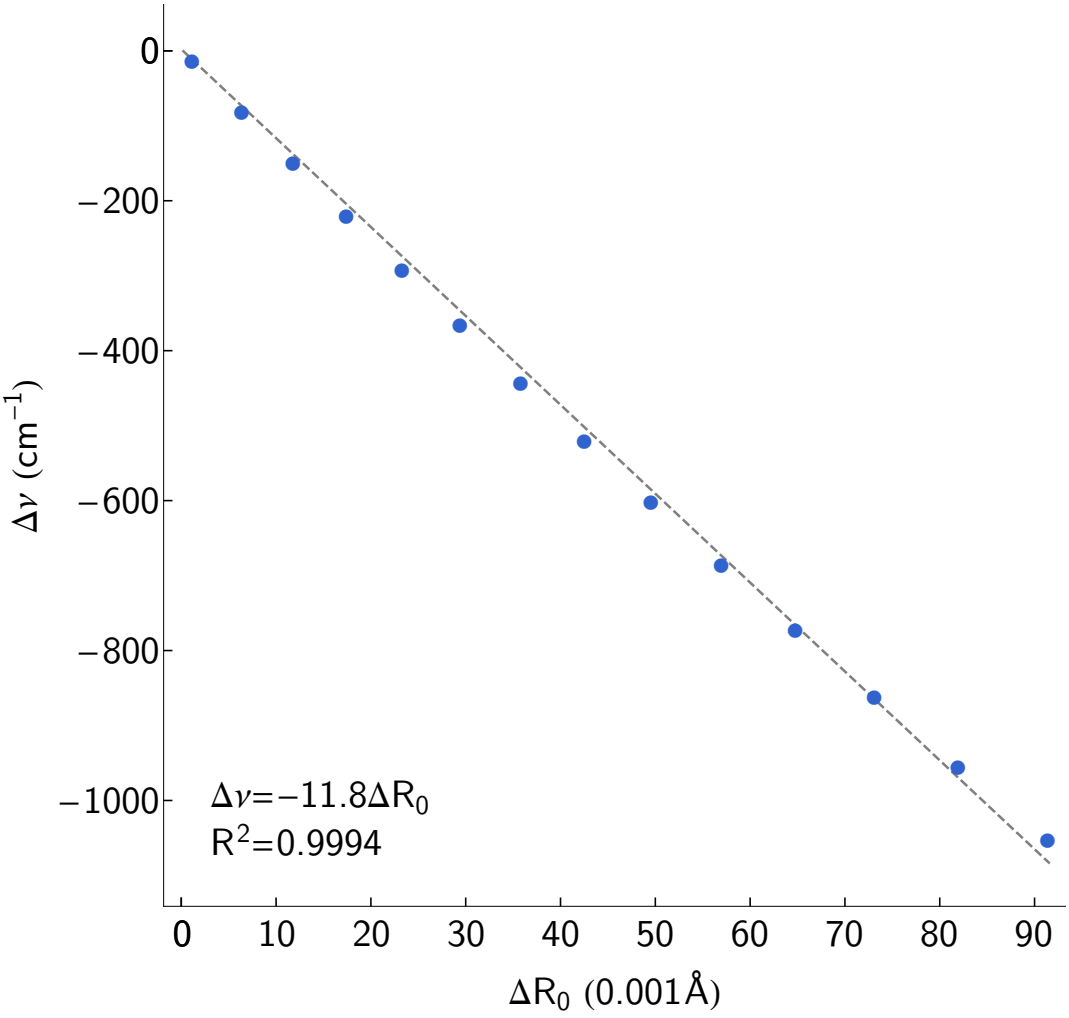

Figure 3.17: The same as Figure 3.16, comparing anharmonic frequencies and zero-point averaged OH bond lengths.

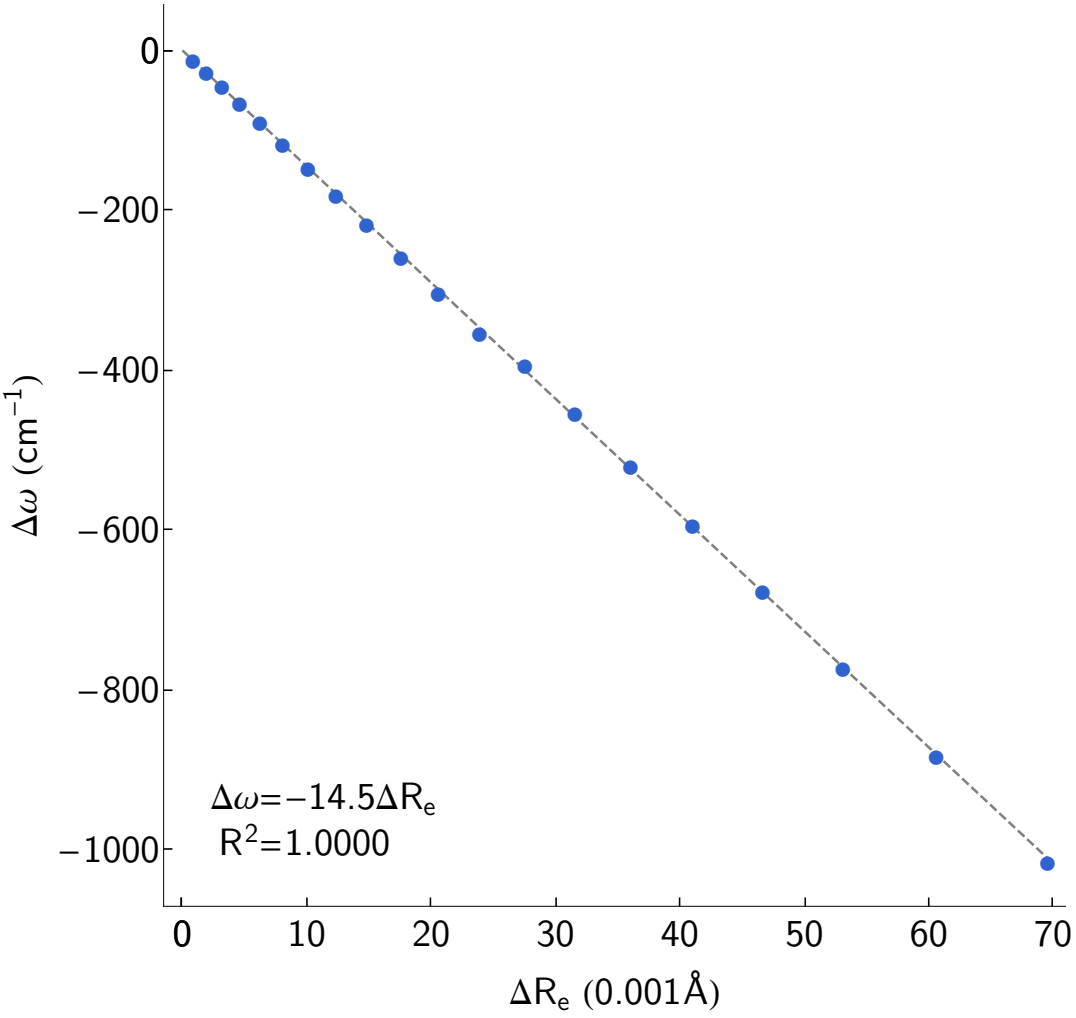

Figure 3.18: The same as Figure 3.16, where the effect of the external field is introduced in the electronic structure calculation, rather than assuming a linear dipole approximation.

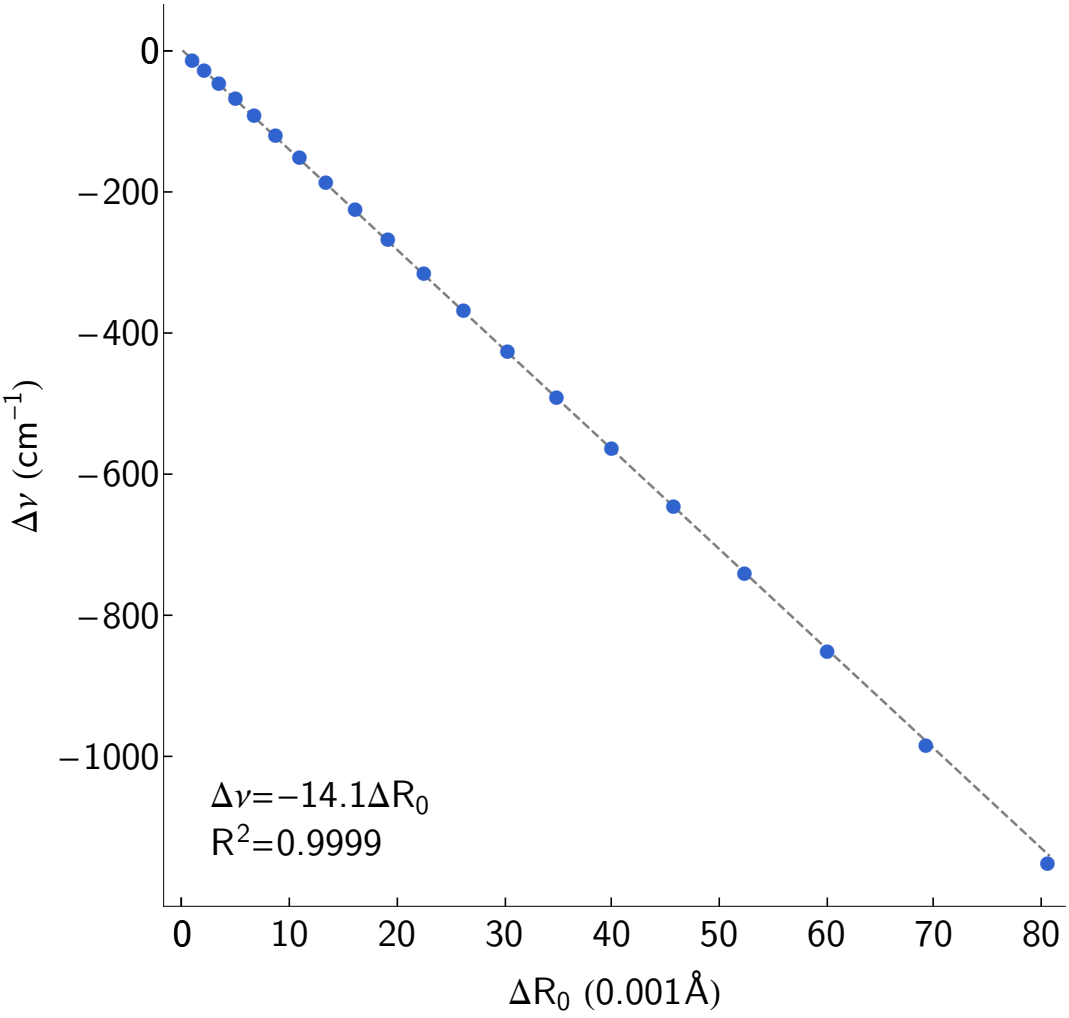

Figure 3.19: The same as Figure 3.18, comparing anharmonic frequencies and zero-point averaged OH bond lengths.

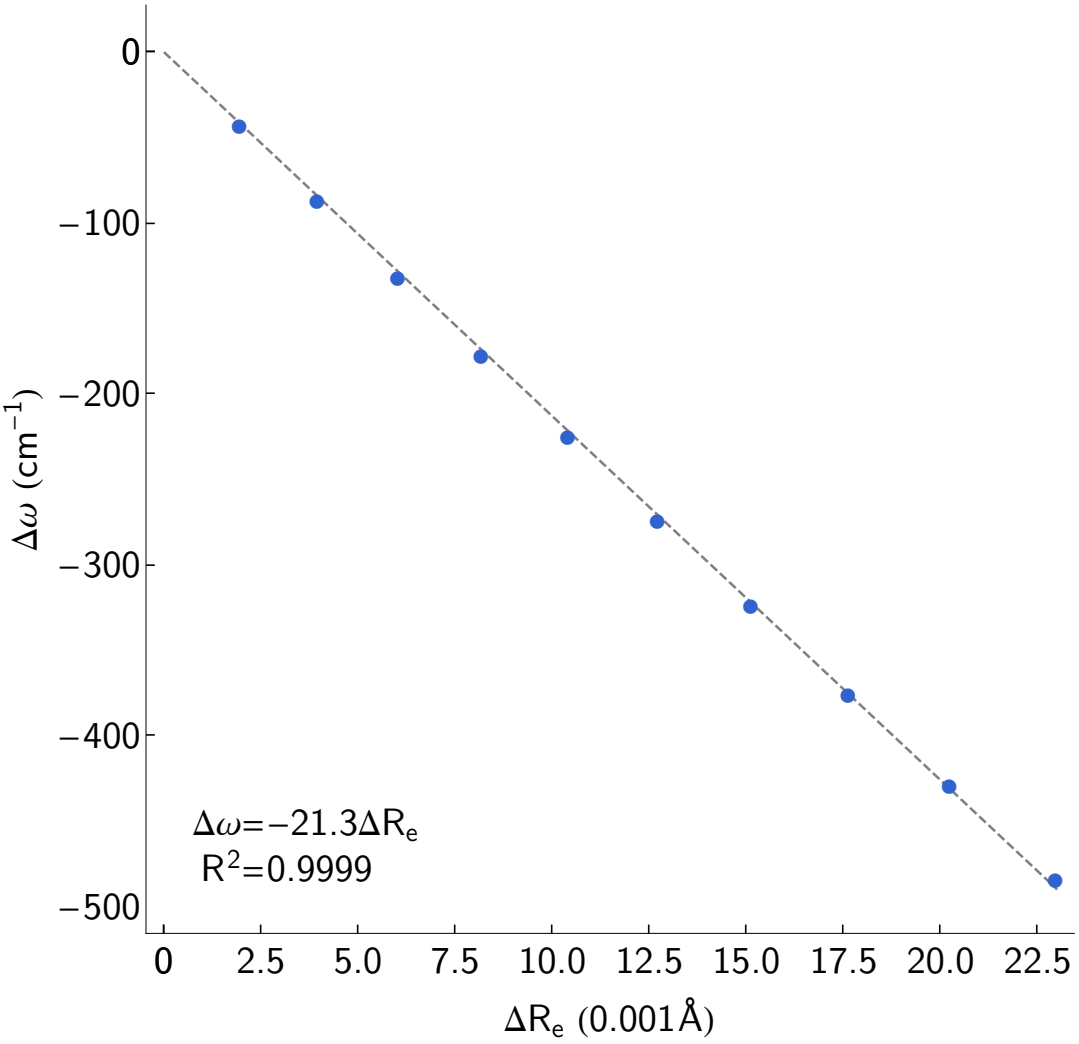

Figure 3.20: The same as Figure 3.14, replacing the linear dipole approximation with a quadratic expansion of the dipole along the hydrogen-bonded OH stretch in water dimer, which has been obtained for $R_{\mathrm{OO}} = 2.97$ Å. The dipole surface and fit are provided in Figure 3.11.

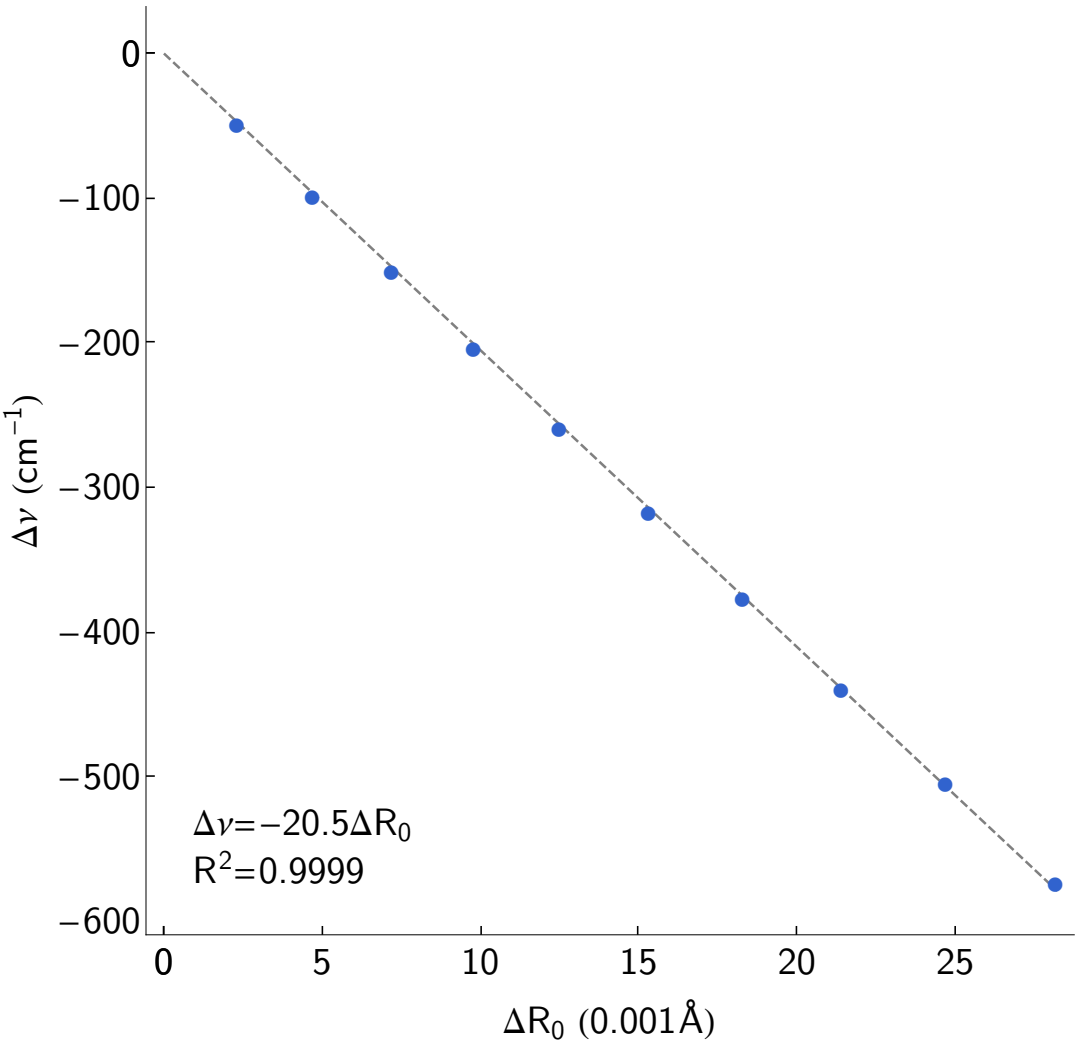

Figure 3.21: The same as Figure 3.20, comparing anharmonic frequencies and zero-point averaged OH bond lengths.

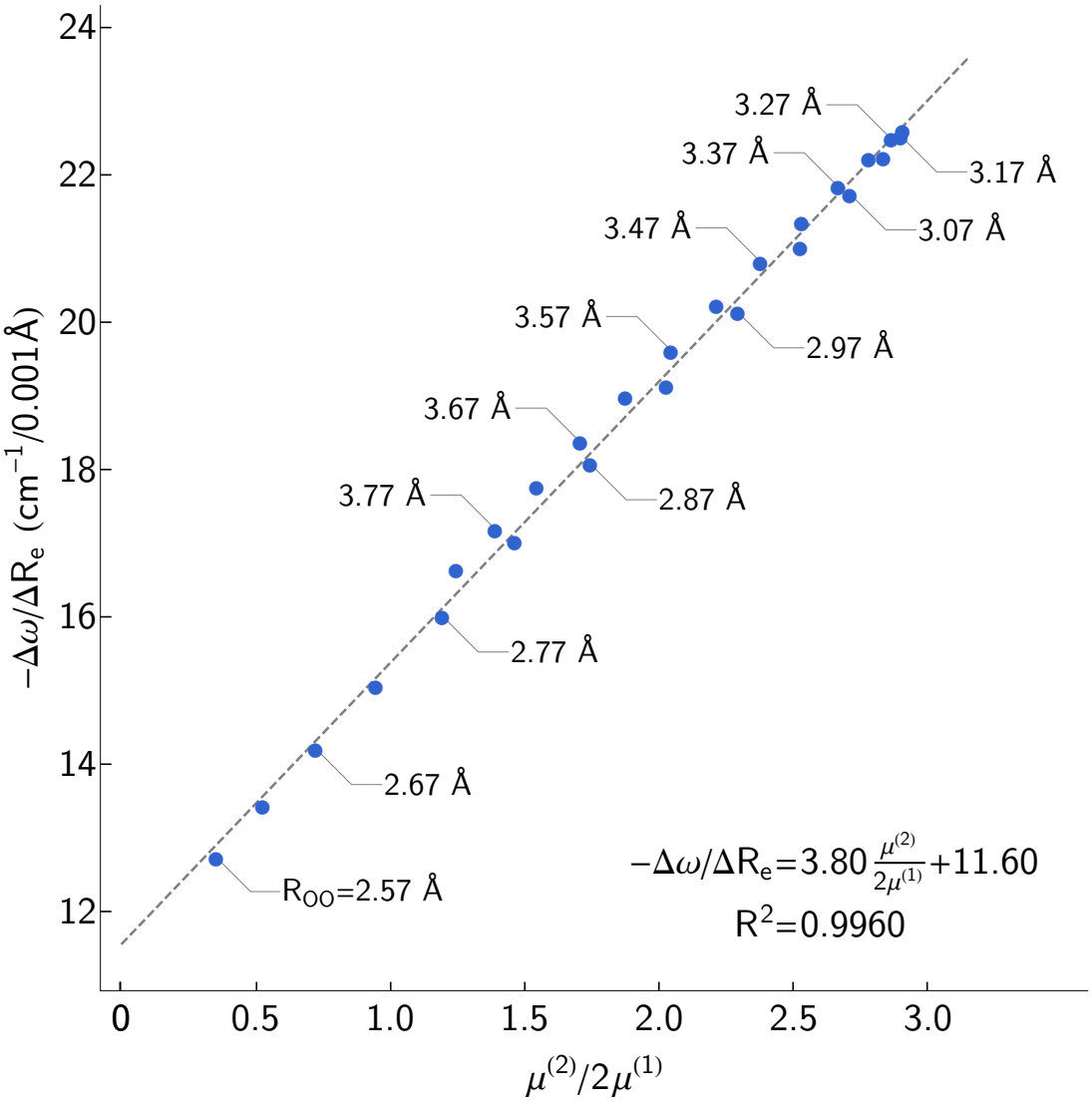

Figure 3.22: Correlations between the $-\Delta\omega/\Delta R_e$ ratio and the ratio of the second and first derivatives of the dipole function. These calculations utilize the Morse potential described in the text and a quaratic fit to the dipole moment along the hydrogen-bonded OH bond in water dimer evaluated at the MP2-aug-cc-pVDZ level of theory. An example of this fit for $R_{OO} = 2.97$ Å is provided in Figure 3.11.

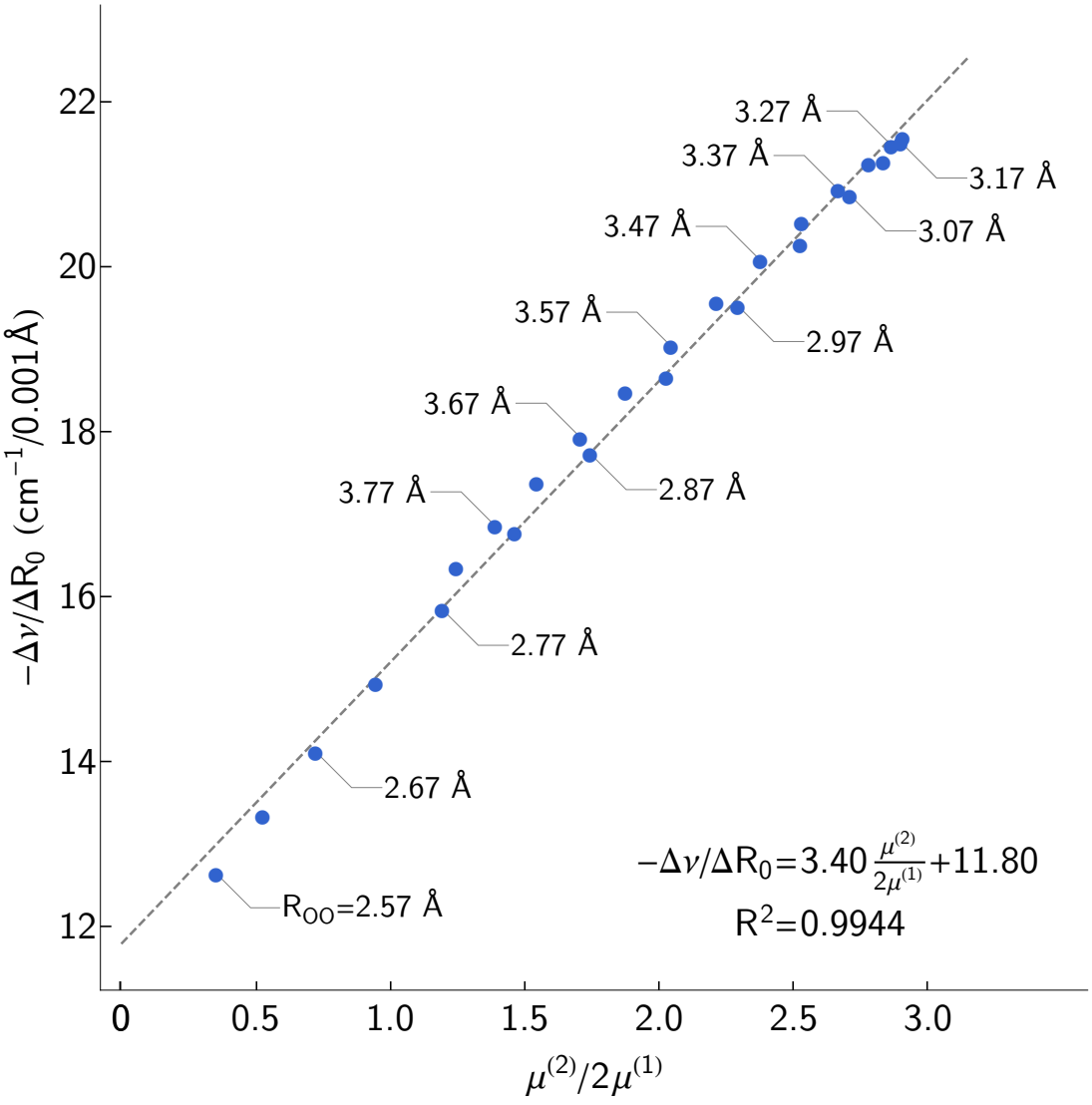

Figure 3.23: The same as Figure 3.22, considering the ratio of the shift in ν to the shift in R_0.

R_{OO} (Å)	$\mu^{(1)}$ ($D \cdot Å^{-1}$)	$\mu^{(2)}$ ($D \cdot Å^{-2}$)	$\mu^{(2)}/\mu^{(1)}$ ($Å^{-1}$)	$\Delta\nu/\Delta R_0$ (cm^{-1}/0.001 Å)	$\Delta\omega/\Delta R_e$ (cm^{-1}/0.001 Å)
2.57	6.09	4.29	0.35	−12.6	−12.7
2.62	5.46	5.74	0.53	−13.4	−13.4
2.67	4.86	7.02	0.72	−14.1	−14.2
2.72	4.28	8.10	0.95	−15.0	−15.1
2.77	3.75	8.96	1.19	−15.8	−16.0
2.82	3.28	9.59	1.46	−16.8	−17.0
2.87	2.86	9.98	1.74	−17.7	−18.1
2.92	2.50	10.1	2.03	−18.7	−19.1
2.97	2.21	10.1	2.29	−19.5	−20.1
3.02	1.96	9.91	2.52	−20.3	−21.0
3.07	1.77	9.57	2.71	−20.9	−21.7
3.12	1.61	9.13	2.83	−21.3	−22.2
3.17	1.49	8.63	2.89	−21.5	−22.5
3.22	1.39	8.09	2.90	−21.6	−22.6
3.27	1.31	7.53	2.86	−21.5	−22.5
3.32	1.25	6.97	2.78	−21.3	−22.2
3.37	1.20	6.42	2.67	−20.9	−21.8
3.42	1.16	5.89	2.53	−20.5	−21.4
3.47	1.13	5.38	2.38	−20.2	−20.8
3.52	1.12	4.90	2.21	−19.6	−20.2
3.57	1.09	4.45	2.04	−19.0	−19.6
3.62	1.07	4.02	1.87	−18.5	−19.0
3.67	1.06	3.62	1.71	−17.9	−18.4
3.72	1.05	3.25	1.54	−17.4	−17.8
3.77	1.05	2.91	1.39	−16.9	−17.2
3.82	1.04	2.59	1.24	−16.3	−16.6

Table 3.5: Parameters Obtained From an Analysis of the One-Dimensional Cuts Through the Water Dimer Potential Along the Hydrogen-Bonded OH Bond

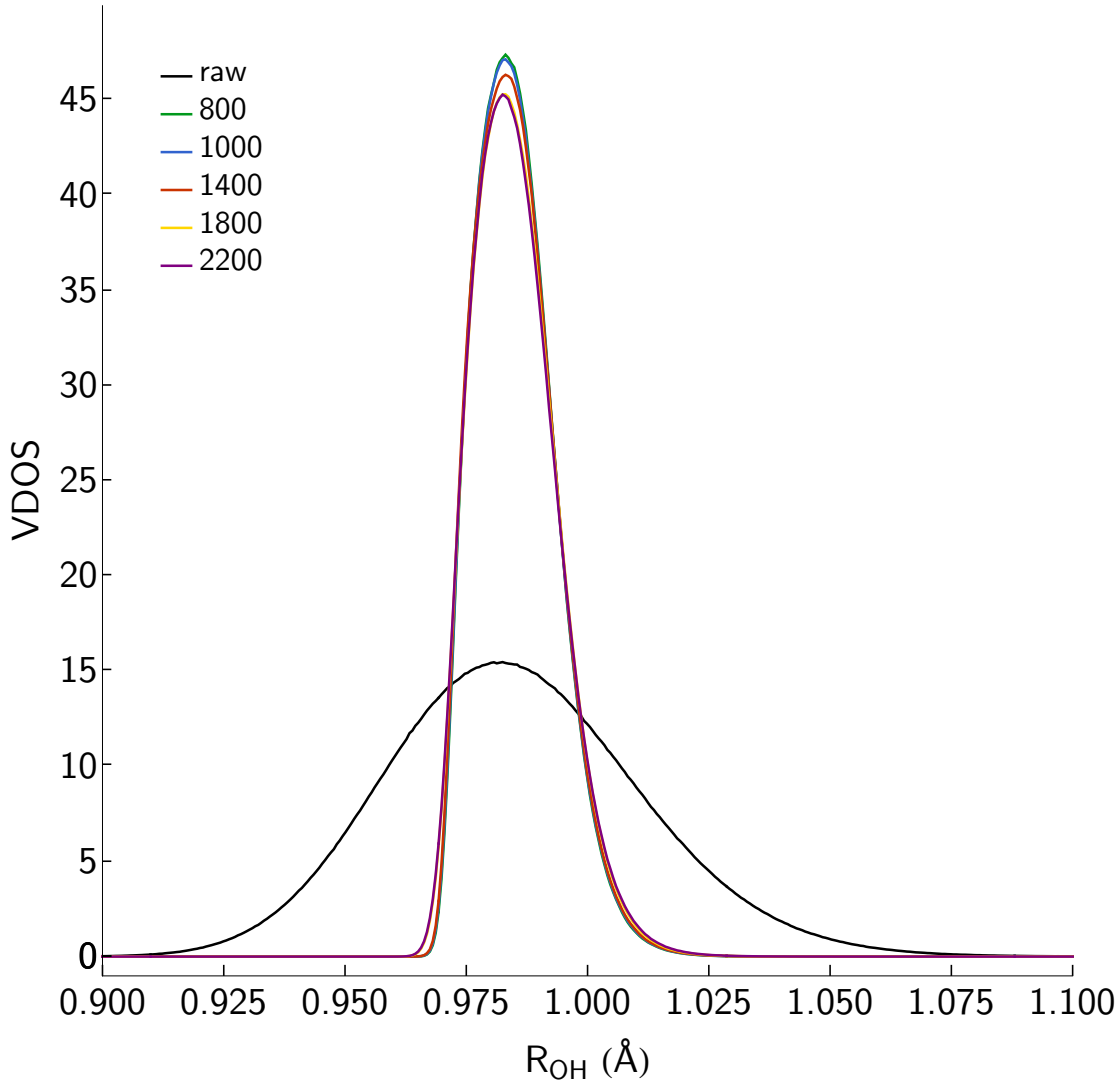

Figure 3.24: Plots of the Fourier filtered OH bond length distribution, obtained from the AIMD simulation of liquid water. The various curves provide the results of the frequency cutoffs (in cm^{-1} used for the Fourier filtering, which have been reported in cm^{-1}. The cutoff of 800 cm^{-1} is used in the reconstruction of the spectrum

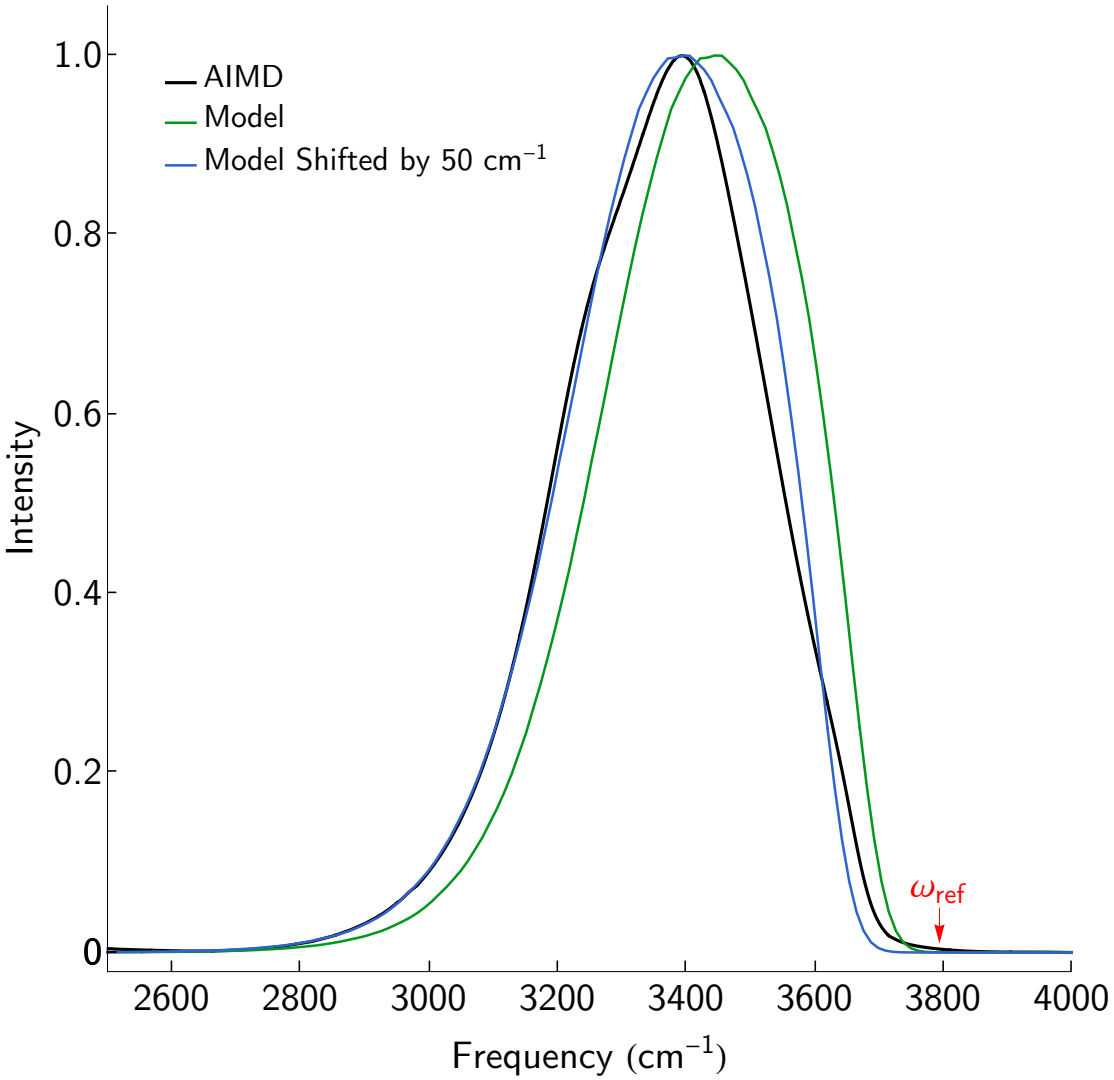

Figure 3.25: The reconstructed infrared absorption spectrum of water (green curve), calculated from the Fourier filtered OH bond distribution obtained with an 800 cmz^{-1} cutoff frequency (green curve in Figure 3.24), the revPBE-D3 dipole moment along the OH bond axis, and the frequency calculated using the -18.8 cm^{-1}/0.001 Å correlation in Figure 3.10. This is compared to a spectrum obtained from *ab initio* MD (AIMD) at the revPBE-D3 level of theory[59] (black curve). To aid in comparison, the IR reconstruction is shifted by 50 cm^{-1} (blue curve) to align the peak with the peak in the AIMD spectrum. The red arrow indicates the value of $\omega_{\text{ref}} = 3793$ cm^{-1} (defined in Eq. 3.21) used to reconstruct the spectrum. In these plots, the intensity has been scaled so the maximum intensity in all the curves is unity.

Chapter 4

THE ROLE OF TUNNELING IN THE SPECTRA OF H_5^+ AND D_5^+ UP TO 7300 CM^{-1}

Reproduced in part with permission from [Mark A Boyer, Chloe S Chiu, David C McDonald, J Philipp Wagner, Jason E Colley, Dylan S Orr, Michael A Duncan, and Anne B McCoy. The role of tunneling in the spectra of $H5^+$ and $D5^+$ up to 7300 cm^{-1}. *J. Phys. Chem. A*, 124(22):4427–4439, jun 2020]

4.1 Introduction

The H_5^+ molecular ion has long been of theoretical and experimental interest. In 1960 Jones and Simpson used H_5^+ as a test system for developing a model to study the effect of delocalization on IR intensity.[64] Two years later, Dawson and Ticknee identified a mass spectrometric signature of this ion in a hydrogen discharge.[65] In this report, they noted that Schaeffer and Thompson had proposed the existence of $H_2 \cdot H_3^+$ in their consideration of H/D exchange between H_3^+ and D_2.[66] Structurally, H_5^+ can be thought of as either a strongly bound complex between H_2 and H_3^+, where the binding energy is roughly 2200 cm^{-1},[67] or as a proton bound complex between two H_2 molecules. Much of the more recent interest in H_5^+ hinges on its role in astronomy, both as a bound species and as an intermediate in the proton transfer following a $H_2 + H_3^+$ collision.

Direct observation of interstellar H_5^+ has yet to be reported. However, observation of H_3^+ was first reported by Oka[68] in 1996, indicating that $H_2 + H_3^+$ collisions must occur. Laboratory measurements of the infrared spectrum of H_5^+ between 3400 and 4000 cm^{-1} were first reported more than thirty years ago by Okumura, Yeh, and Lee.[69] Subsequently Bae[70] reported a spectrum between 6400 and 7900 cm^{-1}. More recently, one of our groups recorded

the mid-IR spectrum of H_5^+ over a larger range of photon energies (from 2500 to 4500 cm^{-1}) as well as the spectrum of D_5^+ between 1500 and 3500 cm^{-1}.[67] In this study, two additional transitions were observed in the H_5^+ spectrum and three peaks were reported for D_5^+. All of these studies exploited the fact that the dissociation energies of H_5^+ and D_5^+ relative to the $H_2 + H_3^+$ and $D_2 + D_3^+$ products are roughly 2230 and 2400 cm^{-1}, respectively. This allowed them to obtain an action spectrum for the ion of interest by monitoring the growth of the H_3^+ or D_3^+ mass channel following the photon absorption of a single photon. In addition, Cheng *et al.* reported far-IR spectra of H_5^+ and D_5^+, which were obtained through an IR-MPD (multi-photon dissociation) experiment using the FELIX free electron laser.[71] This study extended the region of spectral coverage down to 200 cm^{-1} for H_5^+ and between 699 and 2000 cm^{-1} for D_5^+. The spectra obtained in these more recent studies were compared to calculated spectra evaluated using a vibrational configuration interaction approach (VCI).

The history of the assignment of the observed transitions is similarly rich. Due to the lack of a heavy atom, H_5^+ has been termed 'astructural'.[72] While the minimum energy geometry can be described as a complex of H_3^+ with H_2, where the shared proton lies on the axis that connects the centers of mass of the two outer H_2 groups and with the two H_2 groups lying in perpendicular planes, the barrier for proton transfer is well-below the zero-point energy in the vibration that corresponds to the displacement of the shared proton between the outer H_2 units.[67,73] The barrier for the hindered rotation of the outer H_2 groups is also low, and the ground state wave function is also delocalized in this coordinate.[73,74]

The lack of a simple zero-order model for the vibrations in H_5^+ along with the absence of a heavy atom and large changes in the bond lengths and frequencies of the outer H_2 stretches with displacement of the shared proton[75] makes assignment of the spectrum sensitive to the model used in making these assignments. For example, Okumura *et al.* assigned their spectrum based on harmonic frequencies obtained from a normal mode analysis by Yamaguchi *et al.*, which was based on the minimum energy geometry of the cluster.[76,77] This led to a nominal assignment of the peaks at 3532 and 3910 cm^{-1} to the fundamentals in the out-of-phase and in-phase combination of the outer H_2 stretches. Subsequently, Bae used a similar model

to assign the higher-energy peaks as transitions to states with two quanta of excitation in the outer H_2 stretches along with zero or one quantum of excitation in the shared proton stretch. They also identified a lower-energy peak at 4230 cm^{-1}, which was assigned as a transition to a combination band involving the first excited state in the outer H_2 stretches with one quantum of excitation in the shared proton stretch.

More recently, diffusion Monte Carlo (DMC) studies have identified the most probable structure of H_5^+ as the D_{2d} saddle point structure.[73,78] Using this structure as the reference, VCI calculations of the spectra have been performed, and the resulting calculated spectra agree well with the vibrational predissociation and IRMPD spectra obtained for transitions above and below the dissociation limit for the ion, respectively.[67,71] Calculated peaks at 3560, 3950, and 4268 cm^{-1}, which are close in energy and intensity to the peaks in the measured spectrum, have been assigned to the out-of-phase outer H_2 stretch with combination bands involving the shared-proton stretch and the in-phase outer H_2 stretch. Assignment of features below 3000 cm^{-1} in H_5^+ is more complicated due to the large couplings between the shared proton stretch, the breathing (H_2·H_2 stretch) vibration, and the other lower frequency vibrations. Based on a combination of fixed-node DMC studies and two-dimensional calculations that focused on the shared proton stretch and the breathing vibrations, a model has been developed that anticipates a series of peaks in H_5^+ spanning from ∼350-2000 cm^{-1} which are assigned to a progression in the shared-proton with odd numbers of quanta of excitation. The wave functions for these states extend into the H_2+H_3^+ product channel and the nodes in the wave functions lie perpendicular to the reaction coordinate.[79]

The results of two- and four-dimensional calculations using either an adiabatic separation of the shared proton modes[80,81] or MCTDH[82,83] have shown that the major features of the spectrum can be reproduced by a reduced dimensional model that does not include displacements of the shared proton off of the axis that connects the outer H_2 groups and the internal-rotation of the ion. A later nine-dimensional MCTDH calculation has been able to reproduce the spectrum up to ∼7500 cm^{-1}.[84] Based on this calculation, peaks at 3528, 3944, and 4248 cm^{-1} have been assigned to the out-of-phase outer H_2 stretch, an H_3^+ breathing

mode, and a transition to a state with a single quantum of excitation in the shared proton stretch combined with the out-of-phase outer H_2 stretch. The peaks at 6823, 7304, 7681, and 7905 cm^{-1} have all been assigned as two quanta in the outer H_2 stretches combined with 0, 1, 2, and 3 quanta in the shared-proton stretches. While this assignment is generally consistent with earlier studies, it is surprising that some of the above assignments seem to reflect excitation to totally symmetric excited states. Finally, comparison of the results of the nine- and four-dimensional MCTDH calculations shows that the calculated spectra are in fairly good agreement despite a shift in the energies that reflects the missing vibrational degrees of freedom in the lower-dimensional calculation.

Assignment of a calculated spectrum is necessarily sensitive to the choice of coordinates, the size of the basis, and the quality of the potential energy surface that is used. Furthermore, full-dimensional approaches, while providing the ability to reproduce a spectrum with high fidelity can suffer from a corresponding difficulty in interpretation, as teasing apart the contributions of many motions can be a challenging process. In the present study, we develop a four-dimensional model that reproduces the main features in the reported spectra of H_5^+ and D_5^+. This model is based on the observation that the assignments described above focus on the outer H_2 stretches, the shared proton stretch, and the H_2 breathing vibration. Consequently, this model includes only these four vibrational motions. The wave functions and energies derived from this treatment are analyzed in terms of an adiabatic separation of the high-frequency H_2 stretches and the lower-frequency shared proton and H_2 breathing vibrations. Couplings are introduced between states with the same total amount of excitation in the outer H_2 stretches. The combination of the reduced dimensionality and the further adiabatic separation of the high and low-frequency vibrations simplifies the assignment of the calculated transitions.

Spectra based on this four-dimensional model are compared to the previously reported spectra, as well as to our newly-reported spectra between 4850 and 7300 cm^{-1} for both H_5^+ and D_5^+. Based on the analysis of the resulting calculations we suggest a revised description of the assignments of the peaks in the spectra of these ions in which the states that are

accessed correspond to the symmetry allowed combination bands involving the lowest-energy state with the appropriate excitation in the outer H_2 stretch in combination with states with increasing excitation in the shared proton stretch.

4.2 Theory

Before considering the results of this model, we start by describing the model itself. H_5^+ has nine vibrational degrees of freedom. Two describe the outer H_2 bond lengths, two provide the distances between the shared proton and the centers of mass of each of the two H_2 group, and two more are the angles between the vectors that describe the outer H_2 bonds and the vector that connects the centers of mass of the two H_2 groups. The remaining three coordinates include the torsion angle between the two outer H_2 groups and the two coordinates that describe displacements of the shared proton off of the axis that connects the centers of mass of the outer H_2 groups. In the model presented below, we focus on the coordinates that describe the outer H_2 stretches (r_1 and r_2), and the distances between the shared proton and the centers of mass of each of the outer H_2 groups (R_1 and R_2). This choice of coordinates is similar to that used in prior 4D MCTDH work by Valdes and Prosmiti[82,83] as well as adiabatic treatment by Sanz-Sanz *et al.*[80] The remaining coordinates are constrained to their values in the D_{2d} reference geometry. Specifically, the three angles are all constrained to 90° and the shared proton is constrained to lie on the axis that connects the centers of mass of the outer H_2 groups. The D_{2d} structure and the four coordinates that are used in this study are depicted in Fig. 4.1. This structure corresponds to a low-energy transition state structure on the potential,[75] which, while not the lowest energy structure, is the most probable structure of the ion when zero-point energy is taken into account.[73,78] The choice to focus on these four coordinates is motivated by the fact that the displacement of the shared proton between the two outer H_2 groups carries most of the oscillator strength and that the spectral regions of interest correspond to transitions involving excitation of the outer H_2 stretching vibrations. This choice is further justified by considering that the five omitted coordinates have different symmetries than these nominally bright vibrations

and carry significantly less oscillator strength. While transitions involving the other five vibrations will certainly contribute to the spectrum, the zero-order bright states are expected to correspond to transitions in the shared proton stretch that build off of states with two or fewer quanta of excitation in the outer H_2 stretching vibrations.

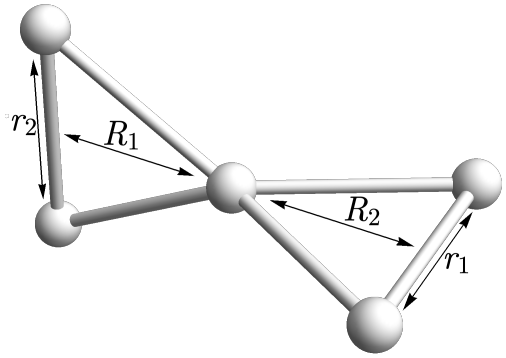

Figure 4.1: The D_{2d} structure of H_5^+ and the coordinates used for the calculations.

4.2.1 Hamiltonian

Based on the structure of H_5^+ shown in Figure 4.1, the reduced dimensional Hamiltonian is given by

$$H(R_1, R_2, r_1, r_2) = \frac{p_{R_1}^2}{2\mu_{R_1}} + \frac{p_{R_2}^2}{2\mu_{R_2}} + \frac{p_{r_1}^2}{2\mu_{r_1}} + \frac{p_{r_2}^2}{2\mu_{r_2}} - \frac{p_{R_1} p_{R_2}}{m_{\mathrm{H}^+}} + V(R_1, R_2, r_1, r_2) \tag{4.1}$$

where μ_{r_i} represents the reduced mass of one of the outer H_2 groups, $m_{\mathrm{H}}/2$, while μ_{R_i} provides the reduced mass of the shared proton, with mass m_{H^+} and one of the outer H_2 groups, which has a mass of $2m_{\mathrm{H}}$

$$\mu_{R_i} = \left(\frac{1}{m_{\mathrm{H}^+}} + \frac{1}{2m_{\mathrm{H}}} \right)^{-1} \tag{4.2}$$

Because we calculate the spectra for the four isotoplogues of H_5^+ in which the four atoms that make up the outer H_2 groups are all the same isotope of hydrogen, we differentiate the mass of the shared proton from that of the atoms in the outer H_2 groups by using m_{H^+} and m_H, respectively.

To simplify the Hamiltonian, rather than using R_1 and R_2 to describe the position of the central proton we use

$$\begin{aligned} a &= \frac{R_1 - R_2}{\sqrt{2}} \\ s &= \frac{R_1 + R_2}{\sqrt{2}} \end{aligned} \tag{4.3}$$

This coordinate choice removes the kinetic coupling term from the Hamiltonian in Eq. 4.1, leading to

$$H(a, s, r_1, r_2) = \frac{p_a^2}{2\mu_a} + \frac{p_s^2}{2\mu_s} + \frac{p_{r_1}^2}{2\mu_{r_1}} + \frac{p_{r_2}^2}{2\mu_{r_2}} + V(a, s, r_1, r_2) \tag{4.4}$$

where

$$\mu_a = \frac{4m_H m_H^+}{4m_H + m_H^+} \tag{4.5}$$

$$\mu_s = 2m_H \tag{4.6}$$

The potential term, $V(a, s, r_1, r_2)$, is constructed as a spline interpolation over an evenly spaced grid of electronic energies that consists of 60 points in R_1 and R_2 and 15 points in r_1 and r_2 evaluated at the MP2/aug-cc-pVTZ level of theory using the Gaussian[85] electronic structure package. In these calculations, R_1 and R_2 range from 0.461 Å to 3.461 Å and r_1 and r_2 range from 0.256 Å to 1.256 Å. It is important to note that the use of the aug-cc-pVTZ basis is necessary for these calculations as the use of the smaller aug-cc-pVDZ basis

gives qualitatively different spectra which do not agree with the measured spectra for this ion. This surprisingly large sensitivity of the calculated spectrum to the basis set used for the electronic structure calculations reflects the very flat potential along a. When the aug-cc-pVDZ basis is used, the equilibrium structure corresponds to the D_{2d} structure shown in Figure 4.1, with $s_e = 1.50$ Å, while with the larger basis, there is a small barrier (73 cm^{-1}) in the D_{2d} geometry, and $s_e = 1.54$ Å. When we take one-dimensional cuts through these potentials along a at the appropriate value of s_e with the outer H_2 bond lengths constrained to their values in the minimum energy geometry, we find that the calculated anharmonic frequencies of the shared proton stretch are roughly 40% larger when the aug-cc-pVDZ basis is used (1000 cm^{-1}) compared to when aug-cc-pVTZ is used (674 cm^{-1}). While such one-dimensional calculations are not expected to provide accurate frequencies for this ion, the sensitivity of this frequency to the basis set used for the calculation anticipates the sensitivity of the higher-dimensional calculations to this choice.

The large sensitivity of the shape of these potential cuts to the basis set raises the question of what would happen if a larger basis were used, and we repeated the analysis using an aug-cc-pVQZ basis. In this case the equilibrium value of s is still 1.54 Å, the barrier height is slightly higher, 90 cm^{-1} and the anharmonic frequency becomes 683 cm^{-1}. These values can also be compared to those reported by Xie *et al.* based on CCSD(T)/aug-cc-pVTZ calculations where the barrier height is 48.4 cm^{-1} and $s_e = 1.54$ Å.

4.2.2 Adiabatic Separation of the High and Low Frequency Vibrations

To facilitate the interpretation of the results of these calculations and to reduce the size of the basis sets required to express the Hamiltonian matrix, the calculations are performed by employing an adiabatic separation of the high-frequency H_2 stretches and the low-frequency displacement of the shared proton between the two H_2 groups. This type of vibrational adiabatic separation has been used to study a number of molecular systems, going back to the work of Johnson and Reinhardt in their study of water.[86] Such a treatment has been shown to be an effective approach to decouple high- and low-frequency vibrational motions.

In the present study, the states are described in terms of two sets of quantum numbers. The first set of quantum numbers provides the excitation of the outer H_2 stretch, ν_{H_2}. Since the H_2 stretch excitation is divided between the two outer H_2 oscillators, for each value of ν_{H_2}, there are $\nu_{H_2} + 1$ adiabatic states. These are identified by the letters A, B and C. The associated wave functions are obtained by solving the two-dimensional Schrödinger equation

$$H^{H_2}(a,s) = \frac{p_{r_1}^2}{2\mu_{r_1}} + \frac{p_{r_2}^2}{2\mu_{r_2}} + V(r_1, r_2; a, s) \tag{4.7}$$

for the $v_{H_2}+1$ wave functions, $\Phi_{v_{H_2},\alpha}(r_1, r_2; a, s)$, and the corresponding energies, $\mathcal{E}_{\nu_{H_2},\alpha}(a,s)$, at each set of values of a and s. In this notation, α represents the specific adiabatic state (A, B, C). In the absence of couplings among the adiabatic states, the wave functions and energies would be obtained by solving the Schrödinger equation based on

$$H^{H^+}_{\nu_{H_2},\alpha} = \frac{p_a^2}{2\mu_a} + \frac{p_s^2}{2\mu_s} + \mathcal{E}_{\nu_{H_2},\alpha}(a,s) \tag{4.8}$$

This approximation reduces the four dimensional problem to a pair of coupled two dimensional problems. Conceptually, this is analogous to creating a set of effective potential energy surfaces that are functions of the coordinates of the shared proton, which are obtained by averaging the four-dimensional potential over the wave functions for the outer H_2 stretches.

While computationally attractive, this separation is only valid when the adiabatic potential energy surfaces remain separated by significantly more than the frequencies of the low-frequency vibrations. This requirement holds for states that have different values of ν_{H_2}, but it is not satisfied by adiabatic states with the same value of ν_{H_2}. Thus non-adiabatic corrections need to be introduced to allow for couplings between these states. These corrections account for the observation that in some geometries, the eigenstates of the Hamiltonian in Eq. 4.7 show a strong dependence on the given value of a and s. These changes in the H_2 wave functions can be viewed as coming in two types. In the first, the average H-H distance and the width of the wave function adjust as the system shifts from H_5^+ to a structure that more closely resembles $H_3^+ \cdot H_2$. While important, this term will couple states with the same

as well as different value of ν_{H_2}. It is also small compared to the resultant change in the nature of the vibrational wave function coming from changes in a near $a = 0$.

At $a = 0$, the D_{2d} symmetry of the ion requires that the vibrationally excited states in the outer H_2 stretches reflect this symmetry. For example, for $\nu_{H_2} = 1$ these states would be the in- and out-of-phase combinations of the states with one quantum of vibrational excitation in one of the H_2 bonds. As the shared proton shifts toward one of the outer H_2 units, the structure of the ion is better described as a complex of H_3^+ and H_2. As the H_2 stretch frequency in H_3^+ is lower than that of H_2, the two outer H_2 oscillators are no longer equivalent, and so the H_2 wave functions more closely resemble local mode states (as opposed to normal mode ones). The lower energy state will have the H_2 stretch in H_3^+ excited, and in the higher energy state the H_2 is excited. In the discussion that follows, we will describe an approach for accounting for this contribution to the non-adiabatic couplings.

4.2.3 Evaluation of the Adiabatic States

Since we are focusing our analysis on the non-adiabatic couplings between states with the same value of the ν_{H_2} quantum number, we start by re-expressing the wave function as

$$\left|\nu_{H_2}, \alpha; a, s\right\rangle = \sum_{j=0}^{\nu_{H_2}} c_j^{\alpha}(a, s) \left|j, \nu_{H_2} - j\right\rangle \tag{4.9}$$

where the $\left|j, \nu_{H_2} - j\right\rangle$ states used in the expansion are obtained by performing a vibrational self-consistent field (VSCF) calculation to obtain a set of separable wave functions based on the Hamiltonian in Eq. 4.7 at the chosen value of (a, s) as described below. The corresponding expansion coefficients, $c_j^{\alpha}(a, s)$ are obtained by evaluating the overlap between these wave functions and the eigenfunctions of Eq. 4.7, $\Phi_{\nu_{H_2},\alpha}(r_1, r_2; a, s)$, at the same value of a and s and with the same value of ν_{H_2}. The coefficients are then scaled to ensure that the $\left|\nu_{H_2}, \alpha; a, s\right\rangle$ states are normalized. With the expressions for the wave functions for the adiabatic states provided by Eq. 4.9, the matrix elements of the coupled Hamiltonian matrix are

$$H^{\nu_{\mathrm{H}_2}}_{\alpha,j,k;\alpha',j',k'} = \sum_l c^{\alpha}_l(a_j, s_k) c^{\alpha'}_l(a_{j'}, s_{k'}) \langle a_j, s_k|T|a_{j'}, s_{k'}\rangle + \mathcal{E}_{\nu_{\mathrm{H}_2},\alpha}(a_j, s_k)\delta_{\alpha,\alpha'}\delta_{j,j'}\delta_{k,k'} \quad (4.10)$$

where the dependence on a and s is expressed in a discrete variable representation (DVR).[4] We can then find the wave functions and energies of this Hamiltonian, noting that the wave functions, $\Psi_{\nu_{\mathrm{H}_2},n}(a, s)$, will have contributions from the $\nu_{\mathrm{H}_2} + 1$ values of α, that is

$$\Psi_{\nu_{\mathrm{H}_2},n}(a, s) = \sum_\alpha \chi_{\nu_{\mathrm{H}_2},n,\alpha}(a, s) \quad (4.11)$$

Given that adiabatic potential energy surfaces are used to obtain the wave functions and energies, a similar adiabatic procedure is also used to obtain the intensities. This is accomplished by evaluating the matrix elements of the dipole surface between the adiabatic states that represent the various levels of excitation of the outer H_2 stretches as a function of a and s. Care must be taken to ensure that the phases of these adiabatic wave functions are consistently defined. These transition moments are then used to evaluate the matrix elements of the dipole moment in the adiabatic representation.

In the SCF procedure, given a value of (a, s), we represent our wave function as

$$\Phi^{\mathrm{SCF}}_{n,m}(r_1, r_2; a, s) = \phi_n(r_1)\varphi_m(r_2) \quad (4.12)$$

and we compute this iteratively by computing each wave function on the potential averaged over the other wave functions. Operationally, this means we compute $\phi_n(r_1)$ by finding the n^{th} eigenvector of the Hamiltonian

$$H(r_1; a, s) = T(r_1) + \langle\varphi_m|V(r_1, r_2; a, s)|\varphi_m\rangle \quad (4.13)$$

and we compute $\varphi_m(r_2)$ by finding the m^{th} eigenvector of the Hamiltonian

$$H(r_2; a, s) = T(r_2) + \langle \phi_n | V(r_1, r_2; a, s) | \phi_n \rangle \tag{4.14}$$

These wave functions are computed via a one dimensional DVR. The overall wave function is computed iteratively until

$$\left\langle \Phi_{n,m}^{\mathrm{SCF}(i)} | \Phi_{n,m}^{\mathrm{SCF}(i-1)} \right\rangle > 0.99 \tag{4.15}$$

Since this is an iterative procedure we need a starting guess for the averaged potential. This guess is chosen by finding the minimum in the potential, $(r_{1,e}, r_{2,e})$, and taking the cut in $r_{2,1}$ for that $r_{2,e}$.

4.2.4 Numerical Details

All wave functions and energies in this study were obtained using a DVR. The underlying basis for these calculations has been described by Colbert and Miller.[87] The energies for the adiabatic potential surfaces were evaluated using 60 points in r_1 and r_2 with both coordinates ranging from 0.5 Å to 2.0 Å. The VSCF wave functions were evaluated using the same grid to facilitate the evaluation of the $c_j^{\alpha}(a, s)$ coefficients in Eq. 4.9. The evaluation of the matrix elements in Eq. 4.10 was performed using a two-dimensional DVR with 100 points in both s and a. For these calculations, a ranged from -2.45 Å to 2.45 Å and s ranged from 0.6 Å to 3.6 Å. All calculations were performed in Mathematica.[88]

4.3 Results and Discussion

4.3.1 Spectrum of H_5^+

To start, we consider the spectra for H_5^+, shown in Fig. 4.2. The previously reported spectrum below 2000 cm^{-1}, obtained in an IRMPD study of the ion,[71] is shown by the grey-shaded region in the top panel of this figure. In the middle panel, we show the spectrum in the region of the fundamental in the outer H_2. This spectrum was obtained by single photon dissociation

of the ion to $H_3^+ + H_2$.[67] Finally, in the bottom panel, previously unreported spectra are shown. The transitions at 6684 and 7159 cm^{-1} along with two additional features at 7490 and 7770 cm^{-1} have previously been reported by Bae and assigned to vibrations involving two quanta of excitation in the outer H_2 stretches.[70] The features between 4500 cm^{-1} and 6000 cm^{-1} have not been previously reported.

Below 3000 cm^{-1}

As noted in the introduction, the series of roughly equally spaced peaks below 3000 cm^{-1}, which are labeled I_a through I_g, can be attributed to a series of transitions from the ground state to states that each have an odd number of quanta in the shared proton stretch.[67,71,79] The associated motion can be thought of as the vibration of a delocalized proton between the two outer H_2 groups. As a result, the wave functions that correspond to excitation of this vibration have amplitude near the minimum in the potential as well as along the wells that correspond to the dissociation channels that lead to the formation of $H_3^+ + H_2$. This can be seen in the plots of the wave functions that were evaluated using the lowest energy adiabatic potential for this ion, shown in Figure 4.3. Excitations to the states plotted correspond to features in the spectrum that carry intensity larger than 1 km mol^{-1}.

The wave functions associated with the states that are accessed in the transitions labeled I_a to I_g in Figure 4.2 are plotted in Figure 4.3, while the 24 lowest-energy states ($E < 3200$ cm^{-1}) are shown in Fig. 4.4. Closer examination of these wave functions shows that the ones that carry larger intensities are characterized as being antisymmetric along a, and have significant amplitude and relatively few nodes in the region where the ground state wave function has amplitude. It is this nearly constant amplitude and relatively few nodes in the excited state wave functions in the configurations where the ground state has amplitude that leads to the surprisingly long progression seen in the calculated spectrum plotted in top panel of Fig. 4.2. This calculation is based on a model in which only excitation in the shared proton is expected to have intensity (s, being a totally symmetric vibration, is not IR active).

This assignment is further supported by a comparison of the scaled results of the four-dimensional calculations, which are shown with red sticks in the top panel of Fig. 4.2 and reported in Table 4.1 (information for the 24 lowest energy states provided in Table 4.2), with the recorded spectrum shaded in grey in the top panel of Figure 4.2. In this Table, the assignment of the number of quanta in the shared proton vibration is determined by the number of nodes in the calculated wave function that are perpendicular to the equipotential contours that extend into the product channel.

Displacements of the shared proton off of the axis that connects the centers of mass of the two outer H_2 groups and the rotation of the outer H_2 groups will lead to shifts in the frequency of the shared proton stretch. Therefore in Fig. 4.2 the calculated transition frequencies have been scaled by 0.802. This scaling factor is the ratio of the calculated frequency of the fundamental in the shared proton stretch of 455 cm^{-1} and the value of 365 cm^{-1}, which is based on nine-dimensional multi-configurational time-dependent Hartree calculations.[82]

The need for this scaling factor can be seen by comparing the results of the current study to the results of prior reduced dimensional (two- and four-dimensional) treatments and to those obtained by a full-dimensional treatment of the spectrum. For example, in Figure 4.6, we compare the present ones to those resulting from analysis of a two-dimensional potential surface, $V(a, s)$, which was obtained by minimizing the electronic energy with respect to the outer H_2 bond lengths.[79] While the relative intensities of the transitions are generally unaffected by the inclusion of the outer H_2 stretches in the calculation, the frequencies are notably lower when using the current four-dimensional approach. Similarly, Valdés and Prosmiti[82] compared the results of four- and nine-dimensional calculations over a comparable spectral range. They found that the fundamental in the shared proton stretch based on a similar four-dimensional calculation was at 505 cm^{-1} while a fully-coupled nine-dimensional calculation gave a value of 365 cm^{-1}.

Consistent with the experiment, the intensity of the transitions in this progression remains large until $\sim$2300 cm^{-1}, after which no additional transitions in this calculated progression

carry significant intensity. Based on Figure 4.3, the excited state that corresponds to the I_g transition, which is the final state in this progression with significant intensity, has nine quanta of excitation in the shared proton vibration. An earlier study[71] identified this transition, which is observed at roughly 2600 cm^{-1}, as involving the second overtone in the shared proton stretch, which is consistent with the amplitude near the potential minimum showing three distinct nodes, and 68% of the amplitude being localized in this region of the potential.

Fundamental in the outer H_2 stretch

Next we consider transitions to states that involve one quantum of excitation in the outer H_2 stretches, shown with blue lines in the middle and lower panels of Fig. 4.2 and identified as transitions II_a to II_h. The energies and wave functions for the states involved in these transitions are evaluated using the adiabatic potentials that correspond to the two states that have $\nu_{H_2} = 1$, and the calculations incorporate the non-adiabatic couplings between these states as described above. To make comparisons to experiment, the position of the II_a peak is shifted to match the position of the feature near 3500 cm^{-1}, and the positions of the remaining peaks associated with transitions to states with $\nu_{H_2} = 1$ are scaled relative to peak II_a by the same 0.802 scaling factor used for the $\nu_{H_2} = 0$ peaks. Below 4500 cm^{-1} the agreement between the measured and calculated spectra is excellent. For the higher-energy features, the agreement is less satisfying, although there is clearly intensity in the calculated spectrum in the regions where there is intensity in the experiment. The missing features likely reflect excitation of degrees of freedom that are not included in the calculation, specifically the bends and internal rotation of the H_2 and H_3^+ subunits that make up the ion.

Given that we have obtained good agreement between the calculated and experimental spectra for peaks II_a to II_c, it is interesting to consider the assignments of the states involved in these transitions. By performing the calculations in an adiabatic representation, we are able to explore the contributions from the adiabatic states that involve the outer H_2 stretches when analyzing the nature of the states that contribute to the observed intensity above 3000 cm^{-1}. The wave functions that correspond to the blue peaks in Fig. 4.2 that are labeled II_a

to II_h are provided in Fig. 4.7. The lower-energy adiabatic potential (State A) corresponds to the out-of-phase combination of the H_2 stretches when the shared proton is equidistant from the centers of mass of the two H_2 units. When the shared proton is displaced toward one of the outer H_2 units the lower energy state is the one for which the vibrationally excited H_2 molecule is closer to the shared proton and the H_2 molecule that is further from the shared proton is in its ground state. Overall, the wave function that is associated with the lower-energy adiabatic surface is antisymmetric with respect to exchange of the two outer H_2 units. The wave functions that are associated with the higher-energy adiabatic potential (State B) are symmetric with respect to this exchange, and when the shared proton is displaced toward one of the H_2 units the other H_2 is the one that is vibrationally excited. This behavior of the wave functions for the outer H_2 stretches can be seen in Figure 4.8.

The assignments for the labeled blue peaks in the spectrum are provided in Table 4.1. The wave functions associated with these transitions are provided in Figure 4.7 (the wave functions for 24 lowest-energy states with $\nu_{H_2} = 1$ are plotted in Fig. 4.4). As the calculation of the $\nu_{H_2} = 1$ wave functions considers two adiabatic surfaces these assignments include both a state label, expressed in terms of the number of nodes in the wave function along the shared proton stretch coordinate, and the fraction of the probability amplitude that is localized on each of the adiabatic potentials. As can be seen, the present assignment of the three peaks identified as II_a, II_b, and II_c departs from the assignments described above. In addition, the fact that we reproduce the spectrum without consideration of the bending vibrations makes the assignment of the II_c feature to an overtone in the bend unlikely. We find that the three peaks in the calculated spectrum are assigned to transitions to states that have most of their amplitude on the lower-energy adiabat (State A) with zero, two, and four quanta of shared proton excitation respectively. There is also a smaller but increasing contribution from the higher-energy adiabat (State B). The pattern continues for the transitions to higher energy states with one quantum of excitation in the outer H_2 stretches.

First Overtone in the outer H_2 stretch

A similar picture emerges for the transitions to states with two quanta of excitation in the outer H_2 stretches. The results of our analysis of the wave functions for these transitions are provided in Fig. 4.11 and Table 4.1 (the wave functions associated with the 24 lowest-energy states with $\nu_{H_2} = 2$ are plotted in Fig. 4.10). For these states, we have shifted the energies of the calculated transitions so that the peak identified as III_a is at the same frequency as the feature in the spectrum at 6684 cm^{-1}, and the relative positions of the $\nu_{H_2} = 2$ features are scaled using the same 0.802 scaling factor used for the peaks with $\nu_{H_2} = 0$.

In this case, the lowest-energy adiabatic surface (State A) corresponds to two quanta of excitation in the antisymmetric outer H_2 stretch. The second adiabat (State B) corresponds to a single quantum of excitation in each of the H_2 molecules. The third and highest-energy adiabat (State C) corresponds to two quanta of excitation in the symmetric outer H_2 stretch. It is notable that for these adiabats, States A and C are symmetric with respect to the exchange of the outer H_2 units while State B is antisymmetric with respect to this exchange. In this case, most of the amplitude remains on the lowest-energy adiabat, and the two observed transitions labeled III_a and III_b correspond to one and three quanta of excitation in the shared proton stretch, respectively.

As noted above, Bae[70] identified two additional features in the spectrum above 7300 cm^{-1} at 7490 and 7770 cm^{-1}, and the feature at 7490 cm^{-1} had larger intensity than the one at 7130 cm^{-1}. Based on the results provided in Fig. 4.11 and Table 4.1, we find that the next two transitions involving states with two quanta in the outer H_2 stretches that carry intensity greater than 0.5 km mol^{-1} occur at 7341 and 7769 cm^{-1} and are less than half as intense as the ones labeled III_a and III_b. A comparison between that spectrum and our calculated spectrum over the same frequency range is provided in Figure 4.12. The agreement is generally good for the two lower-energy features, but the calculation fails to capture the intensity of the peak at 7490 cm^{-1}. The fact that intensity is observed in this region is not entirely surprising, although the peaks are larger than is anticipated by these calculations

as well as the previously reported nine-dimensional MCTDH calculations.[84] The states that are accessed by calculated transitions in this spectral region are labeled III_c and III_d and follow the progression described above with five and seven quanta of excitation in the shared proton stretch.

4.3.2 Tunneling and the Assignment of Combination Bands

An interesting feature of the spectra with zero to two quanta of excitation in the outer H_2 stretches is the similarity between the energy spacings involving the first two peaks built off of the H_2 excitation with $\nu_{H_2} = 1, 2$ (384 cm^{-1},[67] and 475 cm^{-1}) and the fundamental frequency in the shared proton stretch[71] ($\sim$375 cm^{-1}). Based on this similarity in the spacings, it would be reasonable to conclude that the peaks labeled II_a and III_a involve transitions to excited states in the outer H_2 stretch, while II_b and III_b correspond to transitions to combination bands with excitation in one of the outer H_2 molecules and one quantum of excitation in the shared proton stretch. Based on the analysis of the present calculations, this does not seem to be the case. This raises the question of how to reconcile the revised description of the assignments with the nearly constant spacing between these pairs of peaks.

If we perform the calculation of the spectrum based on our adiabatic potentials (without inclusion of the non-adiabatic coupling terms), the agreement between the experimental and calculated spectra deteriorates significantly (see Fig. 4.13). To explore the role of non-adiabatic couplings, we focus on the one-dimensional minimum-energy path potentials (MEPs), shown in Fig. 4.15, which are evaluated as functions of the displacement of the shared proton along the axis that connects the centers of mass of the two outer H_2 groups (a) by minimizing the energy as a function of the distance between the two outer H_2 groups (s) based on the two-dimensional adiabatic surfaces (see Figure 4.14). The reason for the large difference between the spectra obtained with and without consideration of the non-adiabatic couplings reflects the large change in the nature of $\Phi_{\nu_{H_2},\alpha}(r_1, r_2; a, s)$ near $a = 0$. In Figure 4.8 we plot these wave functions for all of the states used in this study when $a = 0.0$ and ± 0.495 Å with $s = 1.8$ Å. As is seen, even a small change in a shifts the wave functions

from normal mode functions to nearly local mode functions with the vibrational excitation in only one of the outer H_2 units.

To better understand the effects of this coupling and to sort out the origin of the discrepancy in assignments, we develop a one-dimensional model that replicates the most important features of the four-dimensional system. To do this, we use the MEPs described above and shown in Fig. 4.15 and then reintroduce the non-adiabatic couplings. From these cuts, we find that the barrier at $a = 0$ increases from approximately 50 cm^{-1} on the $\nu_{H_2} = 0$ surface to roughly 1000 cm^{-1} on the potential surface that corresponds to State A when $\nu_{H_2} = 2$. The increase in the barrier height with excitation of the outer H_2 stretches reflects the 805 cm^{-1} energy difference between the vibrational frequency of the two H_2 stretches when $a = \pm 0.495$ Å, reflecting the 1000 cm^{-1} frequency difference between the H_2 stretch frequency in an isolated H_2 molecule and in H_3^+. When $a = 0$, the local H_2 frequencies are equal and the spacing between the two adiabatic surfaces is reduced to 112 cm^{-1}.

While the dependence of the energy difference between the two H_2 oscillator on the position of the shared proton is responsible for the barrier heights, the height of the tunneling barriers alone is not sufficient to yield the observed pattern in the energy levels. It is only when we introduce the non-adiabatic couplings that we obtain energy-level pattern that is consistent with high-barrier tunneling. Specifically, the energies of the six lowest-energy states with $\nu_{H_2} = 1$ come in pairs of closely spaced levels, and these pairs of levels are separated by larger energy gaps, as seen in Table 4.5. The spacing between the average energies of the states (0) and (1) and states (2) and (3) are calculated to be 372.5 and 377 cm^{-1} for the levels with $\nu_{H_2} = 1$ and 2. These values are both very close to the fundamental frequency of the shared proton stretch. A similar energy level pattern is obtained when we consider the energy levels obtained from the one-dimensional calculation based on the MEP potentials shown in Fig. 4.15 in which the non-adiabatic couplings are considered. The origins of the large influence of the non-adiabatic terms in the Hamiltonian on the appearance of the tunneling doublets in the energy level pattern reflects the large change in the H_2 vibrational wave functions, shown in Figure 4.8, with small changes in a near $a = 0$. By analogy to

electronic structure, this rapid change leads to large derivative coupling terms between the adibatic states near $a = 0$, or, if we had expressed the problem in a diabatic representation, weak couplings between the diabatic states that correspond to particular states associated with the outer H_2 stretches. As a result, although in the one-dimensional representation the two wells in the potentials shown in Figure 4.15 appear to be separated by modest barriers, the coupling between the wave functions localized in the two wells is weak due to the fact that the associated H_2 stretch wave functions associated with the adiabats when $\nu_{H_2} \neq 0$ at positive and negative values of a are orthogonal to each other (see Figure 4.8).

This tunneling behavior is further manifested in the projections of the vibrational wave functions onto a, shown in Fig. 4.16, and in the wave functions obtained from the one-dimensional model, which are shown in Fig. 4.17. As can be seen in the plots in Fig. 4.17 and Fig. 4.16, the pairs of wave functions plotted in the same panel have the same width and can be considered as the in- and out-of-phase contributions of pairs of wave functions, one localized at positive values of a and one at negative values of a. This is exactly the behavior one would expect for tunneling doublets. Additionally, as the energy is increased the widths of both members of the pairs of wave functions increases, as expected for a progression in the excitation of a specific vibration.

Taken together, the revised assignment of the transitions observed in the region of the fundamental in the outer H_2 stretches corresponds to transitions to the symmetric member of tunneling doublets with increased numbers of quanta in the shared proton stretch, with the shared proton shifted toward the H_2 molecule that is vibrationally excited. Likewise, for the transitions to states with two quanta in the outer H_2 stretches, the ones that carry intensity correspond to transitions to the antisymmetric member of tunneling doublets with increasing numbers of quanta in the shared proton stretch, with the shared proton shifted toward the H_2 molecule that is vibrationally excited.

4.3.3 Role of Torsion

Before concluding our discussion of the spectrum of H_5^+, we need to consider the role of the torsional motion on the spectrum. In addition to the shared proton stretch, the torsion of the outer H_2 units reflects a large amplitude vibration in this ion. Earlier studies have demonstrated that the ground state wave function is fully delocalized in this coordinate.[73,74] On the other hand, the results that have been presented so far are based on a cut through the potential with the torsion coordinate constrained to 90°. To check if the above results are sensitive to the value of the torsion angle used in the evaluation of the potential surface, we repeat our calculation of the spectrum using a value of 0° for the torsion angle, which corresponds to the structure shown in Fig. 4.18. Comparing the spectra obtained for these two structures, we find that they are almost identical, as is shown in Fig. 4.19. The fact that the spectrum does not change when the value of the torsion angle is shifted from 90° to 0° suggests that while the torsion is indeed large amplitude, its motion is nearly completely decoupled from the other vibrations considered in this study. This is consistent with the results of earlier work using DMC.[89]

4.3.4 Comparison with D_5^+

We have also evaluated the spectrum for D_5^+, and the comparison between the calculated and recorded spectra are provided in Fig. 4.23. The associated wave functions and assignments can be found in Figures 4.20-4.22 and Tables 4.7-4.9. The calculated spectra in Figure Fig. 4.23 have been shifted and scaled using a procedure that is analogous to that used to adjust the calculated spectrum for H_5^+, and the parameters can be found in Table 4.10. The agreement between the calculated and measured spectra is generally very good, especially when we consider that the transition near 2500 cm^{-1} is near the dissociation threshold for this ion. A similar difference between the calculated and measured intensity of this transition has been noted by Valdés and Prosmiti based on their nine-dimensional MCTDH calculation of the spectrum of the ion.[84] Since the ions are only detected when the vibrationally excited

population dissociates into D_2 and D_3^+ fragments, the diminished intensity in the spectrum compared to calculation is consistent with this excited sate having an energy that is close to the dissociation energy of the ion.

In addition to the previously reported spectra, shown in the upper two panels of Figure 4.23, we also report the spectrum from 4830 - 7300 cm^{-1} in the bottom panel. This spectrum contains four peaks at 4860, 5220, 5495, and 5688 cm^{-1}. Our calculated spectrum agrees well with the experiment with respect to the positions of these peaks, but has some notable differences with respect to the intensities. The difference in intensity compared to the peak at 4860 cm^{-1} can be attributed to the laser power in the experiment in this region being diminished relative to the region above ~5000 cm^{-1}. A more notable difference is the intensity of the peak around 5495 cm^{-1}. In both H_5^+[70] and D_5^+ this third peak has the largest intensity of the four peaks in the spectral regions near the overtone in the outer H_2 or D_2 stretches. Comparing the H_5^+ and D_5^+ spectra, we find that they are very similar once the frequency scale for the D_5^+ spectrum are multiplied by roughly $\sqrt{2}$. It is notable, therefore, that for H_5^+ the nine-dimensional MCTDH calculations show the same difference in intensity for this third peak.[84] A possible explanation for this discrepancy between the calculated and measured intensities is that neither calculation fully accounts for the rotation of the H_3^+ fragment.

Given the otherwise good agreement of the frequencies it is interesting to analyze the wave functions that we have obtained for D_5^+. As we found for H_5^+, the states that are accessed by the transitions to states with $\nu_{D_2} = 2$ have most of their amplitude on State A with increasing quanta of excitation in the shared proton stretch. In the case of the lowest energy bright state the tunneling splitting between this level and the one with no quanta of excitation in the shared proton stretch is less than 1 cm^{-1}. This allows us to explore the relative sizes of the anharmonicity of the H_2 and D_2 stretches based on the frequencies of the lowest energy transition that carries in intensity, which corresponds to excitation of one or two quanta of excitation in the outer H_2 or D_2 stretch.

4.3.5 $H_2D^+H_2$ and $D_2H^+D_2$

Much of the spectroscopy of H_5^+ can be interpreted in terms of the motions of an excess proton that is trapped between two H_2 molecules. While such a bonding structure is not uncommon, and protonated dimers of water,[90] CO_2,[91] and N_2,[92] for example, have displayed similar structures, H_5^+ is unusual in that deuteration not only has a large impact on the amplitude of the shared H^+ or D^+ motion, it also doubles the mass of the molecular cage that traps the excess proton. This in turn has a significant effect on the amplitude of the breathing motion of the outer H_2 or D_2 molecules, which can be seen to be strongly coupled to the shared proton stretch, given the curvature of the ground state wave function shown in the upper left panel of Figure 4.3. As a result, full deuteration of the ion not only affects the amplitude of the shared proton stretch motion, it also limits the extent to which the wave functions extend into the $H_3^+ + H_2$ product channel. Both of these factors lead to the observed shorter progression in the shared proton stretch in D_5^+ compared to H_5^+.

To sort out the contributions to the spectrum from deuterating the central proton as opposed to deuteration of the outer H_2 groups, we also calculate the spectra for $H_2D^+H_2$ and $D_2H^+D_2$, where the isotopically unique atom is the central proton. The resulting spectra are provided in Figures 4.24 and 4.25 while the corresponding energies and wave functions are reported in Tables 4.11-4.13 and Figures 4.26-4.28 for $H_2D^+H_2$ and Tables 4.14-4.16 and Figures 4.29-4.31 for $D_2H^+D_2$. Comparing the spectra shown in Figures 4.2 and 4.23 to those shown in Figures 4.24 and 4.25, we find that the range of the progression in the shared proton stretch is correlated to the masses of the outer H_2 units, while the frequency of this vibration reflects the deuteration of the central proton.

This trend can be understood in terms of the similarity between the ground state wave function, $\Psi_{0,0}(a,s)$, and the excited state wave functions, $\Psi_{\nu_{H_2}>0,n}(a,s)$. To quantify this, we consider the contour of $\chi^2_{0,0,A}(a,s)$, as defined in Eq. 4.11, that contains 99% of the probability amplitude. By evaluating the integrated area of each $\chi^2_{\nu_{H_2},n,\alpha}(a,s)$ over this

region, $\xi_{\nu_{H_2},n,\alpha}$ (see Tables 4.5, 4.8, 4.12, and 4.15), and then evaluating

$$\Xi_{\nu_{H_2},n} = \sum_{\alpha} \xi_{\nu_{H_2},n,\alpha} \tag{4.16}$$

we are able to quantify the degree to which each state is localized near the minima in the potential. To explain the trend we evaluate $\Xi_{n,\nu_{H_2}}$ for the three states with $\nu_{H_2} = 1$ labeled II_a, II_b, and II_c in Figure 4.2 which correspond to the wave functions $\Psi_{1,0}(a,s)$, $\Psi_{1,2}(a,s)$, and $\Psi_{1,4}(a,s)$. For all four deuterated analogs of H_5^+ considered $\Xi_{1,0} \approx 0.92$. However, for H_5^+ and $H_2D^+H_2$ we find that $\Xi_{1,4} \approx 0.65$, while for D_5^+ and $D_2H^+D_2$ we find that $\Xi_{1,4} \approx 0.78$. This indicates that the wave functions for D_5^+ and $D_2H^+D_2$ remain significantly more localized near the minima in the potentials as the shared proton is excited. This reflects a difference in the adiabatic potentials obtained when the outer units are H_2 as opposed to when they are D_2. The ability of the shared proton wave function to extend further away from the minima when H_2 is the outer unit supports a longer progression by reducing the orthogonality with the ground state wave function. It is worth keeping in mind that as $\Psi_{1,n}$ has contributions from $\chi_{1,n,A}$ and $\chi_{1,n,B}$, $\Xi_{1,n}$ will have contributions from $\xi_{1,n,A}$ and $\xi_{1,n,B}$.

In this study, spectra of H_5^+ and D_5^+ from 4830-7300 cm^{-1} have been reported. We have explored the nature of the states that are accessed in these and previously reported spectra using a four-dimensional model Hamiltonian. The calculations were performed by adiabatically separating the outer H_2 modes from the shared proton motions and then introducing non-adiabatic coupling for states with the same amount of outer H_2 excitation. We find that much of the observed intensity reflects the excitation of the shared proton stretch as the wave function extends in to the $H_3^+ + H_2$ dissociation channel with zero, one, and two quanta of outer H_2 excitation. This work demonstrates the effectiveness of a coupled four-dimensional adiabatic treatment to modeling the vibrational excited states of the highly-fluxional H_5^+ and D_5^+ molecular ions.

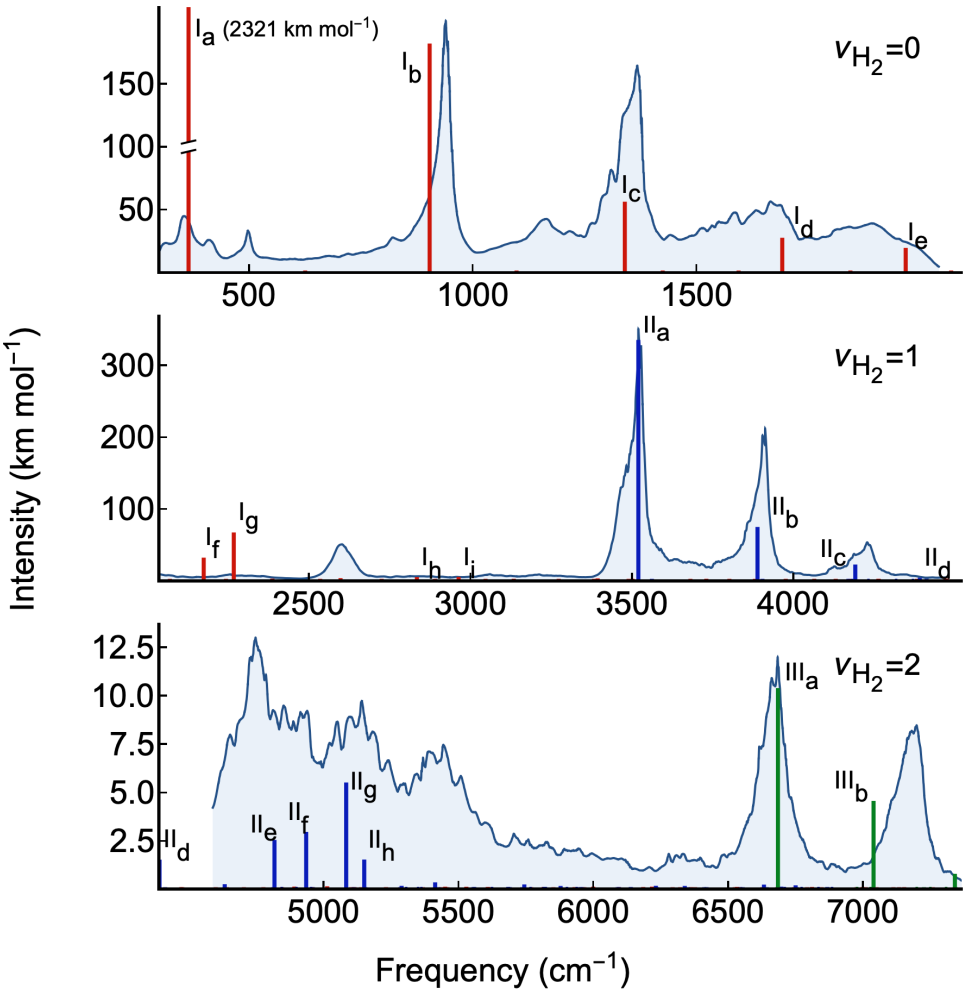

Figure 4.2: Experimental spectra (shaded grey) with calculated spectra (sticks) of H_5^+ overlain. The top panel compares the spectrum reported in Ref. 71 to the calculated transitions with $\nu_{H_2} = 0$ (red sticks). The middle panel compares the spectrum reported in Ref. 67 to the calculated transitions with $\nu_{H_2} = 0$ and $\nu_{H_2} = 1$ (red and blue sticks). The bottom panel compares our newly recorded spectrum reported to the calculated transitions with $\nu_{H_2} = 1$ and $\nu_{H_2} = 2$ (blue and green sticks). The positions of the transitions in the calculated spectrum have been shifted and scaled as described in the text and tabulated in Table 4.10. The intensity of I_a peak extends off the scale of the plot.

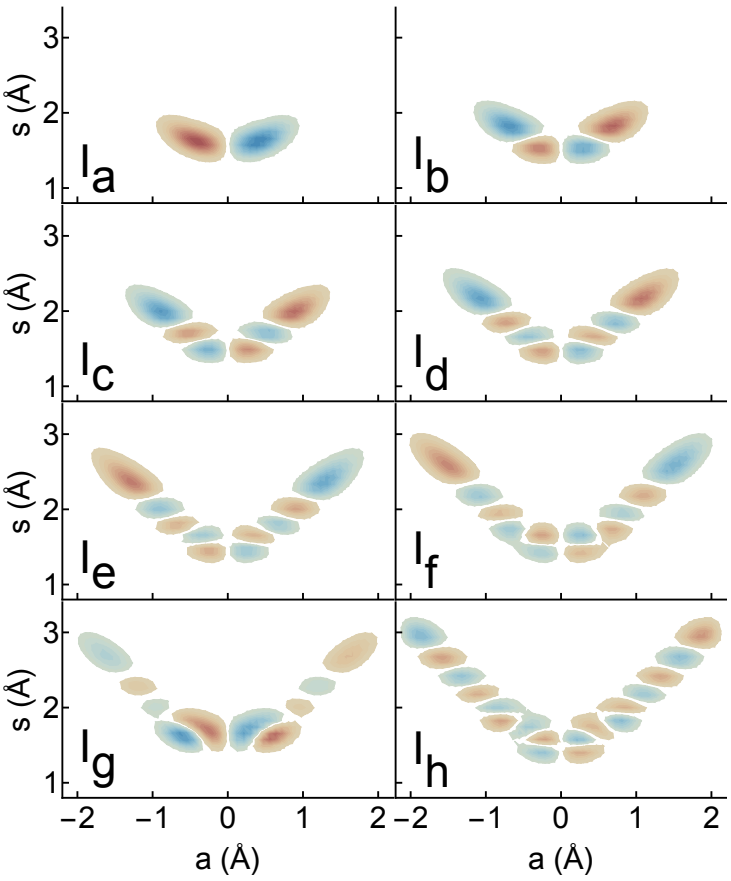

Figure 4.3: Wave functions for the states probed by transitions indicated by red sticks in Figure 4.2 labeled I_a to I_h. The energies, intensities and assignments of transitions to these states are provided in Table 4.1. As there is only one adibatic surface when $\nu_{H_2} = 1$, we only plot $\chi_{0,n,A}$ as defined in Equation 4.11.

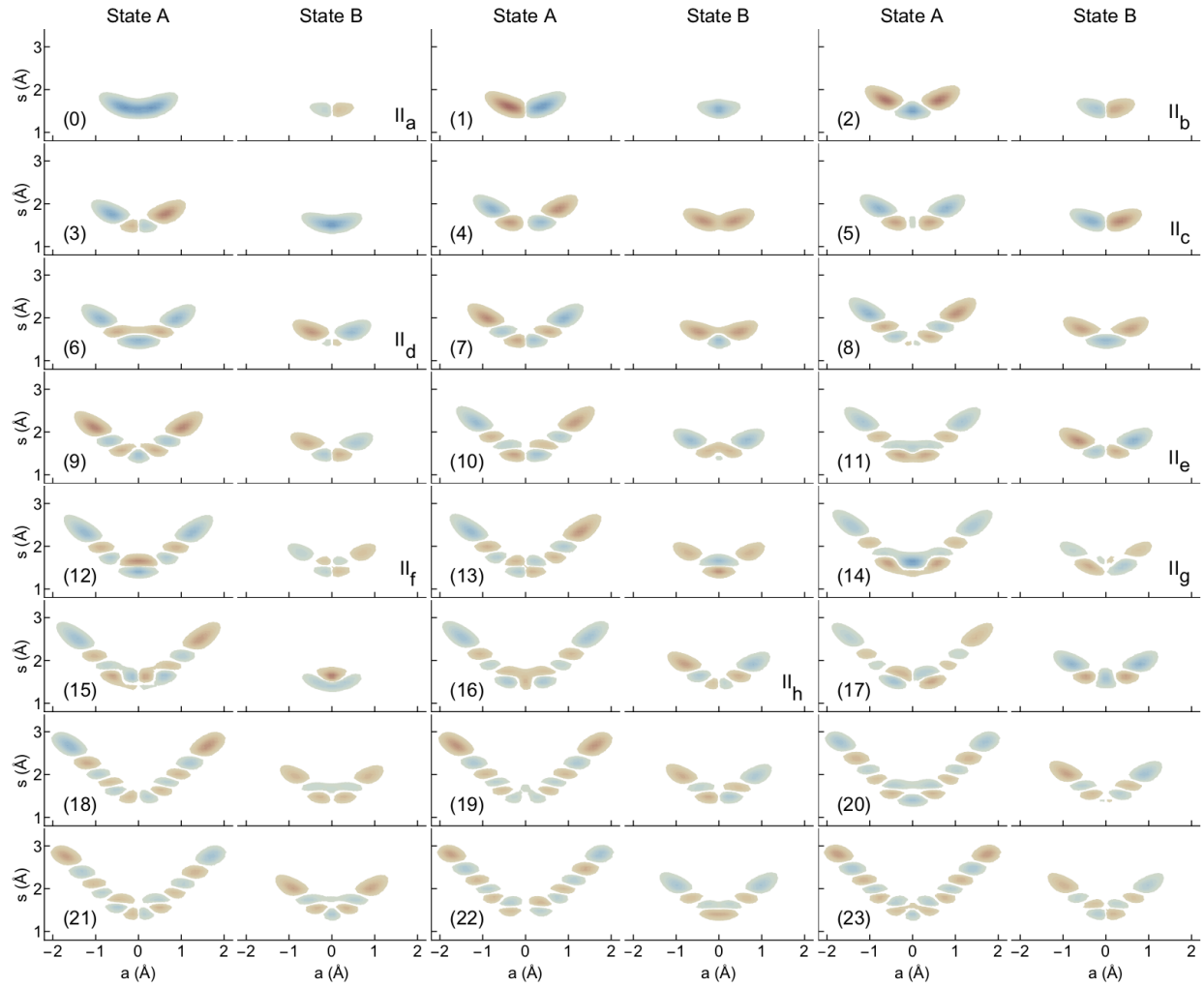

Figure 4.4: The 24 lowest-energy wave functions with $\nu_{H_2} = 1$ for H_5^+, numbered according to increasing energy. The contributions from the State A and State B adiabats are plotted side-by-side. Wave functions corresponding to peaks in Fig. 4.2 are labeled with their peak label in the bottom right of the corresponding plot. The energies and intensities for transitions to these states are tabulated in Table 4.5.

Label[a]	Frequency cm^{-1}	Intensity (km/mol)	State A[b] $n^c_{H^+}$	State A[b] Percent[d]	State B[b] $n^c_{H^+}$	State B[b] Percent[d]	State C[b] $n^c_{H^+}$	State C[b] Percent[d]
I_a	365	2321.20	1	100.00	–	–	–	–
I_b	904	180.41	3	100.00	–	–	–	–
I_c	1340	54.70	5	100.00	–	–	–	–
I_d	1692	26.03	7	100.00	–	–	–	–
I_e	1968	18.00	9	100.00	–	–	–	–
I_f	2174	29.49	11	100.00	–	–	–	–
I_g	2267	64.54	9	100.00	–	–	–	–
I_h	2834	2.41	17	100.00	–	–	–	–
I_i	2963	2.67	17	100.00	–	–	–	–
II_a	3520	332.33	0	94.30	1	5.70	–	–
II_b	3889	72.18	2	79.30	1	20.70	–	–
II_c	4192	19.93	4	54.80	1	45.20	–	–
II_d	4391	1.42	4	67.20	3	32.80	–	–
II_e	4818	2.44	8	52.40	3	47.60	–	–
II_f	4935	2.86	8	85.50	5	14.50	–	–
II_g	5084	5.41	9	78.90	3	21.10	–	–
II_h	5151	1.43	10	63.60	5	36.40	–	–
III_a	6685	10.29	1	97.30	0	2.30	1	0.40
III_b	7040	4.46	3	91.60	0	6.00	1	2.40
III_c[e]	7341	0.69	5	82.30	0	10.30	1	7.40
III_d[e]	7769	1.99	7	70.90	0	4.50	1	24.50
III_e[e]	7923	1.54	9	80.90	1	3.70	1	15.40
III_f[e]	8305	3.52	9	70.50	1	7.70	1	21.90

[a] As identified in Figure 4.2.
[b] The adiabatic states with the same ν_{H_2} in increasing energy as described in Eq. 4.9.
[c] Number of nodes along the proton transfer coordinate.
[d] Percentage of the probability amplitude associated with the adiabatic state.
[e] Not shown in Figure 4.2.

Table 4.1: Frequencies (in cm^{-1}), Intensities (in km mol^{-1}), and Assignments of the Labeled Peaks in Figure 4.2.

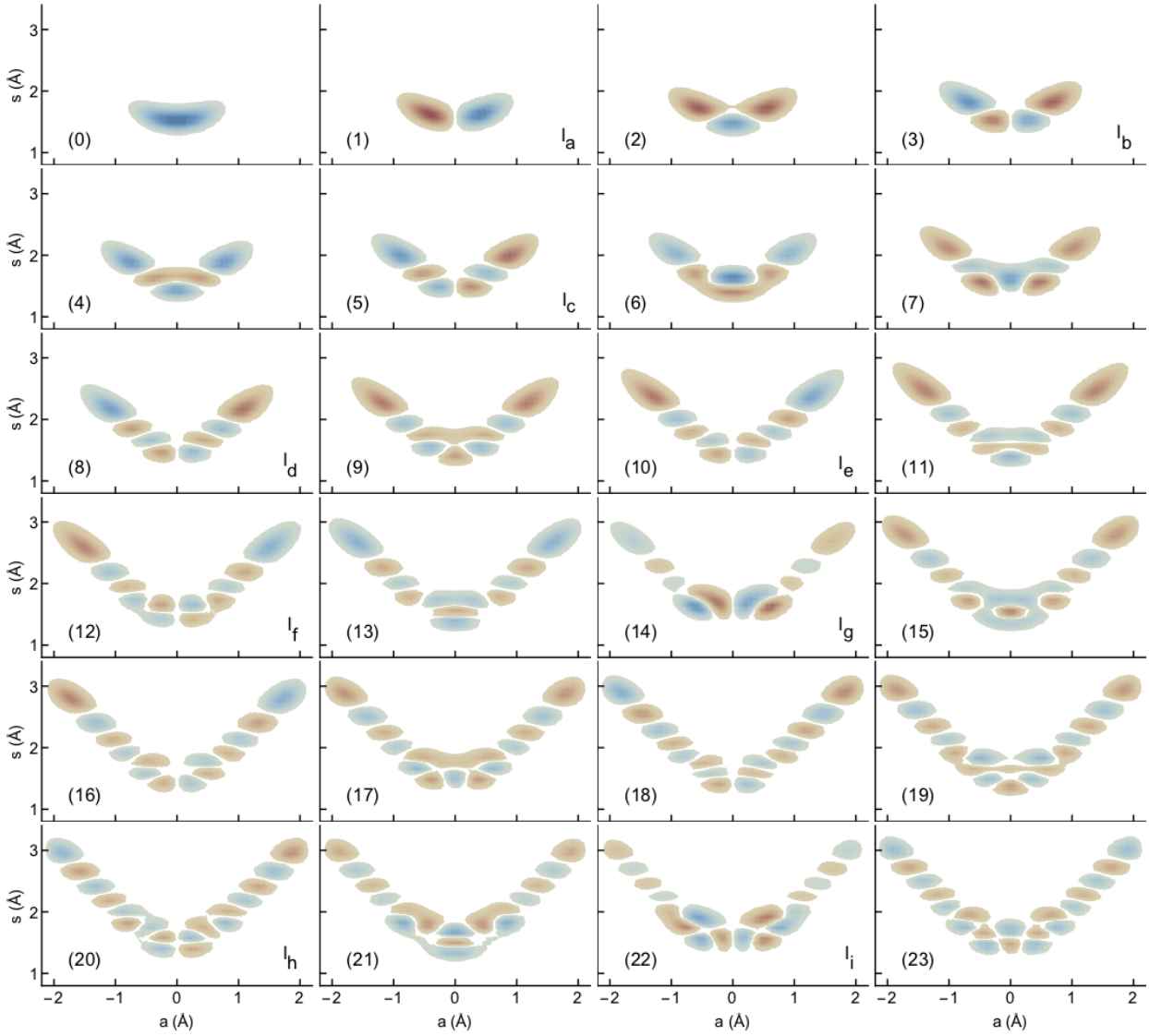

Figure 4.5: The 24 lowest-energy wave functions with $\nu_{H_2} = 0$ for H_5^+, numbered according to increasing energy. Wave functions corresponding to peaks in Fig. 4.2 are labeled with their peak label in the bottom right of the corresponding plot. The energies and intensities for transitions to these states are tabulated in Table 4.2.

State	Label	Freq. (cm^{-1})	Orig. (cm^{-1})	Intensity (km/mol)	$\xi^{a}_{0,n,\mathrm{A}}$	$n^{b}_{\mathrm{H^+}}$
0	–	0	0	0.00	0.99	0
1	$\mathrm{I_a}$	365	455	2321.20	0.95	1
2	–	626	781	0.00	0.83	2
3	$\mathrm{I_b}$	904	1128	180.41	0.59	3
4	–	1098	1370	0.00	0.47	4
5	$\mathrm{I_c}$	1340	1672	54.70	0.37	5
6	–	1425	1778	0.00	0.63	5
7	–	1594	1989	0.00	0.56	6
8	$\mathrm{I_d}$	1692	2111	26.03	0.27	7
9	–	1844	2301	0.00	0.30	8
10	$\mathrm{I_e}$	1968	2455	17.99	0.23	9
11	–	2069	2582	0.00	0.23	10
12	$\mathrm{I_f}$	2174	2713	29.49	0.25	11
13	–	2243	2799	0.00	0.27	10
14	$\mathrm{I_g}$	2267	2829	64.54	0.68	9
15	–	2386	2977	0.00	0.37	12
16	–	2387	2978	0.25	0.21	13
17	–	2535	3163	0.00	0.31	14
18	–	2598	3241	0.95	0.19	15
19	–	2725	3400	0.00	0.29	16
20	$\mathrm{I_h}$	2834	3536	2.41	0.22	17
21	–	2891	3607	0.00	0.36	15
22	$\mathrm{I_i}$	2963	3697	2.67	0.38	17
23	–	3047	3801	0.00	0.30	19

[a] Percentage of the probability amplitude in the 99 percent contour of the ground state probability amplitude.
[b] Number of nodes along the proton transfer coordinate.

Table 4.2: Frequencies and intensities of the 24 lowest-energy states with $\nu_{\mathrm{H_2}} = 0$. The corresponding wave functions are shown in Fig. 4.5.

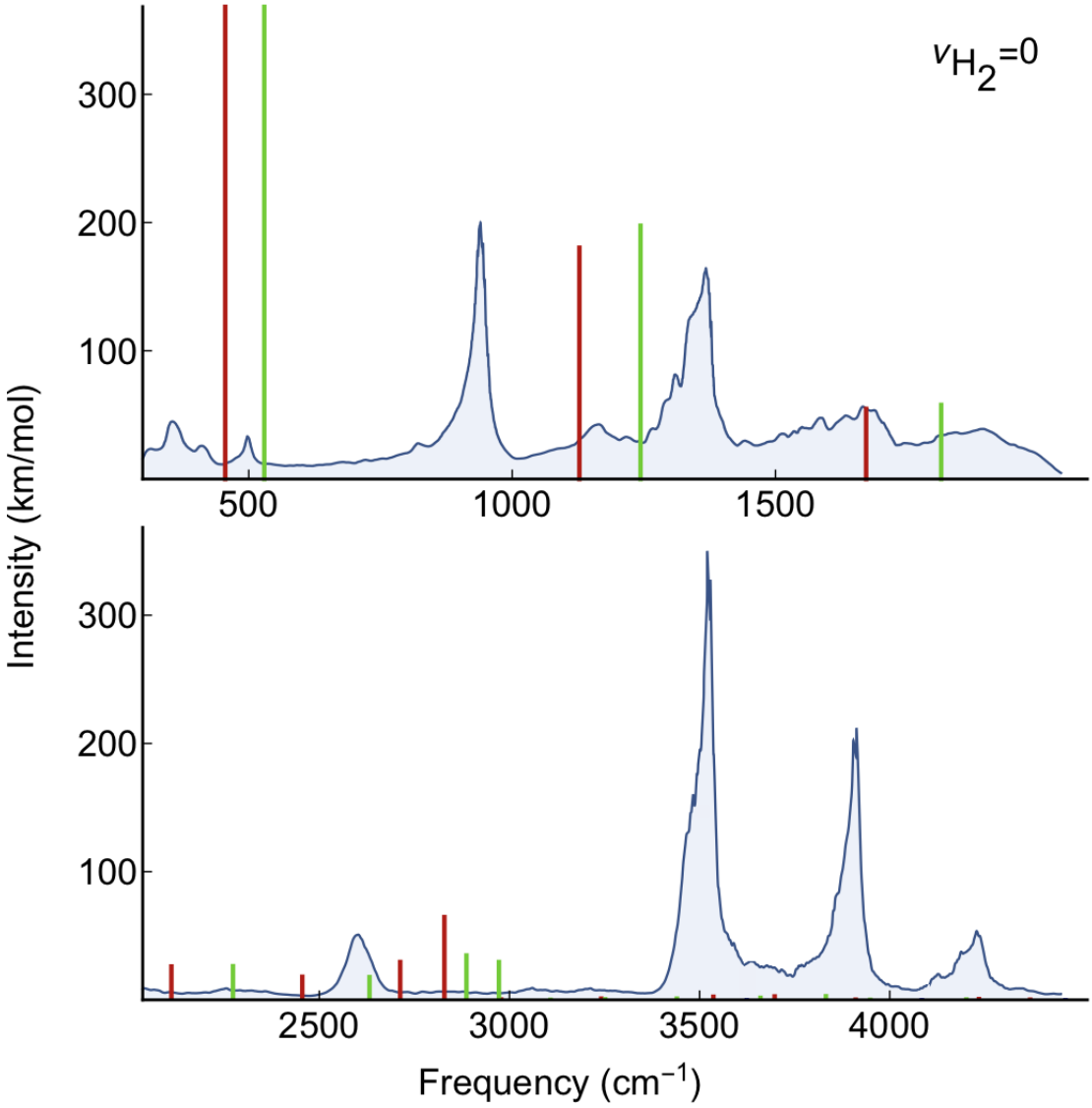

Figure 4.6: Comparison of the stick spectrum of H_5^+ obtained in this work (red) to the spectrum that is generated for states with $\nu_{H_2} = 0$ from a two dimensional potential where the energy is evaluated at the same level of electronic structure theory, but the outer H_2 bond lengths are allowed to optimize (bright green).

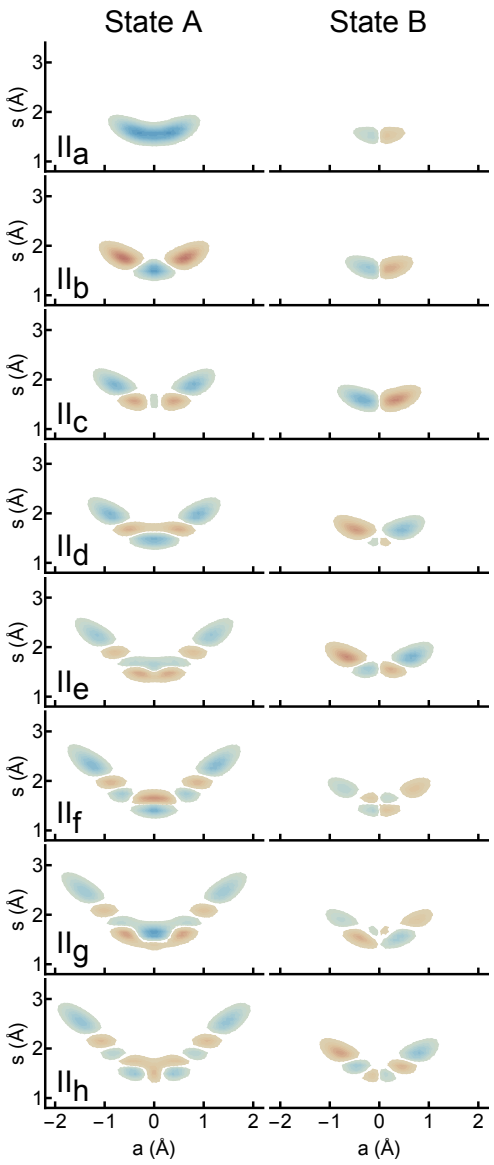

Figure 4.7: Wave functions for the states probed by transitions indicated by blue sticks in Figure 4.2 labeled $\mathrm{II_a}$ to $\mathrm{II_h}$. The energies, intensities and assignments of transitions to these states are provided in Table 4.1. The wave functions are divided into the contributions from the two adiabatic states with one quantum in the H_2 stretch, $\chi_{1,n,\mathrm{A}}$ and $\chi_{1,n,\mathrm{B}}$ as defined in Equation 4.11, which are identified as State A and State B.

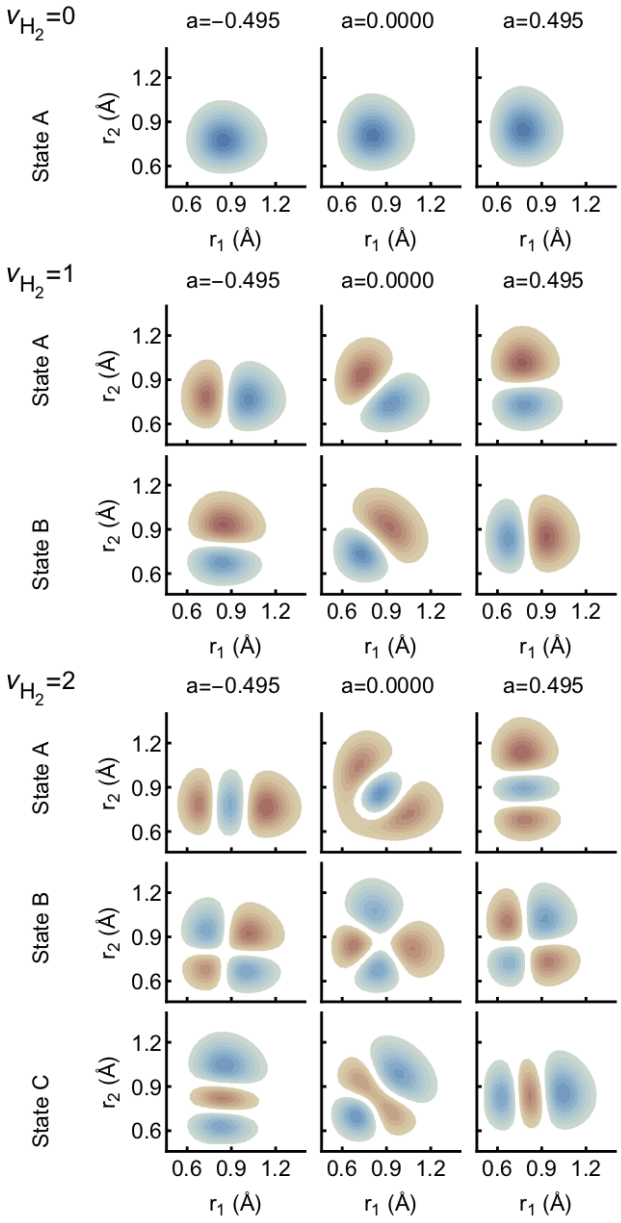

Figure 4.8: Plots of the H_2 wave functions for $a = 0$ and ± 0.495 Å at $s = 1.8$ Å for $\nu_{H_2} = 0, 1, 2$ for H_5^+. The wave functions when $a = \pm 0.071$ Å are provided in Figure 4.9.

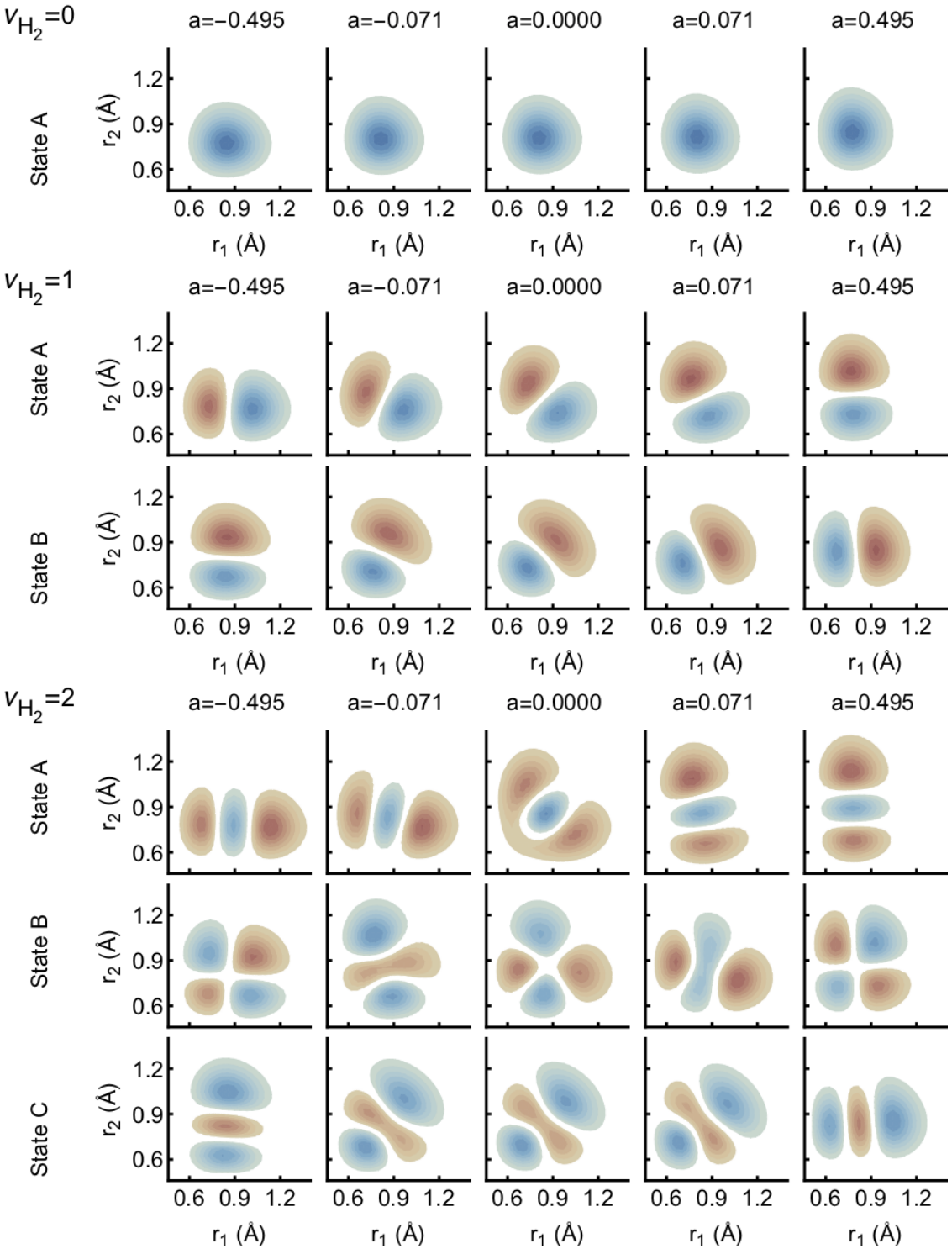

Figure 4.9: Plots of the H_2 wave functions for $a = 0, \pm 0.071, \pm 0.495$ Å at $s = 1.8$ Å for $\nu_{H_2} = 0, 1, 2$ for H_5^+ (The same outer H_2 wave functions are used for $H_2D^+H_2$).

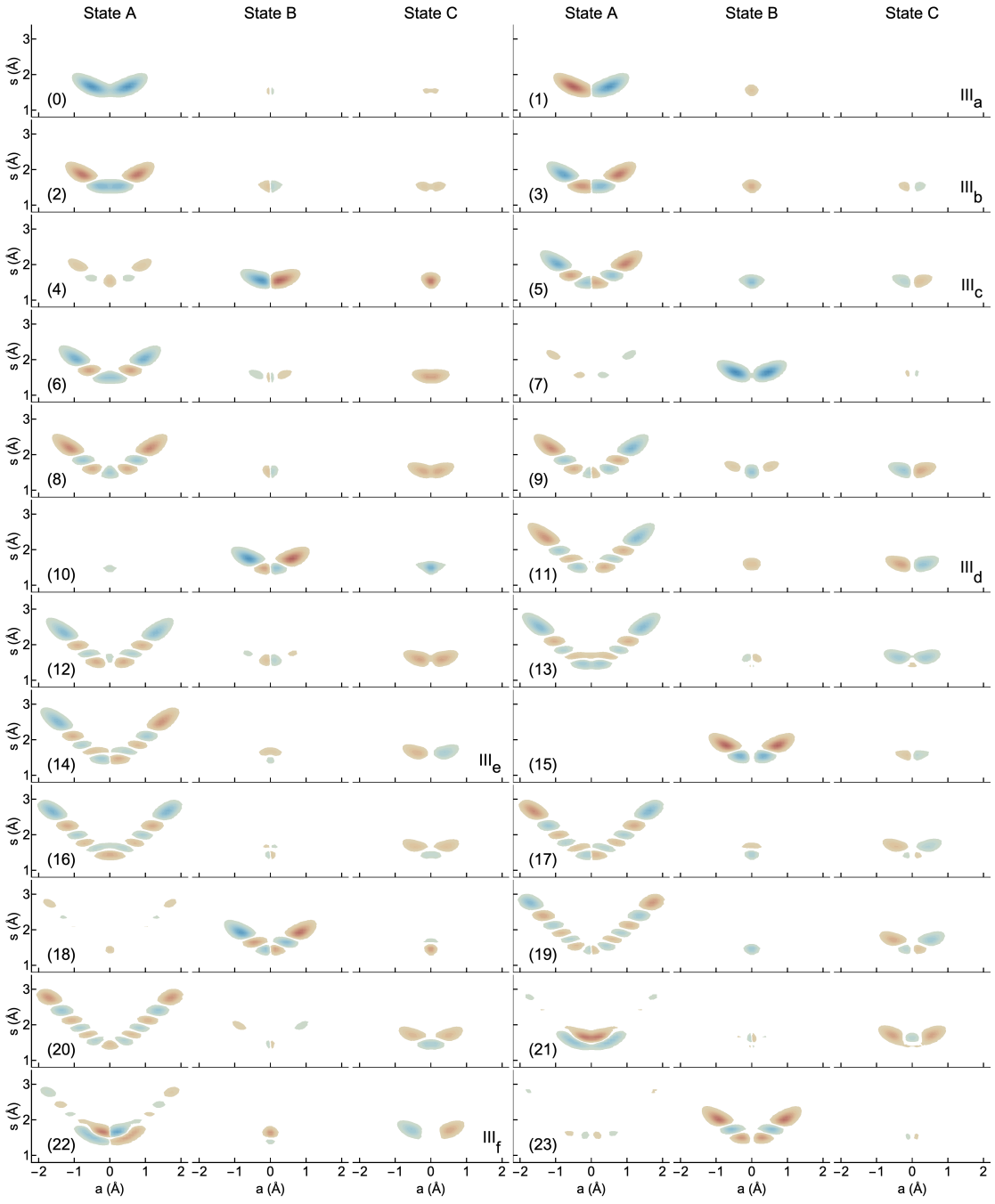

Figure 4.10: The 24 lowest-energy wave functions with $\nu_{H_2} = 2$ for H_5^+, numbered according to increasing energy. The contributions from the State A, State B, and State C adiabats are plotted side-by-side. Wave functions corresponding to peaks in Fig. 4.2 are labeled with their peak label in the bottom right of the corresponding plot. The energies and intensities for transitions to these states are tabulated in Table 4.6.

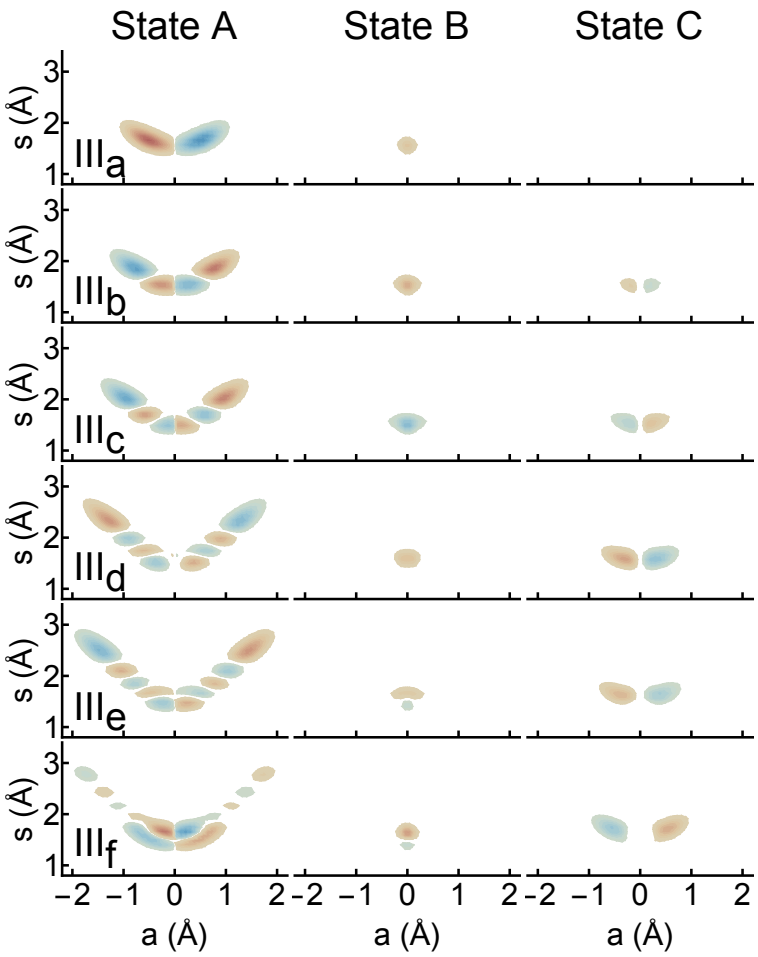

Figure 4.11: Wave functions for the states probed by transitions indicated by green sticks in Figure 4.2 labeled $\mathrm{III_a}$ and $\mathrm{III_b}$. The energies, intensities and assignments of transitions to these states are provided in Table 4.1. The wave functions are divided into the contributions from the three adiabatic states with two quanta in the H_2 stretch, $\chi_{2,n,\mathrm{A}}$, $\chi_{2,n,\mathrm{B}}$, and $\chi_{2,n,\mathrm{C}}$ as defined in Equation 4.11, which are identified as State A, State B, and State C.

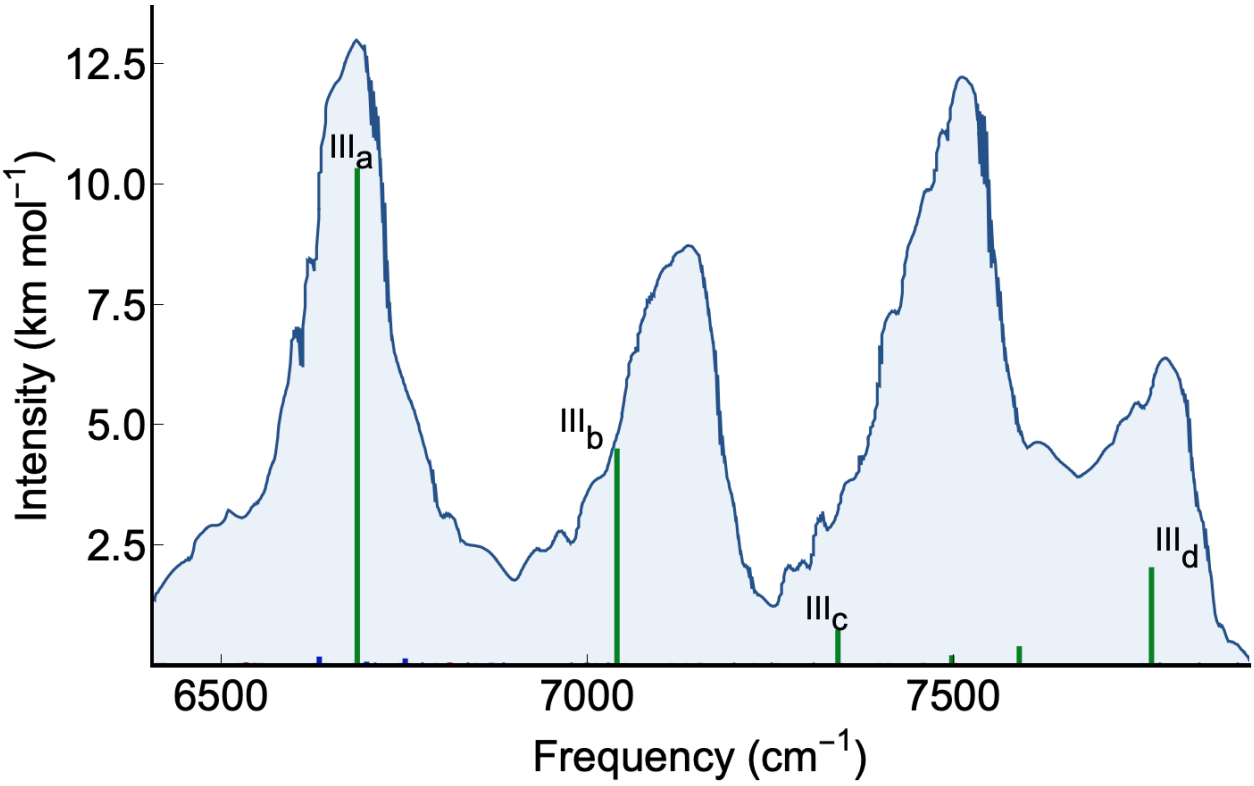

Figure 4.12: Calculated spectrum of H_5^+ (green sticks) in the $\nu_{H_2} = 2$ region of the spectrum compared to the spectrum obtained by Bae[70] (background). Peaks identified in Table 4.1 are labeled.

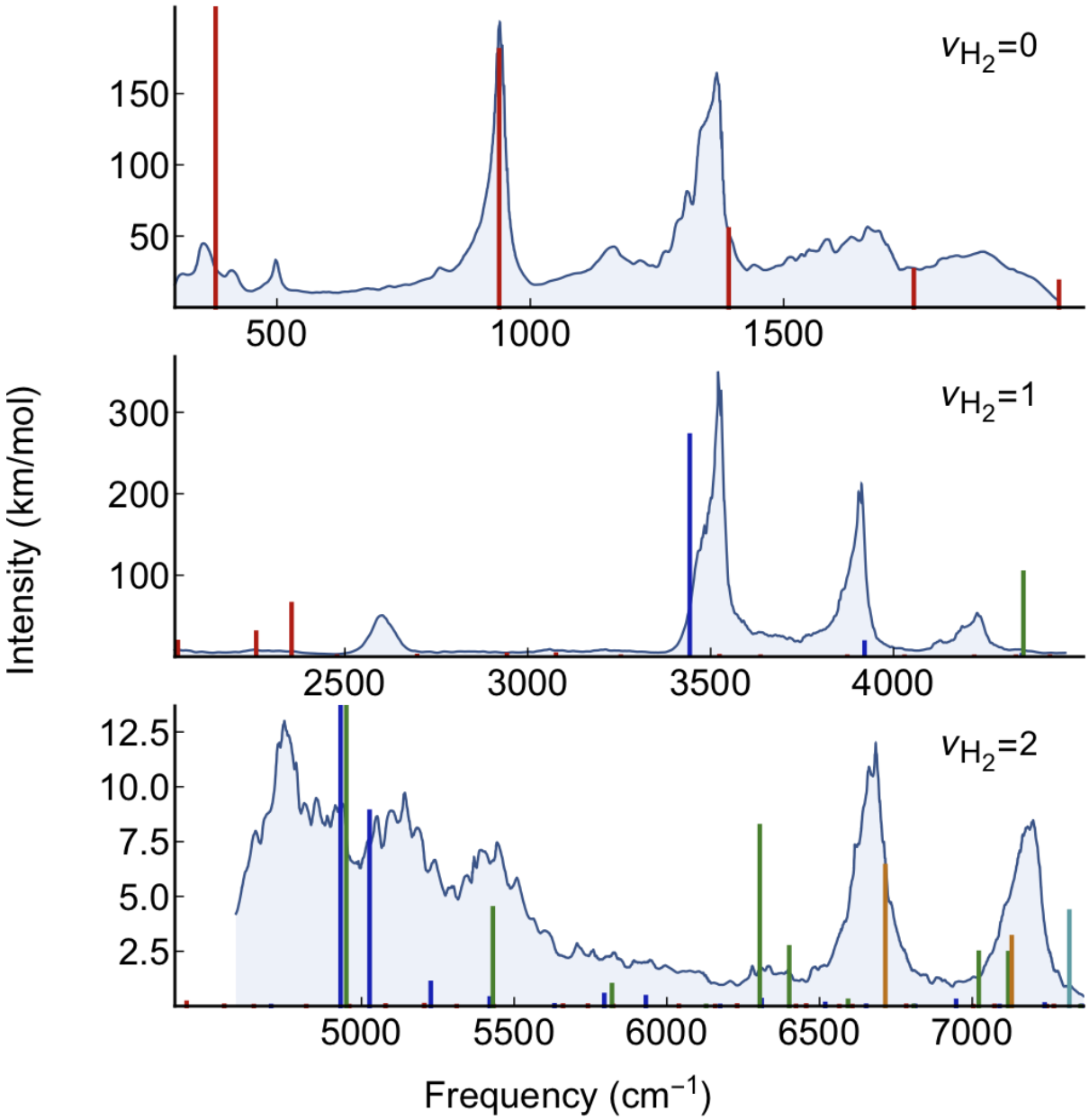

Figure 4.13: Spectrum of H_5^+ obtained when not including the non-adiabatic coupling. Corresponding energies and frequencies are provided in tables 4.3-4.4.

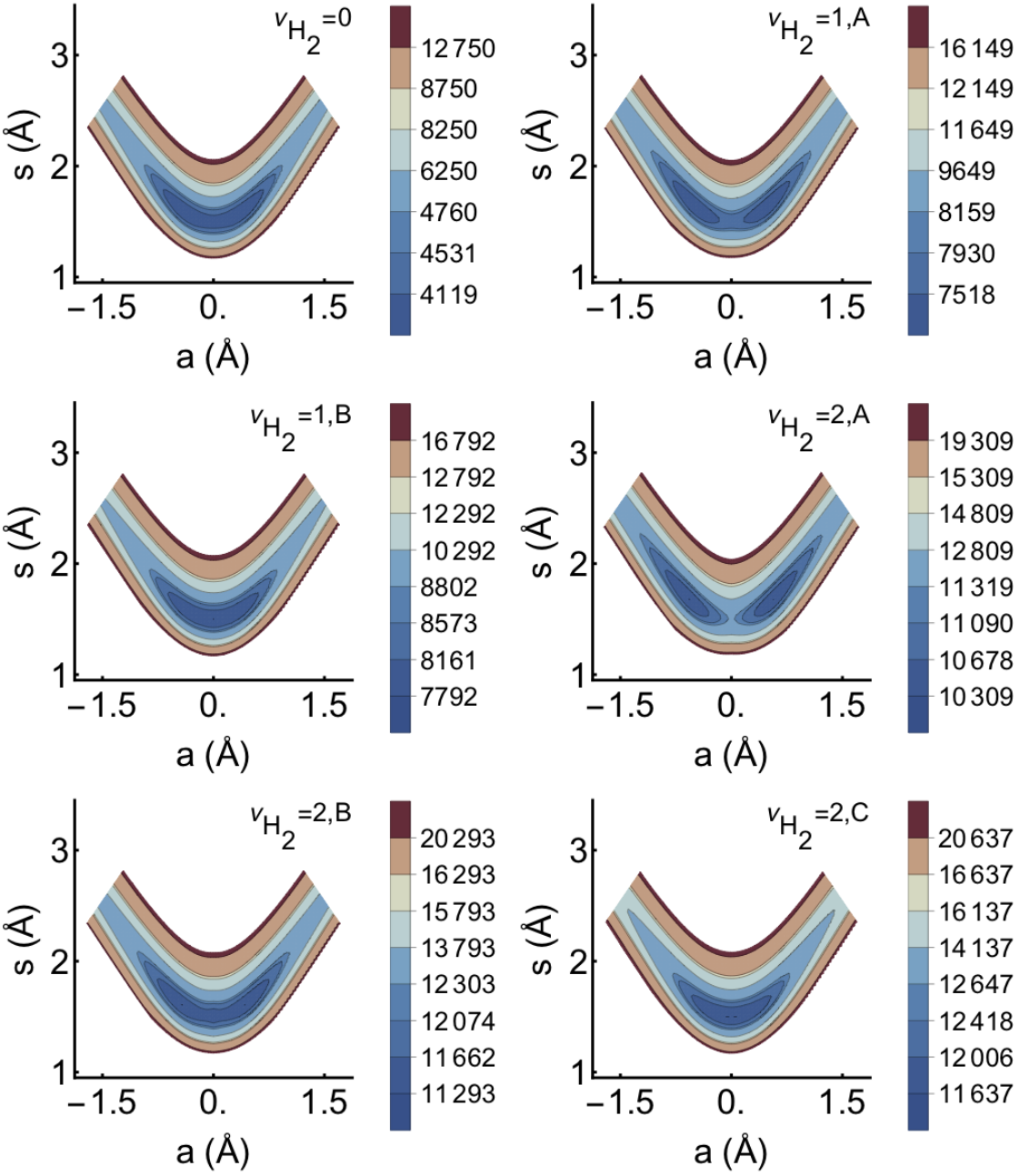

Figure 4.14: The adiabatic potential surfaces used in this study each plotted over a 10000 cm^{-1} range from the minimum on the surface.

State	Frequency cm^{-1}	Intensity (km/mol)
0	3547	271.52
1	3809	0.00
2	4121	17.37
3	4385	0.00
4	4638	1.93
5	4865	0.00
6	5062	0.00
7	5254	0.00
8	5336	14.74
9	5450	8.86
10	5557	0.00
11	5691	1.06
12	5799	0.00
13	5922	0.35
14	6035	0.00
15	6124	0.00
16	6177	0.04
17	6348	0.00
18	6373	0.50
19	6537	0.41
20	6664	0.00
21	6829	0.01
22	6878	0.00
23	6992	0.27

Table 4.3: Frequencies and intensities from the H_5^+ uncoupled calculation per Figure 4.13 ($\nu_{H_2} = 1$, State A).

State	Frequency cm^{-1}	Intensity (km/mol)
0	7864	0.00
1	8480	6.71
2	8806	0.00
3	9236	1.09
4	9421	0.00
5	9791	0.00
6	9842	0.29
7	10130	0.00
8	10338	0.05
9	10491	0.00
10	10722	0.03
11	10784	0.00
12	10853	0.40
13	11035	0.00
14	11085	0.04
15	11257	0.00
16	11339	0.00
17	11446	0.00
18	11587	0.01
19	11615	0.00
20	11764	0.17
21	11826	0.00
22	11928	0.02
23	12050	0.00

Table 4.4: Frequencies and intensities from the H_5^+ uncoupled calculation per figure 4.13 ($\nu_{H_2} = 2$, State C)

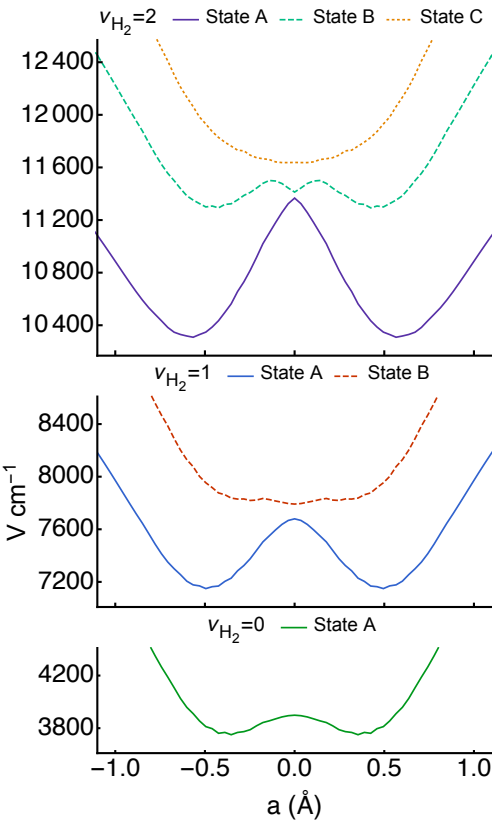

Figure 4.15: The minimum energy paths through the adiabats for $\nu_{\mathrm{H}_2} = 0, 1, 2$. The curves are evaluated by finding the minimum in the potential with respect to s for each value of a.

State	Label	Freq. (cm^{-1})	Orig. (cm^{-1})	Intensity (km/mol)	State A $\xi^a_{1,n,\mathrm{A}}$	State A $n^b_{H^+}$	State A Percent^c	State B $\xi^a_{1,n,\mathrm{B}}$	State B $n^b_{H^+}$	State B Percent^c
0	II_a	3520	3624	332.33	91	0	94.30	6	1	5.70
1	–	3562	3676	0.00	77	1	80.90	19	0	19.10
2	II_b	3889	4084	72.18	58	2	79.30	21	1	20.70
3	–	3904	4103	0.00	37	3	56.10	44	0	43.90
4	–	4170	4435	0.00	27	3	61.50	37	0	38.50
5	II_c	4192	4462	19.93	22	4	54.80	44	1	45.20
6	II_d	4391	4711	1.42	30	4	67.20	29	3	32.80
7	–	4412	4737	0.00	23	5	63.60	33	2	36.40
8	–	4632	5012	0.00	16	7	59.60	33	2	40.40
9	–	4633	5013	0.15	22	6	73.90	21	3	26.10
10	–	4813	5237	0.00	21	7	63.00	23	4	37.00
11	II_e	4818	5243	2.44	22	8	52.40	29	3	47.60
12	II_f	4935	5390	2.86	35	8	85.50	9	5	14.50
13	–	4961	5422	0.00	18	9	67.20	24	3	32.80
14	II_g	5084	5575	5.41	42	9	78.90	15	3	21.10
15	–	5111	5609	0.00	24	11	73.30	26	3	26.70
16	II_h	5151	5659	1.43	19	11	63.60	13	5	36.40
17	–	5155	5663	0.00	24	12	45.30	23	4	54.70
18	–	5283	5824	0.00	13	11	75.40	12	5	24.60
19	–	5289	5831	0.07	10	11	68.30	15	5	31.70
20	–	5414	5987	0.25	20	12	63.70	12	7	36.30
21	–	5426	6002	0.00	15	13	61.40	16	6	38.60
22	–	5555	6163	0.00	13	13	61.40	16	6	38.60
23	–	5559	6168	0.01	14	14	70.90	13	7	29.10

[a] Percentage of the wave function probability amplitude in the 99 percent contour of the ground state probability amplitude.

[b] Number of nodes along the proton transfer coordinate.

[c] Percentage of the probability amplitude associated with the adiabatic state.

Table 4.5: Frequencies, intensities, and percent contributions from the State A and State B adiabats for the 24 lowest-energy states with $\nu_{H_2} = 1$. The corresponding wave functions are shown in Fig. 4.4.

Table 4.6: Frequencies, intensities, and percent contributions from the State A, State B, and State C adiabats for the 24 lowest-energy states with $\nu_{H_2} = 2$. The corresponding wave functions are shown in Fig. 4.10.

State	Label	Freq. (cm^{-1})	Orig. (cm^{-1})	Intensity (km/mol)	State A			State B			State C		
					$\xi^{a}_{2,n,A}$	n_{H^+}	Percent	$\xi_{2,n,B}$	n_{H^+}	Percent	$\xi_{2,n,C}$	n_{H^+}	Percent
0	–	6684	6917	0.00	0.84	0	98.20	0.01	1	0.70	0.01	0	1.10
1	III_a	6685	6918	10.29	0.83	1	97.30	0.02	0	2.30	0.00	1	0.40
2	–	7032	7350	0.00	0.46	2	92.40	0.04	1	4.50	0.03	0	3.10
3	III_b	7040	7360	4.46	0.43	3	91.60	0.06	0	6.00	0.02	1	2.40
4	–	7227	7594	0.00	0.04	4	9.70	0.73	1	74.30	0.16	0	16.00
5	III_c	7341	7737	0.69	0.29	5	82.30	0.10	0	10.30	0.07	1	7.40
6	–	7344	7741	0.00	0.29	4	80.10	0.04	3	3.90	0.16	0	16.00
7	–	7497	7931	0.16	0.02	5	4.70	0.87	0	94.50	0.01	1	0.90
8	–	7589	8045	0.00	0.19	6	77.50	0.04	1	3.90	0.18	0	18.70
9	–	7589	8046	0.35	0.16	7	70.80	0.10	2	10.30	0.19	1	18.90
10	–	7757	8255	0.00	0.01	0	1.70	0.61	3	85.60	0.13	0	12.70
11	III_d	7769	8271	1.99	0.17	7	70.90	0.04	0	4.50	0.24	1	24.50
12	–	7775	8278	0.00	0.18	8	70.30	0.05	3	5.60	0.24	0	24.10
13	–	7920	8459	0.00	0.19	8	78.30	0.02	1	2.40	0.19	2	19.30
14	III_e	7923	8463	1.54	0.18	9	80.90	0.03	1	3.70	0.15	1	15.40
15	–	7997	8555	0.78	0.00	0	0.60	0.47	3	95.40	0.04	1	4.00
16	–	8072	8648	0.00	0.18	10	85.40	0.02	3	2.80	0.11	2	11.80
17	–	8079	8657	0.57	0.16	11	83.60	0.04	1	4.60	0.11	3	11.80
18	–	8201	8809	0.00	0.02	6	5.60	0.30	5	88.20	0.06	1	6.20
19	–	8250	8870	0.24	0.12	13	72.00	0.05	0	5.60	0.19	3	22.50
20	–	8253	8874	0.00	0.13	12	75.30	0.02	3	4.10	0.18	2	20.60
21	–	8294	8925	0.00	0.59	6	69.00	0.03	5	2.90	0.24	2	28.10
22	III_f	8305	8939	3.52	0.56	9	70.50	0.07	1	7.70	0.18	1	21.90
23	–	8404	9062	0.01	0.02	5	5.00	0.34	5	94.10	0.01	1	0.90

[a] Percentage of the wave function in the 99 percent contour of the ground state.
[b] Number of nodes along the proton transfer coordinate.
[c] Percentage of the probability amplitude associated with the adiabatic state.

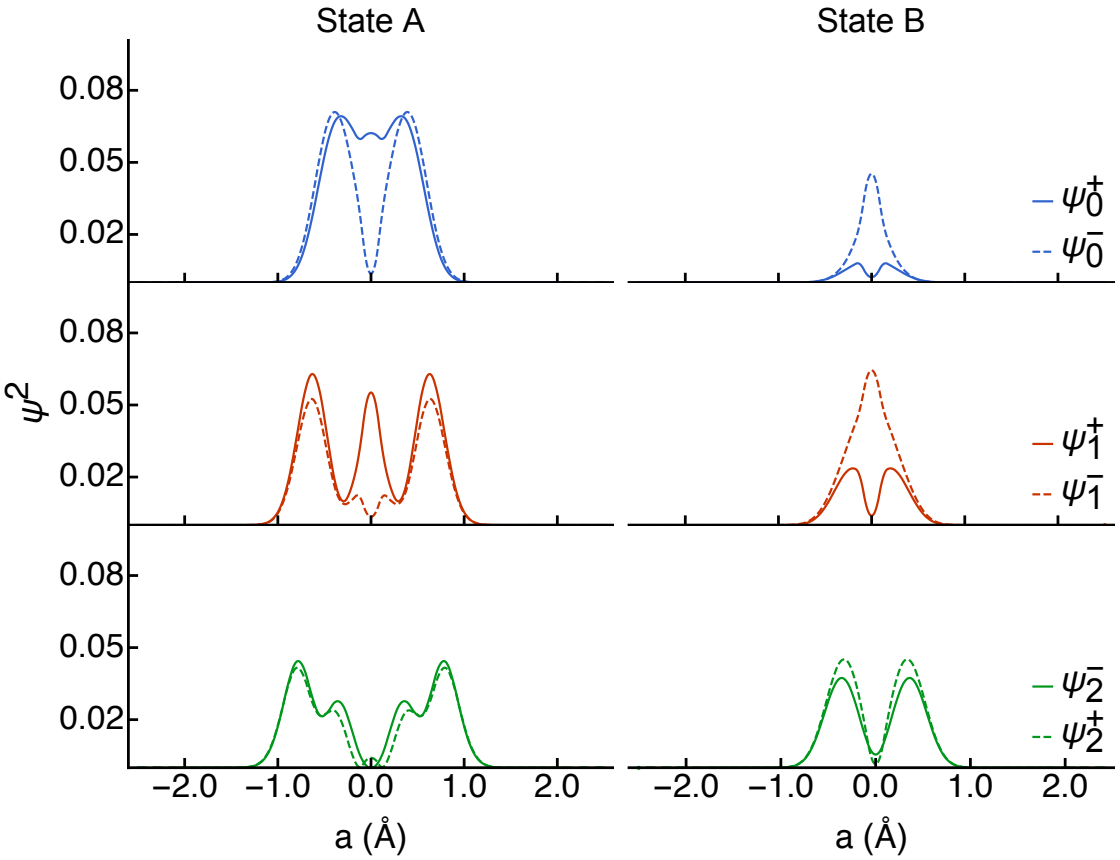

Figure 4.16: Projections of the probability amplitude onto the a coordinate for the six lowest-energy wave functions for H_5^+ with $\nu_{H_2} = 1$. These wave functions are shown in Fig. 4.4. The contributions from the State A and State B adiabats are shown on the left and right columns respectively.

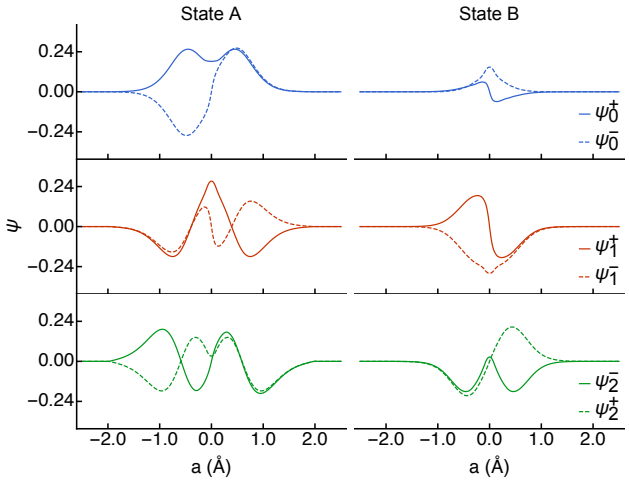

Figure 4.17: The one-dimensional wave functions associated with the six lowest-energy states evaluated using the $\nu_{H_2} = 1$ State A and State B minimum-energy curves shown in Fig. 4.15 with non-adiabatic couplings introduced. The wave functions are divided into the contributions from the State A and State B adiabats. The wave functions for the two lowest-energy states are plotted in the top panel, those for the next two states are plotted in the middle panel, and the final two excited state plotted in the bottom panel.

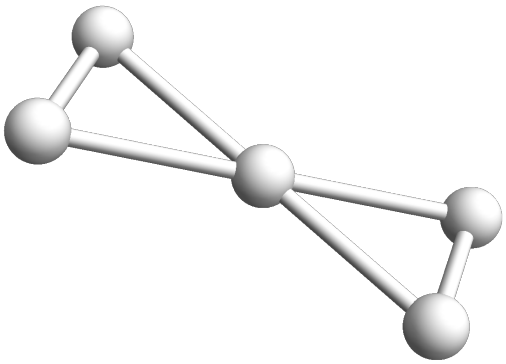

Figure 4.18: The parallel geometry of H_5^+.

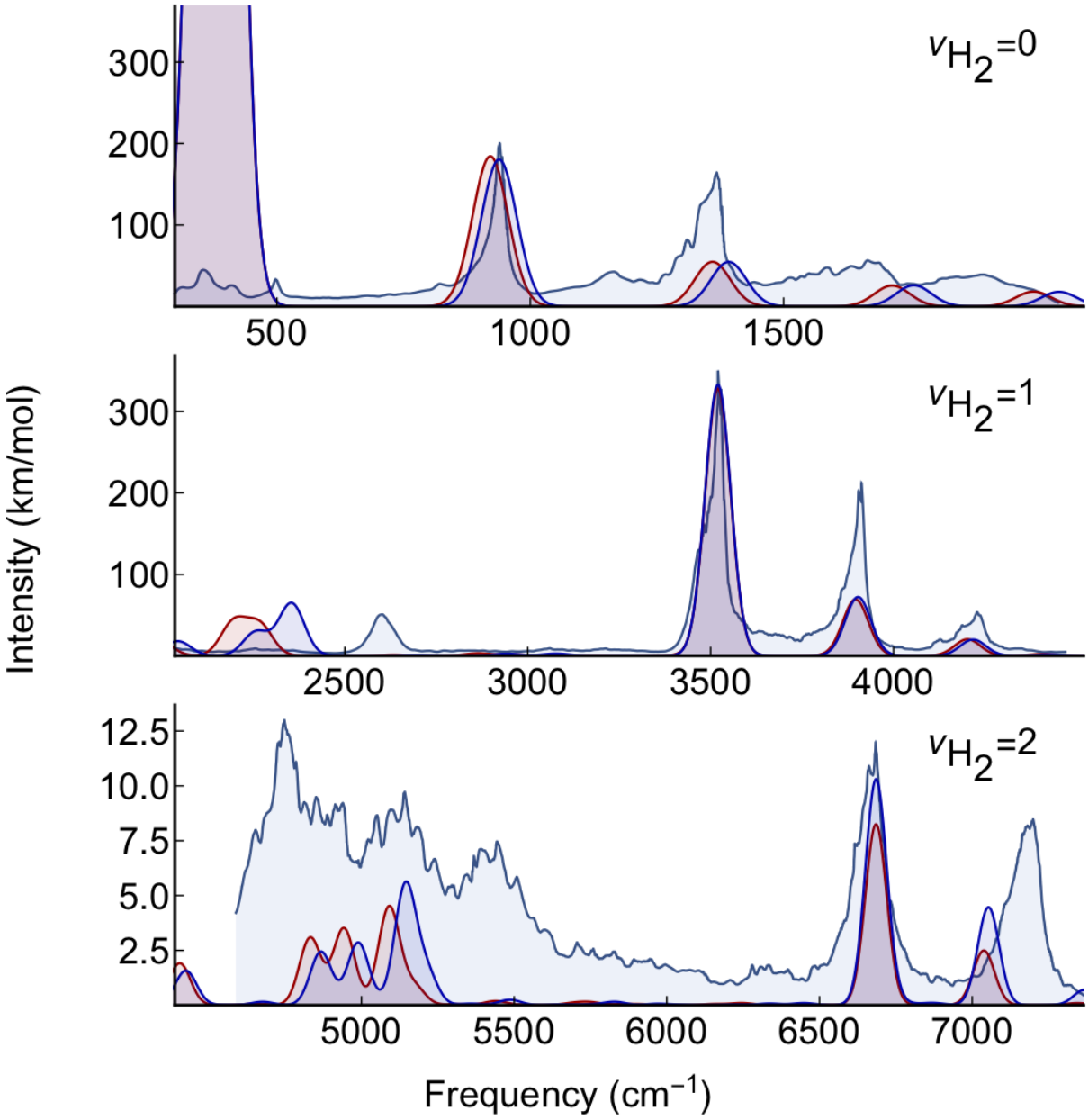

Figure 4.19: Comparison of the calculated spectrum for the parallel geometry spectrum of H_5^+ (blue) shown in Fig. 4.18 and the spectrum for the perpendicular geometry (red) shown in Fig. 4.1. No shifting or scaling was applied to the frequencies. The calculated peaks were convolved with Gaussian with a standard deviation of 50 cm^{-1} to facilitate comparison.

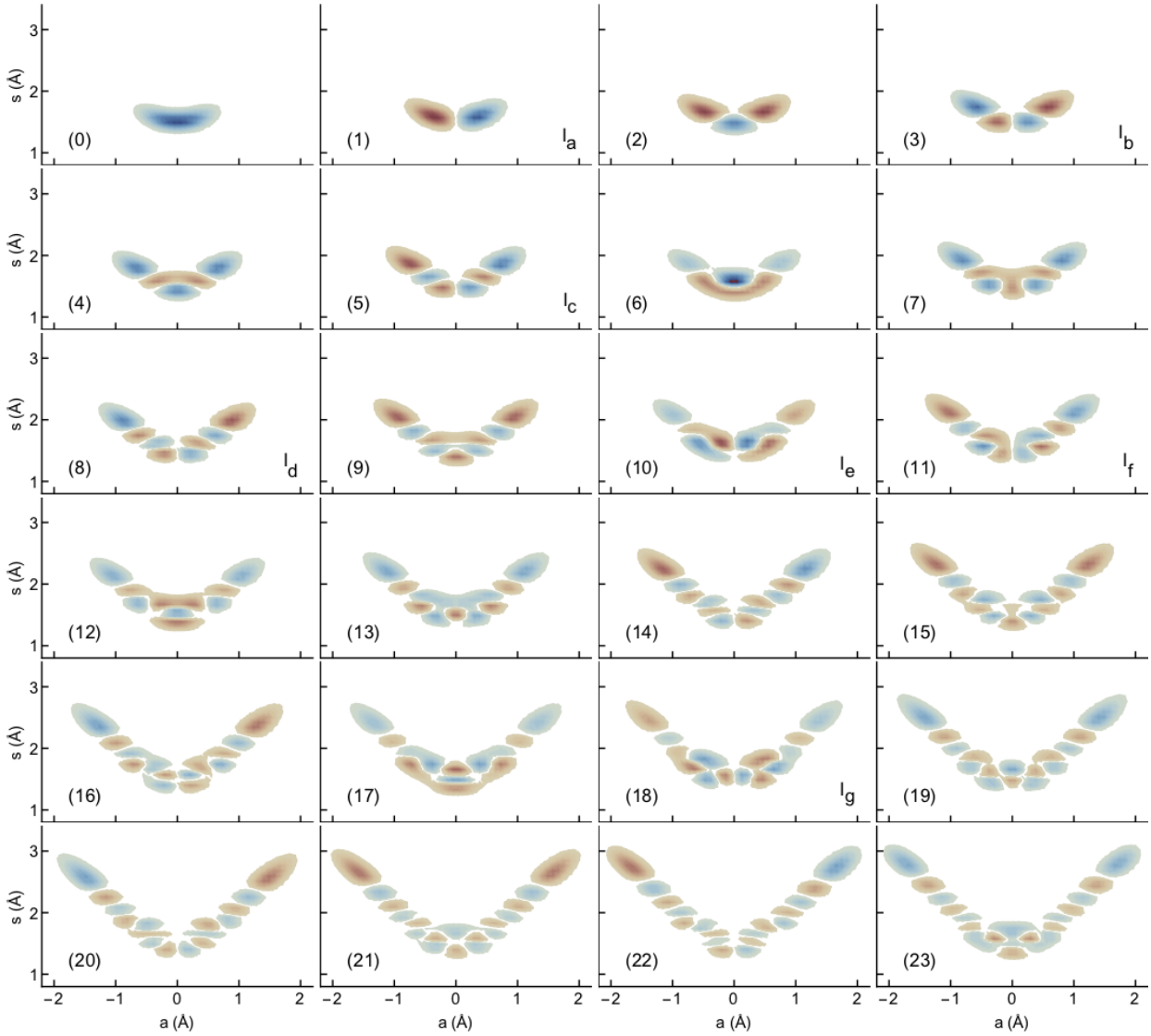

Figure 4.20: The 24 lowest-energy wave functions with $\nu_{H_2} = 0$ for D_5^+, numbered according to increasing energy, analogous to Figure 4.5. Wave functions corresponding to peaks in Fig. 4.23 are labeled with their peak label in the bottom right of the corresponding plot. The energies and intensities for transitions to these states are tabulated in Table 4.7.

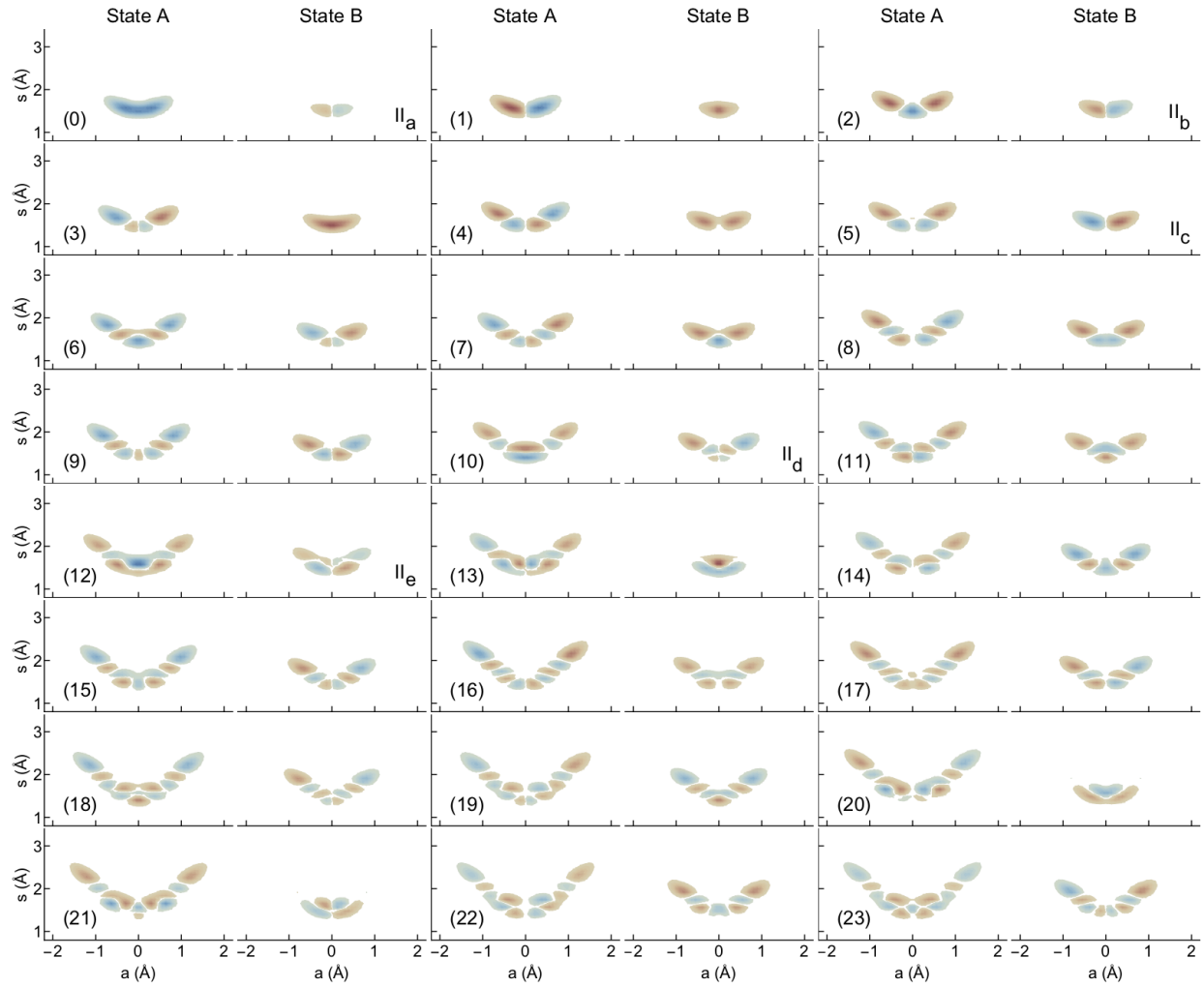

Figure 4.21: The 24 lowest-energy wave functions with $\nu_{H_2} = 1$ for D_5^+, numbered according to increasing energy, analogous to Figure 4.4. The contributions from the State A and State B adiabats are plotted side-by-side. Wave functions corresponding to peaks in Fig. 4.23 are labeled with their peak label in the bottom right of the corresponding plot. The energies and intensities for transitions to these states are tabulated in Table 4.8.

Figure 4.22: The 24 lowest-energy wave functions with $\nu_{H_2} = 2$ for D_5^+, numbered according to increasing energy, analogous to Figure 4.10. The contributions from the State A, State B, and State C adiabats are plotted side-by-side. Wave functions corresponding to peaks in Fig. 4.23 are labeled with their peak label in the bottom right of the corresponding plot. The energies and intensities for transitions to these states are tabulated in Table 4.9.

State	Label	Freq. (cm^{-1})	Orig. (cm^{-1})	Intensity (km/mol)	$\xi_{0,n,A}$	n_{H^+}
0	–	0	0	0.00	99	0
1	I_a	238	296	1218.25	97	1
2	–	438	544	0.00	88	2
3	I_b	641	796	65.47	70	3
4	–	802	996	0.00	55	4
5	I_c	989	1229	20.08	41	5
6	–	1007	1251	0.00	81	5
7	–	1165	1447	0.00	48	6
8	I_d	1290	1603	14.12	39	7
9	–	1424	1769	0.00	34	8
10	I_e	1500	1863	55.50	71	7
11	I_f	1579	1962	5.96	44	9
12	–	1616	2008	0.00	48	8
13	–	1731	2151	0.00	42	10
14	–	1786	2219	0.19	25	11
15	–	1895	2354	0.00	29	12
16	–	1963	2439	0.85	27	13
17	–	2007	2494	0.00	44	12
18	I_g	2050	2547	1.12	40	13
19	–	2091	2598	0.00	27	14
20	–	2147	2668	0.00	18	15
21	–	2211	2747	0.00	18	16
22	–	2269	2819	0.04	14	17
23	–	2319	2882	0.00	24	16

Table 4.7: Frequencies and intensities for the 24 lowest-energy wave functions with $\nu_{H_2} = 0$ for D_5^+, analogous to 4.2. The corresponding wave functions are shown in Fig. 4.20.

State	Label	Freq. (cm^{-1})	Orig. (cm^{-1})	Intensity (km/mol)	State A $\xi_{1,n,A}$	State A n_{H^+}	State A Percent	State B $\xi_{1,n,B}$	State B n_{H^+}	State B Percent
0	II_a	2546	2605	177.03	92	0	93.90	6	1	6.10
1	–	2576	2643	0.00	77	1	80.10	20	0	19.90
2	II_b	2808	2930	36.20	61	2	74.00	26	1	26.00
3	–	2813	2936	0.00	38	3	47.70	52	0	52.30
4	–	3006	3176	0.00	39	3	63.30	36	0	36.70
5	II_c	3020	3194	7.28	28	4	48.80	50	1	51.20
6	–	3185	3398	0.09	33	4	69.80	28	3	30.20
7	–	3204	3423	0.00	21	5	54.90	42	2	45.10
8	–	3370	3628	0.00	23	5	55.90	36	2	44.10
9	–	3387	3649	0.24	22	6	57.30	35	3	42.70
10	II_d	3498	3787	1.56	46	6	68.70	20	5	31.30
11	–	3521	3816	0.00	27	7	59.30	30	4	40.70
12	II_e	3608	3924	2.28	51	6	74.60	21	5	25.40
13	–	3638	3962	0.00	34	7	60.30	37	2	39.70
14	–	3695	4033	0.00	21	7	45.60	26	4	54.40
15	–	3697	4035	0.27	22	8	62.20	18	5	37.80
16	–	3835	4206	0.00	20	9	69.00	15	4	31.00
17	–	3839	4212	0.03	16	8	55.00	20	5	45.00
18	–	3948	4347	0.03	25	10	68.60	11	7	31.40
19	–	3959	4360	0.00	19	11	53.90	20	6	46.10
20	–	4040	4461	0.00	28	11	71.10	27	2	28.90
21	–	4054	4479	0.01	31	12	74.30	24	3	25.70
22	–	4094	4528	0.00	26	11	52.00	21	6	48.00
23	–	4104	4540	0.01	27	12	53.40	18	7	46.60

Table 4.8: Frequencies, intensities, and percent contributions from the State A and State B adiabats for the 24 lowest-energy wave functions with $\nu_{H_2} = 1$ for D_5^+, analogous to Table 4.5. The corresponding wave functions are shown in Fig. 4.21.

Table 4.9: Frequencies, intensities, and percent contributions from the State A, State B, and State C adiabats for the 24 lowest-energy wave functions with $\nu_{H_2} = 2$ for D_5^+, analogous to Table 4.6. The corresponding wave functions are shown in Fig. 4.10.

State	Label	Freq. (cm^{-1})	Orig. (cm^{-1})	Intensity (km/mol)	State A $\xi_{2,n,A}$	State A n_{H^+}	State A Percent	State B $\xi_{2,n,B}$	State B n_{H^+}	State B Percent	State C $\xi_{2,n,C}$	State C n_{H^+}	State C Percent
0	–	4900	5029	0.00	90	0	98.10	1	1	0.60	1	0	1.30
1	III_a	4902	5031	5.20	88	1	96.70	3	0	2.50	1	1	0.80
2	–	5157	5348	0.00	54	2	82.40	15	1	15.30	2	0	2.30
3	III_b	5169	5362	3.61	53	3	87.30	8	0	7.90	5	1	4.80
4	–	5231	5440	0.00	7	4	13.80	65	1	65.60	20	0	20.60
5	III_c	5389	5636	1.47	15	5	40.30	50	0	52.00	8	1	7.70
6	–	5404	5655	0.00	30	4	74.20	3	1	3.00	23	0	22.80
7	–	5422	5678	0.71	13	5	34.00	54	2	56.60	9	1	9.40
8	–	5588	5883	0.00	20	6	50.30	9	1	10.80	38	0	38.90
9	III_d	5590	5886	1.02	23	7	60.30	6	2	6.40	33	1	33.30
10	–	5603	5902	0.00	6	6	14.00	66	3	79.90	6	2	6.10
11	–	5746	6079	0.12	26	7	71.60	3	2	3.80	24	1	24.60
12	–	5746	6080	0.00	26	6	70.90	3	3	3.50	25	2	25.60
13	–	5786	6130	0.01	0	0	0.30	60	2	95.10	4	1	4.60
14	–	5907	6279	0.00	22	8	72.70	6	5	10.30	16	2	17.00
15	–	5910	6284	0.00	19	9	72.30	6	2	6.80	19	3	20.90
16	–	5953	6337	0.00	2	6	4.70	33	5	79.40	15	2	15.90
17	–	6001	6396	0.00	62	6	70.90	4	5	5.60	21	2	23.50
18	–	6005	6401	0.09	57	7	66.50	8	2	8.80	22	3	24.70
19	–	6121	6545	0.00	1	9	5.30	35	5	90.90	4	3	3.80
20	–	6189	6630	0.00	19	10	66.50	4	3	4.00	22	4	29.50
21	–	6191	6633	0.00	21	11	67.30	0	0	0.90	24	3	31.80
22	–	6195	6638	0.00	6	5	6.80	49	7	69.70	22	2	23.50
23	–	6285	6750	0.00	9	12	43.60	23	7	43.30	10	4	13.10

System	Band	Reference[a]	Calculated	Shift[b]	Scale[c]
H_5^+					
	$\nu_{H_2} = 0$	365	455	0	0.802
	$\nu_{H_2} = 1$	3520	3624	104	0.802
	$\nu_{H_2} = 2$	6685	6918	233	0.802
D_5^+					
	$\nu_{H_2} = 0$	238	296	0	0.805
	$\nu_{H_2} = 1$	2546	2605	59	0.805
	$\nu_{H_2} = 2$	4902	5031	129	0.805
$D_2H^+D_2$[d]					
	$\nu_{H_2} = 0$	365	456	0	0.801
	$\nu_{H_2} = 1$	2546	2611	65	0.801
	$\nu_{H_2} = 2$	4904	5070	166	0.801
$H_2D^+H_2$[d]					
	$\nu_{H_2} = 0$	238	333	0	0.716
	$\nu_{H_2} = 1$	3520	3626	106	0.716
	$\nu_{H_2} = 2$	6684	6907	222	0.716

[a] Reference for $\nu_{H_2} = 0$ comes from the 9D calculations of Prosmiti *et al.*[84] Reference for $\nu_{H_2} = 1, 2$ comes from experiment.

[b] Shifts are always negative in sign so only the magnitude is given.

[c] Scaling is applied after the shift. For $\nu_{H_2} = 0$ the scaling is applied to all of the peaks. For $\nu_{H_2} = 1, 2$ the scaling is applied by treating the reference peak as the origin.

[d] For $D_2H^+D_2$ and $H_2D^+H_2$ the reference peaks for $\nu_{H_2} = 0$ are chosen so to match the references for H_5^+ and D_5^+ while those for $\nu_{H_2} = 1, 2$ are chosen to match the references for D_5^+ and H_5^+.

Table 4.10: The scaling factors and shifts applied to the calculated frequencies

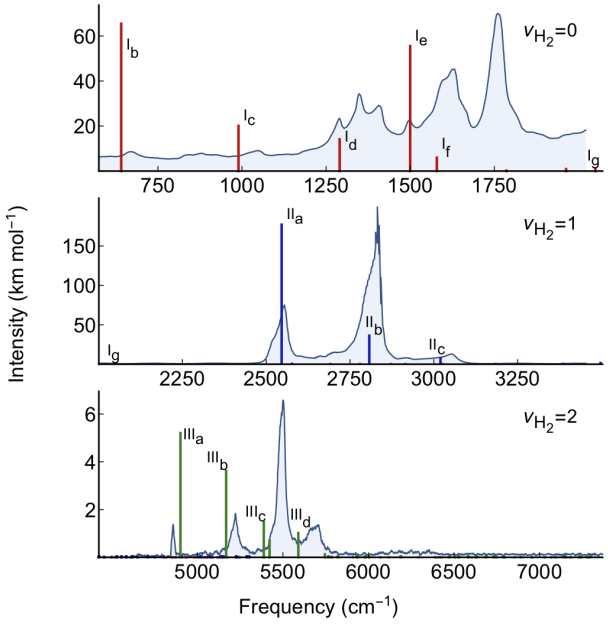

Figure 4.23: Experimental spectra (shaded grey) with calculated spectra (sticks) overlain for D_5^+. The top panel compares the spectrum reported in Ref. 71 to the calculated transitions with $\nu_{H_2} = 0$ (red sticks). The middle panel compares the spectrum reported in Ref. 67 to the calculated transitions with $\nu_{H_2} = 0$ and $\nu_{H_2} = 1$ (red and blue sticks). The bottom panel compares our newly recorded spectrum reported to the calculated transitions with $\nu_{H_2} = 1$ and $\nu_{H_2} = 2$ (blue and green sticks). The positions of the transitions in the calculated spectrum have been shifted and scaled as described in the text and tabulated in Table 4.10.

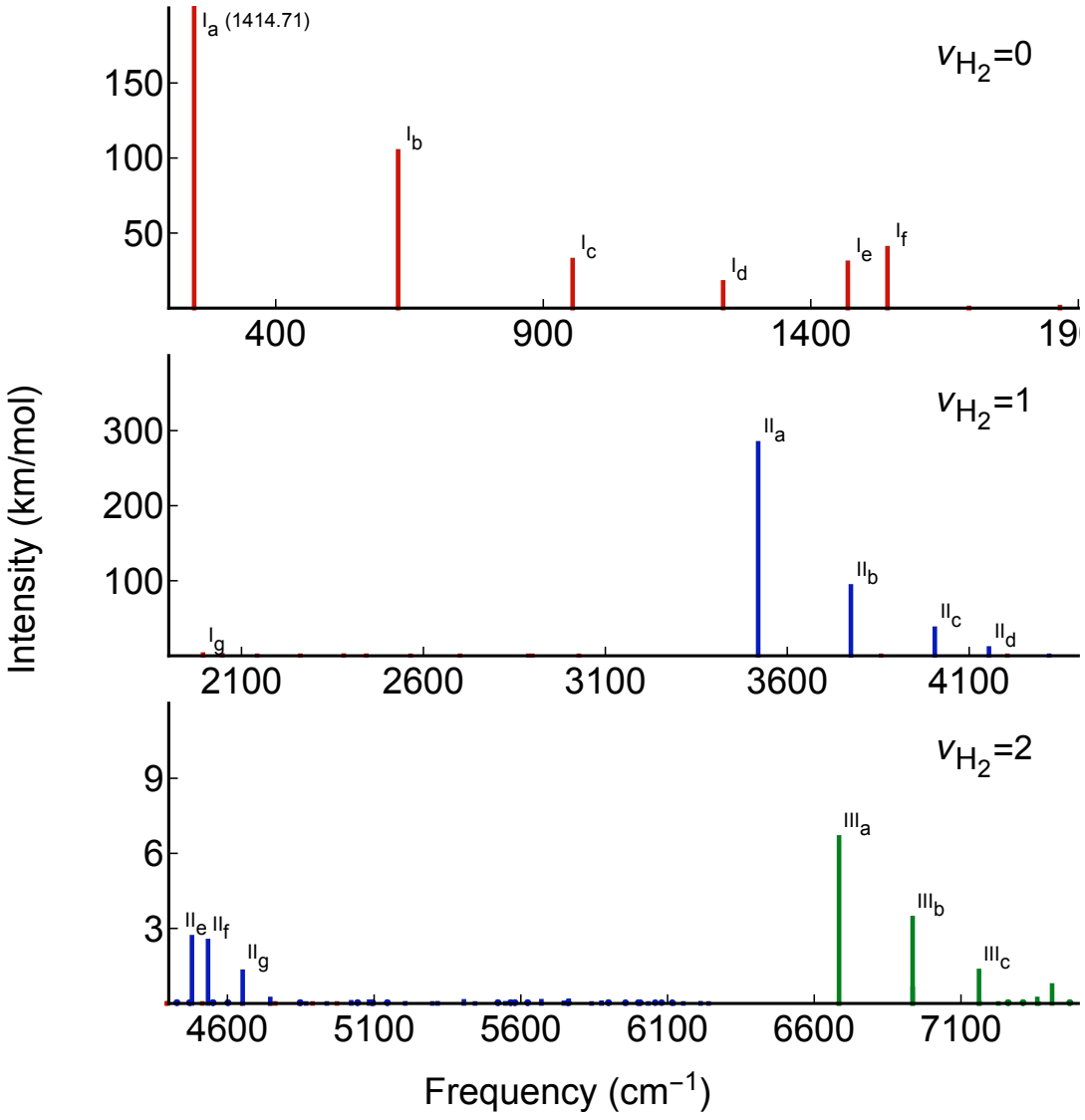

Figure 4.24: Calculated spectrum of $H_2D^+H_2$, analogous to Fig. 4.2. $\nu_{H_2} = 0, 1, 2$ shown in red, blue, and green. The positions of the transitions in the calculated spectrum have been shifted and scaled as described in the text and tabulated in Table 4.10. The intensity of the I_a peak is labeled as it extends off the scale of the plot.

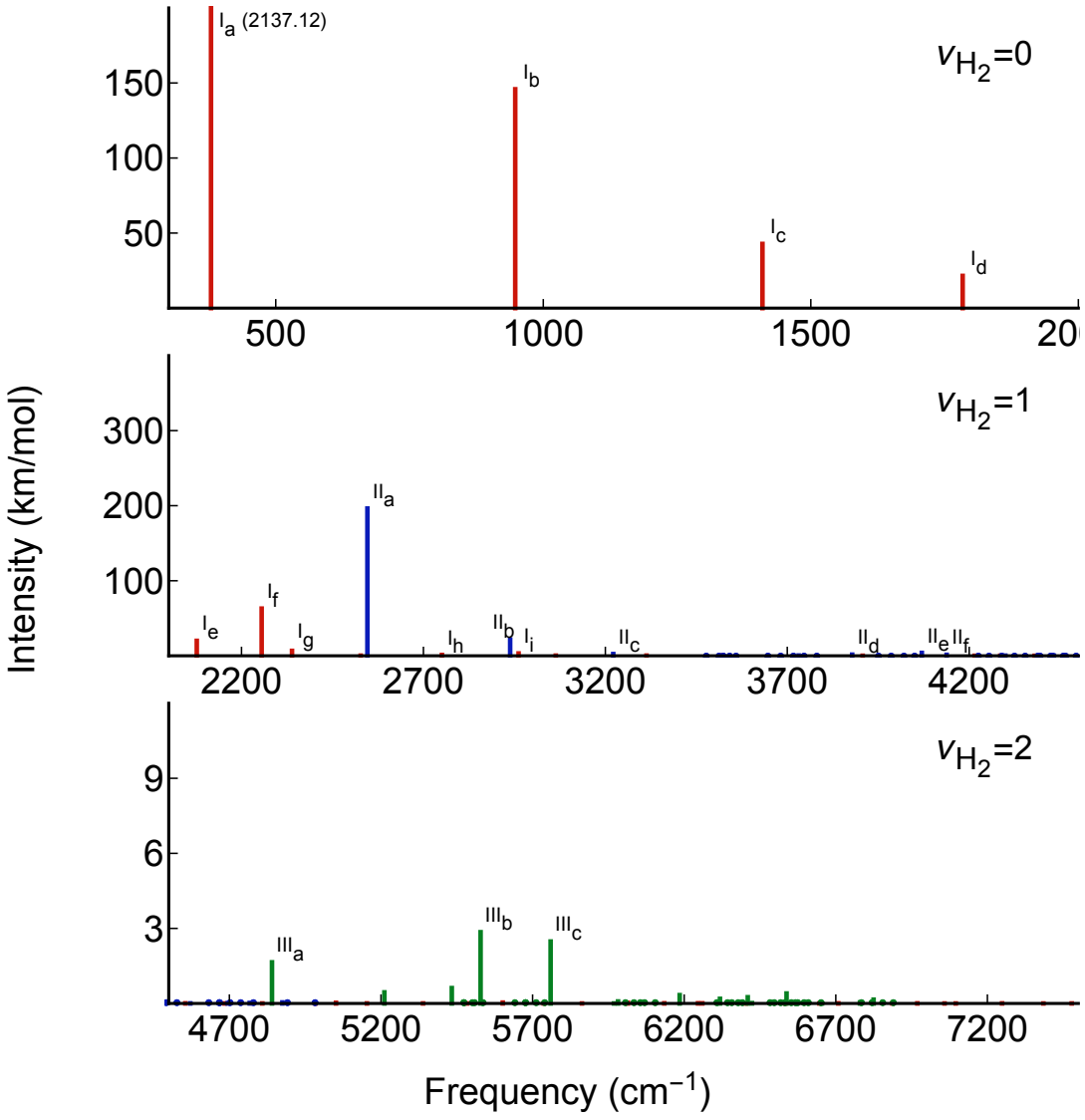

Figure 4.25: Calculated spectra of $D_2H^+D_2$, analogous to Fig. 4.2. $\nu_{H_2} = 0, 1, 2$ shown in red, blue, and green. The positions of the transitions in the calculated spectrum have been shifted and scaled as described in the text and tabulated in Table 4.10. The intensity of I_a peak is labeled as it extends off the scale of the plot.

State	Label	Freq. (cm^{-1})	Orig. (cm^{-1})	Intensity (km/mol)	$\xi_{0,n,A}$
0	–	0	0	0.00	99
1	I_a	248	333	1414.71	96
2	–	429	576	0.00	87
3	I_b	629	845	104.43	67
4	–	767	1030	0.00	54
5	I_c	955	1283	32.01	41
6	–	982	1320	0.00	72
7	–	1128	1516	0.00	54
8	I_d	1236	1661	17.16	37
9	–	1352	1817	0.00	36
10	I_e	1469	1974	30.20	40
11	–	1535	2063	0.00	42
12	I_f	1543	2074	39.95	74
13	–	1664	2237	0.00	41
14	–	1696	2279	0.12	25
15	–	1802	2422	0.00	32
16	–	1866	2507	0.71	20
17	–	1920	2580	0.00	32
18	I_g	1994	2680	1.69	29
19	–	2006	2696	0.00	29
20	–	2047	2751	0.75	32
21	–	2100	2823	0.00	21
22	–	2143	2880	0.02	15
23	–	2197	2953	0.00	20

Table 4.11: Frequencies and intensities for the 24 lowest-energy wave functions with $\nu_{H_2} = 0$ for $H_2D^+H_2$, analogous to 4.2. The corresponding wave functions are shown in Fig. 4.28.

State	Label	Freq. (cm^{-1})	Orig. (cm^{-1})	Intensity (km/mol)	State A $\xi_{1,n,A}$	State A Percent	State B $\xi_{1,n,B}$	State B Percent
0	II_a	3520	3626	283.08	93	96.70	3	3.30
1	–	3544	3659	0.00	84	89.00	11	11.00
2	II_b	3775	3969	92.46	63	86.30	14	13.70
3	–	3796	3998	0.00	44	66.80	33	33.20
4	–	3993	4262	0.00	23	56.00	43	44.00
5	II_c	4005	4279	36.08	26	64.70	35	35.30
6	II_d	4154	4479	9.76	30	59.10	39	40.90
7	–	4162	4489	0.00	29	66.60	32	33.40
8	–	4320	4701	0.03	30	78.60	19	21.40
9	–	4330	4715	0.00	19	60.70	36	39.30
10	–	4472	4905	0.00	24	56.90	33	43.10
11	II_e	4479	4915	2.65	28	50.80	38	49.20
12	II_f	4534	4989	2.50	46	88.10	10	11.90
13	–	4561	5025	0.00	32	67.70	28	32.30
14	II_g	4652	5148	1.27	34	65.50	23	34.50
15	–	4667	5168	0.00	33	65.60	26	34.40
16	–	4746	5274	0.18	19	70.70	15	29.30
17	–	4746	5274	0.00	15	58.00	21	42.00
18	–	4862	5430	0.00	17	69.40	13	30.60
19	–	4868	5438	0.00	14	61.20	18	38.80
20	–	4939	5533	0.00	30	74.20	8	25.80
21	–	4950	5548	0.00	22	65.90	16	34.10
22	–	5021	5643	0.00	20	79.20	20	20.80
23	–	5022	5645	0.05	24	85.30	14	14.70

Table 4.12: Frequencies, intensities, and percent contributions from the State A and State B adiabats for the 24 lowest-energy wave functions with $\nu_{H_2} = 1$ for $H_2D^+H_2$, analogous to Table 4.5. The corresponding wave functions are shown in Fig. 4.27.

Table 4.13: Frequencies, intensities, and percent contributions from the State A, State B, and State C adiabats for the 24 lowest-energy wave functions with $\nu_{H_2} = 2$ for $H_2D^+H_2$, analogous to Table 4.6. The corresponding wave functions are shown in Fig. 4.28.

State	Label	Freq. (cm^{-1})	Orig. (cm^{-1})	Intensity (km/mol)	State A		State B		State C	
					$\xi_{2,n,A}$	Percent	$\xi_{2,n,B}$	Percent	$\xi_{2,n,C}$	Percent
0	–	6684	6906	0.00	80	99.10	1	0.70	0	0.20
1	III_a	6684	6907	6.64	80	99.30	0	0.20	1	0.50
2	III_b	6935	7244	3.41	46	97.20	1	0.90	2	1.90
3	–	6935	7244	0.59	45	96.80	2	2.10	1	1.10
4	III_c	7161	7548	1.30	39	93.30	2	1.80	5	4.90
5	–	7163	7550	0.01	37	92.20	5	5.00	3	2.80
6	–	7227	7636	0.00	2	1.80	81	81.90	16	16.40
7	–	7360	7815	0.18	25	83.90	7	7.60	8	8.40
8	–	7364	7819	0.00	25	85.70	6	6.00	8	8.30
9	–	7410	7882	0.72	2	4.90	87	93.30	2	1.80
10	–	7527	8039	0.01	21	73.30	8	7.90	19	18.90
11	–	7529	8042	0.47	22	76.00	5	5.10	19	18.90
12	–	7587	8119	0.00	1	2.00	68	88.70	9	9.30
13	–	7645	8197	0.12	26	73.80	5	5.00	21	21.20
14	III_d	7645	8198	1.13	28	73.80	4	4.10	22	22.10
15	–	7753	8342	0.29	28	89.20	2	2.70	8	8.10
16	–	7756	8347	0.00	27	89.90	4	4.70	5	5.40
17	–	7758	8350	0.87	1	2.80	53	94.90	2	2.30
18	–	7862	8490	0.05	37	88.20	3	3.20	8	8.60
19	III_e	7863	8490	1.58	33	89.20	2	2.10	9	8.80
20	–	7899	8539	0.13	21	48.10	15	31.90	19	20.00
21	III_f	7904	8545	4.12	33	69.20	1	1.50	28	29.30
22	–	7909	8553	0.05	11	24.30	22	60.60	15	15.00
23	–	7995	8668	0.22	11	83.20	3	3.50	12	13.30

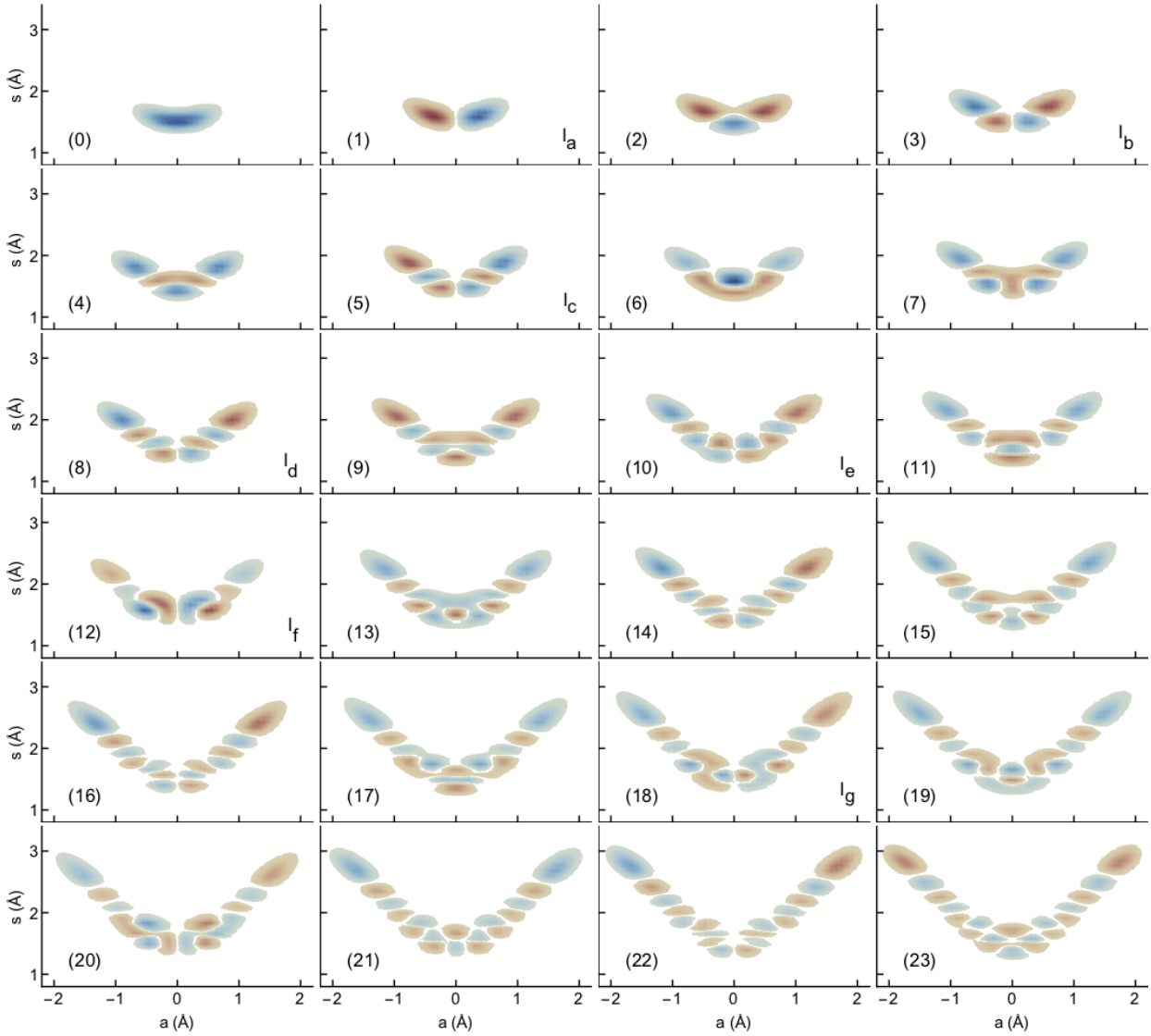

Figure 4.26: The 24 lowest-energy wave functions with $\nu_{H_2} = 0$ for $H_2D^+H_2$, numbered according to increasing energy, analogous to Figure 4.5. Wave functions corresponding to peaks in Fig. 4.24 are labeled with their peak label in the bottom right of the corresponding plot. The energies and intensities for transitions to these states are tabulated in Table 4.11.

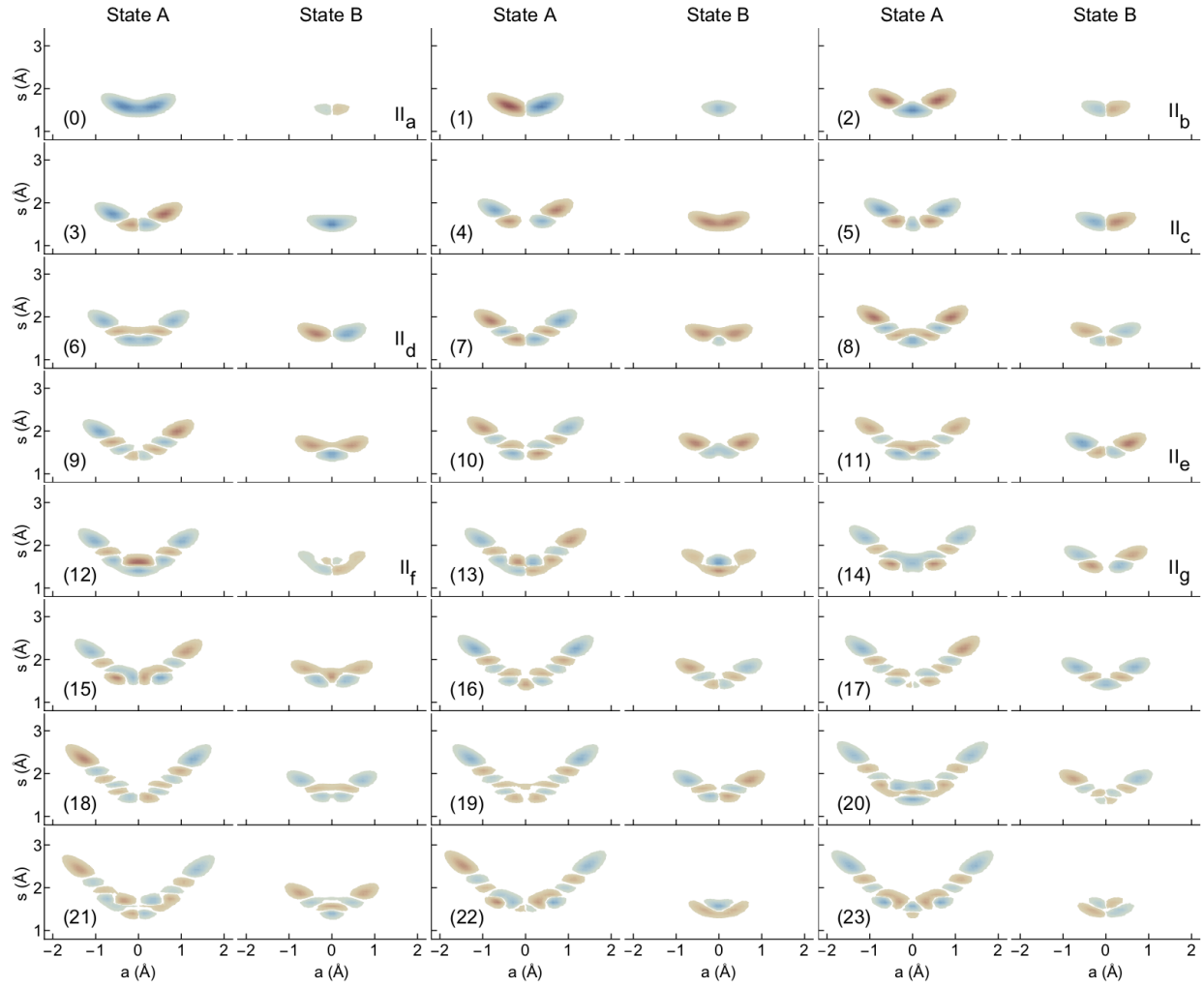

Figure 4.27: The 24 lowest-energy wave functions with $\nu_{H_2} = 1$ for $H_2D^+H_2$, numbered according to increasing energy, analogous to Figure 4.4. The contributions from the State A and State B adiabats are plotted side-by-side. Wave functions corresponding to peaks in Fig. 4.24 are labeled with their peak label in the bottom right of the corresponding plot. The energies and intensities for transitions to these states are tabulated in Table 4.12.

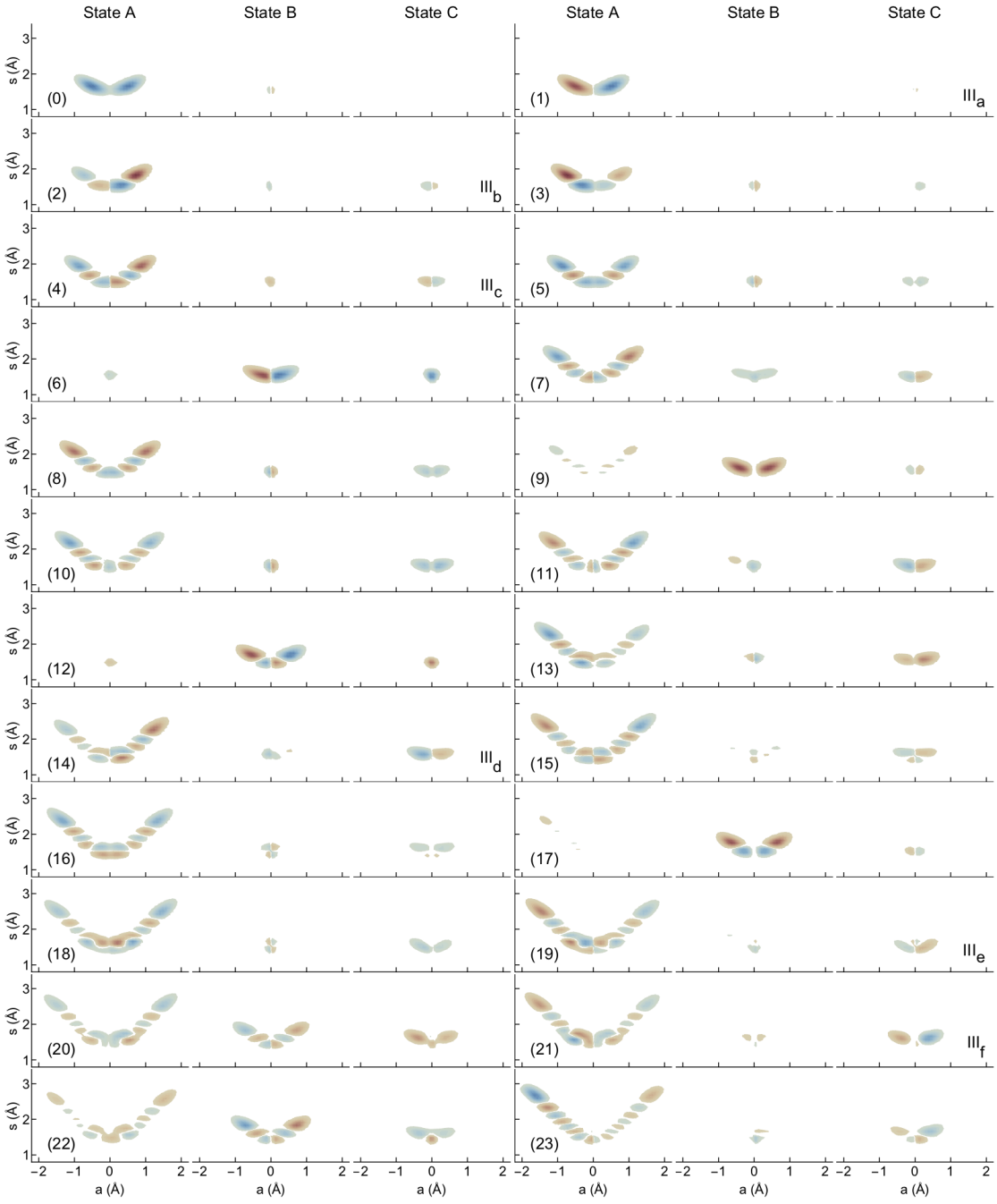

Figure 4.28: Fig. 4.10 for $H_2D^+H_2$. The 24 lowest-energy wave functions with $\nu_{H_2} = 2$ for $H_2D^+H_2$, increasing from left-to-right and row-by-row and are labeled as (n) according to their energy ordering. The projections onto the State A, State B, and State C adiabats are plotted side-by-side. Wave functions corresponding to peaks in Fig. 4.24 are labeled with their peak label in the bottom right of the corresponding plot.

State	Label	Freq. (cm^{-1})	Orig. (cm^{-1})	Intensity (km/mol)	$\xi_{0,n,A}$
0	–	0	0	0.00	99
1	I_a	379	456	2137.12	95
2	–	658	790	0.00	84
3	I_b	948	1139	145.81	60
4	–	1155	1389	0.00	47
5	I_c	1410	1694	42.78	37
6	–	1470	1767	0.00	71
7	–	1653	1987	0.00	49
8	I_d	1784	2144	21.48	28
9	–	1944	2337	0.00	29
10	I_e	2077	2496	19.93	26
11	–	2187	2629	0.00	25
12	I_f	2255	2711	62.90	62
13	I_g	2339	2811	6.58	31
14	–	2361	2838	0.00	35
15	–	2495	2999	0.00	34
16	–	2528	3038	0.21	18
17	–	2666	3204	0.00	25
18	I_h	2751	3306	1.15	20
19	–	2865	3443	0.00	31
20	I_i	2962	3560	3.13	34
21	–	2994	3599	0.00	38
22	–	3064	3682	0.25	27
23	–	3199	3845	0.00	27

Table 4.14: Frequencies and intensities for the 24 lowest-energy wave functions with $\nu_{H_2} = 0$ for $D_2H^+D_2$, analogous to 4.2. The corresponding wave functions are shown in Fig. 4.29. Table 4.2 for $D_2H^+D_2$.

State	Label	Freq. (cm^{-1})	Orig. (cm^{-1})	Intensity (km/mol)	State A $\xi_{1,n,A}$	State A Percent	State B $\xi_{1,n,B}$	State B Percent
0	II_a	2546	2611	196.19	87	89.10	11	10.90
1	–	2588	2662	0.00	65	66.90	33	33.10
2	–	2927	3069	0.00	40	50.40	49	49.60
3	II_b	2938	3083	21.54	54	65.90	34	34.10
4	–	3220	3421	0.00	37	63.00	35	37.00
5	II_c	3222	3424	2.37	30	50.70	47	49.30
6	–	3467	3718	0.00	29	70.80	25	29.20
7	–	3480	3735	0.00	16	52.30	42	47.70
8	–	3714	4015	0.00	24	60.40	26	39.60
9	–	3731	4036	0.35	19	52.30	32	47.70
10	II_d	3878	4213	1.55	37	70.10	14	29.90
11	–	3903	4242	0.00	20	55.60	28	44.40
12	II_e	4070	4443	3.86	45	81.80	16	18.20
13	–	4093	4470	0.00	18	68.70	28	31.30
14	II_f	4138	4525	1.32	25	54.20	16	45.80
15	–	4143	4531	0.00	29	36.50	29	63.50
16	–	4299	4719	0.00	15	73.50	14	26.50
17	–	4299	4719	0.20	13	63.80	16	36.20
18	–	4433	4879	0.18	18	68.10	11	31.90
19	–	4445	4894	0.00	13	57.90	17	42.10
20	–	4561	5033	0.00	13	65.80	12	34.20
21	–	4571	5046	0.00	11	68.30	13	31.70
22	–	4695	5194	0.01	18	50.50	11	49.50
23	–	4703	5204	0.00	14	57.70	12	42.30

Table 4.15: Frequencies, intensities, and percent contributions from the State A and State B adiabats for the 24 lowest-energy wave functions with $\nu_{H_2} = 1$ for $D_2H^+D_2$, analogous to Table 4.5. The corresponding wave functions are shown in Fig. 4.30.

Table 4.16: Frequencies, intensities, and percent contributions from the State A, State B, and State C adiabats for the 24 lowest-energy wave functions with $\nu_{H_2} = 2$ for $D_2H^+D_2$, analogous to Table 4.6. The corresponding wave functions are shown in Fig. 4.31.

State	Label	Freq. (cm^{-1})	Orig. (cm^{-1})	Intensity (km/mol)	State A		State B		State C	
					$\xi_{2,n,A}$	Percent	$\xi_{2,n,B}$	Percent	$\xi_{2,n,C}$	Percent
0	–	4836	5065	0.00	88	94.60	2	1.70	4	3.60
1	III_a	4841	5070	1.64	84	90.80	6	6.40	3	2.80
2	–	5115	5400	0.00	11	13.80	73	73.70	13	12.50
3	–	5211	5516	0.44	45	74.80	13	13.00	12	12.20
4	–	5220	5526	0.00	44	71.10	4	4.40	24	24.50
5	–	5434	5783	0.61	3	6.00	87	93.20	1	0.80
6	–	5523	5890	0.00	22	65.20	3	3.00	31	31.80
7	III_b	5529	5897	2.85	18	58.90	11	11.20	30	29.90
8	–	5703	6107	0.00	5	7.70	62	80.60	12	11.70
9	III_c	5759	6175	2.48	25	64.20	2	1.90	33	33.90
10	–	5764	6181	0.00	22	59.10	9	11.20	29	29.80
11	–	5968	6426	0.00	9	33.20	30	51.10	14	15.60
12	–	5975	6434	0.00	22	74.00	1	2.00	22	24.00
13	–	5982	6442	0.08	10	39.20	28	51.70	8	9.10
14	–	6182	6682	0.00	13	55.30	14	32.50	10	12.10
15	–	6185	6686	0.33	14	69.30	4	4.70	21	26.00
16	–	6192	6695	0.00	4	18.10	19	57.70	21	24.20
17	–	6317	6845	0.00	37	64.50	3	4.30	21	31.10
18	–	6318	6846	0.19	31	61.60	7	7.80	20	30.60
19	–	6406	6952	0.00	33	85.30	5	5.90	8	8.80
20	–	6410	6956	0.25	24	64.80	16	29.00	6	6.30
21	–	6424	6973	0.02	4	17.40	27	77.10	5	5.50
22	–	6526	7095	0.00	11	41.10	23	35.30	17	23.60
23	–	6538	7110	0.40	24	69.50	2	2.60	17	28.00

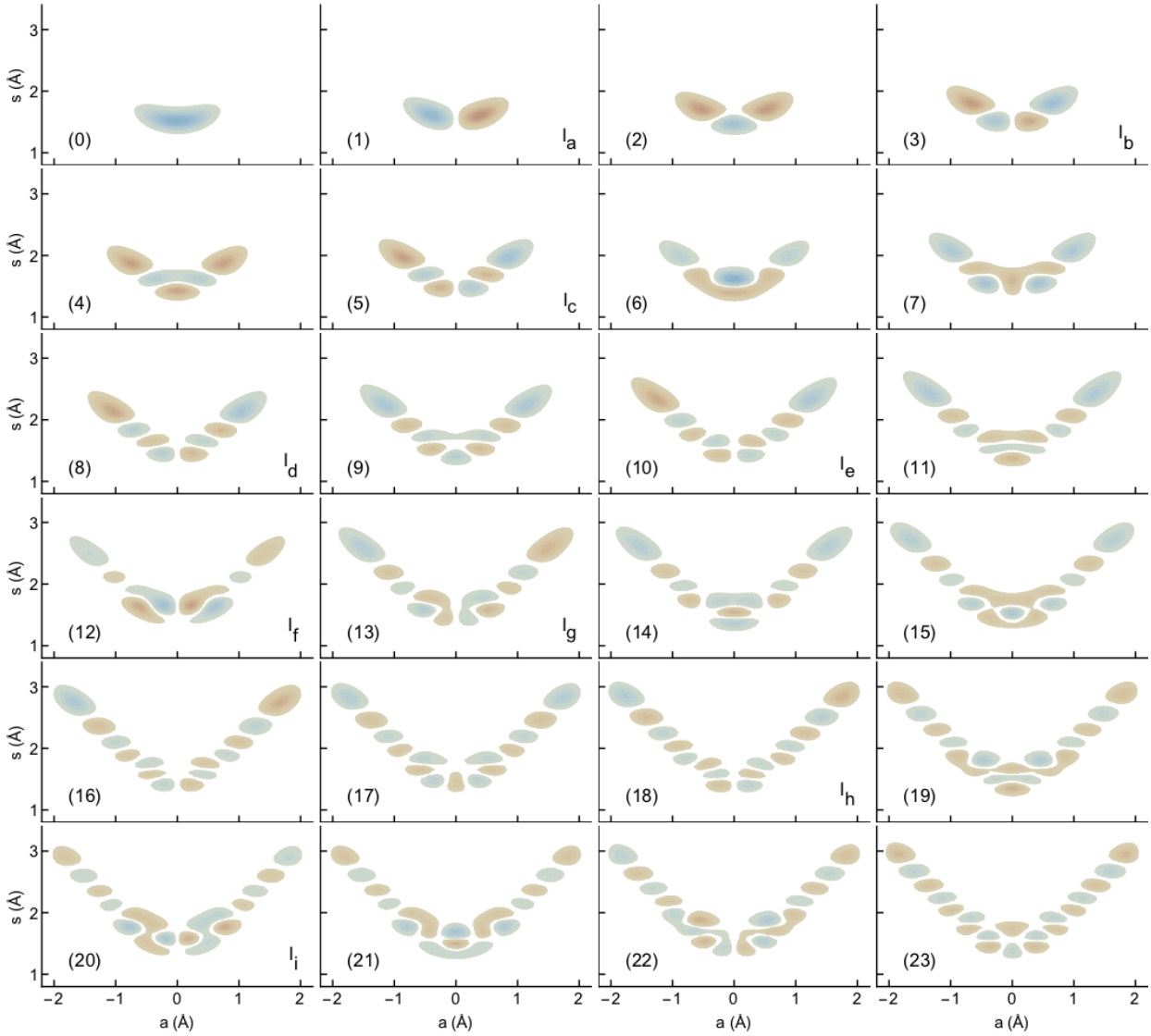

Figure 4.29: The 24 lowest-energy wave functions with $\nu_{H_2} = 0$ for $D_2H^+D_2$, numbered according to increasing energy, analogous to Figure 4.5. Wave functions corresponding to peaks in Fig. 4.25 are labeled with their peak label in the bottom right of the corresponding plot. The energies and intensities for transitions to these states are tabulated in Table 4.14.

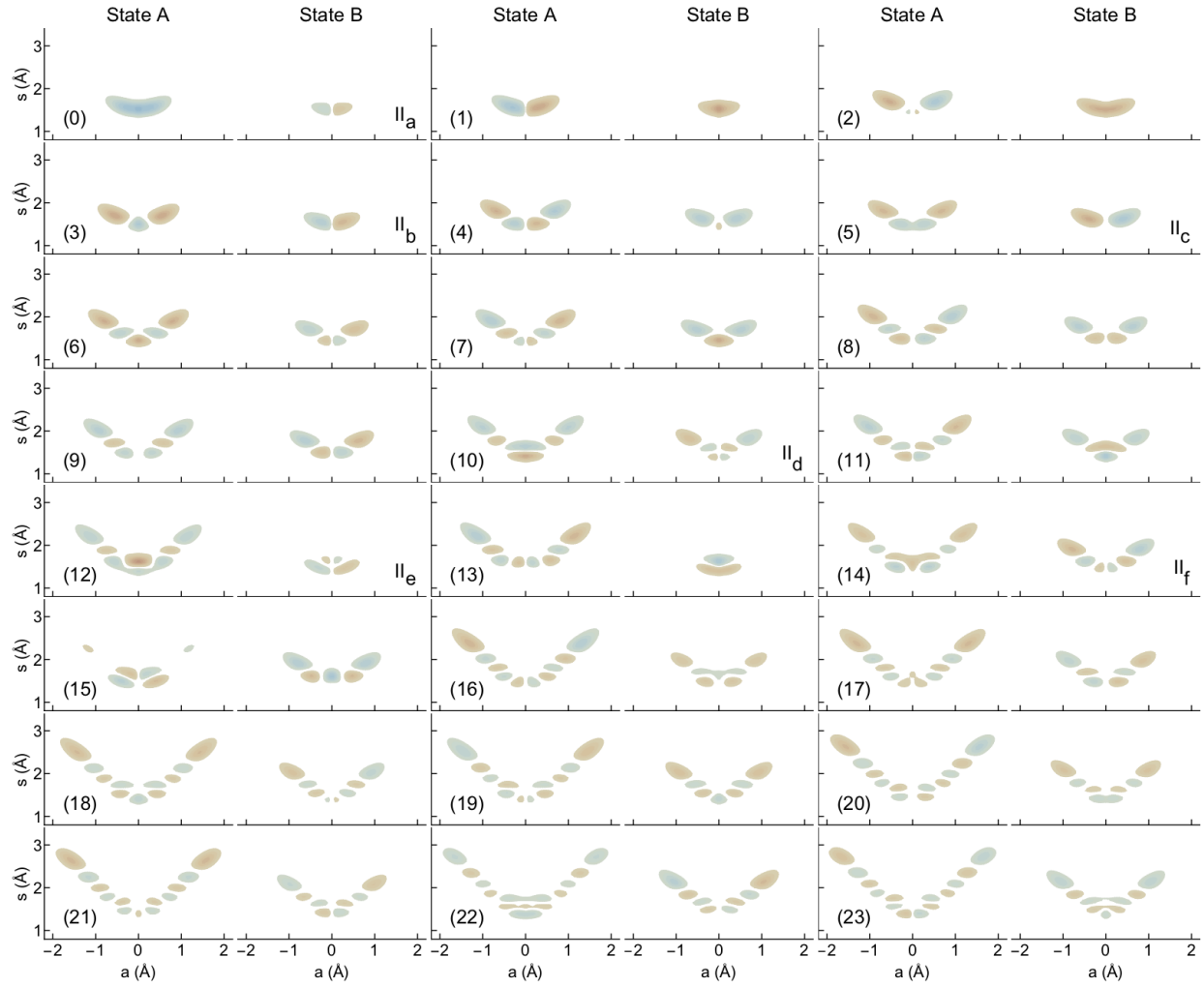

Figure 4.30: The 24 lowest-energy wave functions with $\nu_{H_2} = 1$ for $D_2H^+D_2$, numbered according to increasing energy, analogous to Figure 4.4. The contributions from the State A and State B adiabats are plotted side-by-side. Wave functions corresponding to peaks in Fig. 4.25 are labeled with their peak label in the bottom right of the corresponding plot. The energies and intensities for transitions to these states are tabulated in Table 4.15.

Figure 4.31: The 24 lowest-energy wave functions with $\nu_{H_2} = 2$ for $D_2H^+D_2$, numbered according to increasing energy, analogous to Figure 4.10. The contributions from the State A, State B, and State C adiabats are plotted side-by-side. Wave functions corresponding to peaks in Fig. 4.25 are labeled with their peak label in the bottom right of the corresponding plot. The energies and intensities for transitions to these states are tabulated in Table 4.16.

Chapter 5

A FLEXIBLE APPROACH TO VIBRATIONAL PERTURBATION THEORY USING SPARSE MATRIX METHODS

5.1 Introduction

Vibrational perturbation theory (VPT) provides a powerful approach for making connections between the Schrödinger equation and the vibrational energy levels of a molecule. This approach is an extension of the harmonic treatment of molecular vibrations, where higher order terms in the expansion of the Hamiltonian are treated as perturbations.[2,3,93–96] For a harmonic treatment, a quadratic expansion of the Hamiltonian in displacements of the coordinates from their equilibrium values as well as the momenta that are conjugate to these coordinates provides a good zero-order description of the system of interest based on $3N-6$ harmonic oscillators with frequencies ω_i, and energies given by

$$E_n = \sum_{i=1}^{3N-6} \hbar\omega_i \left(n_i + \frac{1}{2} \right) \tag{5.1}$$

The associated vibrations, the so-called normal modes, are generated from linear combinations of the mass-weighted displacement coordinates, chosen to make the quadratic expansion of the Hamiltonian separable.

One way to move beyond the harmonic treatment of molecular vibrations is to expand the Hamiltonian to higher order in the coordinates and momenta (4th for second order perturbation theory), and use perturbation theory to develop expressions for the anharmonic energies based on this expansion.[2,3] An important difference between vibrational perturbation theory and other forms of perturbation theory is that the expansion of the Hamiltonian in powers of the coordinates and their conjugate momenta provides a natural partitioning

of the corrections as different orders of perturbations, so cubic terms become the first order correction to the Hamiltonian, while quartic terms provide the second order correction. With this expansion, in the absence of near-degeneracies, the energy through second order in the perturbation theory expansion can be expressed as

$$E_n = \sum_{i=1}^{3N-6} \hbar\omega_i \left(n_i + \frac{1}{2}\right) + \sum_{j\geq i} \hbar x_{ij} \left(n_i + \frac{1}{2}\right)\left(n_j + \frac{1}{2}\right) \tag{5.2}$$

The approach, specifically second order vibrational perturbation theory (VPT2), has deep roots in theoretical vibrational spectroscopy, and equations relating the terms in the expansion of the Hamiltonian in normal modes based on the displacements of the Cartesian coordinates of the atom to the terms in the expansion of the energy were worked out by Nielsen in the early 1950's.[3] Subsequently, others have worked out expressions for higher order corrections to the energies,[97] as well as corrections to other properties such as the intensities of transitions to these states.[98–100]

With the ability to write analytic expressions for the evaluation of the vibrational energies from terms in the expansion of the Hamiltonian, the question of whether the reverse process is possible naturally arises. Analysis of the application of perturbation theory to a Morse oscillator shows that the contributions to the energies from the cubic terms in the expansion of the potential are roughly twice as large and opposite in sign compared to the contributions from the quartic terms.[101] Likewise, application of vibrational perturbation theory to two degenerate anharmonic oscillators result in the $x - K$ relationships between the anharmonicites of the isolated oscillators, x_{ll}, and those for the normal modes (x_{ss}, x_{aa} and x_{sa}) as well as the Darling-Dennison coupling constant, K_{ssaa}.[102] Specifically,

$$2\ x_{ss} = 2\ x_{aa} = 0.5\ x_{sa} = K_{ssaa} = x_{ll} \tag{5.3}$$

Such relationships provide important physical insights into the connections between the vibrational constants obtained by fitting the measured transition frequencies and properties of the potential surface.

It would be desirable to be able to obtain a potential from the fit constants. Unfortunately, the problem is under defined even at the harmonic level, where for a $N-$atomic system there can be as many as $(3N-6)(3N-5)/2$ independent force constants, and only $3N-6$ harmonic frequencies. The problem becomes larger as we consider higher order terms in the expansion of the potential. Additionally, in the absence of resonances, the values of the coefficients in Eq. (5.2) obtained using VPT2 are independent of the coordinates in which the Hamiltonian is expanded.[103,104] This is in contrast to other approaches that can be taken to evaluate vibrational spectra, where the coordinates in which the potential is expanded have a substantial effect on the results of the calculation. When the systems become larger and there are accidental degeneracies, such relationships become even more elusive.

While using VPT2 to obtain a path for generating potentials from spectra is not a fully-constrained problem, other insights can be obtained by analyzing the contributions to the x_{ij} coefficients in Eq. (5.2) from the various cubic and quartic terms in the expansion of the potential, or by decomposing the contributions to the transition moment matrix elements $\langle n|\mu|0\rangle$ from terms in the expansion of the potential or dipole function, μ.

There have been a number of implementations of vibrational perturbation theory.[55,96,105,106] In general, these have focused on the final results, e.g. energies, intensities, and other properties, rather than on the ability to obtain insights into the origins of the anharmonicites or intensity. While much of the work has been followed the approach outlined by Nielsen and used a zero-order harmonic basis, several groups have developed implementations of vibrational perturbation theory that are based on the the Hamiltonian and wave functions from vibrational self-consistent field (VSCF) calculations. This approach is directly analogous to the MP2 approach in electronic structure, and have been termed MPVPT2.[107–110] In addition, with the notable exception of the work of Sibert,[96] these implementations of vibrational perturbation theory have focused on normal mode analyses based on linear combinations of displacements of Cartesian coordinates and have utilized the Watson Hamiltonian.[111] While studies by Sibert and co-workers illustrated that the choice of coordinates will not affect the calculated quantities (at least in the absence of resonances)[103] the choice will affect the

decomposition of the wave function and the interpretation of the results.[112] These studies also illustrate that the expansions of the energies and wave functions used in the perturbation theory are not necessarily convergent, even when the Hamiltonian is expanded in bond length-bond angle coordinates and the perturbation theory is taken to high order.[113]

In the present contribution, we describe our recent implementation of vibrational perturbation theory, which is based on the work of Sakurai.[114] The approach is general and the perturbation theory can be performed in any choice of coordinates for which the zero-order Hamiltonian consists of $3N-6$ uncoupled harmonic oscillators. In contrast to many of the currently available implementations of VPT2 that are based on the work of Nielsen, in the implementation described in this work[115] the transformations are performed numerically, which allows for the flexibility both in coordinate choice and the order to which the perturbation theory is taken. One goal of taking such an approach is that it will allow us to decompose the calculated quantities, specifically the transition energies and intensities, and ask how this is affected by the coordinate choice. These questions will be addressed through calculations of the vibrational energies of water, water dimer, and peroxynitrous acid (HOONO) as well as several model systems.

5.2 Theory

In this work, we have implemented Rayleigh-Schrödinger perturbation theory in a way that is easily extended to arbitrary order. This approach is a generalization of the presentations of Sakurai[114] and Kato,[116] to allow for additional flexibility in the form of the Hamiltonian. Specifically, they considered the case when the perturbation is assumed to have a single contribution, which is introduced at first order, e.g $H = H^{(0)} + \lambda W$ whereas we consider the case where the Hamiltonian is expanded to arbitrary order as

$$H = \lambda^0 H^{(0)} + \lambda^1 H^{(1)} + \lambda^2 H^{(2)} + ... \tag{5.4}$$

where the corrections to the Hamiltonian are partitioned based on an expansion in the normal coordinates and their conjugate momenta. When expressed in dimensionless coordinates, all of the contributions to the kth order correction to the Hamiltonian are of order $\hbar^{(k+2)/2}$. The ability to partition perturbation into an expansion in $\hbar$ is a key feature of the standard presentation of vibrational perturbation theory as discussed by Nielsen.[2,3] In the absence of degeneracies or near-degeneracies, this form of the expansion ensures that the resulting energies, intensities and other observables will be independent of coordinate choice.

The work of Nielsen, and much work that has since followed, has involved using perturbation theory to develop analytic expressions for properties of interest. The evaluation of such expressions is computationally efficient, but can be prone to errors in implementation and extension to higher-order is not straightforward. Additionally, the expressions used to evaluate the corrections to the wave function, and from that the energies and other properties, depend on underlying choice of coordinates. Typically, vibrational perturbation theory is applied to an expansion of the Hamiltonian in normal modes that are constructed from linear combinations of the mass-weighted displacements of the Cartesian coordinates, but that does not need to be the case. In contrast, by merging the expansion of the Hamiltonian in

orders of $\hbar$ with the formalism laid out by Sakurai, it is possible to obtain a computationally efficient route to high-order corrections to the energies and wave functions for vibrational problems that is insensitive to the coordinates used to expand the Hamiltonian.

As usual, we start by expanding the wave functions, and energies using an indexing parameter λ

$$|n\rangle = \lambda^0 |n^{(0)}\rangle + \lambda^1 |n^{(1)}\rangle + \lambda^2 |n^{(2)}\rangle + ... \tag{5.5}$$

$$E_n = \lambda^0 E_n^{(0)} + \lambda^1 E_n^{(1)} + \lambda^2 E_n^{(2)} + ... \tag{5.6}$$

Based on the above partitioning of the corrections, all of the $H^{(i)}$ are Hermitian. Additionally, we will take the overlaps among the corrections to the state $|n^{(0)}\rangle$ to be real. Combining Eqs. (5.4)–(5.6), the time-independent Schrödinger equation becomes

$$\begin{aligned}(\lambda^0 H^{(0)} + \lambda^1 H^{(1)} + \lambda^2 H^{(2)} + ...)(\lambda^0 |n^{(0)}\rangle + \lambda^1 |n^{(1)}\rangle + \lambda^2 |n^{(2)}\rangle + ...) \\ = (\lambda^0 E_n^{(0)} + \lambda^1 E_n^{(1)} + \lambda^2 E_n^{(2)} + ...)(\lambda^0 |n^{(0)}\rangle + \lambda^1 |n^{(1)}\rangle + \lambda^2 |n^{(2)}\rangle + ...)\end{aligned} \tag{5.7}$$

Since this needs to be valid when Eq. (5.7) is truncated at any order in λ, we obtain a series of equations

$$\begin{aligned} H^{(0)} |n^{(0)}\rangle &= E_n^{(0)} |n^{(0)}\rangle \\ H^{(1)} |n^{(0)}\rangle + H^{(0)} |n^{(1)}\rangle &= E_n^{(1)} |n^{(0)}\rangle + E_n^{(0)} |n^{(1)}\rangle \\ &\vdots \end{aligned}$$

Rewriting these in more compact notation, for any given order k

$$0 = \sum_{i=0}^{k} \Delta H_n^{(i)} |n^{(k-i)}\rangle \tag{5.8}$$

where

$$\Delta H_n^{(i)} = H^{(i)} - E_n^{(i)}. \tag{5.9}$$

The discussion that follows focuses on the implementation of perturbation theory in the absence of degeneracies or near degeneracies. While the extension to treat systems with degenerate or nearly-degenerate states is straightforward, the identification of the nearly-degenerate states is less so. In the present study, we rely on analyses of the systems that are investigated to identify resonances. In a follow-up study, we will more deeply explore the issue of identifying resonance interactions.

5.2.1 Non-Degenerate Perturbation Theory

The goal in perturbation theory is to obtain the corrections to the wave functions and energies in Eq. (5.8) for a given zero-order state $|n^{(0)}\rangle$ in the basis of zero-order states, $\{|m^{(0)}\rangle\}$, that are eigenstates of $H^{(0)}$. Following Sakurai, this is accomplished by splitting the total state space into a subspace where the diagonal matrix $\Delta H_n^{(0)}$ is invertible and a subspace where it is not. In the absence of degeneracies, the non-invertible part of the total state space, i.e. the part of the space that leads to singularities, contains only the zero-order contribution to the state of interest, $|n^{(0)}\rangle$. When degeneracies are considered, the non-invertable subspace is extended to include all states that are degenerate or nearly degenerate with the state of interest, and the approach described below is used to develop a representation of the Hamiltonian.

To start, we multiply Eq. (5.8) on the left by $\langle n^{(0)}|$ and rearrange the results to obtain an expression for the kth order correction to the energy

$$E_n^{(k)} = \langle n^{(0)}| H^{(k)} |n^{(0)}\rangle + \sum_{i=1}^{k} \langle n^{(0)}| \Delta H_n^{(k-i)} |n^{(i)}\rangle \tag{5.10}$$

Since $\langle n^{(0)}|$ is an eigenstate of $\mathrm{H}^{(0)}$, $\langle n^{(0)}| \Delta H_n^{(0)} |n^{(k)}\rangle = 0$. This leads to the important result

that $E_n^{(k)}$ does not depend on $|n^{(k)}\rangle$, and Eq. (5.10) reduces to

$$E_n^{(k)} = \langle n^{(0)}| H^{(k)} |n^{(0)}\rangle + \sum_{i=1}^{k-1} \langle n^{(0)}| \Delta H_n^{(k-i)} |n^{(i)}\rangle \tag{5.11}$$

which can be evaluated using the previously determined corrections to $|n\rangle$ up to order $k-1$.

To obtain $|n^{(k)}\rangle$ we rearrange Eq. (5.8) as

$$-\Delta H_n^{(0)} |n^{(k)}\rangle = \sum_{i=0}^{k-1} \Delta H_n^{(k-i)} |n^{(i)}\rangle \tag{5.12}$$

Since we showed $E_n^{(k)}$ does not depend on $|n^{(k)}\rangle$, the entirety of the right-hand side of Eq. (5.12) can be evaluated based on lower-order corrections to the energy and wave function for the nth state. If $\Delta H_n^{(0)}$ were invertable, $|n^{(k)}\rangle$ could be evaluated by multiplying both sides of Eq. (5.12) by $-(\Delta H_n^{(0)})^{-1}$. While $\Delta H_n^{(0)}$ is diagonal, since $\Delta H_n^{(0)} |n^{(0)}\rangle = 0$, $\Delta H_n^{(0)}$ is not invertible.

Following Sakurai,[114] we circumvent this problem by dividing the state space into two parts. This is achieved by introducing a pair of projection operators. The first is

$$P_S = |n^{(0)}\rangle \langle n^{(0)}| \tag{5.13}$$

This operator allows us to project onto the the portion of the state space that causes $\Delta H_n^{(0)}$ to be singular. The second projection operator

$$P_O = I - P_S = \sum_{m \neq n} |m^{(0)}\rangle \langle m^{(0)}| \tag{5.14}$$

allows us to project out the singular portion of state space. Next we introduce what Sakurai calls the *perturbation operator*

$$\Pi_O = P_O(-\Delta H_n^{(0)})^{-1} P_O \tag{5.15}$$

By projecting out the portion of state space that causes $\Delta H_n^{(0)}$ to be singular, Π_O is well-defined. In fact, because the matrix representation of $\Delta H_n^{(0)}$, and by extension Π_O, is diagonal, evaluation of Π_O is straightforward for an arbitrarily large state space. Multiplying Eq. (5.12) on the left by Π_O, and taking advantage of $\Pi_O(-\Delta H_n^{(0)}) = P_O$ yields

$$P_O \left|n^{(k)}\right\rangle = \Pi_O \sum_{i=0}^{k-1} \Delta H_n^{(k-i)} \left|n^{(i)}\right\rangle \tag{5.16}$$

Eq. (5.16) provides a straightforward way to evaluate the contributions to kth order correction to $|n\rangle$ from states in the O subspace based on knowledge of $|n^{(i)}\rangle$ with $i < k$.

To obtain the contribution to $|n\rangle$ from $|n^{(0)}\rangle$ we need an additional constraint on the wave function that will allow us to evaluate $\langle n^{(0)}|n^{(k)}\rangle$. Specifically, we introduce the requirement that through order k,

$$\langle n|n\rangle = \sum_{l=0}^{k} \sum_{i=0}^{l} \lambda^l \langle n^{(i)}|n^{(l-i)}\rangle = 1 \tag{5.17}$$

This normalization is important since we are also interested in properties like intensities. As $\langle n^{(0)}|n^{(0)}\rangle = 1$, this means for any $k > 0$,

$$\sum_{i=0}^{k} \langle n^{(i)}|n^{(k-i)}\rangle = 0 \tag{5.18}$$

which can be reexpressed as

$$\langle n^{(0)}|n^{(k)}\rangle = -\frac{1}{2} \sum_{i=1}^{k-1} \langle n^{(i)}|n^{(k-i)}\rangle \tag{5.19}$$

Taken together this provides all the information needed to evaluate $|n\rangle$ to an arbitrary order in perturbation theory.

To summarize, to implement perturbation theory to arbitrary order, we solve a set of iterative equations that can return corrections to the energies and wave functions of a given

zero-order state in the absence of degeneracies

$$E_n^{(k)} = \langle n^{(0)}| H^{(k)} |n^{(0)}\rangle + \sum_{i=1}^{k-1} \langle n^{(0)}| \Delta H_n^{(k-i)} |n^{(i)}\rangle \tag{5.20}$$

$$|n^{(k)}\rangle = \Pi_O \sum_{i=0}^{k-1} \Delta H_n^{(k-i)} |n^{(i)}\rangle - \frac{1}{2} \sum_{i=1}^{k-1} \langle n^{(i)}|n^{(k-i)}\rangle |n^{(0)}\rangle \tag{5.21}$$

To apply these expressions at order k, it is necessary to have obtained corrections to the energies and wave functions through order $k-1$. This differs from the so-called $2n+1$ expressions that appear elsewhere in the perturbation theory literature.[117] Such expressions allow one to obtain corrections to the energies at order $2k+1$ with corrections to the wave functions only up to order k. These have generally been derived considering only a single perturbation to the Hamiltonian, but, following the procedure of Löwdin,[117] similar expressions may be derived for the case of multiple perturbations as treated in this work. While the use of such expressions would lead to savings in the evaluation of the energy, the full expansion of the wave function is still needed to obtain matrix elements of other operators, specifically the dipole moment operator considered in the following discussion.

To obtain other properties of interest, the associated operator, A, is expanded in the normal mode coordinates and conjugate momenta to the desired order, and through order k

$$\langle n| A |m\rangle = \sum_{l=0}^{k} \langle n| A |m\rangle^{(l)} = \sum_{l=0}^{k} \left[\sum_{i=0}^{l} \sum_{j=0}^{l-i} \langle n^{(j)}| A^{(i)} |m^{(l-i-j)}\rangle \right] \tag{5.22}$$

In the present study, we will focus on the intensities, which require expansions of the dipole moment operator, for which we include the constant and linear terms in the expansion of μ in $\mu^{(0)}$, the quadratic terms are in $\mu^{(1)}$ and so forth.

Before concluding this section, we should note that although the equations above assume an expansion of the Hamiltonian or the operator A to kth order if the perturbative expansion of the energy or matrix element of A is desired one can perform the perturbation theory on a truncated expansion of either of these operators. Doing this requires a careful choice of

expansion coordinates in which the higher-order terms in the expansion are small enough to be declared negligible, and can be set to zero. This choice of coordinates is important, however, and as will be explored more in the Results and Discussion.

5.2.2 Degenerate Perturbation Theory

One of the strengths of this approach is the simplicity of the extension to cases where there are degeneracies or near degeneracies. In this case two small adjustments are needed. First, P_S in Eq. (5.13) is replaced by

$$P_S = \sum_{n'} |n'\rangle\, 0\, \langle n'|\, 0 \tag{5.23}$$

where the sum is over $|n^{(0)}\rangle$ as well as all of the states that are nearly degenerate to $|n\rangle$. Additionally, rather than providing energies for each state, the perturbation theory will generate a matrix representation of the Hamiltonian in the space of nearly degenerate states. Obtaining the final energies and wave functions requires the evaluation of the eigenvalues and eigenvectors of this Hamiltonian matrix. Since we are only considering couplings among nearly degenerate states, the dimensionality of the Hamiltonian is much smaller than the basis in which the perturbed wave function is expanded. This has been referred to as a deperturb-and-diagonalize approach.[97]

5.2.3 Hamiltonian Choice and Implementation

The approach for implementing vibrational perturbation theory detailed above, is entirely general, and only requires an expansion of the Hamiltonian through the desired order. The coordinates that are used for the expansion are flexible, although it has been assumed that $H^{(0)}$ consists of a set of uncoupled harmonic oscillators. This allows for the exploration of the effects of coordinate choice both on the calculated properties and on the convergence of the expansions of these properties.

The expansion of the Hamiltonian in the normal modes that are constructed from linear

combinations of the displacements of the mass-weighted Cartesian coordinates have been described in detail by others.[3,118] This Hamiltonian can be reexpressed in terms of normal modes that are linear combinations of the displacements of internal coordinates. Doing this introduces coordinate-dependent mass terms, the so-called Wilson G-matrix elements,[1] as well as a coordinate-dependent pseudopotential, V', which comes from transforming the molecular kinetic energy into internal coordinates.[119] In this work, V' is evaluated using[120,121]

$$V'(q) = \frac{\hbar^2}{8g} \sum_{ij}^{3N-6} G_{ij} \frac{\partial^2 g}{\partial q_i \partial q_j} + \frac{\partial G_{ij}}{\partial q_i} \frac{\partial g}{\partial q_j} - \frac{3}{4g} \frac{\partial g}{\partial Q_i} \frac{\partial g}{\partial Q_j} \tag{5.24}$$

where $g = |I_0|/|G|$ and I_0 is the moment of inertia tensor evaluated at the equilibrium geometry. Because this term is proportional to $\hbar^2$ its constant contribution is included in $H^{(2)}$. Linear terms in the expansion of V' are included in $H^{(3)}$ and so forth. With this in mind, this normal mode Hamiltonian is expanded about a minimum in the potential as

$$H^{(0)} = \frac{1}{2} \sum_{i=1}^{3N-6} \left(p_i G^{eq}_{i,i} p_i + \frac{\partial V^2}{\partial q_i^2} q_i^2 \right) \tag{5.25}$$

$$H^{(1)} = \sum_{n,i,j=1}^{3N-6} \left(\frac{1}{2} p_i \frac{\partial G_{i,j}}{\partial q_n} q_n p_j + \frac{1}{6} \frac{\partial V^3}{\partial q_n \partial q_i \partial q_j} q_n q_i q_j \right) \tag{5.26}$$

$$H^{(2)} = \sum_{n,m,i,j=1}^{3N-6} \left(\frac{1}{4} p_i \frac{\partial G_{i,j}}{\partial q_n \partial q_m} q_n q_m p_j + \frac{1}{24} \frac{\partial V^4}{\partial q_n \partial q_m \partial q_i \partial q_j} q_n q_m q_i q_j \right) + V'(q=0) \tag{5.27}$$

Constructing the Hamiltonian as an expansion in the normal coordinates has benefits beyond the coordinate independence of the calculated properties, noted above. By defining $H^{(0)}$ to consist of uncoupled harmonic oscillators, so $|n^{(0)}\rangle$ represents a harmonic basis, the q_i or p_i operators can only couple zero-order states that differ by one quantum in mode i. Similarly, q_i^2 can only couple states which differ by zero or two quanta in mode i. There are a few direct benefits from this. Focusing on VPT2, $H^{(2)}$ only contributes to $E_n^{(2)}$ through $\langle n^{(0)}| H^{(2)} |n^{(0)}\rangle$. Therefore, the only potential derivatives that contribute are $\partial^4 V/\partial q_i^4$ and $\partial^4 V/\partial q_i^2 \partial q_j^2$. This observation has been exploited in many implementations of VPT2 as the

evaluation of fourth derivatives involving four different coordinates are much more expensive to obtain than those involving one or two.[106,122,123] Further, once the potential has been expanded in one set of normal mode coordinates, it is straightforward to perform the multi-linear transformations needed to obtain the expansion of the potential in an arbitrary choice of normal mode coordinates. A second benefit of this form for the expansion of the Hamiltonian is that $E_n^{(i)}$ is zero when i is odd, and so corrections to the energy only come in at even orders of the perturbation theory expansion.

If one is mostly interested in computing properties, particularly transition moment matrix elements, $\langle m| \mu |n\rangle$, there is a related computational benefit. If vibrational perturbation theory is performed up to order k, then the only terms in the evaluation of $\langle m| \mu |n\rangle$ involving $\langle m^{(k)}|$ or $|n^{(k)}\rangle$ are $\langle m^{(k)}| \mu^{(0)} |n^{(0)}\rangle$ and $\langle m^{(0)}| \mu^{(0)} |n^{(k)}\rangle$. The numbers of elements in the expansions $\langle m^{(k)}|$ and $|n^{(k)}\rangle$ grow factorially with system dimension, while those required to evaluate $\mu^{(0)} |n^{(0)}\rangle$ and $\langle m^{(0)}| \mu^{(0)}$ are in general significantly smaller. As a concrete example, for VPT2 $|n^{(2)}\rangle$ has contributions from $H^{(1)}\Pi_O H^{(1)} |n^{(0)}\rangle$. These terms can change the number of quanta of excitation in a state by up to six. By contrast to the number of terms in the expansion of $|n^{(2)}\rangle$, $\langle m^{(0)}| \mu^{(0)}$ contains at most $2 \times (3N-6)$ terms.

Finally, the representation matrices for $H^{(1)}$ and $H^{(2)}$ that are generated are very sparse. This is in part due to the state-by-state nature of Rayleigh-Schrödinger perturbation theory and in part due to the sources of sparsity describe above. There are modern sparse-linear algebra libraries that are efficient and easy to use, for instance the one distributed in the SciPy package for the python programming language.[124] By leveraging these, the approach described in this work is straightforward to implement. Moreover, the construction of these representation matrices, which makes up the bulk of the computational effort, is trivially parallelizable.

The above considerations have been exploited in our Python implementation of nth order perturbation theory, PyVibPTn.[115] This implementation allows for arbitrary-order perturbation theory using Eq. (5.20) and Eq. (5.21) with flexibile coordinate choice using the expansion of the internal coordinate Hamiltonian described above. For the molecular ap-

plications described in the following section the potential derivatives were obtained from electronic structure calculations at the MP2/aug-cc-pVTZ level of theory/basis, performed using Gaussian 16.[122] The energies for the two-dimensional harmonically coupled anharmonic oscillator system, described below, were also evaluated using a two-dimensional discrete variable representation using 100 grid points spanning from 0 Å to 2.65 Å in each dimension.[11]

5.3 Results and Discussion

As mentioned above, our implementation of vibrational perturbation theory (VPT) provides flexibility with respect to the choice of coordinates used in expanding the Hamiltonian as well as the order to which the perturbation theory is taken. This flexibility allows us to not only look at how these choices affect the energies and intensities coming from the perturbation theory, but also consider the corrections to the energies, wave functions, and intensities. Looking at these corrections it is possible to better understand the physical origins of spectral features, such as whether a transition has intrinsic intensity or whether it is borrowing intensity from a nearby intense transition.

5.3.1 The Morse Oscillator

The natural system for exploring anharmonic effects is the Morse oscillator, which is defined by the Hamiltonian

$$H = \frac{p_r^2}{2\mu} + D_e(1 - e^{-\alpha\Delta r})^2 \tag{5.28}$$

where μ is the reduced mass of the oscillator, D_e is its dissociation energy, Δr is the displacement of the bond length from its equilibrium value, and α determines the breadth of the well. Morse showed in 1929[125] that when we assume that Δr is defined from $-\infty$ to ∞, the corresponding energies are quadratic in $\left(n + \frac{1}{2}\right)$ where

$$E_n/\hbar = \omega\left(n + \frac{1}{2}\right) - \omega x\left(n + \frac{1}{2}\right)^2 \tag{5.29}$$

Here ω is the harmonic frequency and ωx is the anharmonicity constant. Later work has shown that when the Hamiltonian is expressed as a quartic expansion in Δr, second-order perturbation theory provides exact expressions for the energies as well. Higher order perturbation theory, based on higher order expansions of the Morse oscillator Hamiltonian also recover Eq. (5.29).

In the above expression, all of the anharmonicity is included in the potential, which is approximated by an expansion in Δr. Alternatively, the Morse oscillator Hamiltonian can also be expressed in Morse coordinates,[57] $y = (1 - e^{-\alpha \Delta r})/\alpha$, as

$$H = \frac{p_y (1 - \alpha y)^2 p_y}{2\mu} + \frac{1}{2} \left(2 D_e \alpha^2 \right) y^2 - \frac{\hbar^2 \alpha^2}{8\mu} \tag{5.30}$$

In introducing this change of variables, the potential becomes harmonic and the anharmonicities are now in the kinetic term. Additionally, the Hamiltonian is a quartic expansion in y and p_y, and as such the Hamiltonian is exact when the expansion in λ is truncated at second order. Further details about the Morse oscillator Hamiltonian are provided in Section 5.3.3.

The results of applying perturbation theory to these two expansions of the Hamiltonian up to fourth order are shown in Fig. 5.1. Following Sibert,[96] the parameters in the Morse oscillator Hamiltonian have been chosen to model an OH stretch in water with $\omega = 3869.47$ cm^{-1} and $\omega x = -84.11$ cm^{-1}. For the results marked GS, we use colors to indicate the corrections to the energy from specified terms in the expansion of the ground state, $|0\rangle$, the form of which is given by

$$\Delta E_0^{(k)} = \sum_{l=1}^{k} E_0^{(l)} = \sum_{l=1}^{k} \sum_{i=0}^{l} \mathcal{E}_0^{(i,l-i)} \tag{5.31}$$

where

$$\mathcal{E}_0^{(i,l-i)} = \langle 0^{(0)} | \, H^{(i)} \, | 0^{(l-i)} \rangle \tag{5.32}$$

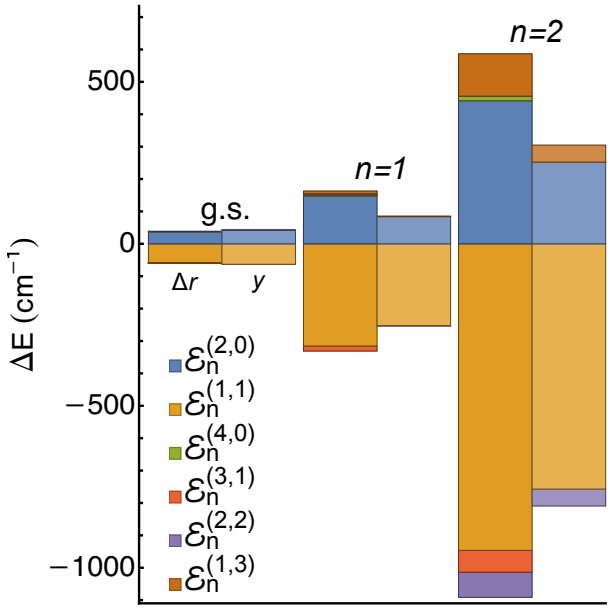

Figure 5.1: Contributions to the zero-point energy (g.s.) and the energies of states with one and two quanta of excitation ($n = 1$ and 2), $\mathcal{E}_n^{(i,j)}$ defined in Eq. (5.32) and Eq. (5.34), based on the one-dimensional Morse oscillator with $\omega = 3869.47$ cm^{-1} and $\omega x = -84.11$ cm^{-1}, when the Hamiltonian is expanded through sixth order in Δr and the Morse coordinate, y. The values of the plotted quantities are provided in Table 5.1.

For the vibrationally excited levels, $n = 1$ or 2,

$$\Delta E_n^{(k)} = \sum_{l=1}^{k} E_n^{(l)} - E_0^{(l)} = \sum_{l=1}^{k} \sum_{i=0}^{l} \mathcal{E}_n^{(i,l-i)} \tag{5.33}$$

where

$$\mathcal{E}_n^{(i,l-i)} = \langle n^{(0)} | \, H^{(i)} \, | n^{(l-i)} \rangle - \mathcal{E}_0^{(i,l-i)} \tag{5.34}$$

At any order of truncation, the value of $\Delta E_n^{(k)}$ will be independent of the choice of coordinates used to expand the Hamiltonian, although the sizes of the individual $\mathcal{E}_n^{(i,l-i)}$ corrections will depend on this choice. Additionally, since the corrections to the energies are only non-zero for even values of l, results are provided for second and fourth order in perturbation theory

Table 5.1: Contributions (in cm^{-1}) to the zero-point energy (g.s.) and the energies of states with up to four quanta of excitation, $\mathcal{E}_n^{(i,j)}$ defined in Eq. (5.32) and Eq. (5.34), based on the one-dimensional Morse oscillator with $\omega = 3869.47$ cm^{-1} and $\omega x = -84.11$ cm^{-1}, when the Hamiltonian is expanded through sixth order in Δr and the Morse coordinate, y.

				Δr			
State	$\mathcal{E}_n^{(2,0)}$	$\mathcal{E}_n^{(1,1)}$	$\mathcal{E}_n^{(4,0)}$	$\mathcal{E}_n^{(3,1)}$	$\mathcal{E}_n^{(2,2)}$	$\mathcal{E}_n^{(1,3)}$	Sum
g.s.	21.8750	−34.3750	0.2307	−0.7255	0.5418	−0.0470	−12.5001
$n = 1$	87.4999	−187.4999	1.3839	−6.1388	1.3923	3.3617	−100.0009
$n = 2$	262.4996	−562.4997	5.5357	−26.3411	−30.3293	51.1309	−300.0038
$n = 3$	524.9992	−1124.9995	14.3006	−69.9824	−230.7077	286.3796	−600.0102
$n = 4$	874.9987	−1874.9991	29.5238	−146.4385	−905.4871	1022.3809	−1000.0212
				y			
State	$\mathcal{E}_n^{(2,0)}$	$\mathcal{E}_n^{(1,1)}$	$\mathcal{E}_n^{(4,0)}$	$\mathcal{E}_n^{(3,1)}$	$\mathcal{E}_n^{(2,2)}$	$\mathcal{E}_n^{(1,3)}$	Sum
g.s.	25.0000	−37.5000	0.0000	0.0000	0.2455	−0.2455	−12.5000
$n = 1$	50.0001	−150.0001	0.0000	0.0000	−0.5804	0.5804	−100.0000
$n = 2$	150.0002	−450.0002	0.0000	0.0000	−20.4464	20.4465	−300.0000
$n = 3$	300.0003	−900.0003	0.0000	0.0000	−126.0268	126.0269	−599.9999
$n = 4$	500.0005	−1500.0006	0.0000	0.0000	−464.1073	464.1075	−999.9999

as all of the contributions to the first and third order corrections to the energies are zero. The second order corrections, $\mathcal{E}_n^{(2,0)}$ and $\mathcal{E}_n^{(1,1)}$, are indicated by the blue and orange bars, respectively, in Fig. 5.1. For the Δr expansion, as noted above, $\mathcal{E}_n^{(1,1)}$ is approximately twice as large as $\mathcal{E}_n^{(2,0)}$ and opposite in sign. Interestingly, when the Hamiltonian is expanded in y and p_y, this ratio is exactly -3:1. These two relations are derived in Section 5.3.3. While both sets of results reflect significant cancellations among the the $\mathcal{E}_n^{(i,j)}$ corrections, the magnitude of the individual corrections are smaller when the Hamiltonian is expanded in y than when the expansion is in Δr. If we are interested in interpreting the origins of anharmonicity, we need to be aware that the interpretation depends on the coordinate choice. While the sum of the blue and orange bars are the same for both expansions, the differences in the sizes of the contributions from $H^{(1)}$ and $H^{(2)}$ is reflected in the coefficients in the expansion of the wave function.

Moving on to the corrections coming in at 4th order, $\mathcal{E}_n^{(4,0)}$, $\mathcal{E}_n^{(3,1)}$, $\mathcal{E}_n^{(2,2)}$, and $\mathcal{E}_n^{(1,3)}$, we see that the sum of these terms is zero, meaning the final energies from VPT4 are the same as those obtained at second order. The most notable difference between the expansions of these corrections in these two coordinate systems is that the Δr expansion has corrections from $H^{(3)}$ and $H^{(4)}$, whereas these terms are zero when the Hamiltonian is expanded in y and p_y. Additionally, the $\mathcal{E}_n^{(4,0)}$ and $\mathcal{E}_n^{(3,1)}$ terms do not cancel and the sum of these terms becomes non-neglible by third excited state. This serves as a reminder that truncation of the expansion of the Hamiltonian will introduce errors if perturbation theory is to be taken to higher order. This issue does not arise for the y coordinates, where $H^{(3)}$ and above are rigorously zero. This, in turn, serves as a reminder that, if one wishes to perform perturbation theory on a truncated expansion of the Hamiltonian, care needs to be taken in the choice of coordinates used to expand the Hamiltonian.

5.3.2 Applying Perturbation Theory to the Morse Oscillator Expanded in Bond Displacements

We start with Hamiltonian for a 1-d oscillator

$$H = \frac{p_r^2}{2\mu} + D\alpha^2(1 - \exp(-\alpha\Delta r))^2 \tag{5.35}$$

where Δr represents a bond displacement and expand the Hamiltonian to fourth order in Δr

$$H = \frac{p_r^2}{2\mu} + \frac{2D\alpha^2}{2}\Delta r^2 - D\alpha^3\Delta r^3 + \frac{7D\alpha^4}{12}\Delta r^4 \tag{5.36}$$

and perform a change of variables to dimensionless coordinates

$$q = \sqrt{\frac{\mu\omega}{\hbar}}\ \Delta r \quad \text{and} \quad p_q = \sqrt{\hbar\mu\omega}\ p_r \tag{5.37}$$

where

$$\omega = \sqrt{\frac{2D\alpha^2}{\mu}} \tag{5.38}$$

Making this substitution and taking advantage of the definition of the anharmonicity,

$$\hbar\omega x = \frac{\hbar^2\omega^2}{4D} = \frac{\hbar^2\alpha^2}{2\mu} \tag{5.39}$$

Making this substitution,

$$H = \frac{\hbar\omega}{2}\left(p_q^2 + q^2\right) - \sqrt{\frac{(\hbar\omega)(\hbar\omega x)}{2}} + \frac{7\hbar\omega x}{12}q^4 \tag{5.40}$$

where the contribution to the energy from $H^{(0)}$ is

$$E_n^{(0)} = \hbar\omega\left(n + \frac{1}{2}\right) \tag{5.41}$$

at second order, the contribution from $H^{(1)}$ is

$$E^{(2,1)} = \sum_m \frac{\left\langle m\left|H^{(1)}\right|n\right\rangle^2}{\hbar\omega(n-m)} = -\frac{\hbar\omega x}{8}\left(15n^2 + 15n + \frac{11}{2}\right) \tag{5.42}$$

while the contribution from $H^{(2)}$ is

$$E^{(2,2)} = \left\langle n\left|H^{(2)}\right|n\right\rangle = \frac{7\hbar\omega x}{8}\left(n^2 + n + \frac{1}{2}\right) \tag{5.43}$$

making the total contribution at 2nd order

$$E_n^{(2)} = -\hbar\omega x\left(n + 1/2\right)^2 \tag{5.44}$$

with $E^{(2,1)} \approx -2E^{(2,2)}$.

5.3.3 Applying Perturbation Theory to the Morse Oscillator in Morse Coordinates

We start with the Hamiltonian in Eq. (5.35), and perform a change of variables from Δr to

$$
\begin{aligned}
y &= \frac{1}{\alpha}\left(1-\exp(-\alpha\Delta r)\right) && (5.45)\\
\Delta r &= -\frac{1}{\alpha}\ln(1-\alpha y) && (5.46)\\
p_r &= (1-\alpha y)p_y && (5.47)
\end{aligned}
$$

and the Jacobian

$$dr = \frac{dr}{dy}dy = (1-\alpha y)^{-1}dy \tag{5.48}$$

Next, we adjust the Schrodinger equation to incorporate the Jacobian into the definition of the wave function to

$$\Psi'(y) = \sqrt{1-\alpha y}\ \Psi(y) \tag{5.49}$$

With this substitution, the Hamiltonian becomes

$$H' = \frac{1}{2\mu}p_y(1-\alpha y)^2 p_y - \frac{\hbar^2\alpha^2}{8\mu} + \frac{2D\alpha^2}{2}y^2 \tag{5.50}$$

Finally we reexpress H' in dimensionless coordinates and momenta,

$$q = \sqrt{\frac{\mu\omega}{\hbar}}\ y \quad \text{and} p_q = \sqrt{\hbar\mu\omega}\ p_y \tag{5.51}$$

Using Eq. Eq. (5.39), and making similar substitutions as before, we can reexpress the Hamiltonian as

$$H' = \frac{\hbar\omega}{2}\left(p_q^2+q^2\right) - \sqrt{2\hbar\omega\hbar\omega x}\ p_q q p_q + \left(\hbar\omega x p_q q^2 p_q - \frac{\hbar\omega x}{4}\right) \tag{5.52}$$

Once again, the contribution from $H^{(0)}$ to the energy is

$$E_n^{(0)} = \hbar\omega\left(n + \frac{1}{2}\right) \tag{5.53}$$

at second order, the contribution from $H^{(1)}$ is

$$E^{(2,1)} = \sum_m \frac{\left\langle m \left| H^{(1)} \right| n \right\rangle^2}{\hbar\omega(n-m)} = -\frac{\hbar\omega x}{2}\left(3n^2 + 3n + \frac{3}{2}\right) \tag{5.54}$$

while the contribution from $H^{(2)}$ is

$$E^{(2,2)} = \left\langle n \left| H^{(2)} \right| n \right\rangle = \frac{\hbar\omega x}{2}\left(n^2 + n + \frac{1}{2}\right) + \frac{\hbar\omega x}{4} \tag{5.55}$$

making the total contribution at 2nd order

$$E_n^{(2)} = -\hbar\omega x\left(n + 1/2\right)^2 \tag{5.56}$$

with $E^{(2,1)} \approx -3E^{(2,2)}$.

Analyzing Corrections to the Wave Function at First Order

As noted in the text, in water, the leading corrections to the wave function comes from the state with one more (or fewer) quanta of excitation in the symmetric OH stretch. In the discussion that follows, we explore the terms in the Hamiltonian that can contribute to the size of this contribution. To keep the discussion more general, we will assume that the quantum numbers that describe the state of interest are expressed as n, and the one that is being excited (e.g. the symmetric stretch) is mode 1. Further, we take advantage of the fact that our basis is a product of uncoupled harmonic oscillators, and our coordinates are dimensionless normal mode coordinates. Based on this, the terms in the Hamiltonian that could couple the state $|n\rangle$ to the state $|m\rangle$, where $|m_1 - n_1| = 1$ and $m_i = n_i$ for $i > 1$ are

$$
\begin{aligned}
H_{\text{coup}} &= \sum_{i=2}^{N}\left[\frac{1}{2}\frac{\partial^3 V}{\partial q_1 \partial q_i^2}q_1 q_i^2 + \frac{1}{2}\frac{\partial G_{ii}}{\partial q_1}q_1 p_i^2 + \frac{\partial G_{1i}}{\partial q_i}p_1\left(p_i q_i + q_i p_i\right)\right] \\
&\quad + \frac{1}{2}p_1\frac{\partial G_{11}}{\partial q_1}q_1 p_1 + \frac{1}{6}\frac{\partial^3 V}{\partial q_1^3}q_1^3
\end{aligned} \tag{5.57}
$$

and

$$
\begin{aligned}
\langle n|H_{\text{coup}}|m\rangle &= \frac{1}{\sqrt{8}}\sum_{i=2}^{N}\left[\frac{\partial^3 V}{\partial q_1 \partial q_i^2} + \frac{\partial G_{ii}}{\partial q_1}\right]\left(n_i + \frac{1}{2}\right)\sqrt{\max(n_1, m_1)} \\
&\quad + \frac{1}{\sqrt{32}}\left[\frac{\partial G_{11}}{\partial q_1} + \frac{\partial^3 V}{\partial q_1^3}\right]\sqrt{\max(n_1, m_1)^3}
\end{aligned} \tag{5.58}
$$

If we compare the size of the contribution of $|m\rangle$ to the first order correction to state $|n\rangle$, when $|n\rangle$ represents the ground state and the first excited in a vibration other than mode 1, mode j, the difference is

$$
\Delta = \frac{1}{\sqrt{32}}\left[\frac{\partial^3 V}{\partial q_1 \partial q_j^2} + \frac{\partial G_{jj}}{\partial q_1}\right] \tag{5.59}
$$

where the relevant derivatives are given in Table 5.4.

5.3.4 Molecular Systems

Moving beyond the one-dimensional Morse oscillator, a next natural system of study is the water monomer. We will investigate this system both through a full *ab initio* treatment and through two- and three-dimensional models. The two-dimensional model considers only the two OH stretching vibrations, and is described by the harmonically coupled anharmonic oscillator Hamiltonian

$$
H = \frac{p_1^2}{2\mu} + \frac{p_2^2}{2\mu} + \frac{\cos\theta_e}{m_{\text{O}}}p_1 p_2 + V(r_1) + V(r_2) + V'(r_1, r_2, \theta_e) \tag{5.60}
$$

Here, μ is the reduced mass of an OH bond, m_{O} is the mass of oxygen, $V(r_1)$ and $V(r_2)$ are Morse potentials, $\theta_e = 104.5°$ is the equilibrium HOH angle, and the equilibrium bond length is $r_e = 0.9575$ Å. The parameters for the Morse potentials are the same as those used for the one-dimensional Morse oscillator, described above. The three-dimensional model starts from Eq. (5.60) and adds the HOH bend dependence in the form of a harmonic potential with a frequency of 1600 cm^{-1} and accounts for the full kinetic energy operator.

The results of applying perturbation theory to the two-dimensional model are provided in Fig. 5.2 and reported in Table 5.2. Of note is the fact that the size of the $\mathcal{E}_n^{(1,1)}$ and $\mathcal{E}_n^{(2,0)}$ corrections follow the same pattern that was seen for the one-dimensional Morse oscillator. Despite treating this system with non-degenerate perturbation theory, the calculated energies are within 1 cm^{-1} of the DVR results for this system for the ground state, the states with one quantum of excitation in one of the OH stretching vibrations, as well as the state with one quantum of excitation in each of the two stretches. These differences increase with additional vibrational excitation. For example, the results of the VPT2 calculations deviate from the DVR results by < 50 cm^{-1} for the states with two quanta of excitation in a single stretch.

When taking the perturbation theory up to 4th order, this difference drops to < 15 cm^{-1}. The DVR and VPT energies are provided in Table 5.2 and are obtained using the discrete variable representation described above.

We next turn to the results for three three-dimensional treatments of water, which are plotted in Fig. 5.3, and the values are provided in Table 5.3. Once the HOH bend is introduced, the choice of coordinates affects the relative sizes of $\mathcal{E}_n^{(2,0)}$ (arising from terms in $H^{(2)}$) and $\mathcal{E}_n^{(1,1)}$ (arising from terms in $H^{(1)}$). This can be seen in the results plotted in Fig. 5.3, where the results obtained from the expansion of the Hamiltonian in normal modes based on the displacements of the Cartesian coordinates (labeled C, darkest shading in Fig. 5.3) and normal modes based on displacements of the OH bonds and HOH angle (labeled I, intermediate shading) are provided. The results for the three-dimensional model in internal coordinates are also provided (labeled 3D, lightest shading). For the purposes of this discussion, we will label the antisymmetric stretch, symmetric stretch, and bend as OH^{a}, OH^{s},

Table 5.2: Energies (in cm^{-1}) for two harmonically coupled anharmonic oscillators with the Hamiltonian given by Eq. (5.60).

State	DVR[a]	VPT2[b]	VPT4[b]
g.s.	3827.31	3827.31	3827.31
$n_a = 1$	3727.98	3727.98	3727.98
$n_s = 1$	3674.29	3674.29	3674.29
$n_a = 1, n_s = 1$	7235.20	7235.28	7235.20
$n_a = 2$	7416.85	7369.36	7431.88
$n_s = 2$	7218.31	7265.71	7203.27

[a]DVR provides the ground state energy/transition frequencies evaluated using a discrete variable representation as described in the text.

[b]VPT2 provides the ground state energy/transition frequencies from second order perturbation theory. VPT4 provides the ground state energy/transition frequencies from fourth order perturbation theory.

and HOH. The coordinate dependence of the sizes of the energy corrections is most notable for the energy difference between the ground state and the $v_{HOH} = 1$ state, where the signs of $\mathcal{E}^{(1,1)}_{HOH}$ and $\mathcal{E}^{(2,0)}_{HOH}$ depend on whether the Hamiltonian is expanded in internal or Cartesian coordinates. Even for the energies of the first excited states in the OH^a or OH^s differences are seen, although in both cases the expected $-2:1$ ratio between $\mathcal{E}^{(1,1)}_n$ and $\mathcal{E}^{(2,0)}_n$ anticipated by the Morse oscillator model expanded in Δr coordinates is observed.

Closer examination of the origins of the changes in the values of $\mathcal{E}^{(1,1)}_0$ and $\mathcal{E}^{(1,1)}_{HOH}$ shows that the leading contributions to the first order correction to the ground state wave function comes from the states with $v^s_{OH} = 1$, while the leading contribution to the first order correction to the wave function for the state with $v_{HOH} = 1$ comes from the state with one quantum of excitation in both the HOH bend and the symmetric OH stretch. The magnitude of the contribution of the state with one additional quantum of excitation in OH^s is larger for the state with $v_{HOH} = 1$ when the Hamiltonian is expanded in internal coordinates, while

Table 5.3: Contributions (in cm^{-1}) to energies of H_2O obtained at second order in perturbation theory, where $\mathcal{E}_n^{(2,0)}$ provides corrections from $H^{(2)}$ and $\mathcal{E}_n^{(1,1)}$ provides corrections from $H^{(1)}$. The reported results are based on quartic expansions of the Hamiltonian in normal modes based on displacements of the Cartesian and the internal coordinates. The results are plotted in Fig. 5.3.

State	Cartesian			Internal		
	$\mathcal{E}_n^{(2,0)}$	$\mathcal{E}_n^{(1,1)}$	Sum	$\mathcal{E}_n^{(2,0)}$	$\mathcal{E}_n^{(1,1)}$	Sum
g.s.	42.0241	−117.6347	−75.6106	81.0958	−156.7085	−75.6126
$v^a_{OH} = 1$	157.5110	−350.2934	−192.7824	195.5946	−388.3766	−192.7819
$v^s_{OH} = 1$	153.8492	−335.1695	−181.3203	200.5211	−381.8409	−181.3198
$v_{HOH} = 1$	−74.1636	24.5679	−49.5957	7.3959	−57.0007	−49.6048

for the ground state wave function the expansion in Cartesian displacements gives a larger contribution from the state with $v^s_{OH} = 1$.

The terms in $H^{(1)}$ based on the expansion of the Hamiltonian for H_2O are provided in Table 5.4. The ones that couple the zero-order state to the state with one additional quantum of excitation in the symmetric stretch are the ones identified as $q^s_{OH}q^s_{OH}q^s_{OH}$, $q^s_{OH}q^a_{OH}q^a_{OH}$ and $q^s_{OH}q_{HOH}q_{HOH}$. The terms in Table 5.4 that only involve the stretching vibrations are dominated by the contributions to the potential derivatives, and the values of these quantities are nearly equal when the Hamiltonian is expanded in internal or Cartesian coordinates. These terms are also at least an order of magnitude larger than any other terms reported in Table 5.4. In contrast, the terms in the row of Table 5.4 identified as $q^s_{OH}q_{HOH}q_{HOH}$ are comparable in magnitude, but have opposite signs when the Hamiltonian is expanded in internal or Cartesian coordinates. The difference in the sign of this term reflects the fact that the bending vibration does not follow Cartesian coordinates.[103,112,126]

The overall contribution to the first order correction to the state of interest from the state with one more quantum of excitation in the symmetric OH stretch depends on the sum of these contributions. While the contribution from the terms that only involve the stretches will be the same for both the ground state and the state with $v_{HOH} = 1$, the

Table 5.4: Contributions to $H^{(1)}$ for H_2O, including the potential derivatives in Cartesian and internal coordinates as well as the first derivatives of the G-matrix elements.

	Cartesian	Internal			
Coordinates (i,j,k)	$\partial^3 V/\partial q_i q_j q_k$	$\partial^3 V/\partial q_i q_j q_k$	$\partial G_{ij}/\partial q_k$	$\partial G_{ik}/\partial q_j$	$\partial G_{jk}/\partial q_i$
$q^s_{\rm OH} q^a_{\rm OH} q^a_{\rm OH}$	−1813.8	−1812.9	−1.0	−1.0	0.3
$q^s_{\rm OH} q^s_{\rm OH} q^s_{\rm OH}$	−1830.4	−1829.4	−0.6	−0.6	-0.6
$q_{\rm HOH} q^a_{\rm OH} q^a_{\rm OH}$	−254.6	−214.1	10.0	10.0	−48.8
$q_{\rm HOH} q^s_{\rm OH} q^s_{\rm OH}$	−69.5	−117.7	13.3	13.3	46.8
$q^s_{\rm OH} q_{\rm HOH} q_{\rm HOH}$	292.1	−132.1	11.5	11.5	−227.2
$q_{\rm HOH} q_{\rm HOH} q_{\rm HOH}$	258.7	323.8	−43.4	−43.4	−43.4

contributions from the coupling terms listed in the row labeled $q^s_{\rm OH} q_{\rm HOH} q_{\rm HOH}$ in Table 5.4 will increase with HOH bend excitation. The fact that these terms are all negative when the expansion is performed in internal coordinates means that excitation of the bend will increase the size of the contribution of the state with one additional quantum of excitation in the symmetric OH stretch to the first order correction to the wave function. In contrast, when the Hamiltonian is expanded in Cartesian coordinates, the size of the contribution of the state with one additional quantum of excitation in the symmetric OH stretch will decrease with bend excitation. Since the energy shift at second order perturbation theory arises from the ratio of the square of this matrix element of $H^{(1)}$ involving the state of interest and the state that is contributing at first order and the energy difference between these two states, the differences described above are responsible to the observed change in sign of $\mathcal{E}^{(1,1)}_{\rm HOH}$ and $\mathcal{E}^{(2,0)}_{\rm HOH}$ in Fig. 5.3.

Likewise, large, negative quartic terms in the expansion of the potential, provided in Table 5.5, that involve both the stretches and the bends when the potential is expanded in Cartesian coordinates are responsible for the negative value of $\mathcal{E}^{(2,0)}_{\rm HOH}$ in this case, whereas the positive values of the quartic kinetic couplings in the internal coordinate representation

provide the positive $\mathcal{E}^{(2,0)}_{\mathrm{HOH}}$ for these coordinates. As expected, when we sum $\mathcal{E}^{(1,1)}_{\mathrm{HOH}}$ and $\mathcal{E}^{(2,0)}_{\mathrm{HOH}}$ the resulting excited state energy is independent of the coordinates used to expand the Hamiltonian. On the other hand, as seen in prior studies,[126] the interpretation of the origins of the anharmonicity as arising from large stretch bend couplings in the potential as opposed to terms in the kinetic energy depends on the choice of coordinates. Similar changes are observed in the analysis of the energy corrections when the energies are evaluated using the three-dimensional model. This further supports the conclusion that this change is reflecting the difference in the description of the bending vibration and not large underlying stretch-bend coupling terms in the potential energy surface for water.

When we look at $(H_2O)_2$, we find that while the overall energy correction at second order perturbation theory is independent of the coordinate choice, the sizes of the corrections to the energy from the terms in the first and second order correction to the Hamiltonian depend more sensitively on the choice of coordinates than was seen for H_2O. Specifically, when the Hamiltonian is expanded in internal coordinates, the sizes of $\mathcal{E}^{(2,0)}_n$ range from 195 to 235 cm^{-1} for the stretches and are smaller than 100 cm^{-1} for all but the lowest frequency vibration. Likewise, the corresponding $\mathcal{E}^{(1,1)}_n$ values are no smaller than -440 cm^{-1} for the OH stretches and no smaller than -125 cm^{-1} for all but the lowest frequency vibration. In addition, $\mathcal{E}^{(1,1)}_n \sim -2\mathcal{E}^{(2,0)}_n$ for all four OH stretching vibrations, as expected from the Morse oscillator model. In contrast, when the Hamiltonian is expanded in normal coordinates that are linear combinations of Cartesian displacements, the signs of the corrections for the OH stretches are reversed and are no longer in the expected $-2:1$ ratio. The magnitudes of the corrections are generally much larger when the Hamiltonian is expanded in these coordinates, and exceed 1000 cm^{-1} in many cases. This is seen in the results plotted in Fig. 5.4, which are also provided in Table 5.6. The origins of these differences can be traced to slow convergence of the expansion of the potential in the large-amplitude low-frequency vibrations, which correspond to hindered rotations of the water molecules, when the Hamiltonian is expanded in normal modes based on the displacements of Cartesian coordinates. This is largely driven by the large-amplitude low-frequency modes which will be particularly poorly represented

by Cartesian displacements.

Finally we look at peroxynitrous acid (HOONO), which is a molecule with an intramolecular hydrogen bond. HOONO contains two low-frequency torsions, neither of which is expected to be well-represented by vibrational perturbation theory.[127–129] The energy shifts obtained by applying VPT2 to the expansions of the Hamiltonian for HOONO in internal and Cartesian coordinates are provided in Fig. 5.5 and Table 5.7. The lowest frequency mode is the hydrogen out-of-plane bending motion (HOO′N) with a harmonic frequency of 355 cm^{-1}. The corrections to the energies of both the hydrogen out-of-plane bend (HOO′N) and nitrogen out-of-plane bend (OO′NO″) modes are very large when the Hamiltonian is expanded in Cartesian coordinates and much smaller when the Hamiltonian is expanded in internal coordinates. Interestingly, the energy of the OH stretching vibration is much larger when the Hamiltonian is expanded in internal coordinates than when it is expressed in Cartesian coordinates. This likely reflects the large anharmonicity in this mode. In fact, the internal coordinate energy corrections are consistent with a Morse oscillator with an anharmonicity of ∼95 cm^{-1}. As was the case for water dimer, when the Hamiltonian is expanded in normal mode coordinates that are based on the internal coordinates $\mathcal{E}_{\mathrm{OH}}^{(1,1)} \sim -2\mathcal{E}_{\mathrm{OH}}^{(2,0)}$, while for the expansion in Cartesian coordinates, the signs of these contributions are reversed. As with $(H_2O)_2$, this deviation of the energy corrections for the OH stretch from expectations based on the Morse oscillator reflects the large corrections arising from the contribution from states with one quantum in the HOO′N torsion to the first order correction to the wave function for the state with $v_{\mathrm{OH}} = 1$.

5.3.5 Properties

Having shown that the value of $\Delta E_n^{(k)}$ in Eq. (5.33) is independent of the normal mode coordinates that are used to expand the Hamiltonian, it is natural to ask if the same holds for other properties. If we partition the normal coordinate expansion of the operator of interest by the order of the terms in the expansion, the corrections to the matrix elements of the operator obtained from perturbation theory will once again be independent of the underlying

coordinate choice. As an example, in the case of the dipole function, the constant and linear terms in the expansion of the dipole are in $\mu^{(0)}$, the quadratic terms are in $\mu^{(1)}$, and the cubic terms are in $\mu^{(2)}$. In this way, the zero-order contribution to the intensity calculation provides the results of the linear dipole/harmonic treatment. Putting the quadratic terms in $\mu^{(1)}$ ensures that the first order correction to the intensity provides the lowest order approximation for the intensities of transitions to states with two or four quanta of excitation. Likewise at second order, we obtain corrections to the intensities for transitions involving one quantum of excitation as well as intensities for transitions to states with three or five quanta of excitation. These observations result from the expression for the kth order correction to the transition moments

$$\langle 0|\, \mu_\alpha \,|n\rangle^{(k)} = \sum_{l=0}^{k} \sum_{i=0}^{k-l} \langle 0^{(i)}|\, \mu_\alpha^{(l)} \,|n^{(k-l-i)}\rangle \tag{5.61}$$

and the fact that, in a harmonic basis, operation by the coordinate or momentum operator can only change the number of quanta in the state by ± 1.

The results for the intensities of the three transitions involving two quanta of excitation in H_2O are shown in Fig. 5.6. Since by symmetry, only one vector component of the transition moment can be non-zero for this molecule, only the non-zero component is plotted. Additionally, to aid in comparison, the sum of the contributions to the transition moment components are denoted by the black dashed lines in the figure. As can be seen, these values are the same when the Hamiltonian is expanded in normal modes based on the Cartesian and internal coordinates. On the other hand, whether the origin of the intensity is primarily from the linear term in the expansion of the dipole moment and higher order terms in the expansion of the Hamiltonian (mechanical anharmonicity) or the harmonic potential ($H^{(0)}$) and higher order terms in the expansion of the dipole (electrical anharmonicity) often depends on the coordinates in which the Hamiltonian and dipole moment operators are expanded.

We choose to focus on combination bands and overtones involving the HOH bend for two reasons. Firstly, the intensities of transitions to the states with one quantum of excitation

are well-described by the linear dipole/harmonic oscillator approximation, and typically the second order corrections to these transition moments are ∼10% of the value of the zeroth order transition moments. Secondly, as noted above, there are only two types of corrections that come in at first order, those that result from the first order corrections to the wave functions with $\mu^{(0)}$ and those that come from $\mu^{(1)}$. This greatly simplifies our analysis as the first case corresponds to mechanical anharmonicity, while the second reflects electrical anharmonicities. Comparing the results presented in Fig. 5.6, we find that the contributions to the intensities for the transition involving the HOH bend and the antisymmetric stretch are the same for both coordinate systems, while the leading contribution to the intensity of the transition to the state with one quantum in the bend and one in the symmetric OH stretch depends on the coordinates that are used to expand the Hamiltonian.

There are two factors reflected in this difference. First, as noted above, the sign of the cubic terms in the expansion of the Hamiltonian that involve the symmetric stretch and bend depend on the coordinates used to expand the Hamiltonian. Likewise, as seen in the results reported in Table 5.9 the sign of the mixed second derivative of the dipole moment with respect to the symmetric stretch and the bend depends on the choice of coordinates. As with the cubic terms in the expansion of the potential reported in Table 5.4, this change in sign reflects the differences in the description of the bend in the two coordinate systems. Taken together, the differences in the description of the transition moment for the transition to the state with one quantum in both the symmetric stretch and bend serve to illustrate the potential challenges in interpreting the origins of anharmonicities. As noted before, while the sum of the various contributions will not depend on the choice of coordinates, the individual contributions will.

In Fig. 5.7 trends for the component of the transition moment along the A principal axis (indicated as a red arrow in Fig. 5.7) for selected transitions in $(H_2O)_2$ are presented. As with H_2O, these results illustrate the effect of coordinates choice on the interpretation of the results. Generally, when internal coordinates are used, the contribution from the higher order terms in the dipole expansion become more important. Interestingly, this trend is exhibited

even for combination bands involving primarily rectilinear motions, such as the combination band of the OO stretch and the symmetric stretch on the acceptor water, OO + OH^s_A, and those involving motions that would not appear strongly coupled, such as the out-of-phase rotation of the two water monomers about OO axis and the acceptor antisymmetric OH stretch, $rot_{OO} + OH^a_A$.

As before, this is reflective of deficiencies in the Cartesian coordinate normal modes.

5.4 Conclusion

A sparse, linear algebra based implementation of Rayleigh-Schrödinger vibrational perturbation theory that allows for flexibility in the expansion of the Hamiltonian used has been described. Our PyVibPTn[115] implementation of this approach provides a powerful tool for investigating the origin of spectral intensity and transition frequencies by looking at which expansion terms lead to the largest corrections. It also provides flexibility in terms of the coordinate system used in the expansions, which aids in interpretation by allowing for the use of coordinates that better follow the true molecular motions than the Cartesian displacement coordinates most commonly used in prior implementations. Good coordinate choice minimizes the amount of cancellation of corrections and coordinate systems beyond the bond-angle-dihedral internal coordinate system, such as generalizations of the Morse y coordinates, could prove even more advantageous for interpretation in more complicated molecular systems.

We have explored the corrections to the wave functions for water in internal and Cartesian coordinates, and found that the contribution of the symmetric OH stretch to the corrections to the HOH bend wave function differs significantly between the two coordinate systems, reflecting the larger coupling between the HOH bend and the OH stretches in Cartesian coordinates. Likewise, we have shown that determining whether combination band intensity arises from mechanical or electrical anharmonicity depends sensitively on coordinate choice, finding that the intensity of combination bands involving nominally rectilinear motions can appear to originate from higher order terms in the potential when the Hamiltonian

is expanded in Cartesian coordinates, while in internal coordinates the intensity appears to reflect higher order terms in the expansion of the dipole surface. Additional applications of the implementation of vibrational perturbation theory described here to studies of two photon excitations of the CH stretching vibrations in the hydroperoxyalkyl radical[130] and the specral signatures of hydrogen bonding in complexes of HOCl and HOD with halide ions[131] have been described elsewhere.

The work described here focused on situations where the energies and intensities were not impacted by near degeneracies, which can be problematic in studies based on perturbation theory. We are currently extending this work to include the identification of resonances in order to appropriately handle them within PyVibPTn.

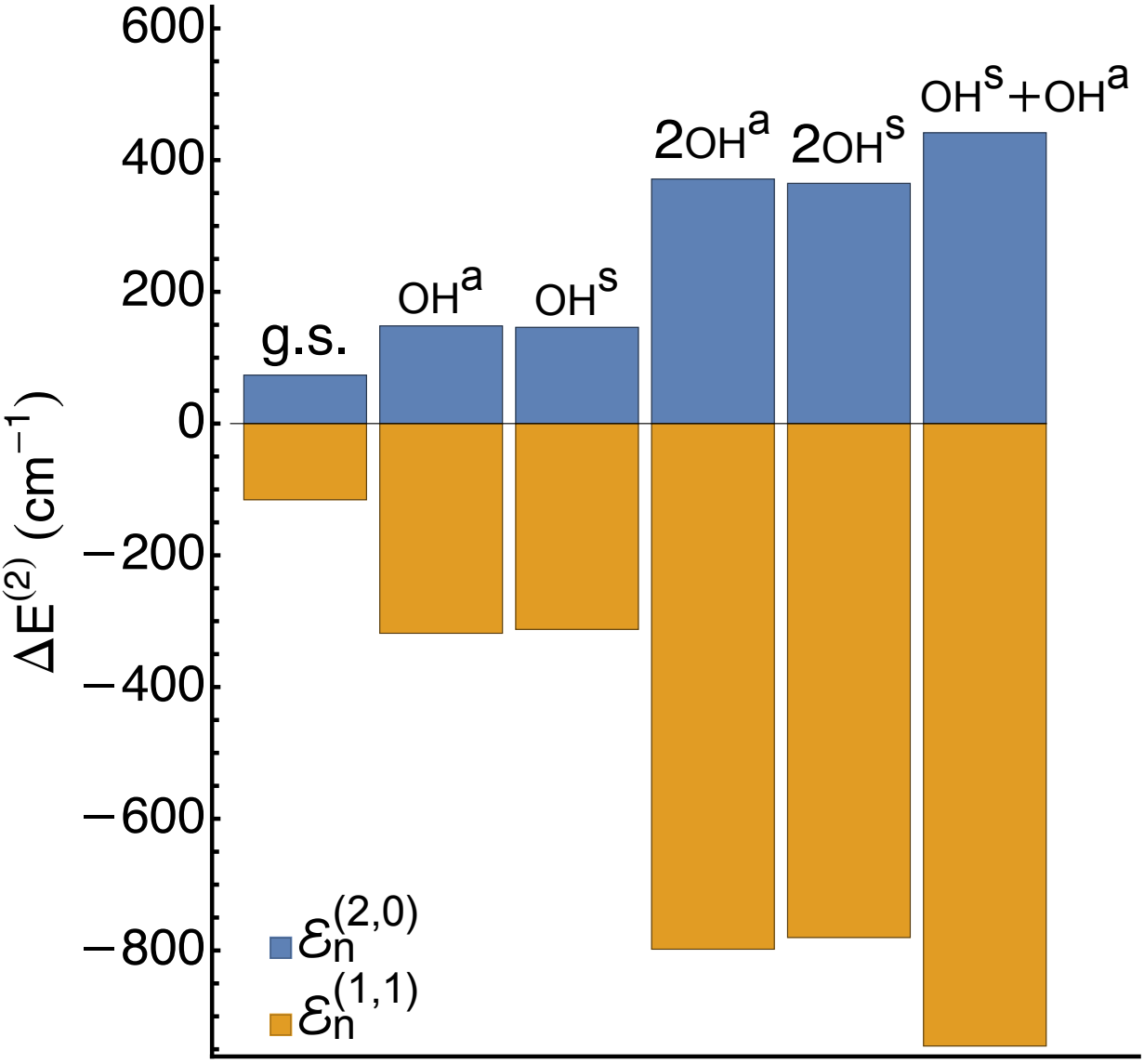

Figure 5.2: Contributions to the zero-point energy (g.s.) and the energies of states with up to two quanta of excitation for the two-dimensional harmonically coupled anharmonic oscillator system defined by Eq. (5.60), $\mathcal{E}_n^{(i,j)}$ defined in Eq. (5.32) and Eq. (5.34), based on the one-dimensional Morse oscillators with $\omega = 3869.47$ cm^{-1} and $\omega x = -84.11$ cm^{-1}. The energies for these states at second and fourth order in perturbation theory as well as the energies evaluated using a discrete variable representation are provided in Table 5.2.

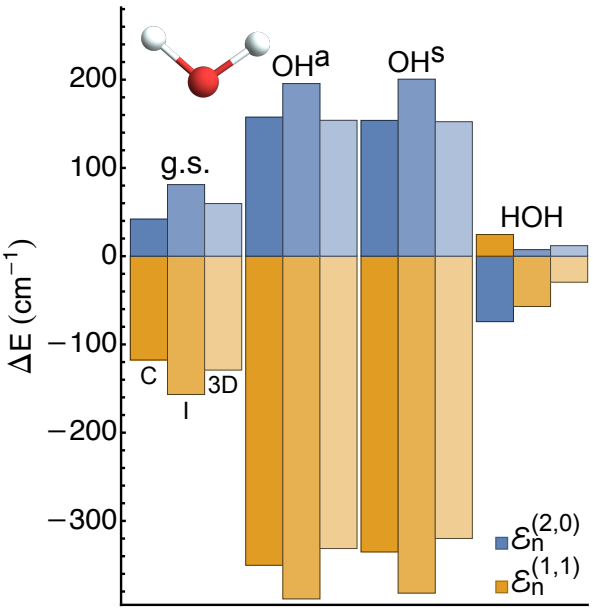

Figure 5.3: Contributions to energies of selected states of water obtained at second order in perturbation theory, where $\mathcal{E}_n^{(2,0)}$ provides corrections from $H^{(2)}$ and $\mathcal{E}_n^{(1,1)}$ provides corrections from $H^{(1)}$. Results are provided for the zero-point energy (g.s.) and the energies of states with one of excitation in the symmetric OH stretch, OH^s, the antisymmetric OH stretch, OH^a and the HOH bend, HOH. The reported results are based on three descriptions of the vibrational Hamiltonian: C) a quartic expansion of the Hamiltonian in normal coordinates based on Cartesian displacements, I) a quartic expansion of the Hamiltonian in normal coordinates based on internal displacements, and 3D) when the potential is approximated by Eq. (5.60) with an additional harmonic bend with $\omega = 1600$ cm^{-1}. The values of the plotted quantities are provided in Table 5.3.

Table 5.5: Contributions (in cm^{-1}) to $H^{(2)}$ for H_2O, including the potential derivatives in Cartesian and internal coordinates as well as the second derivatives of the G-matrix elements.

	Cartesian	Internal						
Coordinates (i,j,k,l)	$\partial^4 V/\partial q_i q_j q_k q_l$	$\partial^4 V/\partial q_i q_j q_k q_l$	$\partial^2 G_{kl}/\partial q_i q_j$	$\partial^2 G_{jl}/\partial q_i q_k$	$\partial^2 G_{jk}/\partial q_i q_l$	$\partial^2 G_{il}/\partial q_j q_k$	$\partial^2 G_{ik}/\partial q_j q_l$	$\partial^2 G_{ij}/\partial q_k q_l$
$q^a_{OH}q^a_{OH}q^a_{OH}q^a_{OH}$	760.4502	764.3620	0	0	0	0	0	0
$q^s_{OH}q^s_{OH}q^a_{OH}q^a_{OH}$	763.2035	763.1641	−0.0001	0.1454	0.1454	0.1454	0.1454	0.2123
$q^s_{OH}q^s_{OH}q^s_{OH}q^s_{OH}$	769.1371	768.5675	0.2158	0.2158	0.2158	0.2158	0.2158	0.2158
$q_{HOH}q^s_{OH}q^a_{OH}q^a_{OH}$	119.8387	92.5363	0.0165	−0.0408	−0.0408	−1.4116	−1.4116	−3.4668
$q_{HOH}q^s_{OH}q^s_{OH}q^s_{OH}$	55.3283	75.0833	0.1385	0.1385	0.1385	−3.5086	−3.5086	−3.5086
$q_{HOH}q_{HOH}q^a_{OH}q^a_{OH}$	−369.8830	−7.6465	−2.6293	0.3963	0.3963	0.3963	0.3963	47.2946
$q_{HOH}q_{HOH}q^s_{OH}q^s_{OH}$	−301.5539	19.9588	4.0463	−1.1507	−1.1507	−1.1507	−1.1507	47.7883
$q^s_{OH}q_{HOH}q_{HOH}q_{HOH}$	−163.3789	−59.7229	7.7403	7.7403	7.7403	−6.8951	−6.8951	−6.8951
$q_{HOH}q_{HOH}q_{HOH}q_{HOH}$	−28.1820	−49.4827	−0.0813	−0.0813	−0.0813	−0.0813	−0.0813	−0.0813

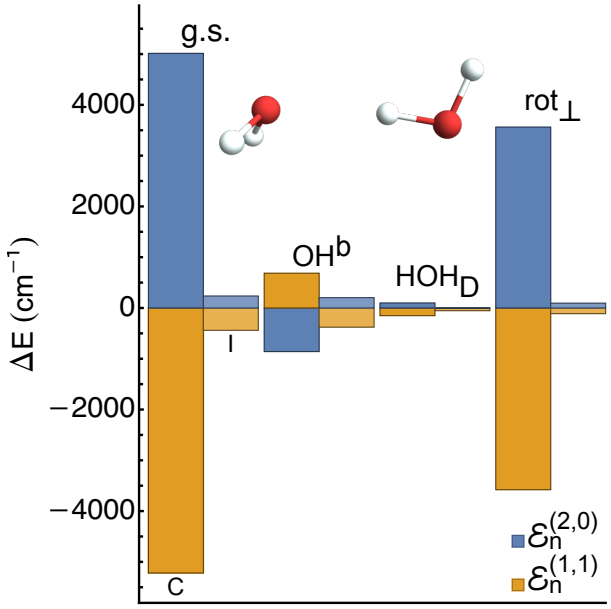

Figure 5.4: Contributions to energies of selected states of water dimer obtained at second order in perturbation theory, where $\mathcal{E}_n^{(2,0)}$ provides corrections from $H^{(2)}$ and $\mathcal{E}_n^{(1,1)}$ provides corrections from $H^{(1)}$. Results are provided for the zero-point energy (g.s.) and the energies of states with one quantum of excitation in the bound OH stretch, OH^b, the HOH bend of the donor water molecule, HOH_D, and the out-of-phase rotations of the two monomers about the axis perpendicular to the plane of symmetry of the complex, $\mathrm{rot}_\perp$. The reported results are based on two descriptions of the vibrational Hamiltonian: C) a quartic expansion of the Hamiltonian in normal coordinates based on Cartesian displacements, I) a quartic expansion of the Hamiltonian in normal coordinates based on internal displacements. The values of the plotted quantities are provided in Table 5.6.

Table 5.6: Contributions (in cm^{-1}) to energies of $(H_2O)_2$ obtained at second order in perturbation theory, where $\mathcal{E}_n^{(2,0)}$ provides corrections from $H^{(2)}$ and $\mathcal{E}_n^{(1,1)}$ provides corrections from $H^{(1)}$. The reported results are based on two descriptions of the vibrational Hamiltonian: Cartesians) a quartic expansion of the Hamiltonian in normal coordinates based on quartic expansions of the Hamiltonian in normal modes based on displacements of the Cartesian and the internal coordinates. Selected transitions are plotted in Fig. 5.4.

State[a]	Cartesian			Internal		
	$\mathcal{E}_n^{(2,0)}$	$\mathcal{E}_n^{(1,1)}$	Sum	$\mathcal{E}_n^{(2,0)}$	$\mathcal{E}_n^{(1,1)}$	Sum
g.s.	5014.8369	−5219.3827	−204.5458	235.1656	−439.7116	−204.5460
$v_{OH_A^a} = 1$	−915.5209	733.9091	−181.6118	195.6823	−377.2943	−181.6119
$v_{OH^b} = 1$	−859.2775	684.8548	−174.4227	202.9660	−377.3888	−174.4228
$v_{OH_A^s} = 1$	−883.2569	716.3186	−166.9383	198.3588	−365.2973	−166.9384
$v_{OH_D^f} = 1$	−506.3871	370.0499	−136.3372	223.4496	−359.7868	−136.3372
$v_{HOH_D} = 1$	97.9036	−151.6619	−53.7583	−3.8285	−49.9298	−53.7583
$v_{HOH_A} = 1$	98.5104	−142.3190	−43.8086	7.9628	−51.7714	−43.8087
$v_{oop} = 1$	831.9775	−957.4894	−125.5119	−0.4689	−125.0430	−125.5119
$v_{ip_D} = 1$	1872.8878	−1927.8671	−54.9794	1.3232	−56.3027	−54.9794
$v_{OO} = 1$	2543.1588	−2571.5487	−28.3899	54.9686	−83.3585	−28.3899
$v_{rot_\perp} = 1$	3562.0310	−3579.5709	−17.5399	94.5916	−112.1315	−17.5399
$v_{rot_{OO}} = 1$	5904.1682	−5906.1242	−1.9560	78.1489	−80.1050	−1.9561
$v_{tor_A} = 1$	8367.2275	−8387.8344	−20.6068	140.9120	−161.5190	−20.6070

[a] A/D subscripts indicate the vibration is on the hydrogen bond acceptor or donor respectively; a/s superscripts indicate the antisymmetric or symmetric combination of the OH stretches on the acceptor; b superscript indicates the bound hydrogen while the f superscript indicates the free hydrogen on the donor; rot $\perp$ is the out-of-phase rotation of the water molecules about an axis that is perpendicular to the plane that contains the donor water molecule, and rot_{OO} is the out-of-phase rotation of the monomers about the OO axis.

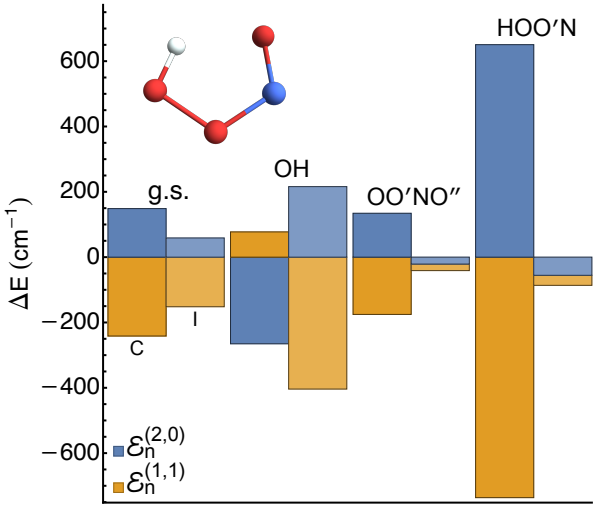

Figure 5.5: Contributions to energies of selected states of HOONO obtained at second order in perturbation theory, where $\mathcal{E}_n^{(2,0)}$ provides corrections from $H^{(2)}$ and $\mathcal{E}_n^{(1,1)}$ provides corrections from $H^{(1)}$. Results are provided for the zero-point energy (g.s.) and the energies of states with one of excitation in the OH stretch, the OO′NO″ torsion, and the HOO′N torsion. The reported results are based on two descriptions of the vibrational Hamiltonian: C) a quartic expansion of the Hamiltonian in normal coordinates based on Cartesian displacements, I) a quartic expansion of the Hamiltonian in normal coordinates based on internal displacements. The values of the plotted quantities are provided in Table 5.7.

Table 5.7: Contributions (in cm^{-1}) to energies of HOONO obtained at second order in perturbation theory, where $\mathcal{E}_n^{(2,0)}$ provides corrections from $H^{(2)}$ and $\mathcal{E}_n^{(1,1)}$ provides corrections from $H^{(1)}$. The reported results are based on quartic expansions of the Hamiltonian in normal modes based on displacements of the Cartesian and the internal coordinates and are plotted in Fig. 5.5.

State	Cartesian			Internal		
	$\mathcal{E}_n^{(2,0)}$	$\mathcal{E}_n^{(1,1)}$	Sum	$\mathcal{E}_n^{(2,0)}$	$\mathcal{E}_n^{(1,1)}$	Sum
g.s.	148.6515	−241.4685	−92.8170	58.7712	−151.8055	−93.0343
$v_{OH} = 1$	−265.2326	77.3160	−187.9165	215.9494	−403.8564	−187.9070
$v_{NO''} = 1$	19.8300	−30.1614	−10.3314	32.6524	−42.9955	−10.3432
$v_{HOO'} = 1$	3.0290	105.4814	108.5104	30.5498	77.8136	108.3633
$v_{O'NO''} = 1$	5.3421	−28.9379	−23.5958	9.8035	−33.4172	−23.6137
$v_{OO'} = 1$	7.8039	−29.9004	−22.0965	16.0402	−38.1372	−22.0970
$v_{O'N} = 1$	37.9814	45.0219	83.0033	45.0572	37.9436	83.0008
$v_{OO'NO''} = 1$	134.2960	−175.3300	−41.0341	−21.1574	−19.9923	−41.1497
$v_{OO'N} = 1$	7.2955	−33.1328	−25.8372	13.5707	−39.4211	−25.8505
$v_{HOO'N} = 1$	650.5459	−736.2930	−85.7471	−55.5574	−30.7592	−86.3166

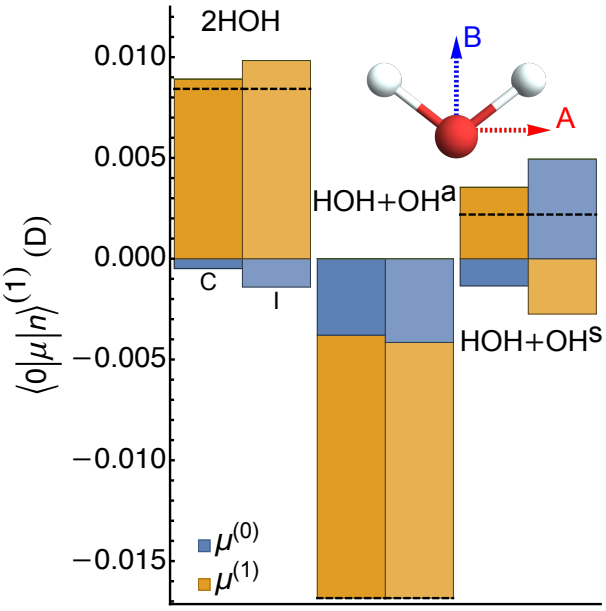

Figure 5.6: Contributions to the component of the transition moment along the A or B principal axis (indicated as red and blue dashed arrows) for selected transitions in water obtained at first order in perturbation theory. The results plotted in blue reflect contributions from $\mu^{(0)}$ and reflect intensity originating from the first order correction to the wave functions, while the results plotted in gold arise from contributions in $\mu^{(1)}$, which contains the quadratic terms in the expansion of the dipole surface. The dashed lines indicate the sum of these two contributions. Results are provided for transition to states with two quanta in the HOH bend, $v_{HOH} = 2$, and the states with one quantum in the bend and one in either the asymmetric or symmetric OH stretch, $v_{HOH} = 1$ and $v_{OH}^{a/s} = 1$. The reported results are based on two descriptions of the vibrational Hamiltonian and dipole surface: C) expansions in normal coordinates based on Cartesian displacements, I) expansions in normal coordinates based on internal displacements. The values of the plotted quantities are provided in Table 5.8. Only the non-zero component of the transition moment is plotted for each transition.

Table 5.8: Contributions (in D) to the component of the transition moment, $\langle 0|\,\mu\,|n\rangle$, along the A or B principal axis (indicated as red and blue dashed arrows in Fig. 5.6) for selected transitions in water obtained at first order in perturbation theory. The contributions from $\mu^{(0)}$ and reflect intensity originating from the first order correction to the wave functions, while the contributions from $\mu^{(1)}$ account for the quadratic terms in the expansion of the dipole surface. Results are provided for transition to states with two quanta in the HOH bend, $\mathrm{v_{HOH}} = 2$, and the states with one quantum in the bend and one in either the asymmetric or symmetric OH stretch, $\mathrm{v_{HOH}} = 1$ and $\mathrm{v_{OH}^{a/s}} = 1$. The reported results are based on two descriptions of the vibrational Hamiltonian: Cartesian) a quartic expansion of the Hamiltonian in normal coordinates based on Cartesian displacements, Internal) a quartic expansion of the Hamiltonian in normal coordinates based on internal displacements. The results are plotted in Fig. 5.6.

State	Cartesian $\mu^{(0)}$		Cartesian $\mu^{(1)}$		Cartesian Sum	
	A	B	A	B	A	B
$\mathrm{v_{HOH}} = 2$	0.00000	−0.00048	0.00000	0.00891	0.00000	0.00843
$\mathrm{v_{HOH}} = 1, \mathrm{v_{OH}^{a}} = 1$	−0.00379	0.00000	−0.01305	0.00000	−0.01684	0.00000
$\mathrm{v_{HOH}} = 1, \mathrm{v_{OH}^{s}} = 1$	0.00000	-0.00135	0.00000	0.00354	0.00000	0.00219
State	Internal $\mu^{(0)}$		Internal $\mu^{(1)}$		Internal Sum	
	A	B	A	B	A	B
$\mathrm{v_{HOH}} = 2$	0.00000	−0.00141	0.00000	0.00983	0.00000	0.00843
$\mathrm{v_{HOH}} = 1, \mathrm{v_{OH}^{a}} = 1$	−0.00415	0.00000	−0.01269	0.00000	−0.01684	0.00000
$\mathrm{v_{HOH}} = 1, \mathrm{v_{OH}^{s}} = 1$	0.00000	0.00494	0.00000	−0.00275	0.00000	0.00219

Table 5.9: Derivatives (in D) of the dipole moment for H_2O that contribute to $\mu^{(1)}$ along the A and B principal axes, indicated by the red and blue arrows in the inset in Fig. 5.6. Derivatives are provided with respect to normal coordinates based on Cartesian displacements (Cartesian) and normal coordinates based on internal displacements (Internal).

	Cartesian		Internal	
Coordinates (i,j)	$\partial^2\mu_A/\partial q_i q_j$	$\partial^2\mu_B/\partial q_i q_j$	$\partial^2\mu_A/\partial q_i q_j$	$\partial^2\mu_B/\partial q_i q_j$
$q^a_{\mathrm{OH}}q^a_{\mathrm{OH}}$	0	−0.003177	0	−0.002815
$q^s_{\mathrm{OH}}q^a_{\mathrm{OH}}$	−0.001334	0	−0.001336	0
$q^s_{\mathrm{OH}}q^s_{\mathrm{OH}}$	0	0.002656	0	0.002718
$q_{\mathrm{HOH}}q^a_{\mathrm{OH}}$	−0.010266	0	−0.009982	0
$q_{\mathrm{HOH}}q^s_{\mathrm{OH}}$	0	0.002787	0	−0.002161
$q_{\mathrm{HOH}}q_{\mathrm{HOH}}$	0	0.009913	0	0.010941

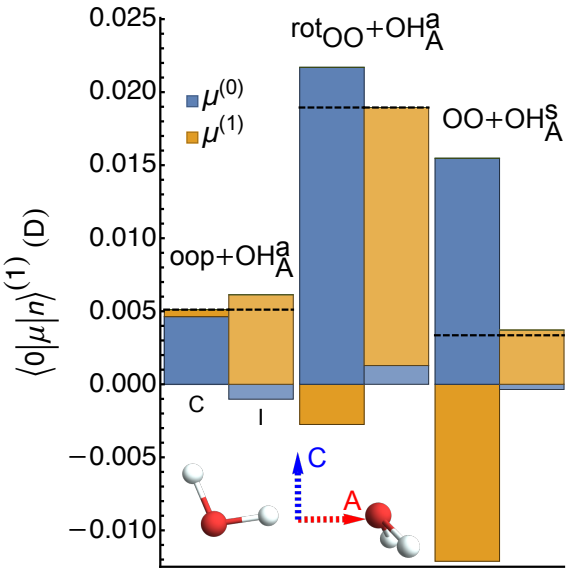

Figure 5.7: Contributions to the component of the transition moment, $\langle 0|\,\mu\,|n\rangle$, along the A principal axis (indicated as red dashed arrow) for selected transitions in water dimer obtained at first order in perturbation theory. The results plotted in blue reflect contributions from $\mu^{(0)}$ and reflect intensity originating from the first order correction to the wave functions, while the results plotted in gold arise from contributions in $\mu^{(1)}$, which contains the quadratic terms in the expansion of the dipole surface. The dashed lines indicate the sum of these two contributions. Results are provided for combination bands with two total quanta of excitation. The combinations are (from left) the bound hydrogen motion out of the plane of symmetry for the complex with the acceptor antisymmetric OH stretch, oop+OH^a_A, the out of phase rotation of the two water monomers about OO axis with the acceptor antisymmetric OH stretch, rot_{OO} + OH^a_A, and the OO stretch with the acceptor symmetric OH stretch, OO+OH^s_A. The reported results are based on two descriptions of the vibrational Hamiltonian and dipole surface: C) expansions in normal coordinates based on Cartesian displacements, I) expansion in normal coordinates based on internal displacements. The values of the plotted quantities as well as the components along the C principal axis (indicated as blue dashed arrow) are provided in Table 5.10.

Table 5.10: Contributions (in D) to the component of the transition moment, $\langle 0|\,\mu\,|n\rangle$, along the A or C principal axis (indicated as red and blue dashed arrows in Fig. 5.7) for selected transitions in water dimer obtained at first order in perturbation theory. The contributions from $\mu^{(0)}$ and reflect intensity originating from the first order correction to the wave functions, while the contributions from $\mu^{(1)}$ account for the quadratic terms in the expansion of the dipole surface. Results are provided for combination bands with two total quanta of excitation. The combinations are the bound hydrogen motion out of the plane of symmetry for the complex with the acceptor antisymmetric OH stretch, oop + $\mathrm{OH}_{\mathrm{A}}^{\mathrm{a}}$, the out of phase rotation of the two water monomers about OO axis with the acceptor antisymmetric OH stretch, $\mathrm{rot}_{\mathrm{OO}}$ + $\mathrm{OH}_{\mathrm{A}}^{\mathrm{a}}$, and the OO stretch with the acceptor symmetric OH stretch, OO + $\mathrm{OH}_{\mathrm{A}}^{\mathrm{s}}$. The results are plotted in Fig. 5.7.

State	Cartesian $\mu^{(0)}$		Cartesian $\mu^{(1)}$		Sum	
	A	C	A	C	A	C
$\mathrm{v}_{\mathrm{oop}}=1, \mathrm{v}_{\mathrm{OH_A}}^{\mathrm{a}}=1$	0.00463	−0.00076	0.00048	0.00181	0.00511	0.00105
$\mathrm{v}_{\mathrm{rot_{OO}}}=1, \mathrm{v}_{\mathrm{OH_A}}^{\mathrm{a}}=1$	0.02170	0.00163	-0.00275	0.00332	0.01895	0.00495
$\mathrm{v}_{\mathrm{OO}}=1, \mathrm{v}_{\mathrm{OH_A}}^{\mathrm{s}}=1$	0.01547	−0.01044	−0.01212	0.00845	0.00336	-0.00199
State	Internal $\mu^{(0)}$		Internal $\mu^{(1)}$		Sum	
	A	C	A	C	A	C
$\mathrm{v}_{\mathrm{oop}}=1, \mathrm{v}_{\mathrm{OH_A}}^{\mathrm{a}}=1$	−0.00102	0.00023	0.00613	0.00082	0.00511	0.00105
$\mathrm{v}_{\mathrm{rot_{OO}}}=1, \mathrm{v}_{\mathrm{OH_A}}^{\mathrm{a}}=1$	0.00128	−0.00037	0.01767	0.00532	0.01895	0.00495
$\mathrm{v}_{\mathrm{OO}}=1, \mathrm{v}_{\mathrm{OH_A}}^{\mathrm{s}}=1$	−0.00036	0.00179	0.00371	−0.00379	0.00336	−0.00199

Chapter 6

A WAVE FUNCTION CORRECTION-BASED APPROACH TO THE IDENTIFICATION OF RESONANCES FOR VIBRATIONAL PERTURBATION THEORY

6.1 Introduction

The simulation of vibrational spectra is a key element in the process of making connections between experimentally observable quantities and the fundamental physics of molecular systems. There are many highly-accurate approaches that have been taken to simulate such spectra. Commonly, methods like discrete variable representations[4,11] (DVR) and local-mode models[132] (LMM) are used to describe individual coordinates. These representations of individual coordinates may then be composed via direct-product bases or similar approaches to obtain representations of the full-dimensional Hamiltonian. Unfortunately, due to the so-called "curse of dimensionality", this simple approach works best only for small systems or in reduced-dimensional models. To extend to higher-dimensional problems, it is common to use approaches like the vibrational self-consistent field/vibrational configuration interaction (VSCF/VCI) method[133] and the multiconfiguration time-dependent Hartree (MCTDH) method,[134] which make use of DVRs and LMMs, but extend them efficiently. These methods provide high-quality spectral information, but can come at a considerable computational cost. As a complement to these highly-accurate but expensive methods, more approximate methods also exist, the best-known likely being the harmonic oscillator model. In the harmonic approximation, the potential energy is approximated by a second-order Taylor series about the minimum-energy geometry. The vibrational Hamiltonian for an N-atom system can then be expressed as

$$H = \sum_{i=1}^{3N-6} \frac{\hbar}{2}\omega_i(p_i^2 + q_i^2) \tag{6.1}$$

where the q_i are the $3N-6$ normal modes, the p_i are the momenta conjugate to the normal modes, and ω_i are the associated frequencies.[1]

For systems where a quadratic approximation to the potential works well—a common case for systems with small-amplitude motions—the harmonic approximation provides good solutions to the full vibrational Schrödinger equation. However, for systems with significant anharmonicity, a better solution is obtained through vibrational perturbation theory (VPT).[2,3,55,93–96,118] In particular, for a vibration with a potential energy that is described by a Morse potential, second-order vibrational perturbation theory (VPT2) provides the exact energy.[125] As the potential energy along a bond stretching coordinate is often well-appoximated by a Morse potential, VPT2 can be expected to provide better energies for the wave functions along these types of coordinates than a variational calculation using the same potential energy surface. On the other hand, in the presence of resonances, that is when states are nearly degenerate and/or strongly coupled, VPT is known to give incorrect answers, the classic example being Fermi resonances.[1,93,135] Such resonances are commonly handled via the deperturb-and-diagonalize method, where terms that couple resonant states are discarded when doing the perturbation theory and then reintroduced via a variational step.[93,97,101,118,135–137] This approach, while effective, requires resonances to be identified so that the effects of the resonances may be properly accounted for.

It is sometimes possible to identify resonances *a priori*. For example, what is now known as Fermi resonance was first discussed by Fermi and Dennison in studies of CO_2.[138] In these works, it was noted that the frequency of the fundamental in the symmetric CO stretching vibration was almost exactly twice the frequency of the doubly-degenerate OCO bending modes, leading to these vibrations being in resonance. Later work by Sibert on H_2CO[139] introduced a collective quantum number, N_t, to account for the polyad of resonances obtained from the relations

$$\nu_1 \approx \nu_5 \approx 2\nu_2 \approx 2\nu_3 \approx 2\nu_4 \approx 2\nu_6 \tag{6.2}$$

For example, the state with one quantum of excitation in mode 5 has the same value of N_t as

the state with one quantum of excitation in both modes 3 and 6, and so there is a resonance between those states. Such polyads have been used in later studies as well.[101]

In the absence of prior knowledge of the important resonances in a system, more automated approaches are required. One approach, used by Handy and coworkers in the development of the SPECTRO program[105] is to consider the differences in harmonic frequencies between transitions. Another, taken in the implementation of vibrational perturbation theory in the CFOUR[106] package is more sophisticated, considering instead the derivatives of the VPT energies with respect to the harmonic frequencies, as outlined by Matthews and Stanton.[140] However, the most widely-used approach is likely the so-called Martin Test,[141] which in its simplest form takes pairs of zero-order states, $|n^{(0)}\rangle$ and $|m^{(0)}\rangle$, and considers the ratio of the coupling between them and their energy difference. This test is obtained by considering the two-by-two coupling matrix with the energy of states $|n^{(0)}\rangle$ and $|m^{(0)}\rangle$ on the diagonal and the coupling between them from perturbation theory. The energies obtained by applying perturbation theory to this matrix are then compared to those obtained via diagonalization, and if the difference is greater than a specified threshold, the states are determined to be in resonance. A common choice for this threshold is 1 cm^{-1}, although values as large as 10 cm^{-1} and as small as 0.1 cm^{-1} have been used in the literature.[55,118]

The Martin test is a reliable, commonly used diagnostic for identifying Fermi resonances and has been used by Barone and coworkers in a recent benchmark study as well as in the implementation of VPT2 in the Gaussian 16 software package.[122,142] It is, however, restricted to the identification of Fermi resonances. Resonances involving states with the same number of quanta of excitation, also known as Darling-Dennison resonances,[143] must be identified by other approaches. This is commonly done by the comparison of energy differences between states, as was done by Barone and coworkers in their recent benchmark study.[142]

Automated approaches are, in general, very successful at accounting for disastrous resonances that lead to obviously incorrect results from VPT. It is worth noting, however, that many resonances have more subtle effects and the identification of such resonances can lead to important changes in the calculated spectrum. For example, in a recent study of

isoprene,[118] Stanton and coworkers found that the simulated spectrum from VPT2 was sensitive to the choice of resonances. In that study, the best agreement with the experimental spectrum was obtained by including not only those resonances identified by the Martin test (for Fermi resonances) and an energy window (for Darling-Dennison resonances), but by also including resonances between all of the CH scissoring modes. This mixture of an automated approach with *a priori* information provided a high-fidelity reproduction of the experimental spectrum.

The previously mentioned automated approaches to resonance identification (energy windows, harmonic derivatives, and the Martin test), are all focused on the VPT corrections to the energies. This focus on energies is not ideal, as Stanton and coworkers have noted that VPT corrections to the transition moments are more sensitive to resonances than the corrections to the energies.[144]

On the other hand, this focus on the energies is entirely logical considering the fact that, for efficiency reasons, most approaches to vibrational perturbation theory build off of work by Nielsen and coworkers and use analytic expressions that encode the corrections to the energies and other properties.[55,98,144–146] This means that corrections to the wave functions are rarely evaluated explicitly. By contrast, in a recent paper (Paper I)[147] the authors described an implementation of VPT building off of work by Kato[116] and Sakurai[114] that uses sparse linear algebra and keeps track of explicit corrections to the wave functions. In this work, we will detail an automated approach to the identification of resonances that uses these explicit corrections to the wave functions. It will provide the beneficial features of the Martin test and energy window approaches while also allowing for the identification of more subtle resonances that manifest more strongly in the corrections to the intensities than the energies.

6.2 Theory

In vibrational perturbation theory, the potential and kinetic energy operators are expanded as Taylor series in the normal mode coordinates and these expansions are used as perturbations.

This provides the following expression for the Hamiltonian

$$H = \lambda^0 H^{(0)} + \lambda^1 H^{(1)} + \lambda^2 H^{(2)} + ... \tag{6.3}$$

where $H^{(0)}$ is the harmonic Hamiltonian, including the terms that are quadratic in p and q. $H^{(1)}$ then includes all terms that are cubic in p and q, $H^{(2)}$ includes all terms that are quartic in p and q, and so forth. The wave functions and energies are also expanded as a formal power series in λ

$$|n\rangle = \lambda^0 |n^{(0)}\rangle + \lambda^1 |n^{(1)}\rangle + \lambda^2 |n^{(2)}\rangle + ... \tag{6.4}$$

$$E_n = \lambda^0 E_n^{(0)} + \lambda^1 E_n^{(1)} + \lambda^2 E_n^{(2)} + ... \tag{6.5}$$

where $|n^{(0)}\rangle$ is an eigenstate of the Hamiltonian in Eq. (6.1) and $E_n^{(0)}$ is the corresponding harmonic energy. In Paper I, we have provided expressions for obtaining corrections to the zero-order energy for any order k, $E_n^{(k)}$, and the corresponding corrections to the wave function, $|n^{(k)}\rangle$, using sparse linear algebra. In that work, we also elaborate on the forms of $H^{(1)}$, $H^{(2)}$, and higher-order perturbations.

The effect of resonances on VPT is to cause the expansions in Eqs. (6.4) and (6.5) to either diverge or simply not to converge. Mechanistically, a resonance occurs between states $|n^{(0)}\rangle$ and $|m^{(0)}\rangle$, when a term of the form $\langle n^{(0)}| H^{(k)} |m^{(0)}\rangle / (E_n^{(0)} - E_m^{(0)})$ becomes too large. This term first occurs in the evaluation of $|n^{(k)}\rangle$ and will contribute to all higher-order corrections. In the notation of Paper I, this comes from

$$|n^{(k)}\rangle = \Pi_O \sum_{i=0}^{k-1} \Delta H_n^{(i)} |n^{(i)}\rangle - \frac{1}{2} \sum_{i=1}^{k-1} \langle n^{(i)}|n^{(k-i)}\rangle |n^{(0)}\rangle \tag{6.6}$$

where

$$\Delta H_n^{(i)} = H^{(i)} - E_n^{(i)} \tag{6.7}$$

$$\Pi_O = (I - |n^{(0)}\rangle \langle n^{(0)}|)(-\Delta H_n^{(0)})^{-1}(I - |n^{(0)}\rangle \langle n^{(0)}|) \tag{6.8}$$

As the perturbation theory is taken to higher order, higher powers of this ratio will enter into the expressions for the corrections to the wave functions. If this term will lead to non-convergence of Eq. (6.4) or Eq. (6.5), this should be noticeable in the corrections to the wave functions.

That is, we know that

$$|n^{(k)}\rangle = \sum_m \langle m^{(0)}|n^{(k)}\rangle \, |m^{(0)}\rangle \tag{6.9}$$

where the expansion coefficients $\langle m^{(0)}|n^{(k)}\rangle$ are obtained by evaluating the matrix-vector products in Eq. (6.6). It is therefore possible to say that a state $|n^{(0)}\rangle$ is resonant with $|m^{(0)}\rangle$ if at any order k, $\langle m^{(0)}|n^{(k)}\rangle$ is larger than a specified threshold. Specifically, if we are performing perturbation theory up to order N, we can define

$$\Xi_{n,m} = \max_{k=0}^{N} \left|\langle m^{(0)}|n^{(k)}\rangle\right| \tag{6.10}$$

and then given a threshold value, $\chi_{\min}$, we say $|n^{(0)}\rangle$ is resonant with $|m^{(0)}\rangle$ if $\Xi_{n,m}$ is greater than $\chi_{\min}$. This leads to a series of pair-wise relations of the form $|n^{(0)}\rangle$ resonant with $|m^{(0)}\rangle$ and $|i^{(0)}\rangle$ resonant with $|j^{(0)}\rangle$ from which a graph of resonant states is constructed.

Similarly to the cyclical resonances noted to be a problem for the Martin test by Stanton and coworkers,[118] the WFC approach also can identify problematic resonances. That is, direct application of WFC algorithm can identify resonances that should not be handled through deperturbation and diagonalization. Our approach to handling this issue is to borrow an idea from implementations of the Martin test and to use an energy window to restrict which states are allowed to be in resonances.[118,142]

The WFC resolves many of the difficulties laid out above for the Martin test. For one, it

allows for a single test that can be applied to both Darling-Dennison and Fermi resonances. Secondly, as the corrections to the wave functions are used directly in evaluating transition intensities, this approach will be sensitive to resonances that affect the intensities more than the energies. Finally, the specified threshold is a dimensionless quantity and therefore treats high- and low-frequency modes equivalently. This is in contrast to the Martin threshold, for which, since vibrational frequencies can range from 50 to 5000 cm^{-1}, a threshold that is appropriate for a high-frequency vibration may not be appropriate for a low-frequency one.

Moreover, the WFC threshold has an easy-to-understand meaning. A threshold value of 1.0 will only identify resonances that contribute to corrections to the wave functions that are larger than the contribution at zeroth order. As perturbation theory assumes the corrections to the wave functions are small, this kind of resonance usually indicates a complete breakdown in the method, such as a case where two zero-order states have exactly or almost exactly the same energy, i.e. $E_n^{(0)} - E_m^{(0)} \approx 0$. By contrast, a threshold value of 0.5 will find corrections that are 50% of the zero-order coefficient, which can change the spectrum obtained, but likely will not correspond to a complete breakdown in the VPT.

Finally, there is a subtlety in the application of the Martin test that is of note. Formally, the Martin test (with a threshold, δ) is expressed as

$$\frac{\langle n^{(0)}| H^{(1)} |m^{(0)}\rangle^4}{(E_n^* - E_m^*)^3} > \delta \tag{6.11}$$

where E_n^* and E_m^* are the deperturbed energies, that is, the energies obtained from VPT2 with the coupling between $|n^{(0)}\rangle$ and $|m^{(0)}\rangle$ removed. This is obtained by comparing the eigenvalues of the matrix

$$\begin{pmatrix} E_n^* & \langle n^*| H |m^*\rangle \\ \langle n^*| H |m^*\rangle & E_m^* \end{pmatrix} \tag{6.12}$$

to the energies obtained by applying first-order perturbation theory to this matrix. Commonly, however, the approximation $(E_n^* - E_m^*) \approx (E_n^{(0)} - E_m^{(0)})$ is made.[118,141] This is justified in the case that states $|n^{(0)}\rangle$ and $|m^{(0)}\rangle$ have similar anharmonicities. As will be noted later

for *cis-cis* HOONO, this approximation does not always hold and whether it is used or not can affect which resonances are identified in significant ways.

6.3 2n+1 Rule

We also note an expression that can prove useful in evaluating the corrections to the energies. It was shown by Wigner that in perturbation theory with a single perturbation, to evaluate the corrections to the energies up to order k it is sufficient to have the corrections to the wave functions only up to order $k/2$. We show here an equivalent derivation for the case of arbitrarily many perturbations

We will start from

$$-\Delta H_n^{(0)} \left|n^{(k)}\right\rangle = \sum_{i=0}^{k-1} \Delta H_n^{(k-i)} \left|n^{(i)}\right\rangle \tag{6.13}$$

and apply on the left with $\langle n^{(j+1)}|$ for some arbitrary j, giving us

$$\left\langle n^{(j+1)}\right| \Delta H_n^{(0)} \left|n^{(k)}\right\rangle = -\sum_{i=0}^{k-1} \left\langle n^{(j+1)}\right| \Delta H_n^{(k-i)} \left|n^{(i)}\right\rangle \tag{6.14}$$

We will also note that

$$\Delta H_n^{(0)} \left|n^{(j+1)}\right\rangle = -\sum_{i=0}^{j} \Delta H_n^{(j+1-i)} \left|n^{(i)}\right\rangle \tag{6.15}$$

and here we can apply on the left with $|n^{(k)}\rangle$, yielding

$$\left\langle n^{(k)}\right| \Delta H_n^{(0)} \left|n^{(j+1)}\right\rangle = -\left\langle n^{(k)}\right| \Delta H_n^{(1)} \left\langle n^{(j)}\right| - \sum_{i=0}^{j-1} \left\langle n^{(k)}\right| \Delta H_n^{(j+1-i)} \left|n^{(i)}\right\rangle \tag{6.16}$$

and then by Hermiticity we can equate Eq. (6.14) and Eq. (6.16). Rearranging that equality,

we then have

$$\langle n^{(j)}|\,\Delta H_n^{(1)}\,|n^{(k)}\rangle = \langle n^{(j+1)}|\,\Delta H_n^{(1)}\,|n^{(k-1)}\rangle + \sum_{i=0}^{k-2}\langle n^{(j+1)}|\,\Delta H_n^{(k-i)}\,|n^{(i)}\rangle \tag{6.17}$$

$$- \sum_{i=0}^{j-1}\langle n^{(k)}|\,\Delta H_n^{(j+1-i)}\,|n^{(i)}\rangle \tag{6.18}$$

which, through p applications of this relation, leads to the expression

$$\langle n^{(0)}|\,\Delta H_n^{(1)}\,|n^{(k)}\rangle = \langle n^{(p)}|\,\Delta H_n^{(1)}\,|n^{(k-p)}\rangle + \sum_{a=1}^{p}\sum_{i=0}^{k-1-a}\langle n^{(a)}|\,\Delta H_n^{(k+1-a-i)}\,|n^{(i)}\rangle \tag{6.19}$$

$$- \sum_{b=2}^{p}\sum_{i=1}^{b-2}\langle n^{(k+1-b)}|\,\Delta H_n^{(b-i)}\,|n^{(i)}\rangle \tag{6.20}$$

$$- \sum_{i=k+1-p}^{k-1}\langle n^{(0)}|\,\Delta H_n^{(k+1-i)}\,|n^{(i)}\rangle \tag{6.21}$$

We then have two cases to consider. First we consider the case of an *odd* value of k. We will let $j = (k-1)/2$. This gives us

$$E_n^{(k)} = \langle n^{(0)}|\,H^{(k)}\,|n^{(0)}\rangle + \sum_{i=1}^{2j}\langle n^{(0)}|\,\Delta H_n^{(k-i)}\,|n^{(i)}\rangle \tag{6.22}$$

$$= \langle n^{(0)}|\,H^{(k)}\,|n^{(0)}\rangle + \langle n^{(0)}|\,\Delta H_n^{(1)}\,|n^{(2j)}\rangle + \sum_{i=1}^{2j-1}\langle n^{(0)}|\,\Delta H_n^{(k-i)}\,|n^{(i)}\rangle \tag{6.23}$$

By applying Eq. (6.21) with $p = j$ and through an impressive amount of fortuitous cancellation, this reduces to

$$E_n^{(k)} = \langle n^{(0)}|\,H^{(k)}\,|n^{(0)}\rangle + \sum_{i=1}^{j}\langle n^{(0)}|\,H^{(k-i)}\,|n^{(j)}\rangle + \sum_{a=1}^{j}\sum_{i=0}^{j}\langle n^{(a)}|\,\Delta H_n^{(k-a-i)}\,|n^{(i)}\rangle \tag{6.24}$$

Similarly, for even k we define $j = k/2$, giving us

$$E_n^{(k)} = \langle n^{(0)}| H^{(k)} |n^{(0)}\rangle + \sum_{i=1}^{2j-1} \langle n^{(0)}| \Delta H_n^{(k-i)} |n^{(i)}\rangle \tag{6.25}$$

$$= \langle n^{(0)}| H^{(k)} |n^{(0)}\rangle + \langle n^{(0)}| \Delta H_n^{(1)} |n^{(2j-1)}\rangle + \sum_{i=1}^{2j-2} \langle n^{(0)}| \Delta H_n^{(k-i)} |n^{(i)}\rangle \tag{6.26}$$

and again by applying Eq. (6.21) with $p = j$, this reduces to

$$E_n^{(k)} = \langle n^{(0)}| H^{(k)} |n^{(0)}\rangle + \sum_{i=1}^{j} \langle n^{(0)}| H^{(k-i)} |n^{(j)}\rangle + \sum_{a=1}^{j-1} \sum_{i=0}^{j} \langle n^{(a)}| \Delta H_n^{(k-a-i)} |n^{(i)}\rangle \tag{6.27}$$

Therefore if we can get corrections to the wave functions through order k, we can write

$$E_n^{(2k+1)} = \langle n^{(0)}| H^{(2k+1)} |n^{(0)}\rangle + \sum_{i=1}^{k} \langle n^{(0)}| H^{(2k+1-i)} |n^{(i)}\rangle + \sum_{a=1}^{k} \sum_{i=0}^{k} \langle n^{(a)}| \Delta H_n^{(2k+1-a-i)} |n^{(i)}\rangle \tag{6.28}$$

$$E_n^{(2k)} = \langle n^{(0)}| H^{(2k)} |n^{(0)}\rangle + \sum_{i=1}^{k} \langle n^{(0)}| H^{(2k-i)} |n^{(i)}\rangle + \sum_{a=1}^{k-1} \sum_{i=0}^{k} \langle n^{(a)}| \Delta H_n^{(2k-a-i)} |n^{(i)}\rangle \tag{6.29}$$

6.4 Results and Discussion

In Fig. 6.1, the results of performing second-order vibrational perturbation theory (VPT2) with resonance handling (blue) and without (red) are shown for CH_4, H_2CO, HNO_3, and HOONO. The corresponding frequencies and intensities are tabulated in the Supporting Info. These systems have been studied previously, including with VPT,[127–129,139,148–150] but are chosen for this work as they broadly demonstrate the different classes of resonance effects common in vibrational problems. All results were evaluated using a partial quartic force field obtained using the Gaussian 16 software package at the MP2/aug-cc-pvtz level of theory and basis,[122] and all VPT2 calculations were performed using the PyVibPTn implementation of the approach described in our previous work.[115,147]

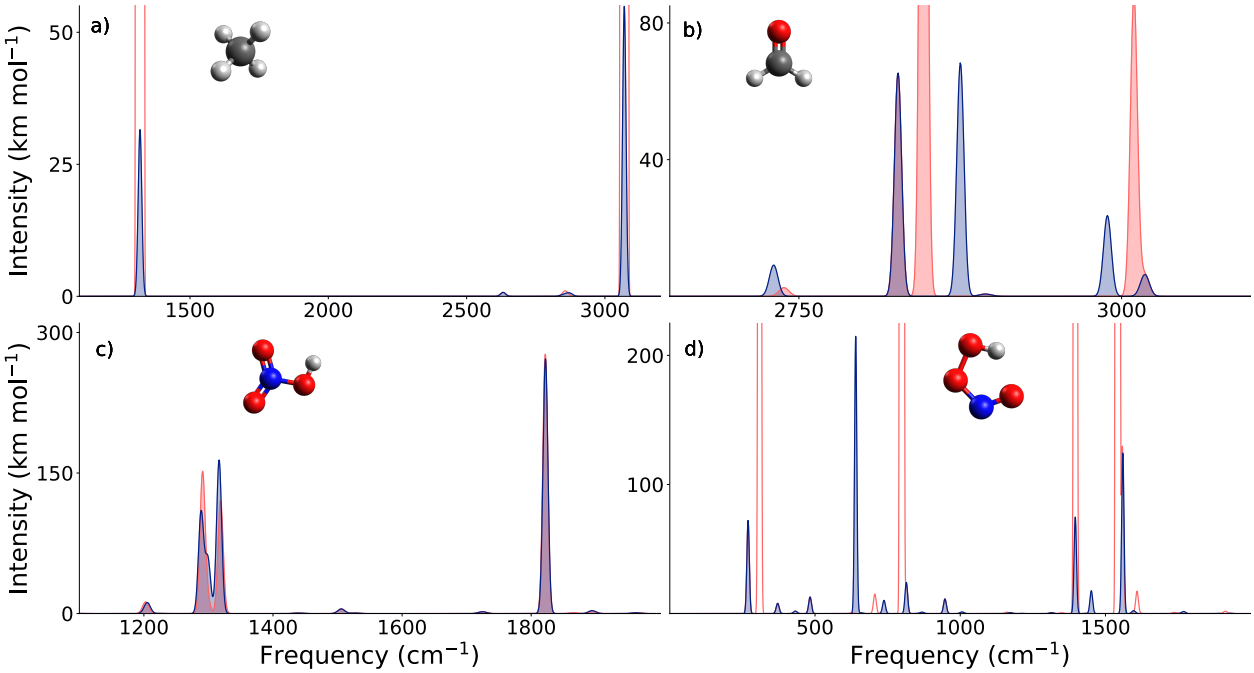

Figure 6.1: Vibrational spectra for with and without resonance handling (blue and red respectively) for (a) CH_4, (b) H_2CO, (c)HNO_3, and (d) HOONO. The corresponding transitions and intensities are provided in Tables 6.1–6.4.

In CH_4 (top left in Fig. 6.1), there is a degeneracy between the CH stretches, but they are completely decoupled due to differences in symmetry. Numerical artifacts, however, lead to small breakages of the symmetries and therefore the decoupling is imperfect in the expansions of $H^{(1)}$ and $H^{(2)}$. The combination of this numerical imperfection with the degenerate CH stretches causes the CH stretch transition intensity to "blow up" (red). On the other hand, the transition frequencies are unaffected by this blow up, lending further credence to the Stanton group's observation that transition moments are more sensitive to resonances than are the energies.[144] By using the WFC approach, however, we easily are able to identify numerical imperfection and once it is corrected, the final intensities are sensible (blue).

There is similarly little change in the transition frequencies of HNO_3 with and without resonance handling. In contrast to CH_4, due to the lack of exact degeneracies, it also displays

only small changes in the transition intensities. The primary difference is in the 1300 cm^{-1} region, where there is a decrease in intensity in the peak around 1290 cm^{-1} and an increase in the intensity of the peak around 1315 cm^{-1}. The first small intensity difference we see corresponds to a transfer of intensity from the state with one quantum of excitation in the HO...N stretch, around 1288 cm^{-1}, to the state with two quanta of excitation in the ONO bend, around 1299 cm^{-1}. The second intensity difference corresponds to an increase in the intensity of the HON bend fundamental from the inclusion of a resonance between the state with one quantum of excitation in the HON bend and the state with one quantum of excitation in both the hydrogen and nitrogen out-of-plane motions. Unlike the first resonance, which is a classic stretch-bend Fermi resonance through states coupled by $H^{(1)}$, this second resonance is between states coupled by $H^{(2)}$ and comes from the fact that the coupling matrix element between these states is large enough (34 cm^{-1}) and the frequency difference is small enough ($\sim$80 cm^{-1}) to cause them to be in resonance. The effect of this resonance on the frequencies of these transitions is minor, yielding 1318 and 1202 cm^{-1} respectively without resonance handling compared to 1316 and 1205 cm^{-1} with resonance handling, however there is an almost 50 km mol^{-1} increase in the intensity of the bend fundamental while the out-of-plane combination band transition has very little change in intensity. That the bend fundamental increases so significantly in intensity when the resonance is introduced likely indicates that the overly large contribution to the correction to the wave function from the out-of-plane combination state led to an overly large destructive effect on the transition moment of the bend fundamental. This resonance would be difficult to identify *a priori* or by considering the changes in the frequencies, but it is easily identified with a method that also considers the effect on the intensities.

As has been seen in prior studies,[139,148] resonances lead to a modulation in both the frequencies and modulation intensities in the spectrum of H_2CO (top right). There is a well-known near-degeneracy between the state with one quantum of excitation in the anti-symmetric CH stretch and the two states with one quantum of excitation the in-plane rock and one in the HCH bend and CO stretch modes respectively. This near-degeneracy leads to

an approximate quadrupling of the transition intensities for these states relative to the case where the resonance is handled. The transition frequencies also shift by about 50 cm^{-1} once the resonance is handled. Further analysis of the effects of resonances on the spectrum of H_2CO will be provided later, but it is worth noting that this important resonance is identified correctly and automatically by the WFC approach.

For HOONO (bottom right in Fig. 6.1), the effects of resonances are most dramatic and there are also clear issues in the spectrum without resonance handling. In the non-resonant spectrum, there are multiple peaks with intensities greater than 5000 km mol^{-1}. In the spectrum with resonances handled, the maximum transition intensity is around 120 km mol^{-1}. There are also a large number of peaks in the spectrum with resonances handled that do no appear in the non-resonant spectrum. This is a manifestation of intensity borrowing from the intense transitions by the nominally dark peaks. In VPT, this most commonly occurs once resonances are introduced, and it would be difficult to identify all of the important resonances without the use of an automated approach.

6.4.1 Analysis of Performance of the Method

The question naturally arises as to how the resonances identified by the WFC approach depend on the choice of the threshold parameter. We will use H_2CO as a case study, owing to the presence of multiple important resonances in its vibrational spectrum. When labeling states, we will borrow notation from Romanowski *et al.*[148] and write $|i_n\rangle^{(0)}$ to indicate the state with n quanta of excitation in mode i and $|i_n j_m\rangle^{(0)}$ to indicate the state with n quanta in mode i and m in mode j. In H_2CO, mode 1 is the symmetric CH stretch, mode 2 is the CO stretch, mode 3 is the HCH bend, mode 4 is the out-of-plane motion of the hydrogens, mode 5 is the anti-symmetric CH stretch, and 6 is the in-plane rocking motion of the hydrogens.

In Fig. 6.2, the vibrational spectrum for H_2CO evaluated with different values for the threshold (blue) is compared to the vibrational spectrum obtained when considering the resonances derived from the polyad quantum number that accounts for Eq. (6.2) (red). This polyad represents the most complete set of resonances we might expect to want to use.

For the largest threshold value tested, 1.0, corresponding to a wave function correction equal to the contribution of the zero-order state itself, we identify only one resonance, between the state with one quantum of excitation in the anti-symmetric CH stretch $|5_1\rangle^{(0)}$, and the state with one quantum of excitation in both the hydrogen in-plane rocking motion and the CO stretch, $|6_1 2_1\rangle^{(0)}$. This resonance arises primarily from near-degeneracy at the harmonic level, the states having harmonic frequencies of 3047 and 3020 cm^{-1} respectively while having only a modest sized coupling matrix element of 57 cm^{-1}. At a threshold of 0.5, or half of the contribution at zero-order, the identified resonances remain the same.

Between values of 0.4 and 0.2 for the threshold, the algorithm includes another resonance, $|5_1\rangle^{(0)} \sim |6_1 3_1\rangle^{(0)}$. This is illustrated in with in Fig. 6.2 and Table 6.5 for a value of 0.3 This resonance, $|5_1\rangle^{(0)} \sim |6_1 3_1\rangle^{(0)}$, arises primarily due to a modest sized coupling element of 48 cm^{-1} between the states, as the harmonic frequencies are separated by over 250 cm^{-1}. Importantly, despite its small coupling the the bright $|5\rangle^{(0)}$ mode and despite the relatively small concomitant shift in the transition energy (8 cm^{-1}) the intensity of the transition nearly quadruples and another peak becomes noticeable in the spectrum.

Finally, at a value of 0.1 (panel (d) in Fig. 6.2) the algorithm identifies resonances including $|1_1\rangle^{(0)}$, although the effect on the spectrum is minor. The triad identified is $|1_1\rangle^{(0)} \sim |3_2\rangle^{(0)} \sim |3_1 2_1\rangle^{(0)}$. It is known that for systems with CH stretches, the stretch is coupled to the overtone in the bend,[118,151] and we note this again for H_2CO, although in this case the resonance is admittedly weak. The origin of the resonance between the stretch fundamental $|1_1\rangle^{(0)}$ and bend overtone $|3_2\rangle^{(0)}$ is a small but signficant coupling matrix element of 25 cm^{-1} with a modest sized difference in the harmonic frequencies, being separated by around 90 cm^{-1}. The third member of this triad is nominally a combination of CO and HCH excitations. However, looking at the mode vectors provided in Figs. 6.3 and 6.4, it is clear that mode 2, the nominal CO stretch, has a large contribution from the HCH bend. Thus this triad could be interpreted to be a classic stretch-bend Fermi resonance, just with the HCH bend contribution distributed over two normal modes.

Empirically, we have found that a threshold value of around 0.3 is effective. At this

threshold, we recover both the resonances that cause the perturbation theory to break down as well as the resonances that have a significant effect on the spectrum without leading to an obvious break down. It is possible that going to a smaller threshold value would lead to the inclusion of more relevant resonances, however the effect of these resonances will be smaller. Moreover, by increasing the size of the resonant space, we come closer to the limit of performing a variational calculation with a quartic force-field. Not only will such a variational calculation be more computationally intensive than a VPT calculation, but it can be expected to yield worse results than VPT, given that for Morse oscillators it is known that VPT2 provides the exact corrections to the harmonic energies. Similarly, by making the resonant space overly large, a greater reliance is placed on the energy window approach to excluding spurious resonances mentioned earlier.

6.4.2 Comparison to Previous Approaches

It is also important to note how the WFC method compares to more traditional approaches. For this, we will consider the Martin test at different energy thresholds for H_2CO. The results of this analysis are plotted in Fig. 6.5 and the corresponding frequencies and intensities are given in Table 6.6. With the common default of 1.0 cm^{-1}, the only resonance in H_2CO identified is $|5_1\rangle^{(0)} \sim |6_1 2_1\rangle^{(0)}$. Decreasing the threshold value to 0.1 cm^{-1}, the other member of the triad previously identified by the WFC approach, $|6_1 3_1\rangle^{(0)}0$, remains unincluded. At a value of 1.0 cm^{-1}, as with the WFC approach at thresholds greater than 0.2, no resonances are identified involving symmetric CH stretch. Once the Martin test threshold is decreased a value of 0.1 cm^{-1}, the resonance $|1_1\rangle^{(0)} \sim |3_2\rangle^{(0)}$ is identified, but the third member of the triad identified by the WFC approach, $|3_1 2_1\rangle^{(0)}$, is not identified.

In HOO′NO″, there is a near-degeneracy between the state with two quanta of excitation in the anti-symmetric combination of the hydrogen and nitrogen out-of-plane bending motions and the state with one quantum of excitation in the O′N stretch. The displacement vectors for these motions are visualized in Figs. 6.7 and 6.8 If this resonance is not handled, there is a "blow up" in the intensity of the O′N stretch. Whether or not this resonance

is identified by the Martin test depends on the form of the denominator used. As seen in Fig. 6.6, if the approximation that $E_n^* - E_m^* \approx E_n^{(0)} - E_m^{(0)}$ is made, this resonance is identified at a threshold value of 1.0 cm^{-1}. By contrast, if the deperturbed energy difference is used in the denominator, due to large differences in anharmonicities in the out-of-plane motions and the O′N stretch, this resonance is not identified. This subtlety–whether or not to use the harmonic or deperturbed energies–is obviated in the WFC approach as the issues with the intensity will be directly reflected in the corrections to the wave functions.

6.5 Conclusion

Different choices of resonances for vibrational perturbation theory can lead to qualitative differences in the simulated spectra obtained. By focusing on the corrections to the wave functions, as explicitly provided in Paper I, it is possible to obtain a method for the identification of resonances that is straightforward and effective with a minimum of ambiguity. This approach, which we call the wave function correction approach, compares favorably to existing methodologies for the identification of resonances, allowing for the identification of both Fermi and Darling-Dennison resonances. It has been shown to be effective in identifying important resonances in both H_2CO and HOONO, and work is ongoing to characterize its performance in systems like the $Br^- \ldots HOCl$ complex which was recently studied using *a priori* identification of resonances through polyads,[8] as well as to determine if any additions should be made to the algorithm when the perturbation theory is extended to higher-order. The algorithm as presented generalizes cleanly to aribtrary order, but given that 4th and higher-order VPT is known to be plagued by resonances,[97] it is possible that further additions similar to energy window condition described above will become necessary. It has also been shown by Stanton and coworkers that a mixed approach to the identification of resonances where polyads are combined with automatic identification can provide a powerful method for the identification of all important resonances.[118] The WFC approach, and its implementation in the PyVibPT*n* package for vibrational perturbation theory is well-suited to this extension as well.

Table 6.1: Transitions with intensities greater than 1.0 km mol^{-1} and corresponding harmonic frequencies and intensities evaluated with and without resonance handling for CH_4. The corresponding spectrum is plotted in panel (a) of Fig. 6.1.

	Harmonic		Anharmonic	
State[a]	Frequency (cm^{-1})	Intensity ($\frac{\text{km}}{\text{mol}}$)	Frequency(cm^{-1})	Intensity ($\frac{\text{km}}{\text{mol}}$)
With Resonance Handling				
0 0 0 0 0 0 0 0 0 1	3204.23246	16.25730	3070.01437	17.43464
0 0 0 0 0 0 0 0 1 0	3204.23246	16.25730	3070.01308	17.43458
0 0 0 0 0 0 0 1 0 0	3204.23246	16.25730	3070.01589	17.43462
0 0 1 0 0 0 0 0 0 0	1356.17500	10.90749	1319.16426	11.22876
0 1 0 0 0 0 0 0 0 0	1356.17500	10.90749	1319.16482	11.22875
1 0 0 0 0 0 0 0 0 0	1356.17500	10.90749	1319.16543	11.22876
0 0 1 0 0 0 0 0 0 1	4560.40746	0.00000	4361.46672	1.14345
1 0 0 0 0 0 0 0 1 0	4560.40746	0.00000	4361.80204	1.14156
0 1 0 0 0 0 0 1 0 0	4560.40746	0.00000	4361.47748	1.14346
Without Resonance Handling				
0 0 0 0 0 0 0 0 0 1	3204.23246	16.25730	3070.02012	5894.13676
0 0 0 0 0 0 0 0 1 0	3204.23246	16.25730	3070.01751	8805462.51540
0 0 0 0 0 0 0 1 0 0	3204.23247	16.25730	3070.02091	8803747.80179
0 0 1 0 0 0 0 0 0 0	1356.17500	10.90749	1319.16578	755093088.45911
0 1 0 0 0 0 0 0 0 0	1356.17500	10.90749	1319.16670	67908.62375
1 0 0 0 0 0 0 0 0 0	1356.17500	10.90749	1319.16653	755100574.67772

[a]State labels correspond to the number of excitations in the corresponding normal mode, ordered by frequency (lowest-to-highest) from left to right.

Table 6.2: Transitions with intensities greater than 1.0 km mol^{-1} and frequencies between 2500 and 3500 cm^{-1} along with corresponding harmonic frequencies and intensities evaluated with and without resonance handling for H_2CO. The corresponding spectrum is plotted in panel (b) of Fig. 6.1.

	Harmonic		Anharmonic	
State[a]	Frequency (cm^{-1})	Intensity ($\frac{\text{km}}{\text{mol}}$)	Frequency(cm^{-1})	Intensity ($\frac{\text{km}}{\text{mol}}$)
With Resonance Handling				
0 0 0 0 0 1	3047.51537	88.36168	2875.10501	68.36121
0 0 0 0 1 0	2973.37769	66.67875	2826.80117	65.48012
0 0 0 1 0 0	1752.95345	67.77454	1721.03944	68.56550
0 0 1 0 0 0	1540.08383	10.68608	1507.98896	9.33306
0 1 0 0 0 0	1266.93205	9.39583	1246.70825	9.95761
1 0 0 0 0 0	1196.88408	7.03821	1180.25175	7.21334
0 0 2 0 0 0	3080.16766	0.00000	3018.00391	6.37681
0 1 0 1 0 0	3019.88550	0.00000	2989.00124	23.62636
0 1 1 0 0 0	2807.01588	0.00000	2730.46698	9.13525
Without Resonance Handling				
0 0 0 0 0 1	3047.51536	88.36168	3009.54043	88.06293
0 0 0 0 1 0	2973.37769	66.67875	2826.80118	65.48014
0 0 0 1 0 0	1752.95344	67.77454	1721.03933	68.56534
0 0 1 0 0 0	1540.08383	10.68608	1507.98986	9.33316
0 1 0 0 0 0	1266.93205	9.39583	1246.70890	9.95765
1 0 0 0 0 0	1196.88408	7.03821	1180.25037	7.21326
0 0 2 0 0 0	3080.16765	0.00000	3018.00619	6.37682
0 1 0 1 0 0	3019.88549	0.00000	2846.65348	344.82602
0 1 1 0 0 0	2807.01587	0.00000	2738.38214	2.53086

[a]State labels correspond to the number of excitations in the corresponding normal mode, ordered by frequency (lowest-to-highest) from left to right.

Table 6.3: Transitions with intensities greater than 1.0 km mol^{-1} and frequencies between 1000 and 2000 cm^{-1} along with corresponding harmonic frequencies and intensities evaluated with and without resonance handling for HNO_3. The corresponding spectrum is plotted in panel (c) of Fig. 6.1.

	Harmonic		Anharmonic	
State[a]	Frequency (cm^{-1})	Intensity ($\frac{\text{km}}{\text{mol}}$)	Frequency(cm^{-1})	Intensity ($\frac{\text{km}}{\text{mol}}$)
With Resonance Handling				
0 0 0 0 0 0 0 0 0 1	3718.06522	97.48009	3537.46363	80.80775
0 0 0 0 0 0 0 0 1 0	1846.23608	275.54771	1822.13108	272.06442
0 0 0 0 0 0 0 1 0 0	1343.42521	123.70163	1316.53350	163.26114
0 0 0 0 0 0 1 0 0 0	1315.91749	188.22394	1288.54509	107.40302
0 0 0 0 2 0 0 0 0 0	1789.03269	0.00000	1724.46691	2.00469
0 0 2 0 0 0 0 0 0 0	1331.60461	0.00000	1299.00336	58.88209
0 1 0 0 0 0 1 0 0 0	1933.08747	0.00000	1894.43104	3.14054
0 0 1 0 1 0 0 0 0 0	1560.31865	0.00000	1505.76928	4.91745
1 0 0 1 0 0 0 0 0 0	1260.34112	0.00000	1205.20731	11.69635
1 1 0 1 0 0 0 0 0 0	1850.00339	0.00000	1782.88136	3.29750
0 1 2 0 0 0 0 0 0 0	1921.26688	0.00000	1873.32002	1.14136
Without Resonance Handling[b]				
0 0 0 0 0 0 0 0 1 0	1846.23608	275.54771	1821.88968	276.89909
0 0 0 0 0 0 0 1 0 0	1343.42521	123.70163	1318.82756	120.49935
0 0 0 0 0 0 1 0 0 0	1315.91749	188.22394	1290.72786	144.06185
0 0 2 0 0 0 0 0 0 0	1331.60461	0.00000	1296.82415	17.95633
0 1 0 0 0 0 1 0 0 0	1933.08747	0.00000	1896.33060	2.13469

[a]State labels correspond to the number of excitations in the corresponding normal mode, ordered by frequency (lowest-to-highest) from left to right.

[a]Transitions that do not change in intensity by more than 0.5 km mol^{-1} without resonance handling are not shown.

Table 6.4: Transitions with intensities greater than 2.5 km mol^{-1} and frequencies smaller than 1600 cm^{-1} along with corresponding harmonic frequencies and intensities evaluated with and without resonance handling for HOONO. The corresponding spectrum is plotted in panel (d) of Fig. 6.1.

	Harmonic		Anharmonic	
State[a]	Frequency (cm^{-1})	Intensity ($\frac{\text{km}}{\text{mol}}$)	Frequency(cm^{-1})	Intensity ($\frac{\text{km}}{\text{mol}}$)
With Resonance Handling				
0 0 0 0 0 0 0 1 0	1568.50212	149.98263	1559.76870	124.49906
0 0 0 0 0 0 1 0 0	1433.60941	79.93619	1396.03746	74.72334
0 0 0 0 0 1 0 0 0	970.87676	12.90991	947.27221	11.24976
0 0 0 0 1 0 0 0 0	836.39478	31.15684	814.30121	24.11139
0 0 0 1 0 0 0 0 0	715.88331	215.78520	640.04794	214.74107
0 0 1 0 0 0 0 0 0	524.09935	25.68226	482.96818	12.83835
1 0 0 0 0 0 0 0 0	355.73348	62.64685	269.51064	72.06465
2 0 0 0 0 0 0 0 0	711.46696	0.00000	432.14827	1.91487
0 0 0 1 1 0 0 0 0	1552.27809	0.00000	1451.22575	17.50188
1 0 1 0 0 0 0 0 0	879.83283	0.00000	737.54541	10.15116
Without Resonance Handling[b]				
0 0 0 0 0 0 0 1 0	1568.50212	149.98263	1558.16075	129.74103
0 0 0 0 0 0 1 0 0	1433.60941	79.93619	1542.06374	120637.70297
0 0 0 1 0 0 0 0 0	715.88331	215.78520	798.92471	67817.90098
0 0 0 2 0 0 0 0 0	1431.76662	0.00000	1396.52898	5986.34756
2 0 0 0 0 0 0 0 0	711.46696	0.00000	309.30539	3323.60709
0 0 0 1 1 0 0 0 0	1552.27809	0.00000	1608.56879	17.27713
1 0 1 0 0 0 0 0 0	879.83283	0.00000	705.92925	15.15432

[a]State labels correspond to the number of excitations in the corresponding normal mode, ordered by frequency (lowest-to-highest) from left to right.

[a]Transitions that change in intensity by less than 0.5 km mol^{-1} or in frequency by less than 5 cm^{-1} without resonance handling are not shown.

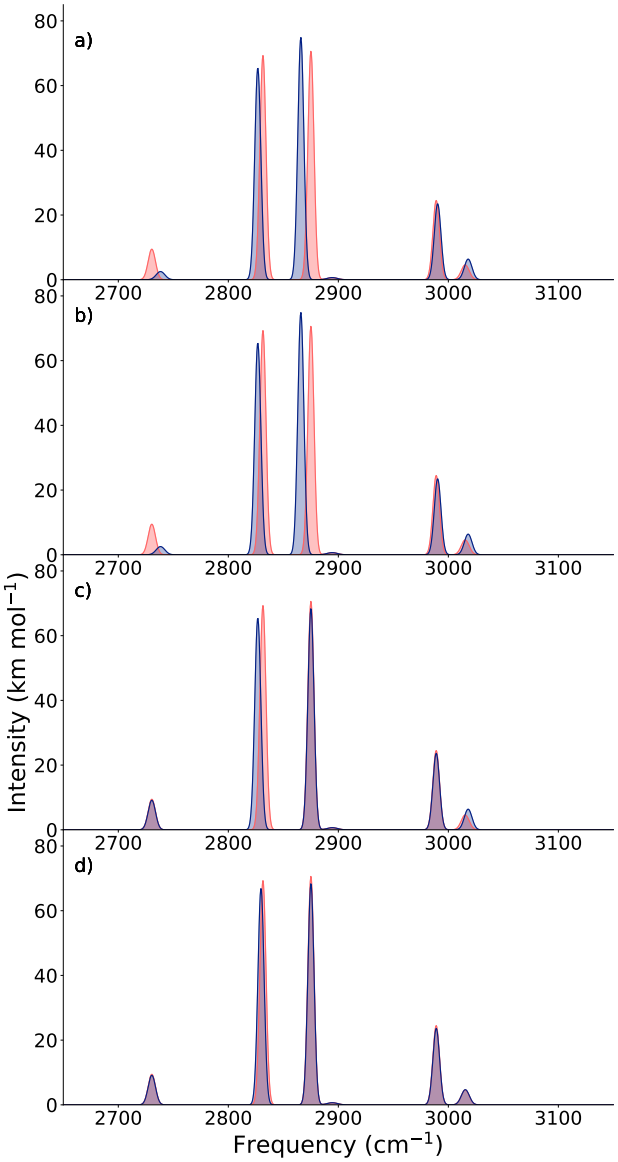

Figure 6.2: Vibrational spectra for H_2CO at threshold values of 1.0 (a), 0.5 (b), 0.3 (c), and 0.1 (d). The corresponding resonant spaces for degeneracy handling are provided in Table 6.5.

Table 6.5: States involved in resonance handling for different values of the threshold for H_2CO along with transition frequencies and intensities. Resonance spaces are grouped by symmetry. The corresponding spectra are plotted in Fig. 6.2.

Threshold	B_2			A_1		
	State	Frequency (cm^{-1})	Intensity (km mol^{-1})	State	Frequency (cm^{-1})	Intensity (km mol^{-1})
1.0	$\|5_1\rangle^{(0)}$	2866	74.87	$\|1_1\rangle^{(0)\,a}$	2827	65.48
	$\|6_1 2_1\rangle^{(0)}$	2990	23.50			
0.5	$\|5_1\rangle^{(0)}$	2866	74.87	$\|1_1\rangle^{(0)\,a}$	2827	65.48
	$\|6_1 2_1\rangle^{(0)}$	2990	23.50			
0.3	$\|5_1\rangle^{(0)}$	2878	65.62	$\|1_1\rangle^{(0)\,a}$	2827	65.48
	$\|6_1 3_1\rangle^{(0)}$	2730	9.14			
	$\|6_1 2_1\rangle^{(0)}$	2989	23.62			
0.1	$\|5_1\rangle^{(0)}$	2875	68.36	$\|1_1\rangle^{(0)}$	2829	67.02
	$\|6_1 3_1\rangle^{(0)}$	2730	9.14	$\|3_2\rangle^{(0)}$	3015	4.68
	$\|6_1 2_1\rangle^{(0)}$	2989	23.62	$\|3_1 2_1\rangle^{(0)}$	3221	0.49

[a]No resonances with this state are identified at this threshold.

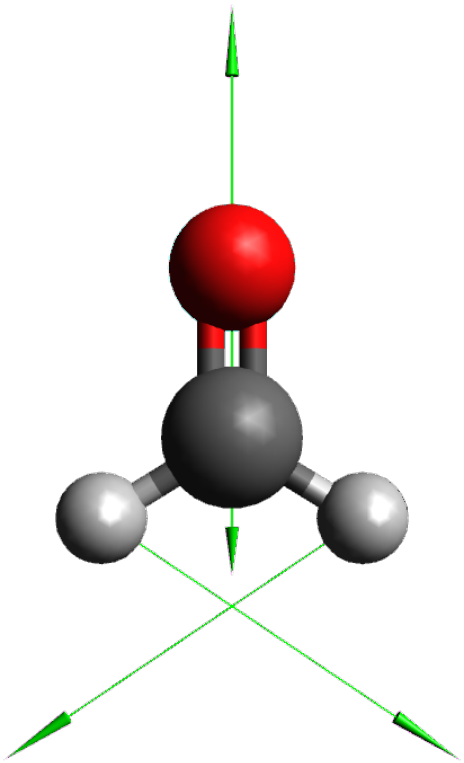

Figure 6.3: Displacement vectors for mode 2 in H_2CO.

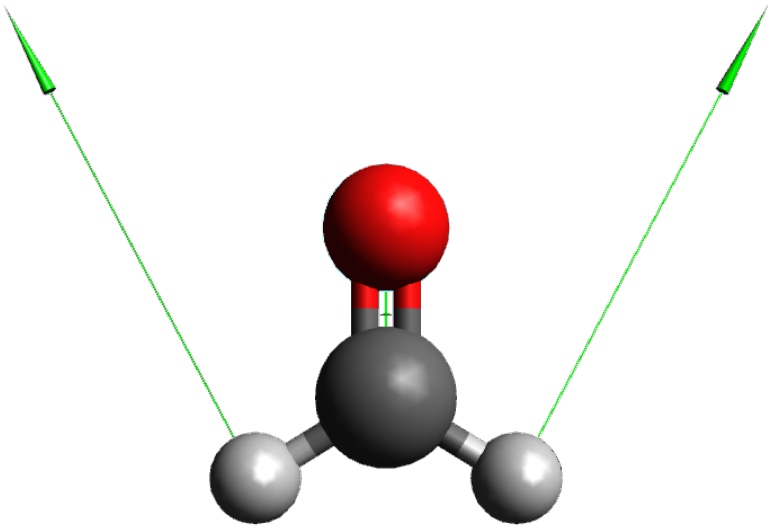

Figure 6.4: Displacement vectors for mode 3 in H_2CO.

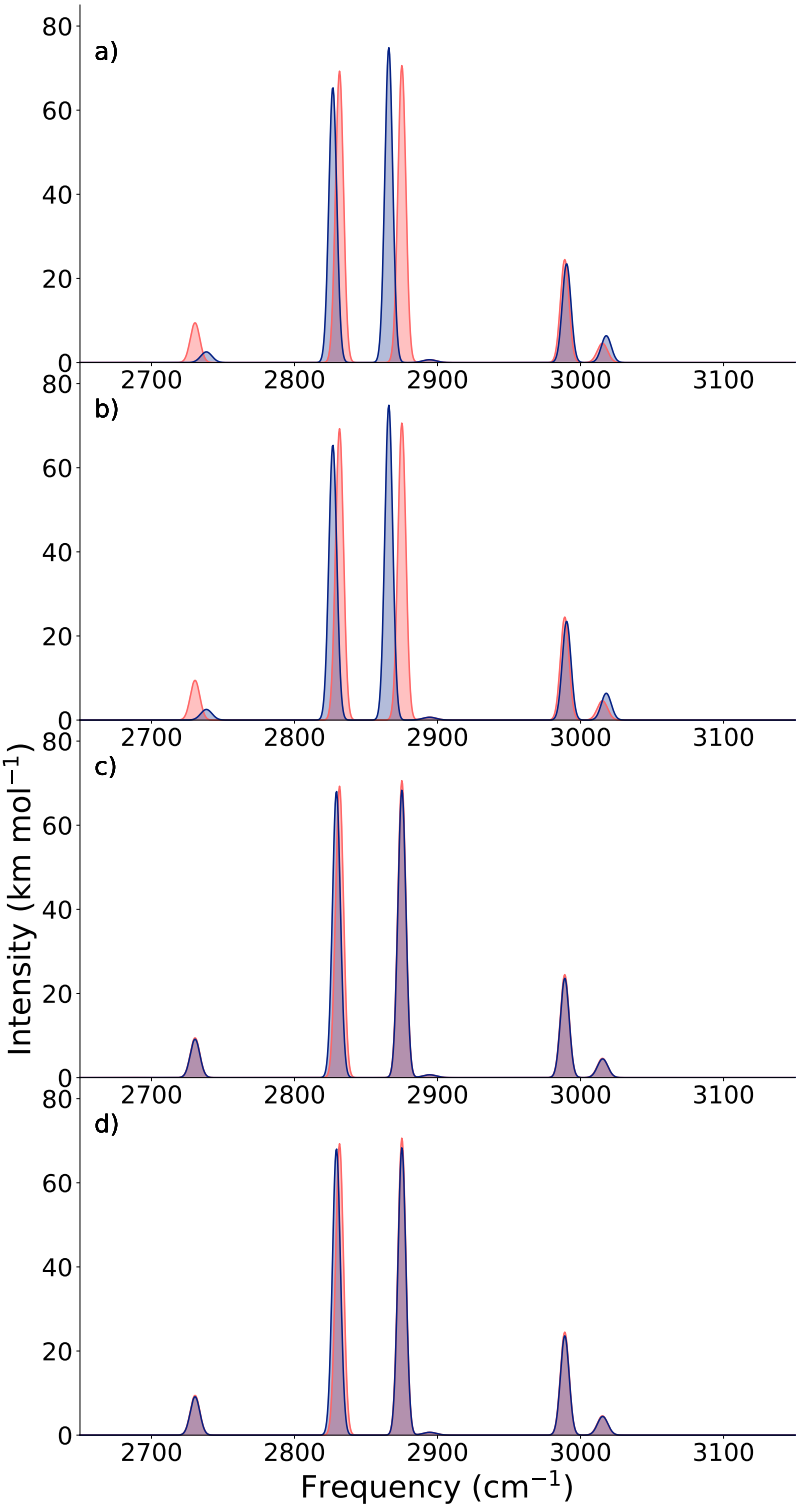

Figure 6.5: Vibrational spectra for H_2CO with resonances identified by the Martin test with threshold values of 1.0 cm^{-1} (a), 0.5 cm^{-1} (b), 0.3 cm^{-1} (c), and 0.1 cm^{-1} (d). The corresponding resonant spaces for degeneracy handling are provided in Table 6.6.

Table 6.6: States involved in resonance handling via the Martin test for different values of the energy threshold for H_2CO along with transition frequencies and intensities. Resonance spaces are grouped by symmetry. The corresponding spectra are plotted in Fig. 6.5.

Threshold	B_2			A_1		
	State	Frequency	Intensity	State	Frequency	Intensity
(cm^{-1})		(cm^{-1})	(km mol^{-1})		(cm^{-1})	(km mol^{-1})
1.0	$\|5_1\rangle^{(0)}$	2866	74.87	$\|1_1\rangle^{(0)\,a}$	2827	65.48
	$\|6_12_1\rangle^{(0)}$	2990	23.50			
0.5	$\|5_1\rangle^{(0)}$	2866	74.87	$\|1_1\rangle^{(0)\,a}$	2827	65.48
	$\|6_12_1\rangle^{(0)}$	2990	23.50			
0.3	$\|5_1\rangle^{(0)}$	2878	65.62	$\|1_1\rangle^{(0)}$	2829	68.15
	$\|63_1\rangle^{(0)}$	2730	9.14	$\|3_2\rangle^{(0)}$	3015	4.45
	$\|62_1\rangle^{(0)}$	2989	23.62			
0.1	$\|5_1\rangle^{(0)}$	2875	68.36	$\|1_1\rangle^{(0)}$	2829	68.15
	$\|6_13_1\rangle^{(0)}$	2730	9.14	$\|3_2\rangle^{(0)}$	3015	4.68
	$\|6_12_1\rangle^{(0)}$	2989	23.62			

[a]No resonances with this state are identified at this threshold.

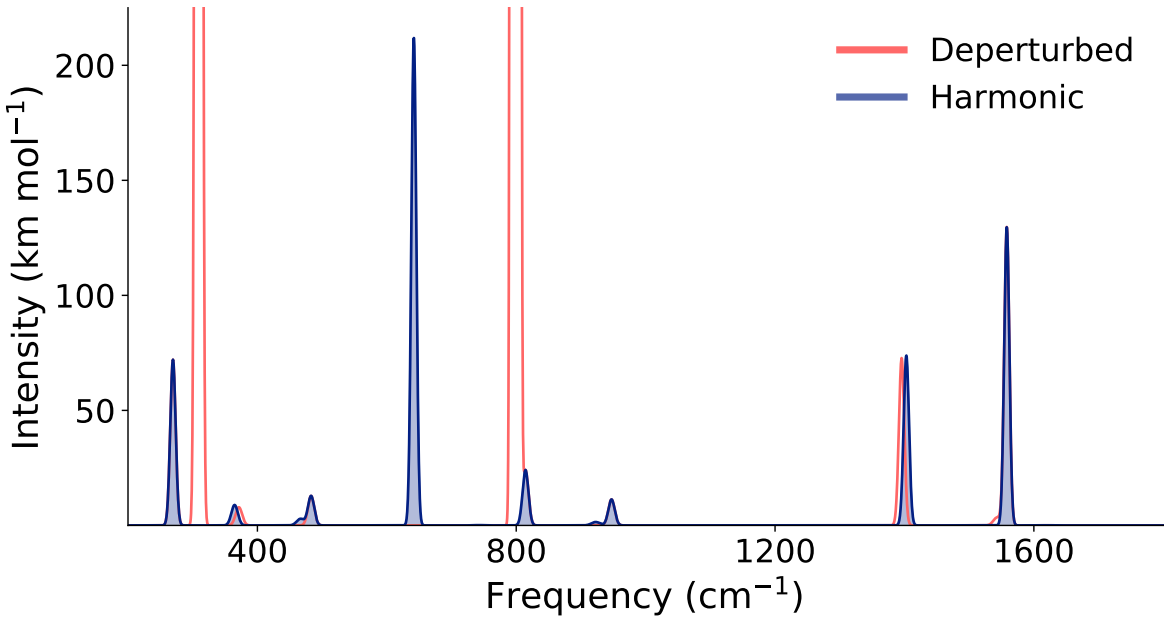

Figure 6.6: Simulated spectra for HOONO using the Martin test with a threshold value of 1 cm^{-1} with the denominator in Eq. (6.11) determined by either the harmonic frequency difference (blue) or the deperturbed energy difference (red).

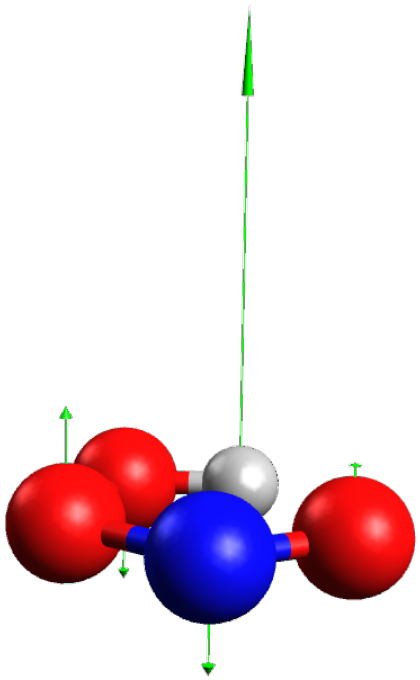

Figure 6.7: Displacement vectors for the normal mode corresponding to the anti-symmetric combination of the out-of-plane hydrogen and nitrogen bending motions in HOONO.

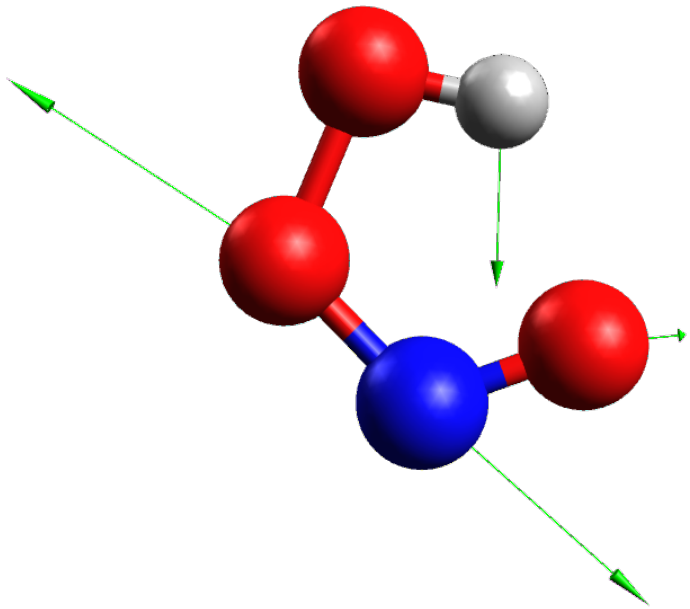

Figure 6.8: Displacement vectors for the O′N stretch mode in HOONO.

Chapter 7

CONCLUSION

The work described above spans the methodological spectrum. After a description of the molecular Hamiltonian and methodologies for developing representations of it, the first application described the use of discrete variable representations along the OO stretching coordinate of the water dimer to investigate the origin of a surprising structure/frequency relationship in hydrogen bonds in water clusters and ion water clusters. In that work, low-dimensional representations provided a validation of a simple analytic model for this relationship as arising from changes in the local electric field upon extension of the OH bond length. By applying that analytic model to AIMD simulations, a good comparison to other theoretical methods for simulating the spectrum of liquid water was obtained,

In the next chapter, the H_5^+ molecular ion was investigated using a four-dimensional model. By using an adiabatic separation of the high-frequency modes from the low-frequency ones, a system of coupled two-dimensional models was obtained. Through the use of two-dimensional discrete variable representations, this pair of coupled 2D models was solved and the forms of the vibrational wave functions of H_5^+ were inspected. It was found that there are strong signatures of tunneling in the spectrum of H_5^+.

In the third chapter, a flexible implementation of vibrational perturbation theory was described. This implementation, which makes use of sparse matrix methods, provides a powerful tool for investigating the origins of spectral intensities in molecular systems. The corrections to the energies and intensities from second- and fourth-order perturbation theory were analyzed and it was found that the use of proper curvilinear internal coordinates leads to potentially better behaved expansions. It was also found that the use of Morse coordinates led to excellent results, and therefor suggests that a generalization of the Morse coordinates

could provide even better results.

In the final chapter, a methodology for the automatic identification of resonances in VPT was described. This method retained all of the benefits of existing approaches while focusing on a the corrections to the wave functions from VPT instead of the corrections to the energies. The algorithm was applied to H_2CO and HOONO and it was found that there are important resonances that standard approaches miss, but which this new method identifies.

These works have been discrete vignettes applying independent methods to independent systems. In the first half, highly-accurate low-dimensional models were used and in the second, more approximate methods were developed and applied. This distinction between the use of low-dimensional, accurate methods and high-dimensional, approximate ones is common, but also artificial. On the one hand, this separation is artificial because there are methods like diffusion Monte Carlo,[5] the vibrational self-consistent field/vibrational configuration interaction approach,[133] and the multiconfiguration time-dependent Hartree method[134] which provide highly-accurate results in high dimensional spaces. More fundamentally, this separation is artificial because the accurate and approximate methods are complementary and can in fact be used together.

It is often the case that in a molecular system there are degrees of freedom that are poorly-treated by approximate methods and there are degrees of freedom for which an approximate treatment is effective. In this case, it is advantageous to avoid doing unnecessary work and to treat this second class of degrees of freedom through the more approximate approaches. It is beyond the scope of this work to explain exactly how this is done, but we have used such an approach in the exploration of vibrational effects in *tert*-butyl hydrogen peroxide and one of its radical analogs.[7,152,153] In that work, the OH stretch and COOH torsion motions were treated through highly-accurate methods, while the effects of the remaining degrees of freedom were treated approximately. Specifically, discrete variable representations were used along with an adiabatic separation of the OH stretch and COOH torsion modes. To account for the remaining degrees of freedom, the potential energy surface along the COOH torsional motion was corrected by adding on the harmonic zero-point energy as a

function of the torsional coordinate using the reaction path normal mode approach. This model therefore accounted for all of the motions in the system, while remaining simple to construct and evaluate. Instead of purely harmonic zero-point energy, it is also possible to imagine including zero-point energy from vibrational perturbation theory calculations. As most of the normal modes of the system were only mildly perturbed by stretch and torsion motions, it is possible to imagine an efficient approach for evaluating the partial quartic force field needed for VPT2. In this approach, the subset of modes that do change significantly in character as the torsion is displaced would first be determined. A partial quartic force field would then be evaluated in this subspace of modes and finally this force field would be used to update the quartic force field at the equilibrium geometry. From this, VPT2 calculations would be possible to perform.

Another possible approach is to use the wave function corrections from perturbation theory as part of a direct-product basis scheme with a DVR. The efficacy of such an approach would depend on how effectively the coupling in the potential can be evaluated between the degrees of freedom that are treated with discrete variable representations and those that are treated with VPT. By the appropriate choice of points used to evaluate the force field used in VPT, it is would also be possible to avoid excess potential evaluations.

BIBLIOGRAPHY

[1] E. B. Wilson, J. C Decius, and P. C. Cross. *Molecular Vibrations*. Dover, New York, 1955.

[2] Harald H. Nielsen. The Vibration-Rotation Energies of Polyatomic Molecules. *Phys. Rev.*, 60(11):794–810, dec 1941.

[3] Harald H. Nielsen. The vibration-rotation energies of molecules. *Rev. Mod. Phys.*, 23:90–136, Apr 1951.

[4] John C. Light and Tucker Carrington. Discrete-Variable Representations and their Utilization. In *Adv. Chem. Phys.*, chapter 4, pages 263–310. Wiley-Blackwell, mar 2007.

[5] James B. Anderson. A random-walk simulation of the schrödinger equation: H_3^+. *J. Chem. Phys.*, 63(4):1499–1503, 1975.

[6] James B. Anderson. Quantum chemistry by random walk. h ^2p, h_3^+ d_{3h} $^1a_1'$, h_2 $^3\sigma_u^+$, h_4 $^1\sigma_g^+$, be ^1s. *J. Chem. Phys.*, 65(10):4121–4127, 1976.

[7] Anne S. Hansen, Trisha Bhagde, Yujie Qian, Alyssa Cavazos, Rachel M. Huchmala, Mark A. Boyer, Coire F. Gavin-Hanner, Stephen J. Klippenstein, Anne B. McCoy, and Marsha I. Lester. Infrared spectroscopic signature of a hydroperoxyalkyl radical (·QOOH). *J. Chem. Phys.*, 156(1), jan 2022.

[8] Santino J Stropoli, Thien Khuu, Joseph P Messinger, Mark A. Boyer, Natalia V. Karimova, Coire F. Gavin-Hanner, Sayoni Mitra, Anton L Lachowicz, Nan Yang, Sean C Edington, R Benny Gerber, Anne B McCoy, and Mark A Johnson. Electronic and mechanical anharmonicities in the vibrational spectra of the H-bonded, cryogenically cooled X^-·HOCl (X=Cl, Br, I) complexes: Characterization of the strong anionic H-bond to an acidic OH group. *The Journal of Chemical Physics*, 156:174303, 5 2022.

[9] Santino J. Stropoli, Thien Khuu, Joseph P. Messinger, Natalia V. Karimova, Mark A. Boyer, Itai Zakai, Sayoni Mitra, Anton L. Lachowicz, Nan Yang, Sean C. Edington, R. Benny Gerber, Anne B. McCoy, and Mark A. Johnson. Preparation and Characterization of the Halogen Bonding Motif in the Isolated Cl^-·IOH Complex with Cryogenic Ion Vibrational Spectroscopy. *Journal of Physical Chemistry Letters*, 13:2750–2756, 3 2022.

[10] E. Bright Wilson. Some mathematical methods for the study of molecular vibrations. *The Journal of Chemical Physics*, 9:76, 12 1941.

[11] D. T. Colbert and W. H. Miller. A novel discrete variable representation for quantum mechanical reactive scattering via the s-matrix kohn method. *J. Chem. Phys.*, 96:1982–1991, 1992.

[12] George H. Gardenier, Mark. A. Johnson, and Anne B. McCoy. Spectroscopic study of the ion-radical h-bond in $h_4o_2^+$. *J. Phys. Chem. A*, 113(16):4772–4779, 2009.

[13] Matthew K. Sprague, Laura A. Mertens, Heather N. Widgren, Mitchio Okumura, Stanley P. Sander, and Anne B. McCoy. Cavity ringdown spectroscopy of the hydroxymethyl-peroxy radical. *J. Phys. Chem. A*, 117(39):10006–10017, 2013.

[14] W. H. Miller, N. C. Handy, and J. E. Adams. Reaction path hamiltonian for polyatomic molecules. *J. Chem. Phys.*, 72:99–112, 1980.

[15] Mark A. Boyer, Ondrej Marsalek, Joseph P. Heindel, Thomas E. Markland, Anne B. McCoy, and Sotiris S. Xantheas. Beyond Badger's Rule: The Origins and Generality of the Structure-Spectra Relationship of Aqueous Hydrogen Bonds. *J. Phys. Chem. Lett.*, 10(5):918–924, mar 2019.

[16] C. Pimentel, George and L. McClellan, Aubrey. *The Hydrogen Bond*. W. H. Freeman And Company, 1960.

[17] Joseph A Fournier, Christopher J Johnson, Conrad T Wolke, Gary H Weddle, Arron B Wolk, and Mark A Johnson. Vibrational spectral signature of the proton defect in the three-dimensional $H^+(H_2O)_{21}$ cluster. *Science*, 344(6187):1009–1012, 2014.

[18] J-W Shin, NI Hammer, EG Diken, MA Johnson, RS Walters, TD Jaeger, MA Duncan, RA Christie, and KD Jordan. Infrared signature of structures associated with the $H^+(H_2O)_n$ ($n = 6$ to 27) clusters. *Science*, 304(5674):1137–1140, 2004.

[19] Conrad T. Wolke, Joseph A. Fournier, Laura C. Dzugan, Matias R. Fagiani, Tuguldur T. Odbadrakh, Harald Knorke, Kenneth D. Jordan, Anne B. McCoy, Knut R. Asmis, and Mark A. Johnson. Spectroscopic snapshots of the proton-transfer mechanism in water. *Science*, 354(6316):1131–1135, 2016.

[20] Mitsuhiko Miyazaki, Asuka Fujii, Takayuki Ebata, and Naohiko Mikami. Infrared spectroscopic evidence for protonated water clusters forming nanoscale cages. *Science*, 304(5674):1134–1137, 2004.

[21] RE Miller. The vibrational spectroscopy and dynamics of weakly bound neutral complexes. *Science*, 240(4851):447–453, 1988.

[22] K Nauta and RE Miller. Formation of cyclic water hexamer in liquid helium: The smallest piece of ice. *Science*, 287(5451):293–295, 2000.

[23] C. J. Fecko. Ultrafast hydrogen-bond dynamics in the infrared spectroscopy of water. *Science*, 301(5640):1698–1702, sep 2003.

[24] Martin Thämer, Luigi De Marco, Krupa Ramasesha, Aritra Mandal, and Andrei Tokmakoff. Ultrafast 2d ir spectroscopy of the excess proton in liquid water. *Science*, 350(6256):78–82, 2015.

[25] HJ Bakker and H-K Nienhuys. Delocalization of protons in liquid water. *Science*, 297(5581):587–590, 2002.

[26] MF Kropman and HJ Bakker. Dynamics of water molecules in aqueous solvation shells. *Science*, 291(5511):2118–2120, 2001.

[27] Anne Willem Omta, Michel F Kropman, Sander Woutersen, and Huib J Bakker. Negligible effect of ions on the hydrogen-bond structure in liquid water. *Science*, 301(5631):347–349, 2003.

[28] Richard M Badger. A relation between internuclear distances and bond force constants. *J. Chem. Phys.*, 2(3):128–131, 1934.

[29] Richard M Badger. The relation between the internuclear distances and force constants of molecules and its application to polyatomic molecules. *J. Chem. Phys.*, 3(11):710–714, 1935.

[30] JC Dearden. Rectilinear correlation between oh stretching frequency and o...o distance in intermoleculary and intramolecularly hydrogen bonded compounds. *Nature*, 206(4989):1147, 1965.

[31] Sotiris S Xantheas and Thom H Dunning Jr. *Ab Initio* studies of cyclic water clusters $(H_2O)_n$, n=1-6. i. optimal structures and vibrational spectra. *J. Chem. Phys.*, 99:8774–8792, 1993.

[32] Xiaosong Li, Lei Liu, and H Bernhard Schlegel. On the Physical Origin of Blue-Shifted Hydrogen Bonds. *J. Am. Chem. Soc.*, 124(32):9639–9647, 2002.

[33] Quanli Gu, Carl Trindle, and Joseph L Knee. Communication: Frequency shifts of an intramolecular hydrogen bond as a measure of intermolecular hydrogen bond strengths. *J. Chem. Phys.*, 137:091101, 2012.

[34] Weizhou Wang, Yu Zhang, Baoming Ji, and Anmin Tian. On the correlation between bond-length change and vibrational frequency shift in halogen-bonded complexes. *J. Chem. Phys.*, 134(22):224303, 2011.

[35] A Lautié, F Froment, and A Novak. Relationship between nh stretching frequencies and n...o distances of crystals containing nh...o hydrogen bonds. *Spec. Lett.*, 9(5):289–299, 1976.

[36] Engen Libowitzky. Correlation of o-h stretching frequencies and o-h...o hydrogen bond lengths in minerals. *Monatshefte für Chemie / Chemical Monthly*, 130(8):1047–1059, Aug 1999.

[37] Jorly Joseph and Eluvathingal D Jemmis. Red-, Blue-, or No-Shift in Hydrogen Bonds: A Unified Explanation. *J. Am. Chem. Soc.*, 129(15):4620–4632, 2007.

[38] A. Novak. Hydrogen Bonding in Solids Correlation of Spectroscopic and Crystallographic Data. In *Large Molecules*, pages 177–216. Springer Berlin Heidelberg, Berlin, Heidelberg, 1974.

[39] Bo Berglund, Jan Lindgren, and Jörgen Tegenfeldt. O-H and O-D Stretching Vibrations in Isotopically Dilute HDO Molecules in Some Solid Hydrates. *J. Mol. Struct.*, 43(2):169–177, feb 1978.

[40] Thomas Steiner. The hydrogen bond in the solid state. *Angew. Chem. Int. Ed.*, 41(1):48–76, 2002.

[41] Kersti Hermansson, Sören Knuts, and Jan Lindgren. The OH Vibrational Spectrum of Liquid Water from Combined *ab Initio* and Monte Carlo Calculations. *J. Chem. Phys.*, 95(10):7486–7496, 1991.

[42] Evangelos Miliordos, Edoardo Aprà, and Sotiris S Xantheas. Optimal geometries and harmonic vibrational frequencies of the global minima of water clusters $(H_2O)_n$, $n = 2-6$, and several hexamer local minima at the ccsd(t) level of theory. *J. Chem. Phys.*, 139(11):114302, 2013.

[43] G. Gilli and P. Gilli. Towards an Unified Hydrogen-Bond Theory. *J. Mol. Struct.*, 552(1-3):1–15, sep 2000.

[44] Ross H. McKenzie, Christiaan Bekker, Bijyalaxmi Athokpam, and Sai G Ramesh. Effect of Quantum Nuclear Motion on Hydrogen Bonding. *J. Chem. Phys.*, 140(17):174508, 2014.

[45] Ram S Bhatta, Prasad P Iyer, Ali Dhinojwala, and Mesfin Tsige. A Brief Review of Badger-Bauer Rule and its Validation from a First-Principles Approach. *Mod. Phys. Lett. B*, 28(29):1430014, 2014.

[46] Yu Zhang, Ning MA, and Wei-Zhou Wang. Correlation between bond-length change and vibrational frequency shift in hydrogen-bonded complexes revisited. *Acta Phys. Chim. Sin.*, 28(3):499–503, 2012.

[47] Kersti Hermansson. Redshifts and blueshifts of oh vibrations. *Int. J. Quantum Chem.*, 45(6):747–758, 1993.

[48] S. A. Corcelli, C. P. Lawrence, and J. L. Skinner. Combined electronic structure/molecular dynamics approach for ultrafast infrared spectroscopy of silute HOD in liquid H_2O and D_2O. *J. Chem. Phys.*, 120(17):8107–8117, may 2004.

[49] C. P. Lawrence and J. L. Skinner. Vibrational spectroscopy of HOD in liquid D_2O. III. spectral diffusion, and hydrogen-bonding and rotational dynamics. *J. Chem. Phys.*, 118(1):264–272, jan 2003.

[50] Joel D. Eaves, Andrei Tokmakoff, and Phillip L. Geissler. Electric field fluctuations drive vibrational dephasing in water. *J. Phys. Chem. A*, 109(42):9424–9436, oct 2005.

[51] Francesco Paesani, Sotiris S. Xantheas, and Gregory A. Voth. Infrared spectroscopy and hydrogen-bond dynamics of liquid water from centroid molecular dynamics with an ab initio-based force field. *J. Phys. Chem. B*, 113(39):13118–13130, oct 2009.

[52] Jared D. Smith, Richard J. Saykally, and Phillip L. Geissler. The effects of dissolved halide anions on hydrogen bonding in liquid water. *J. Am. Chem. Soc.*, 129(45):13847–13856, nov 2007.

[53] Rossend Rey, Klaus B. Møller, and James T. Hynes. Hydrogen bond dynamics in water and ultrafast infrared spectroscopy. *J. Phys. Chem. A*, 106(50):11993–11996, dec 2002.

[54] M. J. Frisch, G. W. Trucks, H. B. Schlegel, G. E. Scuseria, M. A. Robb, J. R. Cheeseman, G. Scalmani, V. Barone, B. Mennucci, G. A. Petersson, H. Nakatsuji, M. Caricato, X. Li, H. P. Hratchian, A. F. Izmaylov, J. Bloino, G. Zheng, J. L. Sonnenberg, M. Hada, M. Ehara, K. Toyota, R. Fukuda, J. Hasegawa, M. Ishida, T. Nakajima, Y. Honda, O. Kitao, H. Nakai, T. Vreven, J. A. Montgomery, Jr., J. E. Peralta,

F. Ogliaro, M. Bearpark, J. J. Heyd, E. Brothers, K. N. Kudin, V. N. Staroverov, R. Kobayashi, J. Normand, K. Raghavachari, A. Rendell, J. C. Burant, S. S. Iyengar, J. Tomasi, M. Cossi, N. Rega, J. M. Millam, M. Klene, J. E. Knox, J. B. Cross, V. Bakken, C. Adamo, J. Jaramillo, R. Gomperts, R. E. Stratmann, O. Yazyev, A. J. Austin, R. Cammi, C. Pomelli, J. W. Ochterski, R. L. Martin, K. Morokuma, V. G. Zakrzewski, G. A. Voth, P. Salvador, J. J. Dannenberg, S. Dapprich, A. D. Daniels, Ö. Farkas, J. B. Foresman, J. V. Ortiz, J. Cioslowski, and D. J. Fox. Gaussian 09 revision d.01. Gaussian, Inc., Wallingford, CT 2009.

[55] Vincenzo Barone. Anharmonic vibrational properties by a fully automated second-order perturbative approach. *J. Chem. Phys.*, 122(1):014108, 2005.

[56] Laura C. Dzugan, Jamie Matthews, Amitabha Sinha, and Anne B. McCoy. Role of torsion-vibration coupling in the overtone spectrum and vibrationally mediated photochemistry of ch$_3$ooh and hooh. *J. Phys. Chem A*, 121(48):9262–9274, 2017.

[57] Lauri Halonen and Tucker Carrington. Fermi resonances and local modes in water, hydrogen sulfide, and hydrogen selenide. *J. Chem. Phys.*, 88(7):4171–4185, 1988.

[58] Laura C. Dzugan, Jamie Matthews, Amitabha Sinha, and Anne B. McCoy. Correction to "role of torsion-vibration coupling in the overtone spectrum and vibrationally mediated photochemistry of ch$_3$ooh and hooh". *J. Phys. Chem. A*, 122(21):4909–4909, 2018.

[59] Ondrej Marsalek and Thomas E. Markland. Quantum dynamics and spectroscopy of *ab initio* liquid water: The interplay of nuclear and electronic quantum effects. *J. Phys. Chem. Lett.*, 8(7):1545–1551, 2017. PMID: 28296422.

[60] Stefan Grimme, Jens Antony, Stephan Ehrlich, and Helge Krieg. A consistent and accurate ab initio parametrization of density functional dispersion correction (dft-d) for the 94 elements h-pu. *J. Chem. Phys.*, 132(15):154104, 2010.

[61] Florian Weigend and Reinhart Ahlrichs. Balanced basis sets of split valence, triple zeta valence and quadruple zeta valence quality for h to rn: Design and assessment of accuracy. *Phys. Chem. Chem. Phys.*, 7(18):3297–3305, 2005.

[62] E. J. Bylaska, W. A. de Jong, N. Govind, K. Kowalski, T. P. Straatsma, M. Valiev, D. Wang, E. Apra, T. L. Windus, J. Hammond, P. Nichols, S. Hirata, M. T. Hackler, Y. Zhao, P.-D. Fan, R. J. Harrison, M. Dupuis, D. M. A. Smith, J. Nieplocha, V. Tipparaju, M. Krishnan, Q. Wu, T. Van Voorhis, A. A. Auer, M. Nooijen, E. Brown, G. Cisneros, G. I. Fann, H. Fruchtl, J. Garza, K. Hirao, R. Kendall, J. A. Nichols, K. Tsemekhman, K. Wolinski, J. Anchell, D. Bernholdt, P. Borowski, T. Clark, D. Clerc,

H. Dachsel, M. Deegan, K. Dyall, D. Elwood, E. Glendening, M. Gutowski, A. Hess, J. Jaffe, B. Johnson, J. Ju, R. Kobayashi, R. Kutteh, Z. Lin, R. Littlefield, X. Long, B. Meng, T. Nakajima, S. Niu, L. Pollack, M. Rosing, G. Sandrone, M. Stave, H. Taylor, G. Thomas, J. van Lenthe, A. Wong, , and Z. Zhang. Nwchem, a computational chemistry package for parallel computers, version 5.1, 2007.

[63] Mark A Boyer, Chloe S Chiu, David C McDonald, J Philipp Wagner, Jason E Colley, Dylan S Orr, Michael A Duncan, and Anne B McCoy. The role of tunneling in the spectra of $H5^+$ and $D5^+$ up to 7300 cm^{-1}. *J. Phys. Chem. A*, 124(22):4427–4439, jun 2020.

[64] Walter D Jones and William T Simpson. Calculation of Delocalization Contribution to Infrared Intensity. *J. Chem. Phys.*, 32(6):1747–1756, 1960.

[65] P. H. Dawson and A. W. Ticknee. Detection of H_5^+ in the Hydrogen Glow Discharge. *J. Chem. Phys.*, 37(3):672–673, 1962.

[66] O A Schaeffer and S O Thompson. The Exchange of Hydrogen and Deuterium in the Presence of Electrons and Ultraviolet Radiation. *Radiat. Res.*, 10(6):671, 1959.

[67] Timothy C Cheng, Biswajit Bandyopadhyay, Yimin Wang, Stuart Carter, Bastiaan J Braams, Joel M Bowman, and Michael A Duncan. Shared-Proton Mode Lights up the Infrared Spectrum of Fluxional Cations H_5^+ and D_5^+. *J. Phys. Chem. Lett*, 1:758–762, 2010.

[68] T R Geballe and T Oka. Detection of H_3^+ in Interstellar Space. *Nature*, 384(November):334, 1996.

[69] M. Okumura, L. I. Yeh, and Y. T. Lee. Infrared spectroscopy of the cluster ions $h_3^+ \cdot (h_2)_n$. *J. Chem. Phys.*, 88(1):79–91, 1988.

[70] Young K. Bae. Observation of High-Lying Vibrational Predissociation States of H_5^+. *Chem. Phys. Lett.*, 180(3):179–181, may 1991.

[71] Timothy C Cheng, Ling Jiang, Knut R Asmis, Yimin Wang, Joel M Bowman, Allen M Ricks, and Michael A Duncan. Mid- and Far-IR Spectra of H_5^+ and D_5^+ Compared to the Predictions of Anharmonic Theory. *J. Phys. Chem. Lett*, 3:24, 2012.

[72] Csaba Fábri, János Sarka, and Attila G. Császár. Communication: Rigidity of the Molecular Ion H_5^+. *J. Chem. Phys.*, 140(5):051101, feb 2014.

[73] Zhou Lin and Anne B. McCoy. Investigation of the structure and spectroscopy of h_5^+ using diffusion monte carlo. *J. Phys. Chem. A*, 117(46):11725–11736, 2013.

[74] Janos Sarka, Csaba Fabri, Tamas Szidarovszky, Attila G. Csaszar, Zhou Lin, and Anne B. McCoy. Modeling rotations, vibrations and rotational couplings in astructural molecules: A case study based on the h_5^+ molecular ion. *Mol. Phys.*, 113:1873–1883, 2015.

[75] Zhen Xie, Bastiaan J Braams, and Joel M Bowman. Ab-Initio Global Potential-Energy Surface for $H_5^+ \rightarrow H_3^+ + H_2$. *J. Chem. Phys.*, 122(22):8790, 2005.

[76] Yukio Yamaguchi, Jeffrey F. Gaw, and Henry F. Schaefer. Molecular clustering about a positive ion. structures, energetics, and vibrational frequencies of the protonated hydrogen clusters h+3, h+5, h+7, and h+9. *The Journal of Chemical Physics*, 78(6):4074–4085, 1983.

[77] Yukio Yamaguchi, Jeffrey F. Gaw, Richard B. Remington, and Henry F. Schaefer, III. The h_5^+ potential energy hypersurface: Characterization of ten distinct energetically low-lying stationary points. *J. Chem. Phys.*, 86(9):5072–5081, 1987.

[78] Paulo H Acioli, Zhen Xie, Bastiaan J Braams, and Joel M Bowman. Vibrational Ground State Properties of H_5^+ and its Isotopomers from Diffusion Monte Carlo Calculations. *J. Chem. Phys.*, 128(10):104318, 2008.

[79] Zhou Lin and Anne B. McCoy. Signatures of Large-Amplitude Vibrations in the Spectra of H_5^+ and D_5^+. *J. Phys. Chem. Lett.*, 3(24):3690–3696, 2012.

[80] Cristina Sanz-Sanz, Octavio Roncero, Alvaro Valdés, Rita Prosmiti, Gerardo Delgado-Barrio, Pablo Villarreal, Patricia Barragán, and Alfredo Aguado. Infrared spectrum of H_5^+ and D_5^+ : The simplest shared-proton model. *Phys. Rev. A - At. Mol. Opt. Phys.*, 84(6), 2011.

[81] Alvaro Valdés, Patricia Barragán, Cristina Sanz-Sanz, Rita Prosmiti, Pablo Villarreal, and Gerardo Delgado-Barrio. Theoretical simulations of the vibrational predissociation spectra of H_5^+ and D_5^+ clusters. *Theor. Chem. Acc.*, 131(4):1–7, 2012.

[82] Álvaro Valdés and Rita Prosmiti. Theoretical Investigation of the Infrared Spectra of the H_5^+ and D_5^+ Cations. *J. Phys. Chem. A*, 117(39):9518–9524, oct 2013.

[83] Álvaro Valdés and Rita Prosmiti. First-Principles Simulations of Vibrational States and Spectra for H_5^+ and D_5^+ Clusters Using Multiconfiguration Time-Dependent Hartree Approach. *Spectrochim. Acta - Part A Mol. Biomol. Spectrosc.*, 119:26–33, 2014.

[84] Álvaro Valdés and Rita Prosmiti. Theoretical Predictions on the Role of the Internal H_3^+ Rotation in the IR Spectra of the H_5^+ and D_5^+ Cations. *Phys. Chem. Chem. Phys.*, 16(13):6217–6224, apr 2014.

[85] M. J. Frisch, G. W. Trucks, H. B. Schlegel, G. E. Scuseria, M. A. Robb, J. R. Cheeseman, G. Scalmani, V. Barone, B. Mennucci, G. A. Petersson, H. Nakatsuji, M. Caricato, X. Li, H. P. Hratchian, A. F. Izmaylov, J. Bloino, G. Zheng, J. L. Sonnenberg, M. Hada, M. Ehara, K. Toyota, R. Fukuda, J. Hasegawa, M. Ishida, T. Nakajima, Y. Honda, O. Kitao, H. Nakai, T. Vreven, J. A. Montgomery, Jr., J. E. Peralta, F. Ogliaro, M. Bearpark, J. J. Heyd, E. Brothers, K. N. Kudin, V. N. Staroverov, R. Kobayashi, J. Normand, K. Raghavachari, A. Rendell, J. C. Burant, S. S. Iyengar, J. Tomasi, M. Cossi, N. Rega, J. M. Millam, M. Klene, J. E. Knox, J. B. Cross, V. Bakken, C. Adamo, J. Jaramillo, R. Gomperts, R. E. Stratmann, O. Yazyev, A. J. Austin, R. Cammi, C. Pomelli, J. W. Ochterski, R. L. Martin, K. Morokuma, V. G. Zakrzewski, G. A. Voth, P. Salvador, J. J. Dannenberg, S. Dapprich, A. D. Daniels, Ö. Farkas, J. B. Foresman, J. V. Ortiz, J. Cioslowski, and D. J. Fox. Gaussian. 09 Revision D.0. Gaussian, Inc., Wallingford, CT 2009.

[86] Bruce R Johnson and William P Reinhardt. Adiabatic Separations of Stretching and Bending Vibrations: Application to H_2O. *J. Chem. Phys.*, 85(8):4538–4556, 1986.

[87] Daniel T. Colbert and William H. Miller. A Novel Discrete Variable Representation for Quantum Mechanical Reactive Scattering via the S-matrix Kohn Method. *J. Chem. Phys.*, 96(3):1982–1991, feb 1992.

[88] Wolfram Research, Inc. Mathematica, Version 11.2. Champaign, IL, 2017.

[89] Melanie L. Marlett, Zhou Lin, and Anne B. McCoy. Rotation/torsion coupling in h_5^+, d_5^+, h_4d^+, and hd_4^+ using diffusion monte carlo. *J. Phys. Chem. A*, 119(35):9405–9413, 2015.

[90] Eric G. Diken, Jeffrey M. Headrick, Joseph R. Roscioli, Joseph C. Bopp, Mark A. Johnson, and Anne B. McCoy. Fundamental Excitations of the Shared Proton in the $H_3O_2^-$ and $H_5O_2^+$ Complexes. *J. Phys. Chem. A*, 109(8):1487–1490, mar 2005.

[91] G. E. Douberly, R. S. Walters, J. Cui, K. D. Jordan, and M. A. Duncan. Infrared Spectroscopy of Small Protonated Water Clusters, $H^+(H_2O)_n$ ($n = 2 - 5$): Isomers, Argon Tagging, and Deuteration. *J. Phys. Chem. A*, 114(13):4570–4579, apr 2010.

[92] B. Bandyopadhyay, T. C. Cheng, and M. A. Duncan. Proton Sharing in Hydronium-Nitrogen Clusters Probed with Infrared Spectroscopy. *Int. J. Mass Spectrom.*, 297(1-3):124–130, nov 2010.

[93] Arthur Adel and David M. Dennison. The infrared spectrum of carbon dioxide. Part I. *Phys. Rev.*, 43(9):716–723, may 1933.

[94] Wave H. Shaffer, Harald H. Nielsen, and L. H. Thomas. The rotation-vibration energies of tetrahedrally symmetric pentatomic molecules. i. *Phys. Rev.*, 56(9):895, nov 1939.

[95] Robert C. Herman and Wave H. Shaffer. The calculation of perturbation energies in vibrating rotating polyatomic molecules. *J. Chem. Phys.*, 16(5):453, dec 1948.

[96] Edwin L. Sibert. Theoretical studies of vibrationally excited polyatomic molecules using canonical van vleck perturbation theory. *J. Chem. Phys.*, 88(7):4378–4390, 1988.

[97] Justin Z. Gong, Devin A. Matthews, P. Bryan Changala, and John F. Stanton. Fourth-order vibrational perturbation theory with the watson hamiltonian: Report of working equations and preliminary results. *J. Chem. Phys.*, 149(11):114102, 2018.

[98] Andrew. Willetts, Nicholas C. Handy, William H. Green, and Dylan. Jayatilaka. Anharmonic corrections to vibrational transition intensities. *J. Phys. Chem.*, 94(14):5608–5616, 1990.

[99] P. Geerlings, D. Berckmans, and H. P. Figeys. The influence of electrical and mechanical anharmonicity on the vibrational transition moments of diatomic and polyatomic molecules. *J. Mol. Struct.*, 57(C):283–297, jan 1979.

[100] Julien Bloino and Vincenzo Barone. A second-order perturbation theory route to vibrational averages and transition properties of molecules: General formulation and application to infrared and vibrational circular dichroism spectroscopies. *J. Chem. Phys.*, 136(12):124108, mar 2012.

[101] Laura C. Dzugan, Jamie Matthews, Amitabha Sinha, and Anne B. McCoy. Role of torsion-vibration coupling in the overtone spectrum and vibrationally mediated photochemistry of ch_3ooh and hooh. *J. Phys. Chem. A*, 121(48):9262–9274, 2017.

[102] Kevin K. Lehmann. On the relation of child and lawton's harmonically coupled anharmonic–oscillator model and darling–dennison couplings. *J. Chem. Phys.*, 79(2):1098–1098, 1983.

[103] Anne B. McCoy and Edwin L. Sibert. Perturbative calculations of vibrational (j=0) energy levels of linear molecules in normal coordinate representations. *J. Chem. Phys.*, 95(5):3476–3487, 1991.

[104] Anne B. McCoy, Laura C Dzugan, Ryan J DiRisio, and Lindsey R Madison. Spectral signatures of proton delocalization in $h^+(h_2o)_{n=1-4}$ ions. *Faraday Discuss.*, 212:443–466, 2018.

[105] J. F. Gaw, A. Willetts, W. H. Green, and N. C. Handy. Spectro version 3.0. In Joel M. Bowman, editor, *Advances in Molecular Vibrations and Collision Dynamics*, volume 1B. JAI Press, Greenwich, CT, 1990.

[106] J. F. Stanton, J. Gauss, L. Cheng, M. E. Harding, D. A. Matthews, and P. G. Szalay. CFOUR, coupled-cluster techniques for computational chemistry, a quantum-chemical program package. With contributions from A.A. Auer, A. Asthana, R.J. Bartlett, U. Benedikt, C. Berger, D.E. Bernholdt, S. Blaschke, Y. J. Bomble, S. Burger, O. Christiansen, D. Datta, F. Engel, R. Faber, J. Greiner, M. Heckert, O. Heun, M. Hilgenberg, C. Huber, T.-C. Jagau, D. Jonsson, J. Jusélius, T. Kirsch, K. Klein, G.M. KopperW.J. Lauderdale, F. Lipparini, J. Liu, T. Metzroth, L.A. Mück, D.P. O'Neill, T. Nottoli, D.R. Price, E. Prochnow, C. Puzzarini, K. Ruud, F. Schiffmann, W. Schwalbach, C. Simmons, S. Stopkowicz, A. Tajti, J. Vázquez, F. Wang, J.D. Watts and the integral packages MOLECULE (J. Almlöf and P.R. Taylor), PROPS (P.R. Taylor), ABACUS (T. Helgaker, H.J. Aa. Jensen, P. Jørgensen, and J. Olsen), and ECP routines by A. V. Mitin and C. van Wüllen. For the current version, see http://www.cfour.de.

[107] Joon O. Jung and R. Benny Gerber. Vibrational wave functions and energy levels of large anharmonic clusters: A vibrational scf study of ar_{13}. *J. Chem. Phys.*, 105:10682–10690, 1996.

[108] Lawrence S. Norris, Mark A. Ratner, Adrian E. Roitberg, and R. B. Gerber. Møller–plesset perturbation theory applied to vibrational problems. *J. Chem. Phys.*, 105(24):11261–11267, 1996.

[109] Ove Christiansen. Møller–plesset perturbation theory for vibrational wave functions. *J. Chem. Phys.*, 119(12):5773–5781, 2003.

[110] Ove Christiansen. Vibrational structure theory: New vibrational wave function methods for calculation of anharmonic vibrational energies and vibrational contributions to molecular properties. *Phys. Chem. Chem. Phys.*, 9:2942–2953, 2007.

[111] James K.G. Watson. Simplification of the molecular vibration-rotation hamiltonian. *Mol. Phys.*, 15(5):479–490, 1968.

[112] Anne B. McCoy. The role of electrical anharmonicity in the association band in the water spectrum. *J. Phys. Chem. B*, 118(28):8286–8294, 2014.

[113] Anne B. McCoy and Edwin L. Silbert. Perturbative approaches to highly excited molecular vibrations of h_2o, d_2o, and hdo. *J. Chem. Phys.*, 92(3):1893–1901, 1990.

[114] J.J. Sakurai. *Modern Quantum Mechanics - Revised Edition.* Addison-Wesley Pub. Co, Reading, Massachusetts, 1994.

[115] Mark A. Boyer and Anne B. McCoy. PyVibPTn, a general package for vibrational perturbation theory, October 2021.

[116] Tosio Kato. *Perturbation Theory for Linear Operators.* Springer-Verlag, New York, 1976.

[117] Per Olov Löwdin. Studies in Perturbation Theory. IX. Connection Between Various Approaches in the Recent Development—Evaluation of Upper Bounds to Energy Eigenvalues in Schrödinger's Perturbation Theory. *J. Math. Phys.*, 6(8):1341, dec 1965.

[118] Peter R. Franke, John F. Stanton, and Gary E. Douberly. How to vpt2: Accurate and intuitive simulations of ch stretching infrared spectra using vpt2+k with large effective hamiltonian resonance treatments. *J. Phys. Chem. A*, 125(6):1301–1324, 2021.

[119] John H. Frederick and Clemens Woywod. General formulation of the vibrational kinetic energy operator in internal bond-angle coordinates. *J. Chem. Phys.*, 111(16):7255–7271, 1999.

[120] R. Meyer and Hs. H. Günthard. General internal motion of molecules, classical and quantum-mechanical hamiltonian. *J. Chem. Phys.*, 49(4):1510–1520, 1968.

[121] Herbert M. Pickett. Vibration—rotation interactions and the choice of rotating axes for polyatomic molecules. *J. Chem. Phys.*, 56(4):1715–1723, 1972.

[122] M. J. Frisch, G. W. Trucks, H. B. Schlegel, G. E. Scuseria, M. A. Robb, J. R. Cheeseman, G. Scalmani, V. Barone, G. A. Petersson, H. Nakatsuji, X. Li, M. Caricato, A. V. Marenich, J. Bloino, B. G. Janesko, R. Gomperts, B. Mennucci, H. P. Hratchian, J. V. Ortiz, A. F. Izmaylov, J. L. Sonnenberg, D. Williams-Young, F. Ding, F. Lipparini, F. Egidi, J. Goings, B. Peng, A. Petrone, T. Henderson, D. Ranasinghe, V. G. Zakrzewski, J. Gao, N. Rega, G. Zheng, W. Liang, M. Hada, M. Ehara, K. Toyota, R. Fukuda, J. Hasegawa, M. Ishida, T. Nakajima, Y. Honda, O. Kitao, H. Nakai, T. Vreven, K. Throssell, J. A. Montgomery, Jr., J. E. Peralta, F. Ogliaro, M. J. Bearpark, J. J. Heyd, E. N. Brothers, K. N. Kudin, V. N. Staroverov, T. A. Keith, R. Kobayashi, J. Normand, K. Raghavachari, A. P. Rendell, J. C. Burant, S. S. Iyengar, J. Tomasi, M. Cossi, J. M. Millam, M. Klene, C. Adamo, R. Cammi, J. W. Ochterski, R. L. Martin, K. Morokuma, O. Farkas, J. B. Foresman, and D. J. Fox. Gaussian 16 revision c.01, 2016. Gaussian Inc. Wallingford CT.

[123] Raghunathan Ramakrishnan and Guntram Rauhut. Semi-quartic force fields retrieved from multi-mode expansions: Accuracy, scaling behavior, and approximations. *J. Chem. Phys.*, 142(15):154118, 2015.

[124] Pauli Virtanen, Ralf Gommers, Travis E. Oliphant, Matt Haberland, Tyler Reddy, David Cournapeau, Evgeni Burovski, Pearu Peterson, Warren Weckesser, Jonathan Bright, Stéfan J. van der Walt, Matthew Brett, Joshua Wilson, K. Jarrod Millman, Nikolay Mayorov, Andrew R. J. Nelson, Eric Jones, Robert Kern, Eric Larson, C J Carey, İlhan Polat, Yu Feng, Eric W. Moore, Jake VanderPlas, Denis Laxalde, Josef Perktold, Robert Cimrman, Ian Henriksen, E. A. Quintero, Charles R. Harris, Anne M. Archibald, Antônio H. Ribeiro, Fabian Pedregosa, Paul van Mulbregt, and SciPy 1.0 Contributors. SciPy 1.0: Fundamental Algorithms for Scientific Computing in Python. *Nature Methods*, 17:261–272, 2020.

[125] Philip M. Morse. Diatomic molecules according to the wave mechanics. ii. vibrational levels. *Phys. Rev.*, 34(1):57–64, 1929.

[126] Edwin L. Sibert, James T. Hynes, and William P. Reinhardt. Fermi resonance from a curvilinear perspective. *J. Phys. Chem.*, 87(12):2032–2037, 1983.

[127] E. X. Li, I. M. Konan, M. I. Lester, and A. B. McCoy. Spectroscopic characterization of peroxynitrous acid in cis-perp configurations. *J. Phys. Chem. A*, 110:5607–13, 2006.

[128] Xu Zhang, Mark R. Nimlos, G. Barney Ellison, Mychel E. Varner, and John F. Stanton. Infrared absorption spectra of matrix-isolated cis, cis-hoono and its ab initio ccsd(t) anharmonic vibrational bands. *J. Chem. Phys.*, 124:084305, 2006.

[129] Xu Zhang, Mark R. Nimlos, G. Barney Ellison, Mychel E. Varner, and John F. Stanton. Vibrational overtone spectrum of matrix isolated cis, cis-hoono. *J. Chem. Phys.*, 126:174308, 2007.

[130] Anne S. Hansen, Trisha Bhagde, Yujie Qian, Alyssa Cavazos, Rachel M. Huchmala, Mark A. Boyer, Coire F. Gavin-Hanner, Stephen J. Klippenstein, Anne B. McCoy, and Marsha I. Lester. Infrared spectroscopic signature of a hydroperoxyalkyl radical (·qooh). *J. Chem. Phys.*, 156(1):014301, 2022.

[131] Santino J. Stropoli, Thien Khuu, Mark A. Boyer, Natalia V. Karimova, Coire Gavin-Hanner, Sayoni Mitra, Anton L. Lachowicz, Nan Yang, R. Benny Gerber, Anne B. McCoy, and Mark A. Johnson. Electronic and mechanical anharmonicities in the vibrational spectra of the H-bonded, cryogenically cooled X^{--}·HOCl (X=Cl, Br, I) complexes: Characterization of the strong anionic H-bond to an acidic OH group. Submitted to J. Chem. Phys., Manuscript No. JCP21-AR-04312, 2022.

[132] Bryan R. Henry. Use of local modes in the description of highly vibrationally excited molecules. *Accounts of Chemical Research*, 10:207–213, 6 1977.

[133] Joel M. Bowman. The self-consistent-field approach to polyatomic vibrations. *Acc. Chem. Res.*, 19:202–208, 1986.

[134] H. D. Meyer, U. Manthe, and L. S. Cederbaum. The multi-configurational time-dependent hartree approach. *Chemical Physics Letters*, 165:73–78, 1 1990.

[135] Marie Louise Grenier-Besson, Gilbert Amat, and Harald H. Nielsen. Higher-order rotation-vibration energies of polyatomic molecules. vi. *The Journal of Chemical Physics*, 36:3454, 7 1962.

[136] Harald H. Nielsen. The vibration-rotation energies of polyatomic molecules part ii. accidental degeneracies. *Physical Review*, 68:181, 10 1945.

[137] R. D. Amos, N. C. Handy, W. H. Green, D. Jayatilaka, A. Willetts, and P. Palmieri. Anharmonic vibrational properties of ch_2f_2 : A comparison of theory and experiment. *The Journal of Chemical Physics*, 95:8323, 8 1998.

[138] David M. Dennison. The vibrational levels of linear symmetrical triatomic molecules. *Physical Review*, 41:304, 8 1932.

[139] Edwin L. Sibert. Rotationally induced vibrational mixing in formaldehyde. *The Journal of Chemical Physics*, 90:2672–2683, 3 1989.

[140] Devin A Matthews and John F Stanton. Quantitative analysis of Fermi resonances by harmonic derivatives of perturbation theory corrections. *Mol. Phys.*, 107(3):213–222, 2009.

[141] Jan M. L. Martin, Timothy J. Lee, Peter R. Taylor, and Jean Pierre François. The anharmonic force field of ethylene, c_2h_4, by means of accurate ab initio calculations. *J. Chem. Phys.*, 103(7):2589–2602, 1995.

[142] Qin Yang, Marco Mendolicchio, Vincenzo Barone, and Julien Bloino. Accuracy and Reliability in the Simulation of Vibrational Spectra: A Comprehensive Benchmark of Energies and Intensities Issuing From Generalized Vibrational Perturbation Theory to Second Order (GVPT2). *Front. Astron. Sp. Sci.*, 8:77, may 2021.

[143] Byron T. Darling and David M. Dennison. The water vapor molecule. *Physical Review*, 57:128, 1 1940.

[144] Juana Vázquez and John F. Stanton. Treatment of fermi resonance effects on transition moments in vibrational perturbation theory. *Mol. Phys.*, 105(1):101–109, 2007.

[145] Masaharu Toyama, Takeshi Oka, and Yonezo Morino. Effect of vibration and rotation on the internuclear distance. *Journal of Molecular Spectroscopy*, 13:193–213, 1 1964.

[146] Juana Vázquez and John F. Stanton. Simple(r) algebraic equation for transition moments of fundamental transitions in vibrational second-order perturbation theory. *Mol. Phys.*, 104(3):377–388, 2006.

[147] Mark A. Boyer and Anne B. McCoy. A flexible approach to vibrational perturbation theory using sparse matrix methods. *J. Chem. Phys.*, 156(5):054107, feb 2022.

[148] Hubert Romanowski, Joel M. Bowman, and Lawrence B. Harding. Vibrational energy levels of formaldehyde. *The Journal of Chemical Physics*, 82:4155, 6 1998.

[149] Sergey V. Krasnoshchekov and Nikolay F. Stepanov. Polyad quantum numbers and multiple resonances in anharmonic vibrational studies of polyatomic molecules. *The Journal of Chemical Physics*, 139:184101, 11 2013.

[150] Y. Miller, G. M. Chaban, and R. B. Gerber. Theoretical study of anharmonic vibrational spectra of hno3, hno3–h2o, hno4: Fundamental, overtone and combination excitations. *Chemical Physics*, 313:213–224, 6 2005.

[151] Evan G. Buchanan, Jacob C. Dean, Timothy S. Zwier, and Edwin L. Sibert. Towards a first-principles model of fermi resonance in the alkyl ch stretch region: Application to 1,2-diphenylethane and 2,2,2-paracyclophane. *J. Chem. Phys.*, 138(6):064308/1–11, 2013.

[152] Anne S. Hansen, Rachel M. Huchmala, Emil Vogt, Mark A. Boyer, Trisha Bhagde, Michael F. Vansco, Casper V. Jensen, Alexander Kjærsgaard, Henrik G. Kjaergaard, Anne B. McCoy, and Marsha I. Lester. Coupling of torsion and OH-stretching in tert-butyl hydroperoxide. I. The cold and warm first OH-stretching overtone spectrum. *J. Chem. Phys.*, 154(16):164306, apr 2021.

[153] Emil Vogt, Rachel M. Huchmala, Casper V. Jensen, Mark A. Boyer, Jens Wallberg, Anne S. Hansen, Alexander Kjærsgaard, Marsha I. Lester, Anne B. McCoy, and Henrik G. Kjaergaard. Coupling of torsion and OH-stretching in tert-butyl hydroperoxide. II. The OH-stretching fundamental and overtone spectra. *J. Chem. Phys.*, 154(16):164307, apr 2021.